Probing the accretion physics of Sagittarius A*

Sebastiano Daniel Maximilian von Fellenberg

München 2022

Probing the accretion physics of Sagittarius A*

Sebastiano Daniel Maximilian von Fellenberg

Dissertation
der Fakultät für Physik
der Ludwig-Maximilians-Universität
München

vorgelegt von
Sebastiano Daniel Maximilian von Fellenberg
aus Zürich

München, den 13.10.2021

Erstgutachter: Prof. Dr. Reinhard Genzel
Zweitgutachter: Prof. Dr. Andreas Burkert
Tag der mündlichen Prüfung: 08.12.2021

Contents

List of Figures

List of Tables

Zusammenfassung

Das Galaktische Zentrum und das darin befindende massereiche Schwarze Loch Sagitarrius A* (Sgr A*) stellt einen der exotischsten Orte des Universums dar, welcher der Menschheit bekannt ist. In dieser Dissertation untersuche ich zwei verschiedene Aspekte des Galaktischen Zentrum: den Akkretionsfluss in der direkten Umgebung von Sgr A*, sowie die Verteilung der jungen Sterne, die sich in der unmittelbaren Nachbarschaft des Schwarzen Loches befinden.

Die in dieser Disseration vorgestellte Arbeit hat zu drei neuartigen Beobachtungen der spektralen Energieverteilung (englisch: Spectral Energy Distribution, SED) von Sgr A* geführt, welche ich in den ersten drei Kapitel vorstelle. Im letzten Kapitel der Thesis stelle ich meine Resultate zur Population von jungen Sterne im Galaktischen Zentrum vor.

Das erste Kapitel handelt von dem gleichzeitigen Nachweis von Sgr A* in zwei Ferninfrarot-Beobachtungsbändern bei Wellenlängen von 160 µm und 100 µm. Dies sind die ersten Beobachtungen von Sgr A* in diesem Wellenlängenbereich und wurden mit der PACS Kamera on-board des Weltraumteleskops Herschel aufgezeichnet. Die Messung wurden mit Hilfe einer maßgeschneiderten Datenreduktion ermöglicht, die eine differentielle Flussmessungen im Ferninfroten mit einem bisher unerreichten Rauschpegel erlaubt. Dies führt zum ersten Nachweis des variablen Flusses mit einer Signifikanz von 4.5σ bei 160 µm und 1.6σ bei 100 µm. Die Entdeckung des variablen Flusses bestätigt, dass die SED im Sub-mm-Bereich ihr Maximum erreicht und ermöglicht die Bestimmung der Elektronendichte, der Magnetfeldstärke und der Elektronentemperatur im Akkretionsfluss. In Kombination mit modernen ALMA-Beobachtungen von Sgr A* deuten diese Ergebnisse auf niedrigere Sub-mm-Flüsse hin als bis dato angenommen wurde. Die Messergebnisse erfordern aus diesem Grund höhere Elektronentemperaturen im Akkretionsfluss. Dies deutet darauf hin, dass der Akkretionsfluss im Sub-mm- und teilweise auch im mm-Bereich optisch dünn ist.

Im zweiten Kapitel nutze ich die ersten drei Jahre der interferometrischen GRAVITY-Beobachtungen, welche am Very Large Telescope Interferometer durchgefuehrt wurden, um die Flussverteilung von Sgr A* im Nahinfraroten zu untersuchen. Aus den GRAVITY-Daten erstelle ich die erste kohärente Flussmessung von Sgr A*, die 2019 mit dem neuartigen Dual-Beam-Beobachtungsmodus beobachtet wurde. Zusätzlich, verwende ich Lichtkurven aus den Jahren 2017 und 2018, die bereits in der Literatur veröffentlicht wurden. Aufgrund der sehr hohen räumlichen Auflösung von GRAVITY wird diese Sgr A*-Flussmessung nicht durch das Licht von nahegelegenen Sternen gestört, was ähnliche auf adaptive Optik gestützte Studien in der Vergangenheit stark einschränkte. Außerdem konnte ich

das Licht des Akkretionsflusses von Sgr A* zu jedem Messzeitpunkt nachweisen, eine Neuerung gegenüber den vorherrgehenden Studien, in welchen nur hellere Zustände von Sgr A* beobachtet werden konnten. Infolgedessen bin ich in der Lage, die erste rein empirische und nicht konfusionslimitierte Flussverteilung von Sgr A* zu erstellen und die 2.2 µm-Flussquantile zu messen. Durch den Vergleich mehrerer statistischer Modelle der Flussverteilung kann ich nachweisen, dass die Flussverteilung logarithmisch rechtsschief ist und nur schlecht durch eine Lognormalverteilung beschrieben wird. Im Gegensatz dazu ist die Flussverteilung gut durch ein Zweikomponentenmodell beschrieben: eine Log-Normalverteilung zur Beschreibung der Ruheemission in Kombination mit einer zweiten Komponente, die einem Potenzgesetz folgt. In diesem Szenario werden die hellen Nahinfrarot- und Röntgenflares in lokalisierten und aufgeheizten Zonen des Akkretionsstroms erzeugt, die sich von der variablen Ruheemission unterscheiden.
Das dritte Kapitel in dieser Dissertation untersucht die Eigenschaften eines solchen Flares. Ich berichte über den Nachweis eines simultanen hellen Nahinfrarot- und eines moderaten Röntgenflare. Hierbei verwende ich die Kontrollkamera von GRAVITY, um H-Band-Beobachtungen gleichzeitig zu den interferometrischen K-Band-Beobachtung zu erstellen. Desweiteren kombiniere ich diese beiden Nahinfrarot-Lichtkurven mit gleichzeitigen Beobachtungen durch die Weltraumteleskope Spitzer, Chandra und NuSTAR.
Mit Hilfe der so gewonnen Flussmessung modelliere ich die Emissionsregion im Flare-Szenario. Ich berechne die SED des Flares unter Berücksichtigung der Synchrotron- und Synchrotron-Selbst-Compton-Emission. Dies erlaubt mir, die Eigenschaften der für die Emission verantwortlichen Elektronenpopulation abzuleiten. Hierbei stelle ich fest, dass die mäßige Röntgenemission entweder sehr hohe Teilchendichten erfordert oder eine Teilchenverteilung erfordert, die bei Lorentz-Faktoren, die dem Röntgenband entsprechen, abgeschnitten ist.
Für das letzte Kapitel der Disseration analysiere ich SINFONI Archivdaten der zentralen $\sim 30'' \times 30''$ Bogensekunden des Galaktischen Zentrums. Diese Analyse führt zum bis dato größten spektroskopischen Katalog dieser Region. Durch die Kombination dieser Daten konnte ich über 2800 Sterne in jung und alt klassifizieren. Über 200 junge Sterne konnten spektroskpisch identifiziert werden. Für 35 dieser junge Sterne konnte eine vollständige Lösung der Orbitgleichungen gefunden werden. Für die anderen 166 Sterne sind nur fünf von sechs Phasenraumkoordinaten bekannt. Ich stelle eine neue, und statistisch formale, Methode vor, welche die Bestimmung der Posteriorverteilung der Phasenraumkoordinaten erlaubt. Diese neue Methode erlaubt es mir, die Posteriorverteilung der Orbitelemente zu bestimmen und die Posteriorverteilung des Drehmoments der jungen Sterne zu bestimmen. Damit kann ich zeigen, dass mindestens vier verschiedene kinematische Strukturen im Galaktischen Zentrum statistisch signifkant sind. Ich bestätige die Präsenz der bekannten verdrehten Sternenscheibe, die sich im Uhrzeigersinn dreht, und der Sternenscheibe im Gegenuhrzeigersinn. Desweiteren kann ich eine neue Sternenscheibe im Galaktischen Zentrum nachweisen. Diese reichhaltige dynamische Struktur ist konsistent mit einer lokalen Bildung der jungen Sterne. Ich favorisiere die Entstehung der jungen Sternen nach Kollision zweier Molekülgaswolken.

Summary

The Galactic Center, and the massive black hole Sagittarius A* (Sgr A*) therein, represent one of the most exotic places known to mankind. In this thesis, I present two aspects of the Galactic Center: the accretion flow in the direct proximity of the massive Black Hole and the distribution of young stars in its neighbourhood.

The thesis has led to three novel observations of Sgr A*'s spectral energy distribution (SED), which I present in the first three chapters of the thesis. In the last chapter of the thesis, I present my results on the young star population found in the Galactic Center.

In the first chapter, I report on the simultaneous detection of Sgr A* in two far-infrared observation bands at 160 µm and 100 µm. These are the first observations of Sgr A* in this wavelength regime obtained using the PACS camera on-board the Herschel space-telescope. The measurements are enabled by a custom-tailored data reduction pipeline, which allow far-infrared differential flux measurements in the Galactic Center at an unprecedented noise level. This led to the detection of variable flux at a significance level of 4.5σ at 160 µm and 1.6σ at 100 µm. The detection of variable flux confirms the turn-over of the SED in the sub-mm, and constrains the electron density, magnetic field strength and electron temperature. The results, in combination with modern ALMA observations of Sgr A*, imply lower than previously measured sub-mm fluxes of Sgr A* which require higher electron temperatures. This implies that the accretion flow is optically thin in the sub-mm, and parts of the mm regime.

In the second chapter, I use the first three years of interferometric GRAVITY observations to study the flux distribution of Sgr A*. I derive the first coherent flux measurement of Sgr A* obtained from the novel dual beam observing mode in 2019. Furthermore, I use light curves of the year 2017 and 2018 which were published in literature before. Due to the very high spatial resolution of GRAVITY Sgr A*'s flux is unconfused from the light of near-by stars, which severely limited similar adaptive optics-assisted studies in the past. This allows, for the first time, to detect Sgr A* at times it is observed with GRAVITY. In consequence, I report the first purely-empirically derived and unconfused flux distribution of Sgr A* and am able to infer the 2.2 µm flux quantiles. I compare several statistical probability distributions to the observed flux distribution. I find that the flux distribution is log-right skewed and only poorly described by a log-normal distribution. The flux distribution is well described by a two-component model: a quiescent log-normal distribution in combination with a powerlaw tail. This manifests the two component consistent of a flaring and quiescence state scenario proposed for Sgr A*. In this scenario,

occasional bright near-infrared and X-ray flares are generated in localized and heated zones of the accretion flow, which are distinct from the variable quiescence emission.
In the third chapter of this thesis, I study the properties of such a flare. I report the detection of a simultaneous near-infrared bright and moderate X-ray flare. I use the acquisition camera of GRAVITY to derive simultaneous H-band observations alongside the interferometric K-band observation. I combine the two near-infrared light curves with simultaneous observations obtained by the Spitzer, Chandra and NuSTAR spacecrafts. With the help of these flux measurements I model the emission region in the flare-scenario and compute the flare's SED taking into account synchrotron and synchrotron self-Compton emission. This allows me to derive the properties of electron population responsible for the emission. I find that the moderate X-ray emission either requires very high particle densities or a particle distribution which is cut at Lorentz factors corresponding to the X-ray band.
In the last chapter of the thesis I present the largest spectroscopic survey of the Galactic Center to date ($\sim 30'' \times 30''$). Combining all available SINFONI observations of the Galactic Center allows me to classify over 2800 stars into young and old stars. My work now includes over 230 young stars, for 35 of which full orbital solutions have been determined. For the other 198 young stars only five of six phase space coordinates are known. I present a new, and statistically rigours method to determine their posterior phase space distribution. This allows to determine the posterior distribution of orbital elements, and, specifically, to determine the ensemble angular momentum direction. Using the new statistical method I show that at least four kinematic structures in the Galactic Center are statistically significant. I confirm the presence of a warp of the clockwise disk, and the presence of a counter-clockwise disk. In addition to the previously introduced, but disputed kinematic features, I show that third disk of young stars is present in the Galactic Center. This rich dynamical structure is consistent with an in-situ star formation scenario, and specifically, I favour a star formation event after the collision of two giant molecular clouds.

Chapter 1

Introduction

1.1 A massive Black Hole in the center of our Galaxy

Almost 90 years ago, Karl Jansky pointed his “merry-go-around” antenna in the backyard of the Bell Laboratories to the sky. He quickly detected a source of radio radiation coming from outside the earth’s atmosphere, and first thought it to be a phenomenon related to the sun. Continuing his observations for over a year led him to discard his original hypothesis: the location of the source correlated with the sidereal time and would shift slightly from day-to-day, only to to arrive at its original location after a year had passed. While he considered different explanations, he found his observations best explained by an extra-solar radio signal (Jansky, 1933b), marking the first detection of a radio source outside the solar system. This spectacular discovery led to significant recognition in the scientific community and general public (Smothers, 1998). It was Jansky himself who realized the peculiarity of the observation: “This possible explanation proves even more intresting when it is discovered that the coordinates given by the data are very nearly the same as those for the center of the Milky Way, the coordinates of which point are approximately right ascension 17 hours, 30 minutes, declination - 30 degrees (in the Milky Way in the direction of Sagittarius) [...]” (Jansky, 1933a). Just how interesting his observations would unravel to be, however, was of course never revealed to him. In the following century, more and more evidence was collected which ultimately led to the ‘discovery of a supermassive compact object at the centre of our galaxy’ – for which the 2020 Nobel Prize in Physics was awarded to Prof. Reinhard Genzel and Prof. Andrea Ghez.

1.1.1 Early observational evidence

Balick and Brown, 1974 detected a very bright radio source at 2.7 GHz and 8.1 GHz using the National Radio Astronomy Observatory while studying the gas structure of the inner most region of the Galactic Center. The source was unresolved, and they placed a source size limit of less than one arcsecond on the source’s extension. By referencing the source location to the infrared sources discovered in the Galactic Center (Rieke and Low, 1973), Balick and Brown, 1974 concluded that the source must be present therein – and that it in fact might even define the Galactic Center. It was quickly determined that the size of the source must be very small, and that the apparent increase in source size with wavelength was due to dust scattering (Kellermann et al., 1977). The radio spectrum of this novel source was determined to be flat/slowly rising, confirming the non-thermal nature of the source. From this, e.g. Brown et al., 1978 inferred a brightness temperature of larger than 1×10^7 K, a magnetic field strength of ~200 G and concluded that the source must be smaller than 10 AU. While Lynden-Bell, 1969 suggested the existence of a black hole in the Sagittarius A region, and Lynden-Bell and Rees, 1971 even listed the detection of a compact radio source as a critical observation for the establishment of one, the authors of the early radio observations were remarkably cautious about drawing that conclusion. Kellermann et al., 1977 hypothesised that the newly detected source Sgr A* could be the electromagnetic counterpart to a Black Hole. In contrast, the group of authors around Brown, Lo and Balick seemed to favour a radio binary star scenario in which energetic accretion from one source to another caused the observed emission. Remarkably, Balick and Brown, 1974 did not once mention black holes in their detection paper.

1.1.2 Collecting circumstantial evidence

Around the same time, the first infrared observations with resolution high enough to resolve point sources in the central 20″ of the Galactic Center were published (Neugebauer et al., 1978; Becklin et al., 1978). Therein, the first observations of the now famous infrared sources (IRS#) were presented. In those papers, it was quickly concluded that the near infrared counterpart to Sgr A* was not observed, but the sources were of stellar nature or were gas emission clouds. Soon after, in a series of papers, the group around C. H. Townes studied the gas dynamics of the gas clouds in the central 20″ using infrared observations of the 12.8 µm Neon II emission line (Wollman et al., 1976; Wollman et al., 1977; Lacy et al., 1979; Lacy et al., 1980; Lacy et al., 1982).
They inferred that a large mass must be responsible for the cloud velocity dispersion of ~100 km/s and line velocities of up to 260 km/s. They preferred a peaked central mass of $\sim 5 \times 10^6\, M_\odot$ in addition to a similarly massive, but extended, stellar component. The statistical significance of the result was low due to the small number of clouds. In the last paper of the series (Lacy et al., 1982), they concluded that a massive Black Hole is not necessary to explain their observations. However, these observations had tantalized the community on the possible existence of a massive black hole as origin of the radio source Sgr A*: In a proceedings article of the 1982 API conference on the Galactic Center M.J. Rees wrote: "The compact radio source at the Galactic Center seems unique in our Galaxy – it is unlikely to be a pulsar, a radio star or a supernova. When we find a unique object in a unique location, it is not "ad hoc" to invoke a special explanation." (Rees, 1982). In the same article, he proposed the first theoretical model of Sgr A* as an accreting black hole based on low-level accretion onto a massive black hole, fed only by interstellar gas. Therein, he noted that the radio emission observed was consistent with a torus of electrons emitting thermal synchrotron emission with $\gamma_e < 10$ at a radius of $r > 10 r_g$.

Despite this early excitement, the establishment of Sgr A* as luminous counterpart of

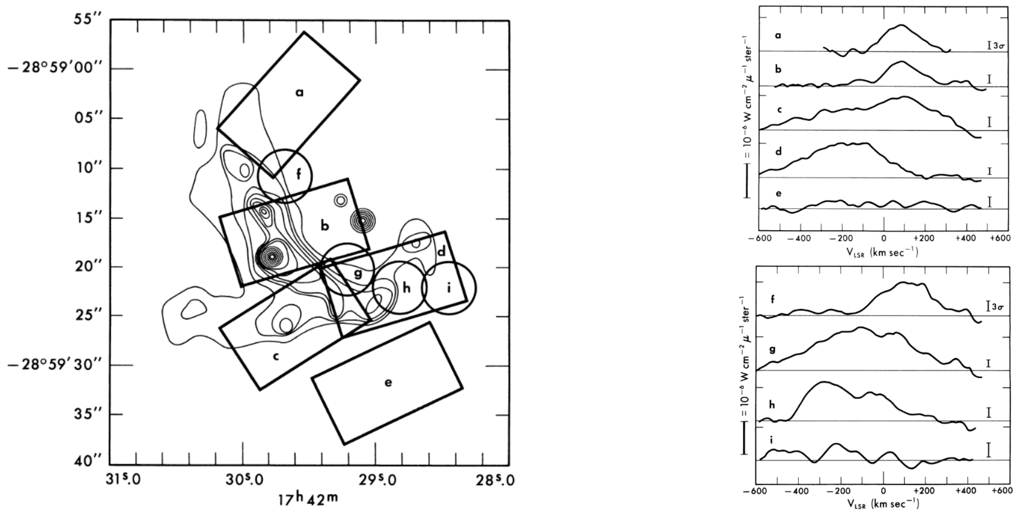

Figure 1.1: Dispersion measurement of the central parsecs of the Galaxy, presented in Wollman et al., 1977. The large radial velocity dispersion were the first indications from dynamical measurements that the Galactic Center might harbour a black hole. The left panel shows the location of apertures for which the radial profiles were extracted. The right panel shows the corresponding radial velocity dispersion determined from the Neon II emission line.

a black hole was still two decades away. Crawford et al., 1985 combined infrared observations and sub-mm observations of gas streams to better constrain the mass distribution in the Galactic Center. They found the mass distribution to be inconsistent with that of a spherical isothermal star cluster, and again found evidence for the presence of a point mass$\sim 5 \times 10^6\, M_\odot$. Genzel and Townes, 1987 reviewed and further refined the measurement of the mass distribution in the Galactic Center. They showed that the mass distributed flattened in inner the inner parsec of the Galaxy and that it requires a dark mass of $2.5 \ldots 3 \times 10^6$ $\mathrm{M}_\odot$ (Figure 1.2). They considered the case that this dark mass is a massive Black Hole “substantial, but not fully convincing”. They argued that observed radio emission from Sgr A* does not require a massive black hole, but could also be explained by a ‘normal’ black hole with mass below $100\, M_\odot$. In arguing for a black hole they preferred the gas motion and dynamics arguments, which however many viewed as not convincing (enough) because the gas dynamics are influenced by other forces than gravity as well (Genzel, 2021).

At the end of the 80s, Sgr A*’s SED was for the first time constrained in the sub-mm regime (Zylka and Mezger, 1988; Zylka et al., 1992; Serabyn et al., 1992). These observations showed that the flat/slowly rising radio spectrum was inverted at wavelengths shorter than 10 mm.

By the mid 90s the following observational facts of the long wavelength SED of Sgr A* had been established, which I summarize by following chapter 6.1 of the review by Morris and Serabyn, 1996 (see also discussion above):

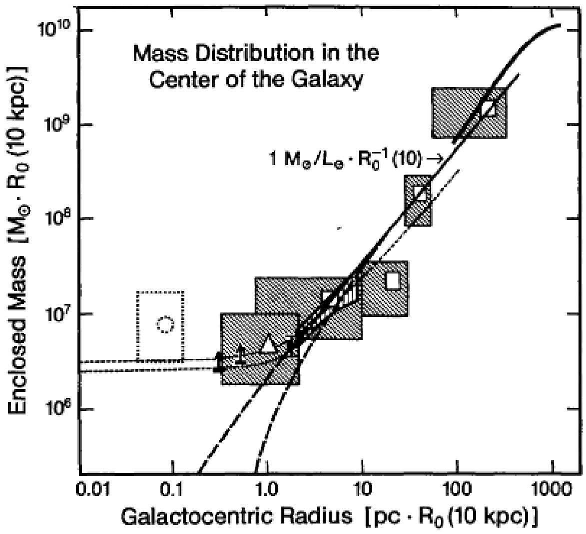

Figure 1.2: The mass distribution of the inner 1000 parsec of the Galaxy, adapted from Genzel and Townes, 1987. The thin black line shows the mass distribution derived from the 2 µm surface brightness distribution, which is continued by the dashed line to 0.1 pc. The continued line fails to match the observations, which are matched by the thin dotted line which includes a central point mass of $3 \times 10^6 M_\odot$.

- Sgr A* was resolved in VLBI observations at radio frequencies. However, the observed source size is not the intrinsic source size, but the size of the scatter-broadened halo of the intrinsic source. The measured size decreases proportional to λ^2, consistent with a foreground scattering screen. The smallest measured source size at that time was 124 µas.

- This radio flux of Sgr A* is variable. The variability is on the order of a few 10% on a longer than day time scale.

- Sgr A* shows a flat / slowly rising radio SED ($F_\nu \propto \nu^{0...0.3}$) from 1 GHz to 100 GHz.

- At frequencies higher than 100 GHz, Sgr A* spectrum shows an excess of emission which dominates the luminosity.

- At frequencies higher than 670 GHz, observations of Sgr A* were not feasible and only upper limits existed.

- Stringent constraints on the near infrared flux of Sgr A* of a few milli-Jansky implied that the spectra had to fall off steeply in the far-infrared or mid-infrared regime, which constrained the total luminosity of the radio source to ~40 $L_\odot$. This luminosity estimate placed the Black Hole candidate many orders of magnitude below its Eddington luminosity.

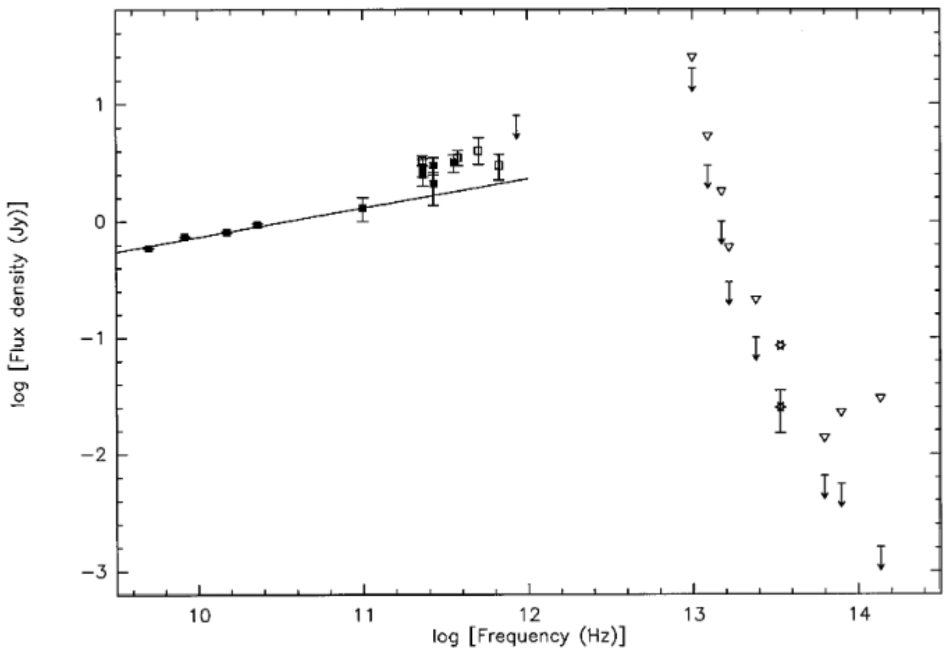

Figure 1.3: Measured radio spectrum of Sgr A*, presented in Morris and Serabyn, 1996.

This prompted a wide range of theoretical attention to modeling the radio source as an accretion flow of a massive black hole. Falcke et al., 1993 modeled the radio and sub-mm emission using a jet-disk model and argued that the jet would be $<$ 1 mas due to the low accretion. Melia, 1992; Melia et al., 1992; Melia, 1994 studied accretion flow models of Sgr A* and estimated a mass of $\sim 2 \times 10^6$ $M_\odot$ based on the radio and sub-mm SED. Narayan et al., 1995; Abramowicz et al., 1995 introduced the concept of an advection-dominated accretion flow for Sgr A*. In such an accretion flow the energy transport is processed through advection rather than being radiated. This is achieved by decoupling the electron and ion temperatures, i.e. the energy transfer between the hotter ions and the cooler electrons is suppressed. Because the emission is assumed to be synchrotron emission, the lighter electrons dominate the emission, explaining the faintness of the sources. Their modeling satisfied radio and sub-mm emission measurements of Sgr A* and respected the existing upper limits in the mid and near infrared and was again consistent with a Black Hole with a mass of a few million solar masses (Figure 1.4).

Despite this, a central mass of a few million solar masses was not required by the radio observations of the spectrum: Ozernoy, 1989 presented a variety of alternative models: young pulsars, very massive stars, low-mass X-ray binaries, or a moderate mass Black Hole with mass of 300 $M_\odot$. Following up, Ozernoy, 1993 presented calculations that could explain the observed luminosity by wind accretion on to a moderate mass Black Hole.

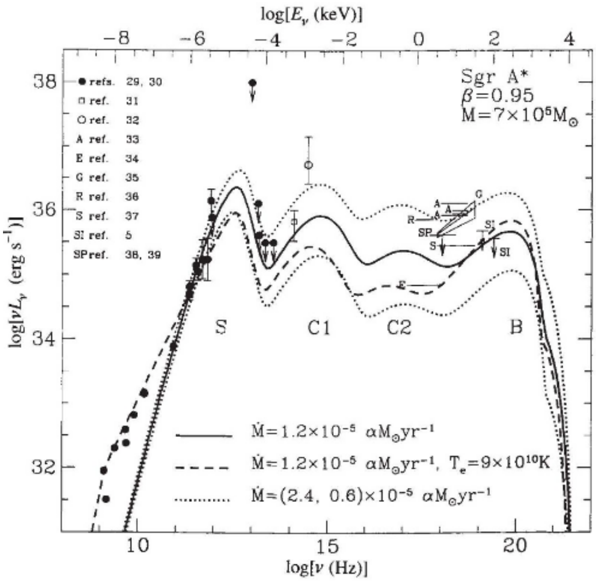

Figure 1.4: Advection Dominated Accretion Flow model of Sgr A* presented in Narayan et al., 1995: The ion temperature is decoupled from the electron temperature. This can explain the faintness of Sgr A* in the context of a million solar mass Black Hole. The model yields a good fit to the radio, mm and sub-mm data.

1.1.3 S2 – the smoking gun

Eckart et al., 1995 initiated the era of near infrared imaging of the Galactic Center with a resolution sufficient to resolve individual stars (Figure 1.5). Using shift-and-add speckle imaging as well as polarimatry they confirmed that none of the known IRS sources corresponded to the radio source. Eckart and Genzel, 1996 and Genzel et al., 1997 quickly added the proper motions of the first of these stars. They showed that the radial velocity dispersion of the stars increased towards the center, following a Keplerian profile, and showed that this increase was again consistent with the massive black hole hypothesis. Ghez et al., 1998 improved and confirmed these observations independently; and Ghez et al., 2000 measured the first accelerations of these stars which showed that the determination of full orbital solutions of the innermost stars would become feasible in the imminent future.

Ultimately, Schödel et al., 2002a were the first to determine the first full orbital solution of the star closest to the Black Hole: S2. This allowed for the first geometrical determination of the mass enclosed in its orbit: $(3.6 \pm 1.5) \times 10^6$ M$_\odot$, ultimately proving that Sgr A* is a Black Hole beyond reasonable doubt.

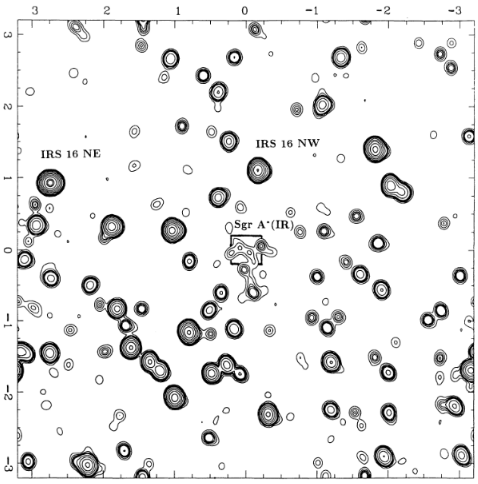

Figure 1.5: First NIR image to resolve stars in the central 3 arcseconds of Galaxy presented by Eckart et al., 1995. The images shows the star S2 close to apo-center, and showed that Sgr A* was not resolved as a continuum source.

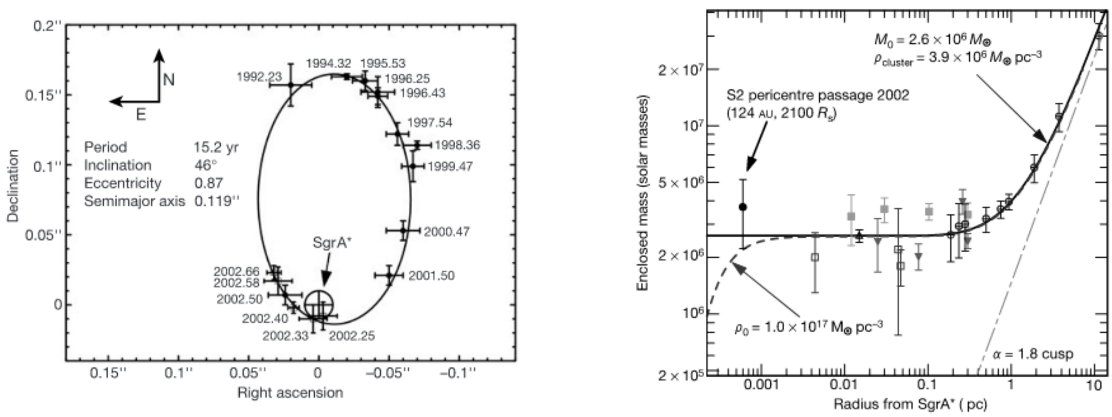

Figure 1.6: Left: Orbit of S2 around Sgr A* and right: the mass distribution in the central 0.001 to 10 pc of the Galaxy both presented by Schödel et al., 2002b. The astrometric measurements of the star showed that it is on a $\sim$16 yr orbit around Sgr A*, constraining the enclosed mass to $(3.6\pm1.5)\times10^6$ $M_\odot$. This improved the mass distribution substantially (compare with Figure 1.2), and showed beyond reasonable doubt that Sgr A* must harbour a massive Black Hole.

1.2 Observations of the accretion flow of Sagittarius A*

At around the same time the existence of a massive Black Hole in the Galactic Center was confirmed by the measurement of the stellar motions around it, Sgr A*'s variable emission in other wavelength regimes was reported. First, Baganoff et al., 1999 (and subsequent proceedings, refereed publication Baganoff et al., 2003a) reported the detection of a quiescent X-ray source at the location of Sgr A*. Soon after, Baganoff et al., 2001a reported the first detection of a bright X-ray flare from Sagittarius A*. Just two years later, with the advent of AO-assisted images of the Galactic Center, Sgr A*'s near infrared counterpart was discovered by Genzel et al., 2003a.
In the following two decades, Sgr A*'s spectrum, variability, polarization, and even dynamical properties have been closely studied. In the next three sub-sections I summarize the commonly accepted observational facts that have since been established.

1.2.1 The radio, millimeter, sub-millimeter and far infrared observations

The radio SED of Sgr A* has been closely monitored, however, the facts established in the late 80s and 90s have not been dramatically challenged. Sgr A* is a variable radio source, with moderate variability on time scales of a few hours to days, most of which can be attributed to the source itself and not foreground effects (Macquart and Bower, 2006). Further, its flat/ slowly rising radio spectrum has been confirmed again and again, as have the λ^2 size dependence of its radio size (for a review, see for instance Genzel et al., 2010). Compared to the 90s, the advent of sub-mm interferometer arrays like BIMA, the Sub-mm Array (SMA) as well as ALMA, have established the presence of the "sub-mm bump", first reported by Zylka and Mezger, 1988 (Bower et al., 2003; Brinkerink et al., 2015; Liu et al., 2016). Here, the higher spatial resolution allows to better discern the source flux from the radiation of the surroundings. This enabled better photometry, but also allowed for un-confused measurements of the polarization. Bower et al., 2003 reported an intrinsic linear polarization of around 10%, which allowed for measurements of the rotation measure. Modern state-of-the-art ALMA observations confirmed these measurements and established a rotation measure of $5 \times 10^5\,\mathrm{radm}^2$. Using rotation measurements of a close-by pulsar as reference (Eatough et al., 2013), it could be shown that the Faraday rotation responsible for the the large rotation measure is induced in the inner $\sim$10 $\mathrm{R_S}$. From this an average mass flow rate $1 \times 10^{-8}\,M_\odot\,\mathrm{yr}^{-1}$ could be established, which showed little variation in the last two decades. Furthermore, the 230 GHz flux of Sgr A* is circularly polarized on the order of 1% (Bower et al., 2015; Bower et al., 2018).
Dexter et al., 2014 analyzed a large set of ALMA and SMA sub-mm lightcurves and determined a variability time scale of a few hours and the typical RMS at 230 GHz ranges from 30% to 60%. The sub-mm flux distribution is non-Gaussian and right-skewed, and peaks at a flux of $\sim$3 Jy (Subroweit et al., 2017).

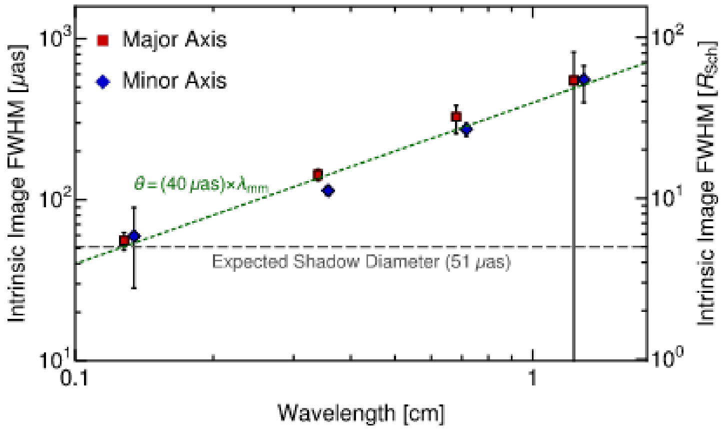

Figure 1.7: Radio size of the intrinsic source in Sgr A* as function of λ, reported by Johnson et al., 2018.

The λ^2 size scaling of the scattered source is very well established, with regular updates on the accuracy of the relation (e.g. Johnson et al., 2015; Johnson et al., 2018). By estimating the scattering kernel, the intrinsic source size can be measured, and affirming the quadratic size scaling with λ. Figure 1.7 shows a recent measurement of the relation by Johnson et al., 2018. At the time of writing, the Event Horizon Telescope (EHT) collaboration has not reported results on the first resolved images of the central 100 µas yet. Their analysis of the 3.5 mm VLBI images revealed a source with semi-major axis size of ~120 µas consistent with being circular once the scattering is taken into account (Issaoun et al., 2019).
At wavelengths shorter than 500 µm ground-based observations of Sgr A* become more and more difficult due to obscuration from the atmosphere. Bower et al., 2019 report the shortest wavelength observation using an interferometric measurement. Stone et al., 2016 reported a putative detection of variable flux at 250 µm using a differential flux measurement with Herschel. The first paper of this thesis extends the SED coverage of Sgr A* into the far infrared with a first detection of the variable flux component of Sgr A* at 160 and 100 µm.

1.2.2 Mid and near infrared observations

Between 100 µm and 4.5 µm only upper limits on the flux of Sgr A* are available (e.g. Schödel et al., 2011). Here, soon to be conducted space-observations of Sgr A* using the future James-Webb-Space-Telescope are expected to yield measurements of the variable, and average mid- and far-infrared flux.
In the mid and near infrared Sgr A* is regularly observed. Its variability has been studied by many authors (e.g. Do et al., 2009; Dodds-Eden et al., 2011). Recently, in a series of papers Hora et al., 2014 and Witzel et al., 2018 have published day-long differential light curves obtained from Spitzer mid-infrared observations. These long light curves allow to study the power spectrum of the variability. The long-term power spectrum is a power-law,

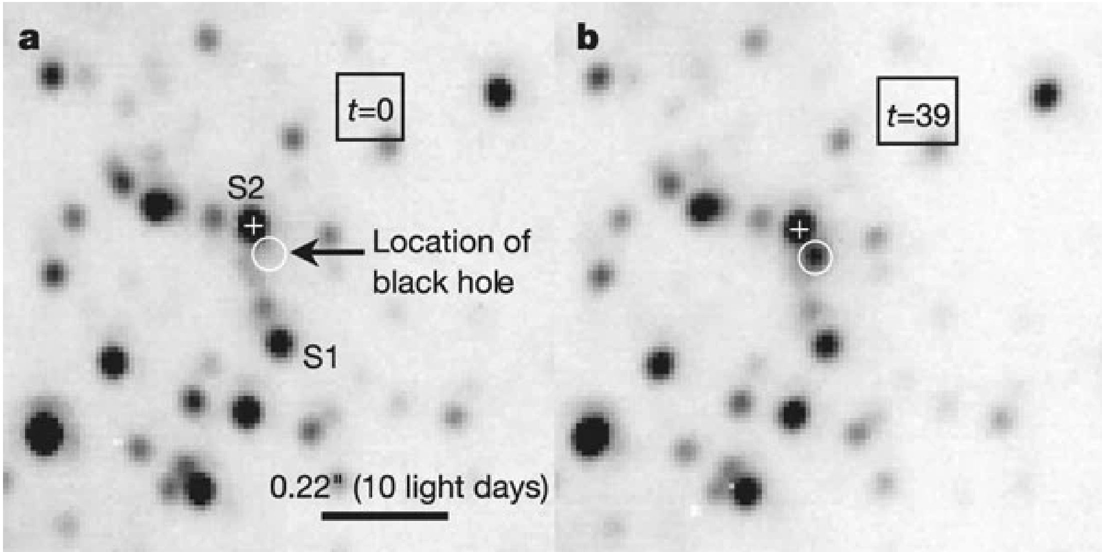

Figure 1.8: First near infrared observations of a Sgr A* flare by Genzel et al., 2003a.

with a powerlaw slope of -2.12 ± 0.12. The power density decays to uncorrelated white noise with a characteristic time scale of ∼240 min. There are indications of a second short-time scale spectral break at ∼3 min, after which the power spectrum seems to steepen to values ~ -6. The authors are however cautious if the secondary break is significant. Sgr A* is best studied in the near-infrared K-band (∼2.2 µm), in which the stars surrounding it are regularly monitored. In the K-band (and all other NIR and mid-infra-red observations) Sgr A* shows constant variability, intermittent by very bright flux excursions. By studying the flux distribution in the K- and L-band Dodds-Eden et al., 2011 showed that Sgr A* is a log-normally distributed source. If bright flares occur, the flux distribution is even more right-skewed, which led Dodds-Eden et al., 2011 to postulate that the brightest flux excursions are generated in a secondary physical process. This was contested in Witzel et al., 2012 and Witzel et al., 2018, where such a power-law tail to the flux distribution was not significant due to the difficulty to disentangle source flux from surrounding stellar sources. The detection of a very bright flare by Do et al., 2019, however, indicated that that indeed such a high flux tail exists (see Do et al., 2019, and G. Witzel private com.). The second paper of this thesis presents a study of the flux distribution of Sgr A* obtained with the 4-telescope interferometer instrument GRAVITY. The very high spatial resolution of GRAVITY overcomes the confusion limit of 10-meter class telescopes and thus allows to disentangle Sgr A*'s flux from those of the stars around it. The study revealed that Sgr A* is continuously detected, and that its bright flares indeed stand out against the log-normal quiescence flux. Furthermore, this allowed to determine quantiles of the flux distribution, establishing a median source flux density of (1.1 ± 0.3) mJy.

Given that the flux density of Sgr A* at its sub-mm peak is around ∼3 Jy and its near-infrared flux is more than a thousand times fainter, it is clear that the overall spectral slope between the sub-mm and near infrared has to be falling. The exact spectral slope

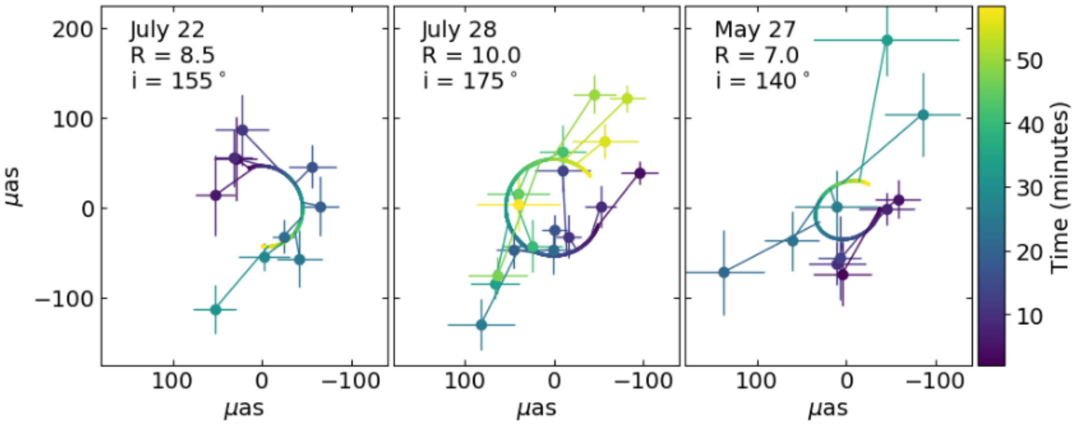

Figure 1.9: Dynamical measurement of light centroid for three flares observed with GRAVITY in 2018 (GRAVITY Collaboration et al., 2018a; Gravity Collaboration et al., 2020d). The line shows of the best fit general relativistic orbit of a point-mass on a free-fall orbit around Sgr A*.

is however difficult to measure. Hornstein et al., 2007 have argued for a flux density independent spectral index of $F_\nu \propto \nu^{-0.6\pm0.2}$. On the contrary, Gillessen et al., 2006 and others have argued for a flux density dependent spectral index that increases with flux density. In the statistical analysis of Witzel et al., 2018 a clear correlation of the spectral index with K- and M-band flux density is found. Using spectroscopic H- and K-band data, Ponti et al., 2017 presented a bright NIR flare with slight variations in spectral index as function of flux density. Similarly, the third paper in this thesis presents a bright flare with temporally resolved near-infrared SED. For this flare, a slight variation of the K- to H-band spectral slope was observed.

The first detected flares (Figure 1.8 Genzel et al., 2003a) showed characteristic peak features in their light curve, with a time scale comparable to the innermost stable orbit of Sgr A*. While many flares show such characteristic peaks, a modulation with a characteristic frequency corresponding to the innermost stable orbit was not fully convincingly shown (e.g. Do et al., 2009; Witzel et al., 2018). Thus it was not possible to establish dynamical measurements from the light curve alone.

GRAVITY Collaboration et al., 2018b reported the first dynamical observations of the accretion flow of Sgr A* (Figure 1.9). In this paper, three bright near infrared flares were reported, which showed circular motion around the mass center of the Sgr A*. The time scale of the flares was on the order of one to two hours, and the light curve was double peaked. For one of the flares, polarimetric measurements were conducted. This flare showed a linear polarization fraction of ∼30% and a characteristic ‘loop’ in the Q-U plane. Through modeling the emission as a hot spot embedded in an ambient field, Gravity Collaboration et al., 2020b inferred a structured magnetic field, with a substantial poloidal component. Through modeling the measured motion of three flares with a free falling point-mass and relativistic ray-tracing GRAVITY Collaboration et al., 2018b; Gravity

Collaboration et al., 2020d, inferred an orbital radius of $4.5\,\mathrm{R_S}$, a hot-spot size of $2.5\,\mathrm{R_S}$ and a line of sight-inclination of 140°.

1.2.3 X-ray observations

The Galactic Center is now routinely studied with the X-ray observatories Chandra, XMM-Newton and NuSTAR (e.g. Neilsen et al., 2013; Barrière et al., 2014; Neilsen et al., 2015; Ponti et al., 2015). The X-ray source consistent with Sgr A* has two components, one that extends to Bondi-radius scales with a luminosity of 3.5×10^{33} erg/s, typically thought to originate from a thermal plasma not associated with the radio source (Baganoff et al., 2003a; Yuan et al., 2003b). The second component is irregularly occurring flares, that can reach up to a few 1×10^{35} erg/s. These flares show a power-law or log-normal distribution on top of a Poissonian background (Neilsen et al., 2015). The bright X-ray flares show a power-law spectrum, and for flares robustly detected with NuSTAR this power-law extends up to to the highest energies detectable ($\sim$70 keV, Barrière et al., 2014). However, the near infrared bright, and X-ray moderate flare presented in the last paper of this thesis seems to indicate that a truncation at higher energies is possible. The large and fast variability of the flares constrain the physical location of the flare to be very close to the black hole (Barrière et al., 2014). The X-ray and NIR flares strongly correlate temporally. Typically, X-ray flares are shorter than their NIR counterparts (e.g. Ponti et al., 2017, and flare presented in this thesis). Boyce et al., 2019 found X-ray flares leading NIR flares by a 10 to 20 minute margin significant at $\sim 1\sigma$, but not at $\sim 3\sigma$. The flare analysed here, does not show a significant temporal lead in X-ray (Boyce et al. 2021, in prep.).

1.2.4 The infra-red to X-ray flare picture

The observations above, and the results of this thesis, have lead to a comprehensive picture of the mechanism behind the near infra-red and X-ray variable flux. The sub-mm flux peaks at around 500 µm, and is consistent with a single-temperature, thermal electron plasma which radiates synchrotron emission. The electron temperature in the plasma is $T_e = 10^{11}$ K, the electron density is $n_e \sim 10^{6 \ldots 7}$ cm^{-3} and the magnetic field strength is a few tens of Gauss. The emission is optically thin in the $\sim$1.3 mm observing band, and the peak is set by the critical frequency of synchrotron and not the transition from optically thin to optically thick (e.g. Liu et al., 2016; Bower et al., 2019, and first paper in this thesis). It is not clear whether the thermal emission extends to the near infrared. If so, it requires hotter zones in the accretion flow which extend the SED into the mid and near infrared. Due to the absence of constraining observations in the far and mid-infrared it is not established if this indeed happens. There is, however, no shortage of theoretical attempts that allow to heat electrons accordingly (e.g. Ressler et al., 2017; Davelaar et al., 2018; Dexter et al., 2020).

It is much more difficult to explain the observed rising spectrum of the NIR flares (in $\nu^\alpha \propto \nu F_\nu$) with such a thermal extension of the sub-mm component. The concurrent observation of X-ray flux during the NIR flares further requires the flare SED to extend many orders of magnitudes. Furthermore, the statistical analysis of the light curve revealed that the flux distribution is log-right skewed, and the right-skewedness is induced by the flux contribution of bright flares (Dodds-Eden et al., 2011; Witzel et al., 2018; Do et al., 2019, and second paper presented in this thesis). Consequently, the flares have been modelled with either synchrotron only or some combination of synchrotron and Compton up-scattered emission (e.g. Baganoff et al., 2001a; Genzel et al., 2003a; Yusef-Zadeh et al., 2006; Dodds-Eden et al., 2009; Dodds-Eden et al., 2010; Eckart et al., 2012; Ponti et al., 2017, and third paper of this thesis). While different in the subtleties of the models, these models all share that the emission originates from a distinct part of the accretion flow in which electrons are heated into a non-thermal electron distribution. Yuan et al., 2009 proposed that magnetic reconnection in the accretion flow, in analogy to solar flares, could cause the electron acceleration. Modern particle in cell (PIC) simulations of plasmas show that magnetic reconnection as well as turbulent electron heating could serve as viable heating mechanisms (Sironi and Beloborodov, 2020; Wong et al., 2020; Werner and Uzdensky, 2021); and there have been recent attempts to incorporate these mechanisms into simulations of the acceleration flow (Ball et al., 2016; Mao et al., 2016; Dexter et al., 2020; Dexter et al., 2020; Ripperda et al., 2020; Scepi et al., 2021).

In this infra-red to X-ray flare picture, the flares present a unique opportunity to test the strong field limit of General Relativity: If the flares result from transiently accelerated electrons in the accretion flow, which continue their free-fall orbit around Sgr A* after their initial acceleration, they can serve as test particles to probe the space-time metric around the black hole. The observation of the trajectories of three bright flares presented by GRAVITY Collaboration et al., 2018a are consistent with this picture, yield the first step in precise measurements of flare orbits and thus General Relativity. Already now, they yield the best constraints on the enclosed mass within their orbit of a few Schwarzschild radii. This is more than a factor of thousand better than the constraints obtained from close-by stars. These observations, and coming observations of flares will thus serve as corner stones for precision tests of General Relativity in the coming decade.

1.3 Young stars in the Galactic Center

In parallel to the discovery revolving around the Black Hole, the stars in its vicinity have been subject of intense study. Given that number of stars increase towards the Galactic Center, the presence of stars in the Galactic Center was expected. Indeed, the first infrared images that were able to peer through the dust extinction veil quickly revealed a large population of stars (Neugebauer et al., 1978; Becklin et al., 1978). These observations showed very bright, old giant, super giant and asymptotic giant branch stars. However, about a decade after these very first images, a population of very hot main sequence stars were detected (Allen et al., 1990; Krabbe et al., 1991). In the following I will first summarize the observations of these young stars in the Galactic Center. In a second step, I will discuss the different formation scenari that have been discussed in their context.

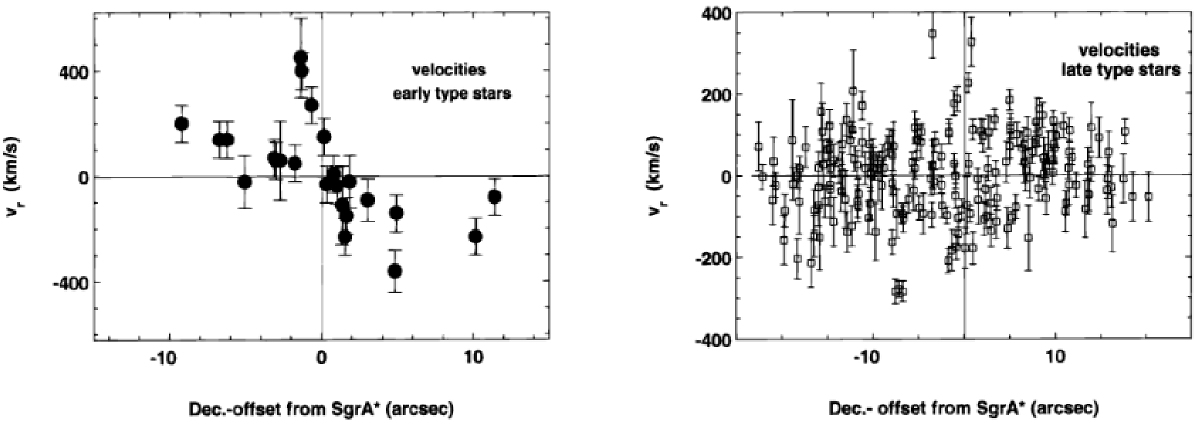

Figure 1.10: Radial veloctiy of young and old stars as function of projected distance presented by Genzel et al., 1996. The young stars show an ordered motion and are aligned in a “ring”.

1.3.1 Observations of the young stars

Allen et al., 1990 found several puzzling Br-γ emitting regions, and argued that of one these sources is a ‘young’ star of spectral type WN9/Ofpe, (see also Forrest et al., 1987 for an earlier but un-refereed detection, in which the authors however argued for an other-the-stellar nature.). Krabbe et al., 1991 used Fabry-Perot imaging of the Helium I line map observations of the Galactic center which had the necessary spatial and spectral resolution to detect more of these young stars, confirming their overabundance. These observations were subsequently confirmed and refined by many other studies (Krabbe et al., 1995; Blum et al., 1995; Libonate et al., 1995; Tamblyn et al., 1996).

In the following, the He-emission lines were identified with post-main sequence Wolf-Rayet (WR) type stars. This type of stars has such a short life expectancy that their formation must not have dated back more than a few million years.

After the presence of young stars was established, Krabbe et al., 1995 and Genzel et al., 1996 compiled an extensive list of radial velocities of the young and old stars in the Galactic Center. They showed that there was no preferred radial velocity direction as function of projected separation for the old stars. In contrast, the young stars showed a clear rotating pattern, and are aligned in a “ring” (Figure 1.10). These measurements were then confirmed in follow up-studies (Eckart and Genzel, 1997; Paumard et al., 2001).

With time, the number of known young stars increased. Genzel et al., 2000 presented an updated list of young stars, with velocity measurements of around 100 stars. These authors again showed that while the old stars are consistent with belong to a spherical (isotropic) cluster, the young stars rotate highly order manner. Most of the investigated young stars (29) showed a clockwise rotation, consistent with a stellar disk. The presence of this clockwise disk was in the following further corroborated by Levin and Beloborodov, 2003 who determined the 3D direction using a χ^2 fit to the observed stellar velocities.

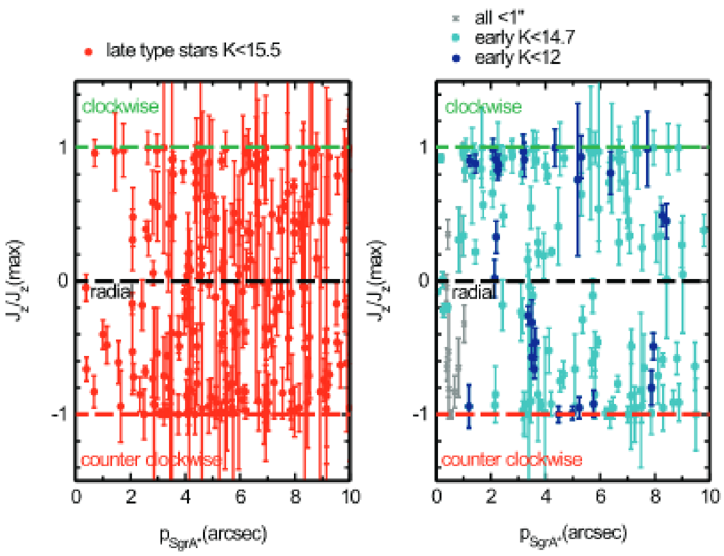

Figure 1.11: Projected angular momentum of the young and old stars in the Galactic Center as function of projected distance presented by Genzel et al., 2003. The old stars do not show a preferred angular momentum direction. The young stars show three different populations: a fraction of bright young (O and WR type) stars rotating in a clock wise disk, a fraction of brighter young stars (O and WR type, but also fainter) stars rotating in a counter-clockwise disk, and a population of fainter stars closer-in with random and more eccentric orbits.

The puzzle of the young stars was further complicated once the temporal baseline of observations and the ever increasing spatial resolution allowed for proper motion measurements of the inner most stars. Both Ghez et al., 1998 and Genzel et al., 2000 investigated the motions of these inner most stars ($> 1''$). Using spectroscopic observations, Genzel et al., 2000 found that these stars too are predominately young. However, the inner most young stars are fainter than the clockwise disk stars, and are typically main sequence B-stars. Using using high resolution and AO-assisted spectroscopy Ghez et al., 2003; Eisenhauer et al., 2005 confirmed this classification. These fainter, closer-in stars do not show the ordered clockwise motion of the O and WR, but show more random, eccentric orbits.
The last puzzle of the kinematic distribution of the young stars was added once the further out regions of the Nuclear Star Cluster were spectroscopically mapped out. Genzel et al., 2003 extended the study of young (and old) stars in the central region. They showed that in addition to the clockwise oriented brighter young star population and the more eccentric, randomly oriented inner young stars, a third population of brighter young stars in counter-clockwise rotation around the black hole exists (see Figure 1.11). Paumard et al., 2006 presented the first larger survey of the central five to ten arcseconds of the Galactic Center that was obtained entirely through integral field spectroscopy. They identified 50 young stars belonging to the clockwise disk system and 20 stars belonging to the counter-clockwise disk. The density of stars in both disks decreases with powerlaw functionality;

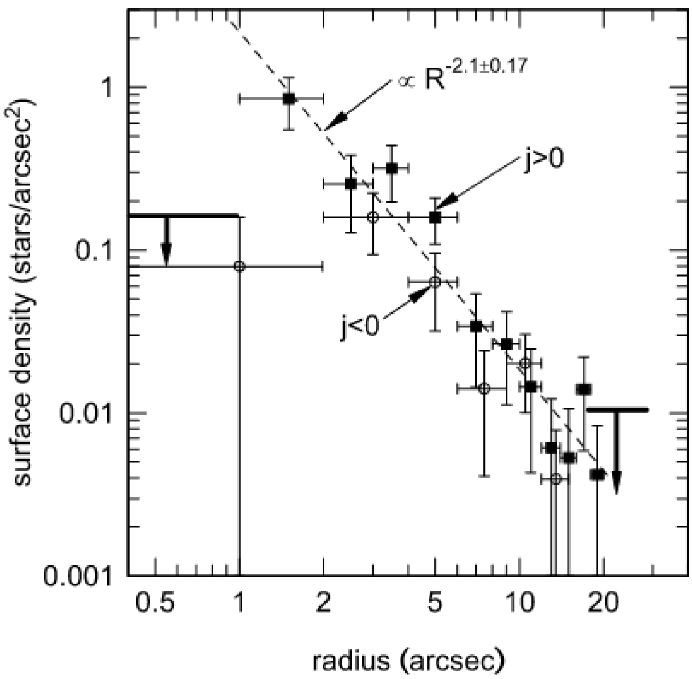

Figure 1.12: Surface density of young stars presented by Paumard et al., 2006. The filled points are derived from members of the clockwise disk system, the open circles show members of the counter clockwise disk system. The the powerlaw exponent of ~ -2.1 is derived from a thin disk model of a star disk. The counter clockwise disk starts at larger projected radii of $\sim 4''$, but shows the same slope as the clockwise disk stars.

the powerlaw exponent is $\alpha = -2.1 \pm 0.17$. They further confirm the sharp cut-off of ordered angular momentum of the clockwise disk in the inner most region found by Ghez et al., 1998; Genzel et al., 2000. Similarly, the counter-clockwise disk system shows a cut-off, albeit at larger radii of $\sim 3''$. They found that the orbits of the clockwise disk stars are rather circular, with eccentricities ~ 0.3, while the counter-clockwise disk stars have higher eccentricities.

With the advent of AO-assisted integral field spectroscopy by SINFONI (Bonnet et al., 2004), and its high resolution spectra of the young stars, their mass, age and metallicity could be accurately measured (Eisenhauer et al., 2005). Martins et al., 2007 used a radiative transfer code for stellar atmospheres called CMFgen (Hillier and Miller, 1998) to model stellar atmospheres of the WR and other young stars. They found that young stars in the clockwise disk have masses of ranging from $20\,M_\odot$ to $60\,M_\odot$. The authors determined the metallicity of the young stars to be roughly twice that of the sun. Confirming the findings of previous studies (Genzel et al., 2000; Paumard et al., 2001; Genzel et al., 2003; Paumard et al., 2006), these detailed atmospheric models reveal that the stars must have formed in a single star forming event not more than six million years ago. I show such a high resolution spectrum, and the best fit stellar atmosphere model on the left side of

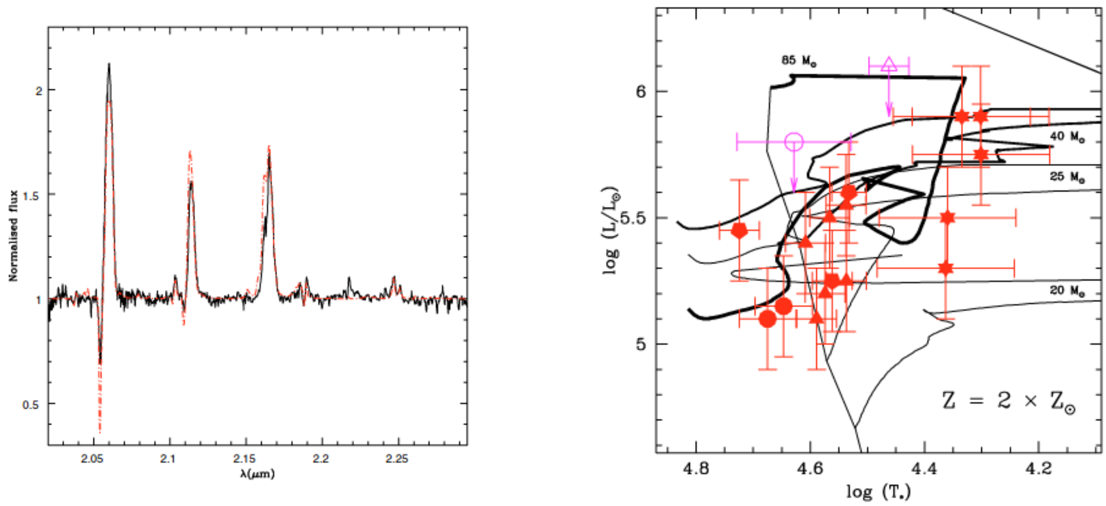

Figure 1.13: Right: K-band spectrum of the WN5/6 type star IRS13E2 together with best fit stellar atmosphere model. Right: Hertzsprung-Russel diagram of the 18 WR type stars studied. Both figures from Martins et al., 2007.

Figure 1.13. The right side of Figure 1.13 shows the Hertzsprung-Russel diagram of the 18 studied WR type stars.

The disputed kinematic structure of the young stars

The work of the late 90's and early 2000' established the presence a random population of B-stars in the central arcsecond the Galaxy, a clockwise disk extending from one to a few arcsecond, and a third counter-clockwise disk at larger distance from the black hole. However, in 2006, Lu et al., 2006 presented their first results on the dynamical properties of the young stars in the Galactic Center. They confirmed the basic findings of the clockwise disk found in the previous studies. While they confirm the presence of counter-clockwise moving stars, they argued the that the number of counter-clockwise moving stars is lower than reported in the early studies. Explicitly, they found only seven counter-clockwise moving stars, much less than found in Paumard et al., 2006. Finding inconsistent inclinations for a many of the counter clockwise stars, they argue that the counter clockwise feature is not significant. Three years later, the same group of authors update their findings using an updated set of astrometric and spectroscopic observations. In this study, they introduced a new statistical method which is now established: Monte Carlo sampling of stellar orbits under the assumption of a prior distribution of the missing z coordinate (Lu et al., 2009). Explicitly, they assumed an uninformed (flat) distribution of accelerations in a fixed black hole potential. This allowed them to draw random samples of the z coordinate, while taking into account the maximum allowed acceleration of the star based on its projected distance:

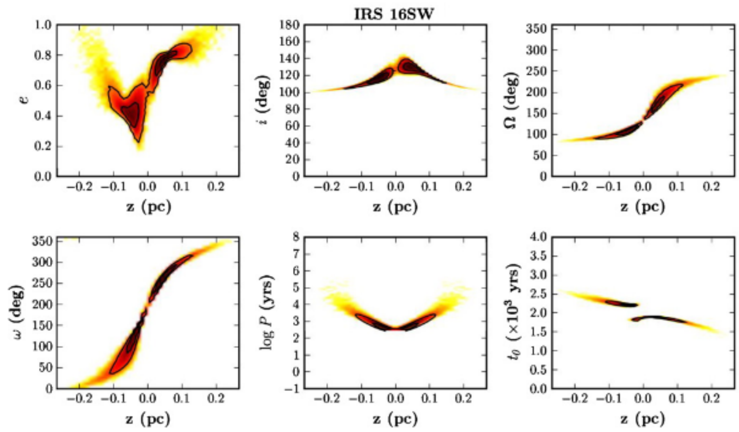

Figure 1.14: Posterior orbital element distribution for the star IRS16SW, assuming a prior z distribution(Lu et al., 2009)

$$a_{max} = \frac{GM}{\rho} \tag{1.1}$$

$$z_{a_{max}} = \sqrt{\frac{(-GM\rho)^{2/3}}{\mathcal{U}(0, a_{max})^{2/3}} - \rho}, \tag{1.2}$$

where $\rho = \sqrt{x^2 + y^2}$ is the projected distance. In combination with the other five phase space coordinates, determined from astrometric and spectroscopic observations, the posterior distribution of orbital elements can thus be calculated. An example of such a posterior distribution is shown in Figure 1.14. The clockwise disk stars have similar angular momenta and thus their posterior distributions overlap. This method therefore allows to determine the properties of the proposed star disk(s) by means of quantitative. By comparing their observations with simulations of an isotropic cluster Lu et al., 2009 reaffirmed their previous conclusion: the counter-clockwise disk is not significant.

However, the statistical method proposed by Lu et al., 2009, was in following refined by Bartko et al., 2009. In contrast to the agnostic uniform acceleration prior, these authors opted for a more informed approached: They assumed that the surface density distribution of the young stars is powerlaw, which had been confirmed in earlier analysis (see Figure 1.12). This information was than used to construct the so-called "stellar cusp prior". For this prior, the projected distance of a star, and the assumption of a powerlaw star distribution is used to derive a z-prior distribution. Using this different z-prior, Bartko et al., 2009 found the counter-clockwise disk to be significant. They further found that, at least under their prior assumption on the z-distribution, the angular momentum direction of the clockwise disk changes as function of radius. This was interpreted as a 'disk warp' of the clockwise disk. An illustration of the warped clockwise disk, together with the counter-clockwise disk is shown in Figure 1.15.

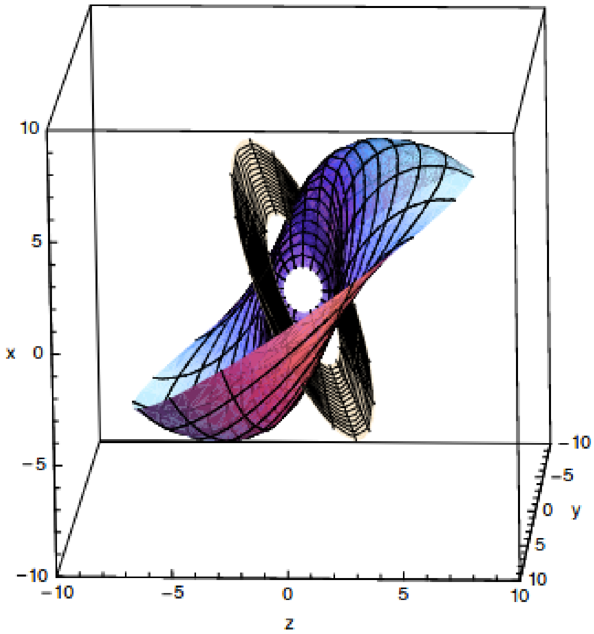

Figure 1.15: Schematic illustration of the warped clockwise disk together with the counter clockwise disk presented by Bartko et al., 2009. The angular momentum of the clockwise disk changes as function of radius, causing the disk to warp.

These findings were again challenged by Yelda et al., 2014. Using the uniform acceleration prior, these authors argued that neither the count-clockwise disk nor the warp of the clockwise disk are significant.

While somewhat technical, these subtle differences in the significance of kinematic features have important consequences on the star formation history of the young stars in the Galactic Center, which I will discuss in the next subsection.

1.3.2 Formation of the young star cluster

The observed star young star population(s) in the Galactic Center is a long standing problem for theoretical star formation studies. Given that the main sequence lifetime of the bright (O-WR type) young stars is only a few million years, their formation must have happened in the immediate past of the Galaxy. The observed population requires a star formation mass of $\sim 1.5 \times 10^4\, M_\odot$ (Krabbe et al., 1995). However, there is no evidence currently on-going star formation in the Galactic Center (Genzel et al., 2003). Thus the stars must have formed either by in-spiraling from outside the Galactic Center, have formed in in-falling gas clouds or haven been rejuvenated by star collisions (e.g.: Alexander, 2005).

In the following, I will discuss these three candidate processes along the lines of the review of Alexander, 2005 and the discussion of Genzel et al., 2003.

Rejuvenation of old stars

Morris, 1993 proposed that old stars in the Galactic Center may collide and thus rejuvenate and only appear to be young. However it was quickly shown that the collision rate for the stars at larger separation of $0.05''$ was to low to be a viable mechanism for young stars other than the isotropically distributed B-stars(Alexander, 1999). Thus, while theoretically intriguing, this scenario cannot explain the vast majority of young stars in the Galactic Center. Furthermore, the detailed study of the spectra of the young B-stars has revealed that these stars appear quite normal (Genzel et al., 2003). There is however a population of gas-cloud like objects in the central arcseconds which maybe remnants of such old-star collisions(Ciurlo et al., 2020).

In-spiraling of a young star cluster In order to explain the presence of the young stars in the Galactic Center, a suitable close-by star formation region needs to exist. Two such star formation regions exist: The Quintuplet cluster and the Arches cluster Intriguingly, the stars therein are fairly comparable to those in the Galactic Center (e.g. Gerhard, 2001). Such a young star cluster can migrate towards the Galactic Center via dynamical friction. For instance Portegies Zwart et al., 2003 showed that such a comparable cluster could migrate from a few parsec distance to the Galactic Center. However, in order to be stable against loosing a considerable fraction of stars, the cluster needs to collapse to very high density or possess a stabilizing central intermediate mass black hole (Hansen and Milosavljević, 2003). While the presence of an intermediate mass Black Hole in the Galactic Center is not ruled out, the parameter space for such a massive object has been substantially narrowed (Gravity Collaboration et al., 2020a, Gravity Collaboration, in prep.). Even if such a migration scenario is feasable, it is expected that a migrating cluster would leave a trail of young stars. However, large scale spectroscopy observations of the Galactic Center field have not revealed a large number of “trailing” young stars (Feldmeier-Krause et al., 2015), adding further evidence against the in-spiral scenario. This scenario is further complicated if more than one disk is present. If the counter-clockwise disk is significant, its presences would multiple cluster to have fallen in (e.g. Genzel et al., 2003). Thus, and especially if the secondary kinematic features are indeed significant, the in-spiraling scenario is disfavoured.

Star formation in an in-falling gas cloud

There are substantial gas reservoirs in the Galactic Center, such as the circum nuclear disk (CND). While the CND is clumpy, the gas density in its clumps is too low for effiecent star formation to take place (). Thus, in order to initiate star formation in the CND some external pressure would need to be exerted (Alexander, 2005). Three pathways to initiate star formation in the Galactic Center have been discussed: a Galactic Center duty-cycle, where star formation is triggered by radiation pressure exerte from elevated accretion onto Sgr A*; star-formation in by-chance captured gas cloud, where the formation is triggered by tidal pressures during the settlement of the gas; or a collision and subsequent accretion

of two gas clouds which compresses the gas enough to initiate star formation.
The first scenario was proposed by Morris et al., 1999. In that paper, a galactic center duty cycle between the hot and very bright O-WR type stars, the CND and the accretion flow of Sgr A* was proposed. The current population of WR and O type stars produce sufficient radiation pressure to prevent the CND to further collapse onto Sgr A*. However, once these stars reach the end of their life time, the gas of the CND starts to accret onto Sgr A*. A bright accretion disk forms. The radiation pressure from the accretion disk subsequently shocks the gas in the surrounding clouds, which initiates the star-formation. Once enough, bright and hot WR and O type stars have been formed, their radiation pressure stabilizes the gas against accretion, which stops the star formation and resets the duty cycle.
In the second scenario, the star-formation happens directly in a large scale accretion disk around Sgr A* (e.g. Levin and Beloborodov, 2003; Bonnell and Rice, 2008). In order for stars to form, parts of the accretion disk need to become self-gravitating. The problem with such a scenario is the immense tidal sheer that Sgr A* exerts on the disk: for star formation to begin the gas needs to be compressed by a factor of more than a thousand compared to the density in the CND (Genzel et al., 2003).
Despite this difficulty, several simulations now demonstrate that star-formation in gas clouds or accretion disks in the direct proximity of Sgr A* can occur. Nayakshin, 2006 showed in semi-analytical simulations that star-formation in an in-falling gas cloud is in principle possible. Bonnell and Rice, 2008; Nayakshin et al., 2007 and Löckmann and Baumgardt, 2009 further refine this scenario. They demonstrate that several observations of the young star disks, like warp of the clockwise disk reported by Bartko et al., 2009, are compatible and, indeed expected, with such a local formation scenario. Hobbs and Nayakshin, 2009 showed that cloud-cloud collision can indeed send two gas-clouds on plunging orbits in which star-formation can occur. In this intriguing scenario, two clouds accrete onto Sgr A*. They do not form a single accretion disk but multiple gas-streamers around Sgr A*. These gas streamers can have very different eccentricities, which mainly depend on the initial conditions of the cloud-collision (see Figure 1.16 for an example of such a cloud collision). Importantly, a considerable fraction of the gas settles in close proximity of the black hole. Star-formation can occur both in the gas steamers and the central accretion disk, with very different angular momenta and eccentricities.

In the last paper of this thesis I will present new evidence for this latter scenario, by showing that the kinematic distribution of the young stars is very rich. I find at least three main kinematic features, which have different eccentricities. Using a new, and mathematically more rigorous, z-prior I am able to clearly define the significance of our observations against an isotropic cluster. Using this new prior, and a substantially improved spectroscopic coverage of the Galactic Center, I will show that the warp of the clockwise disk (Bartko et al., 2009), as well as the counter clockwise disk/streamer (Genzel et al., 2003) are significant. Furthermore, I will introduce a third disk/streamer of young stars. These observations fit remarkably well with the predictions made by the simulations of cloud collisions presented in Hobbs and Nayakshin, 2009: The inner accretion disk shows lower eccentricities, and is warped. This shows that a considerable fraction of young stars

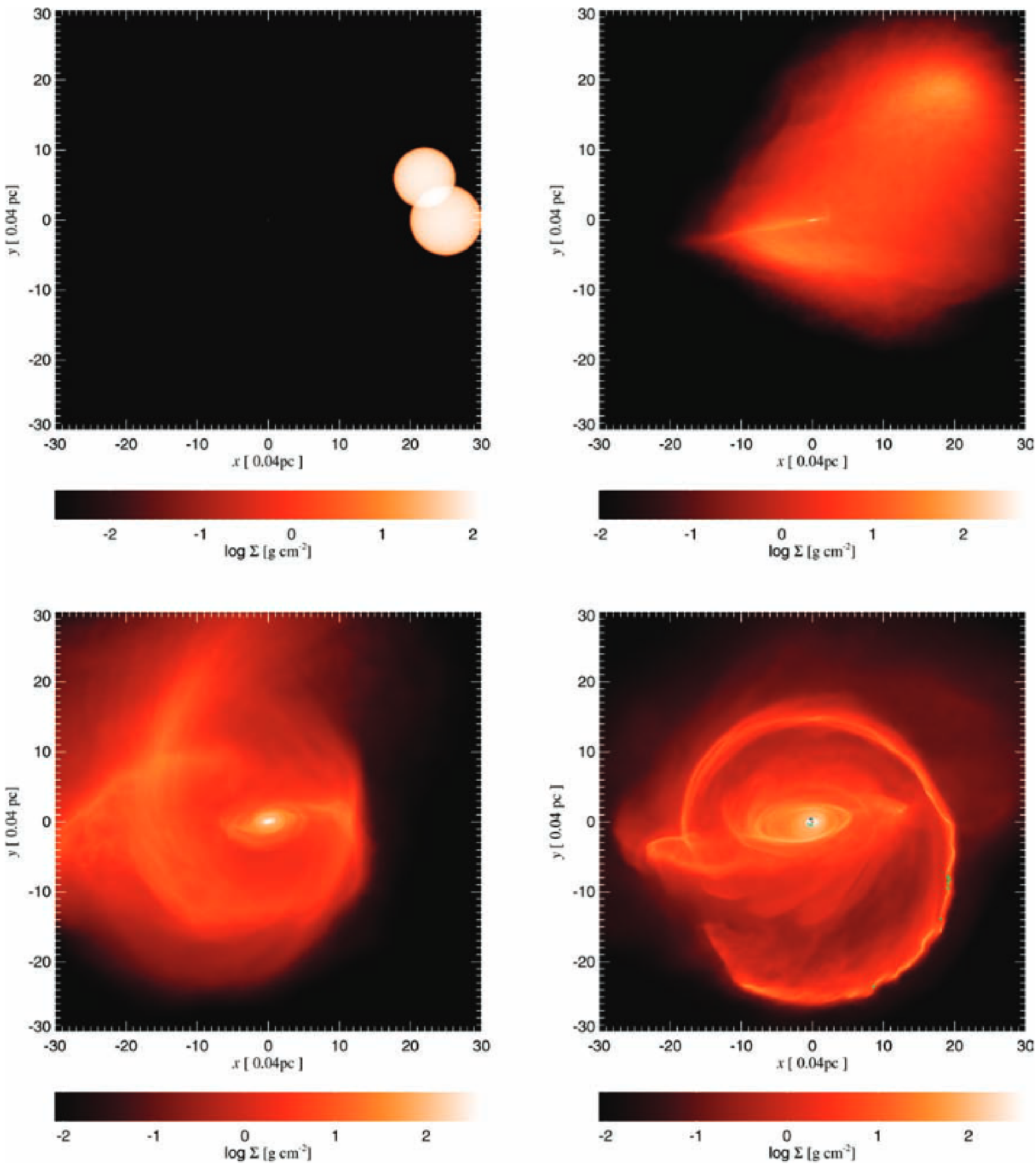

Figure 1.16: Simulations of a gas cloud collision with subsequent accretion and star-formation presented by Hobbs and Nayakshin, 2009. After the initial collision, the two clouds accrete with in several different gas-streamers, in which star-formation occurs. Furthermore, a considerable fraction of the gas settles in close proximity of the black hole, forming stars.

can be attributed to not only a central disk, but at least two more gas disks at larger separations from the black hole. In these disks or streams, the eccentricities are much higher than in the central disk, in line with the theoretical prediction. I thus argue that star formation after a collision and subsequent accretion of two CND clouds is a likely explanation for the young stars in the Galactic Center.

Chapter 2

A Detection of Sagittarius A* in the Far-Infrared

Original Publication: S.D. von Fellenberg, S. Gillessen, J. Graciá-Carpio, T. K. Fritz, J. Dexter, M. Bauböck, G. Ponti, F. Gao, M. Habibi, P. M. Plewa, O. Pfuhl, A. Jimenez-Rosales, I. Waisberg, F. Widmann, T. Ott, F. Eisenhauer, R. Genzel
Published in The Astrophysical Journal: Sebastiano D. von Fellenberg et al 2018 ApJ 862 129
Abstract: We report the first detection of the Galactic Center massive black hole, Sgr A*, at 100 µm and 160 µm. Our measurements were obtained with PACS on board the Herschel satellite. While the warm dust in the Galactic Center is too bright to allow for a direct detection of Sgr A*, we measure a significant and simultaneous variation of its flux of $\Delta F_{\nu \hat{=} 160\mu m} = (0.27 \pm 0.06)$ Jy and $\Delta F_{\nu \hat{=} 100\mu m} = (0.16 \pm 0.10)$ Jy during one observation. The significance level of the variability in the 160 µm band is 4.5σ, and the corresponding variability in the 100 µm band is significant at 1.6σ. We find no example of an equally significant false positive detection. Conservatively assuming a variability of 25% in the FIR, we can provide upper limits to the flux. Comparing the latter with theoretical models, we find that 1D radiatively inefficient accretion flow models have difficulties explaining the observed faintness. However, the upper limits are consistent with modern observations by ALMA and the Very Large Array. Our upper limits provide further evidence for a spectral peak at 1×10^{12} Hz and constrain the number density of $\gamma \sim 100$ electrons in the accretion disk and/or outflow.

2.1 Introduction

The Galactic Centre massive black hole, Sgr A*, and its accretion flow have long been established as a one of kind laboratory that grants access to exceptional physical phenomena (Genzel et al., 2010). The emission stemming from the accretion flow (and or outflow) has been measured throughout many parts of the electromagnetic spectrum ranging from the radio (Melia and Falcke, 2001), the mm (Zhao et al., 2003)), the sub-mm (Falcke et al.,

1998) and the NIR (Genzel et al., 2003a) to the X-ray (Baganoff et al., 2001c) regime. These measurements make up the spectral energy distribution (SED) of Sgr A*. The power, variability and spectral slope vary substantially throughout the SED. Reflecting that, the different parts of the SED have been given different phenomenological names: the radio part is 'flat' (i.e. the flux is approximately log-constant, Serabyn et al., 1997) and thus dubbed the flat radio tail; the spectral slope increases and peaks in the mm to sub-mm domain of the SED (Falcke et al., 1998). This peak has sometimes been referred to as the 'sub-mm bump'.

At wavelengths shorter than 1 mm the observation of Sgr A* becomes more difficult due to obscuration from the atmosphere. Sgr A* has been observed with the Caltech Submillimeter Observatory (CSO) at wavelengths down to 350 μm (e.g. Yusef-Zadeh et al., 2009a). Stone et al., 2016 report 'highly significant variations' of the deviation from the mean flux and a 'minimum time-averaged flux density' of $\langle \Delta F_{\nu \widehat{=} 250\mu\mathrm{m}} \rangle = 0.5$ Jy using the SPIRE instrument on-board Herschel.

At even shorter wavelengths only upper limits exist, until Sgr A* reappears in the NIR, where its variable outbursts are frequently recorded (Genzel et al., 2003a; Dodds-Eden et al., 2009). In the optical and UV regime, dust extinction makes observations of Sgr A* impossible.

In the X-ray regime, both a variable as well as a constant flux component are observed. The constant X-ray flux has a spatial extension consistent with the Bondi radius ($\sim 1" \widehat{=} 10^5$ Schwarzschild radii) of Sgr A* (Baganoff et al., 2003b; Xu et al., 2006). The variable flux is thought to originate from the innermost part (≈ 10 $\mathrm{R_S}$) of the accretion flow (Barrière et al., 2014).

Sgr A* is a variable source at all observable wavelengths (Genzel et al., 2010). However, it is not clear whether the variability in different spectral regimes is physically connected (Dexter et al., 2014). It has been established that all X-ray flares are accompanied by a NIR flare. But the converse is not true (Dodds-Eden et al., 2009).

Both the NIR (Do et al., 2009) and the (sub)-mm variability shows red noise characteristics. The sub-mm emission has a characteristic time scale of $\tau = 8$h (Dexter et al., 2014).

The fractional variability increases throughout these wavelength regimes. In the cm, mm and sub-mm regime the variability is in the order of a few tens of percent. In the NIR regime the range of the variability increases and is of the order of a few hundred percent. In the X-ray regime it is yet a magnitude larger (Genzel et al., 2010).

Based on these observational constraints, the emitting material has been modeled by two broad classes of models: Radiatively Inefficient Accretion Flow (RIAF) models and jet models. Both types of model can explain the observed SED.

In RIAF models, two populations of electrons exist: a thermal population producing the emission in the sub-mm and mm regime and an accelerated fraction of (non-thermal) power law electrons producing the flat radio tail at longer wavelengths (Yuan et al., 2003b; Yuan et al., 2004).

In such an accretion flow the released energy is advected inwards rather than radiated away (and thus the flow is radiatively inefficient). The accretion flow has a geometrically thick and optically thin disk (Ichimaru, 1977; Rees, 1982; Narayan and Yi, 1994; Yuan et al.,

2003b; Yuan and Narayan, 2014).
In the jet models, relativistic, optically thick and symmetric jets are responsible for the radio and mm emission as well as the constant X-ray flux. The jet model is motivated phenomenologically from the observed jets in many known low-luminosity active galactic nuclei such as M81 or NGC4258 (Falcke and Markoff, 2000).
In this context, the emission is produced either by the bulk accretion flow (Mościbrodzka et al., 2009; Dexter et al., 2010; Shcherbakov et al., 2012) or at the jet wall (Mościbrodzka and Falcke, 2013; Chan et al., 2015). The latter scenario naturally results from the expected preferential heating of electrons in magnetized regions (Howes, 2010; Ressler et al., 2017) and reproduces the radio spectrum with purely thermal electrons. In the former scenario, an additional non-thermal component is required (Özel et al., 2000; Yuan et al., 2003b; Broderick and Narayan, 2006; Mao et al., 2017; Chael et al., 2017). Several of these works are also time-dependent and can produce the observed mm and to some extent the NIR variability (Dexter et al., 2009; Dolence et al., 2012; Dexter and Fragile, 2013; Chan et al., 2015; Ressler et al., 2017). However, no simulation so far produces large X-ray flares (but see Ball et al., 2016, which can reproduce the X-ray/NIR observations by the stochastic injecting non-thermal electrons).
Until now, due to the obscuration by the atmosphere, as well as the technical challenges far-infrared (FIR) detectors pose, the FIR regime of Sgr A* has not been constrained. This regime is important though, as the luminosity of the accretion flow is thought to turn over in this regime. Being able to constrain the SED in the FIR would make it possible to narrow down the many degeneracies still present in theoretical models of the accretion flow. This is especially interesting in the context of 3D simulations, where the number of free parameters allow a wide range of simulations to fit the data.
In this paper, we present novel Herschel[1] FIR measurements and a first detection of Sgr A* at $\lambda = 100\ \mu$m and $\lambda = 160\ \mu$m. In section 2.2 we present the observations and the data reduction. In section 2.3 we describe the results. These are discussed in section 2.4. Finally, we summarize our results in section 2.5 and give an outlook.

2.2 Observations and Reductions

Our observations consist of five slots of coordinated observations in March 2012 with the PACS instrument (Poglitsch et al., 2008) onboard the ESA Herschel Space Observatory (Pilbratt et al., 2010), parallel X-ray observations with the Chandra[2] (Weisskopf et al., 2000) and XMM-Newton[3] (Jansen et al., 2001; Strüder et al., 2001) observatories, and the near-infrared NACO camera (Lenzen et al., 2003; Rousset et al., 2003) mounted on UT4 at the VLT observatory. The observing times and the exposure times for the individual instruments are listed in Table 2.1.

[1] *Herschel* is an ESA space observatory with science instruments provided by European-led Principal Investigator consortia and with important participation from NASA.
[2] Obsids: 13856,13857 & 14413
[3] Obsids: 0674600601, 0674600701, 0674601101, 0674600801 & 0674601001

Instrument	03/13/2012	03/15/2012	03/17/2012	03/19/2012	03/21/2012	Exposure time / Bins
PACS	05 : 13 – 13 : 05	05 : 03 – 12 : 55	05 : 17 – 13 : 09	05 : 08 – 13 : 00	05 : 06 – 12 : 58	10 min
NACO - K	–	08 : 04 – 08 : 49	08 : 18 – 09 : 47	07 : 35 – 10 : 05	07 : 19 – 10 : 07	4 min
NACO - L	–	09 : 36 – 10 : 15	05 : 48 – 10 : 04	08 : 04 – 10 : 07	06 : 08 – 10 : 08	1 min
XMM-Newton	03 : 52 – 09 : 23	04 : 47 – 08 : 42	02 : 30 – 09 : 50	03 : 52 – 09 : 48	03 : 31 – 09 : 41	5 min
Chandra	–	08 : 45 – 19 : 45	08 : 58 – 19 : 49	–	06 : 46 – 11 : 12	5 min

Table 2.1: Observation time in UT for all available instruments.

The PACS camera had two bolometer arrays: one operating at either 70 μm or 100 μm (the 'blue' and 'green' bands respectively) and one operating at 160 μm (the 'red' band). Three of the five slots used the blue band filter and two the green band filter (March 17 and March 19). The parallel X-ray ($2-10$ keV) and NIR (K and L' band) observations were scheduled to observe as much in parallel as possible.

We used the scan observing mode for PACS. We chose a scanning pattern that creates images with a total exposure of 10 minutes each. The X-ray observations are binned to 300 seconds exposures; the NACO K and L' band observations have a cadence of 4 and 1 minute respectively. When feasible the NIR filters of NACO were switched to allow for quasi-parallel K and L' observations.

A quick look at the images obtained with the standard pipeline reveals that Sgr A* is not readily seen. There is, however, bright thermal dust emission from the circumnuclear disk (CND, Etxaluze et al., 2011, see Figure 2.1 and Appendix A1.1). Subtracting this constant emission from the individual exposures allows us to look for a variable component of Sgr A*. The subtraction creates a data cube of 40 residual maps per observation. The residual maps are dominated by systematic artefacts which make it, at first glance, impossible to detect Sgr A* as a variable source. To remove these systematic errors we chose an approach in which we remove the respective dominant artefact step-by-step. In the following we describe how we obtained the images (subsec. 2.2.1) and the residual maps (subsec. 2.2.2).

2.2.1 Standard reduction

To create the images, we use the HIPE pipeline (Ott, 2010) and the JScanam map maker (Graciá-Carpio et al., 2015). We keep the standard settings and only change the source masking parameter. This ensures that, in source regions, JScanam's algorithm removes the 1/f noise based on averages. This protects the real signal of a source from being removed. We tune this parameter such that the source masks do not cover too much area (a good value for the coverage being $\sim 30\%$, J. Graciá-Carpio priv. comm.). Additionally, we create a square source mask which covers Sgr A* over an area of $6''$, $7''$ and $12''$ (4×4 px) in accordance with Herschel's beam sizes at the three wavelengths. This creates 40 individual images for each observation.

2.2.2 Improved reduction of maps

Here, we detail the steps beyond the standard reduction which enable us to reach a sensitivity of ~ 0.1Jy/beam.

Pointing correction

The Herschel satellite experienced absolute pointing offset errors on the order of $1''$ to $2''$ (Sánchez-Portal et al., 2014). This creates strong, spatially correlated patches in the residual maps at regions of high intensity.

To remove these artefacts, we computed the offsets and aligned each cube with its first map. Naively, one would expect that this removes the pointing offset errors. The pointing errors, however, impair the performance of JScanam. This is because the pointing errors in the individual exposures smear out the averaged image of all individual exposures of an observation. This averaged image is used by JScanam to robustly calculate the detector read-out noise. Therefore, the pointing errors hinder an optimal removal of the detector read out noise, which in turn leads to an imprecise calculation of the offsets. To overcome this, the pointing correction needs to be handled iteratively. In example, we need to re-reduce the pointing-corrected cube and re-compute the pointing offsets several times until we end up with the final pointing offset corrected data cube. We refer to Appendix A1.2 for details of this procedure. A similar procedure has been applied by Stone et al., 2016 for their Herschel/SPIRE maps. Our procedure creates a pointing-corrected data cube of 40 images per observation. We plot a color composite image obtained in this manner in Figure 2.1. The image shown is the highest resolution images of the Galactic Center in the FIR to date. The median images of the individual bands are shown in Appendix A1.1.

Median subtraction and affine coordinate transform

Next, we perform a pixel-wise median subtraction. In order to align the maps with the median map and to correct for other linear distortions, we apply affine coordinate transformations to the individual maps. The parameters are obtained numerically from minimizing the residual maps. This produces a data cube of 40 residual maps for each observation.

Periodic pattern removal

In the residual maps, a periodic strip pattern is the dominant artefact. To remove this pattern, we Fourier transformed the residual maps. In the Fourier transformed maps, the periodic pattern manifests itself as a few symmetrical peaks. We masked these peaks with the median intensity of the Fourier-transformed maps and back transformed the masked maps.

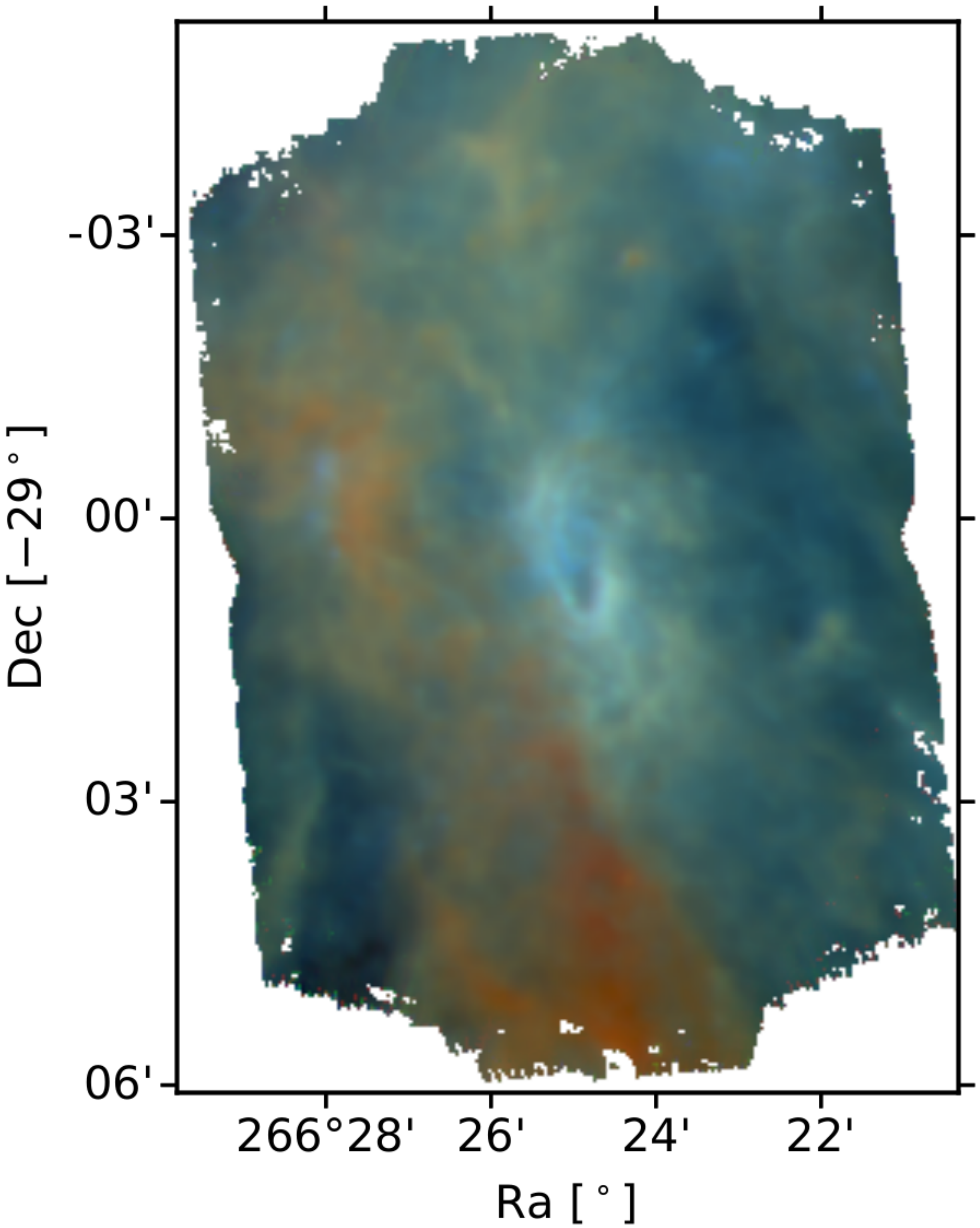

Figure 2.1: Composite FIR image of the Galactic Center, generated using the algorithm of Lupton et al., 2004. We have scaled the intensity of the red band according to $I_r' = I_r^{0.9}$, the intensity of the green band $I_g' = I_g^{0.6}$ and the intensity of the blue band $I_b' = I_b^{0.5}$.

Linear drift removal

For each cube, we noticed a small linear drift of the flux, i.e. the residual maps showed a linear increase or decrease of flux over the course of each observation. We verified that this is the case for pixels at least one beam away from Sgr A*. This trend can be removed, pixel by pixel, by subtracting a linear fit from each pixel's light curve. Or, in more technical terms, we remove the linear trend by fitting and subtracting a linear function along the time axis of the residual map data cube for each spatial pixel.

Smoothing and running mean

In order to smooth any remaining smaller-than-resolution artefacts, we convolved the residual maps with the band's respective PSF, which is available from the instrument control center's (ICC) website[4]. We corrected the PSF for the missing energy fraction as provided by the ICC and adjusted the pixel scale. In addition to the spatial smoothing, we computed a temporal running mean for each map of width three.

Manual fine tuning

The median subtraction (Subsec. 2.2.2) and the linear drift removal procedure (Subsec. 2.2.2) assume that there is no source flux. Variable flux from Sgr A* will appear as an excursion in the light curves of the respective pixels, effectively skewing our linear drift correction. This issue can be overcome in the case when the increase or decrease of flux from Sgr A* happens only for a part of the observation. In this case, we reiterate steps 2.2.2 to 2.2.2, excluding images and maps with excess flux at the position of Sgr A*. However, such a procedure requires a priori knowledge of the presence of flux and potential outliers can be mistaken as flux from Sgr A*. In consequence, we only apply this manual fine tuning of the reduction in the case when a believable flux excursion is detected (i.e., when the bands are correlated or a point source is discernible in the residual maps). Once we opted for such a manual fine tuning, we applied it to all pixels of a map equally. Explicitly, we applied this manual fine tuning to the observations of March 15, 17 and 19. The details of the manual fine tuning are discussed in Appendix A1.4.

2.2.3 Light curves

In order to obtain light curves of Sgr A* we calculated the best fit amplitude C of the ICC PSF to the pixel in which Sgr A* is expected to be found. We weighted the fit with the standard deviation maps provided by the standard reduction. As the maps were smoothed with the PSF (Subsection 2.2.2), we smoothed the PSF with itself. This accounts for the wider FWHM of point sources in the smoothed map. The FWHM ($\hat{\sigma}$) of a Gauss fit, fitted to the convolved PSF, yields: $\hat{\sigma}_{\mathbf{r}} = (15.7'', 19.0'')$; $\hat{\sigma}_{\mathbf{g}} = (9.0'', 10.0'')$ and $\hat{\sigma}_{\mathbf{b}} = (8.7'', 9.7'')$. The Gauss fit is allowed to rotate.

[4] `http://tinyurl.com/pacs-psf`

Error

Because of the complicated source structure at the Galactic Centre, we decided to use reference regions as a proxy to estimate the photometric noise, as the formal fit error would not capture the true uncertainty. The reference regions were chosen by applying the following selection criteria:

1. The median intensity of the pixel in question should lie within 0.3 to 2 times the intensity of the Sgr A* pixel in the median image.
2. The pixel in question should lie within 44 pixels ($\hat{=}$ 66″, 74.8″ and 123.2″ for the blue, green and red band respectively) of Sgr A*.
3. All pixels within one beam of Sgr A* are excluded as reference points.

These constraints ensure that:

1. a) only regions of the sky are chosen which have a comparable intensity (and therefore photon noise) to that of Sgr A*;
2. b) enough scanning coverage[5] is guaranteed, and the coverage is approximately constant;
3. c) the variability of Sgr A* does not perturb the estimate of the noise.

To calculate the noise, we draw 40 uncorrelated random positions within the reference regions. We then extracted light curves of the reference points. The scatter of the these reference light curves serves as a proxy to the noise. In the figures below, the reference light curves are represented by thin grey lines.
We compute the error on C as the sum of the spatial and temporal variance:

- We calculate the standard deviation $SD_{t_n}(x, y)$ of the reference light curves for each map at time t_n. $SD_{t_n}(x, y)$ probes the quality of the reduction for each map.
- In addition, we calculated the mean of the standard deviation SD_{ref} of the reference light curves. The mean of SD_{ref} measures the intrinsic variation of the maps.

We estimate the error of Sgr A*'s flux as the quadratic sum of these two values:

$$\sigma_{t_n} = \sqrt{< SD_{ref} >^2 + SD_{t_n}(x, y)^2} \tag{2.1}$$

where σ_{t_n} is the error for each map.
The temporal error SD_{ref} and the spatial error $SD_{t_n}(x, y)$ are correlated. Our ansatz overproduces the real error and thus is a conservative estimate of the error.

[5]The scanning coverage corresponds to the ratio of the exposure time of an actual camera pixel and that of an image pixel. Due to pixelation this is not constant and degrades quickly at the borders of the image. This results in a higher uncertainty for pixels with low scanning coverage, for details see drizzle method (Fruchter and Hook, 2002) and HIPE documentation.

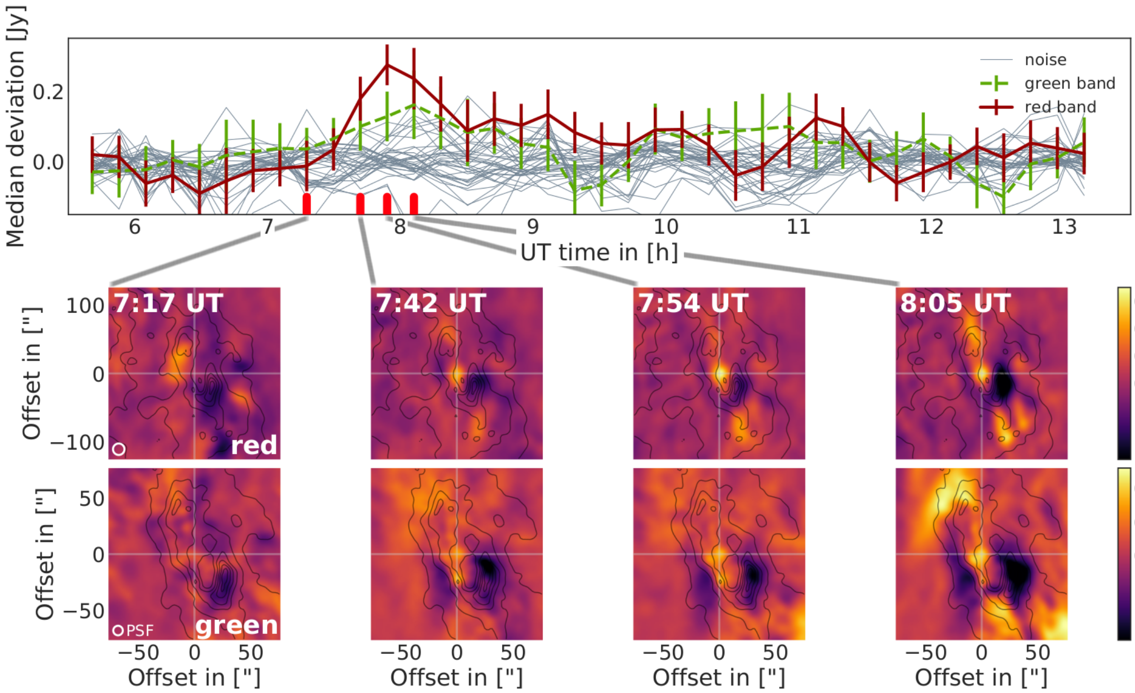

Figure 2.2: The FIR variability on March 17: The upper panel shows the light curves of the red and green bands, as well as the reference light curves of the red band. Below are the residual maps which show the variable flux of Sgr A*. The contour lines are intensity profiles of the respective median images. A point source is visible at the position of Sgr A*.

2.2.4 Parallel observations

The parallel NIR observations were obtained with NACO (Lenzen et al., 2003; Rousset et al., 2003), and the images were reduced following the procedure described in Dodds-Eden et al., 2009. We aligned the images using the bright isolated star S30. We combined images without discernible flares and created a median image. This median image was then subtracted from the individual images, creating residual maps. Aperture photometry was performed on the residual maps and the standard deviation of region without apparent sources between S2 and S30 calculated. We calibrate the flux as the ratio to the median S2 flux, where we assume a flux of 17.1 mJy in the K band and a black-body (Gillessen et al., 2017).

The parallel X-ray observations are presented in Ponti et al., 2015. For the XMM-Newton observations the diffuse background emission dominates the the quiescence X-ray flux of Sgr A*. To account for this we subtract the mean flux of all XMM-Newton observations from the light curves. The error of the background subtraction is estimated from the standard deviation of the light curves.

2.3 Results

For clarity we only discuss the March 17 and March 19 observations, for which we detect flux from Sgr A*. The other observations are discussed in Appendix A1.5.

2.3.1 Light curves

March 17

Figure 2.2 shows the light curves from the observations on March 17. A significant and correlated increase of flux was measured in both the red and the green band. Defining the significance as the ratio of the peak flux to the error estimated from the reference light curves, the red band signal is significant at 4.5 σ and the green band is significant at 1.6 σ. The flux peaks at around 8:20 UT to 8:30 UT. The red light curve remains above zero for about two hours. The green light curve drops to zero about an hour after the peak. Figure 2.3 shows all available light curves from this observation.

Comparison with the parallel observations The FIR activity is accompanied by NIR flaring with five consecutive, distinguishable peaks. There is no parallel X-ray flare. The first recorded NIR peak occurs roughly at 6:30 UT to 6:40 UT, which would imply a delay of $\sim$ 80 min compared to the FIR peak. The association between the two events is unclear.

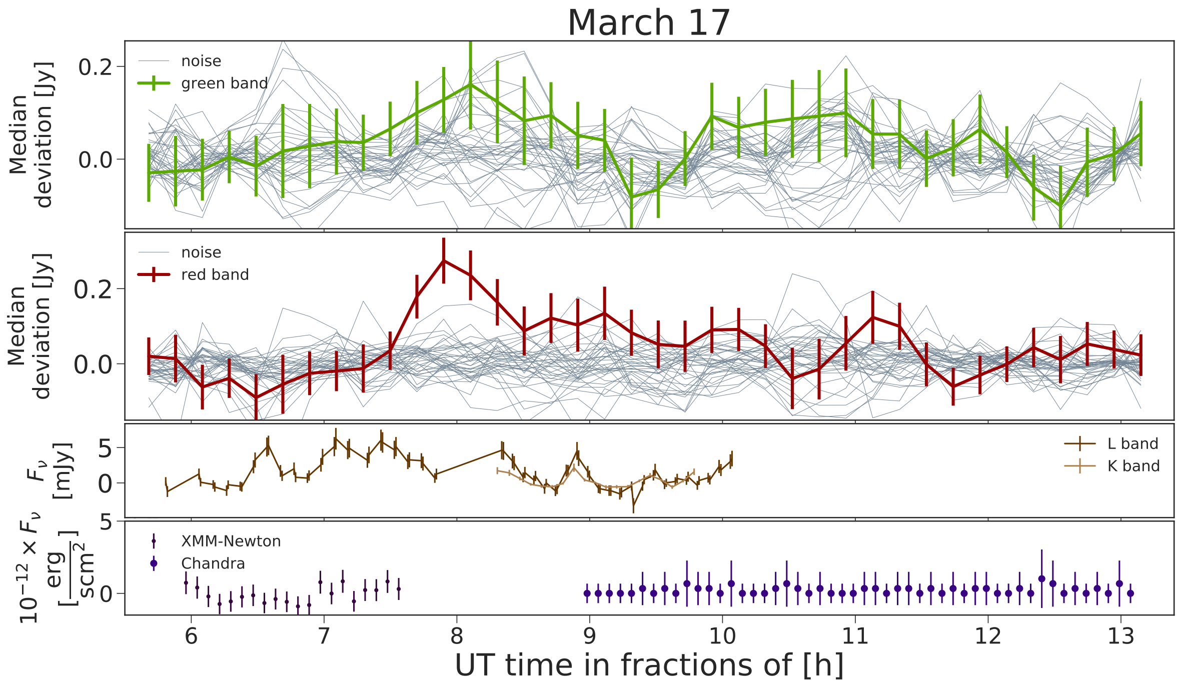

Figure 2.3: Multiwavelength observation from March 17, 2012. The top two panels give the red and green band FIR light curves. The grey lines are the light curves of the reference points. Below are the parallel K and L band NIR and $2-10$ keV X-ray observations.

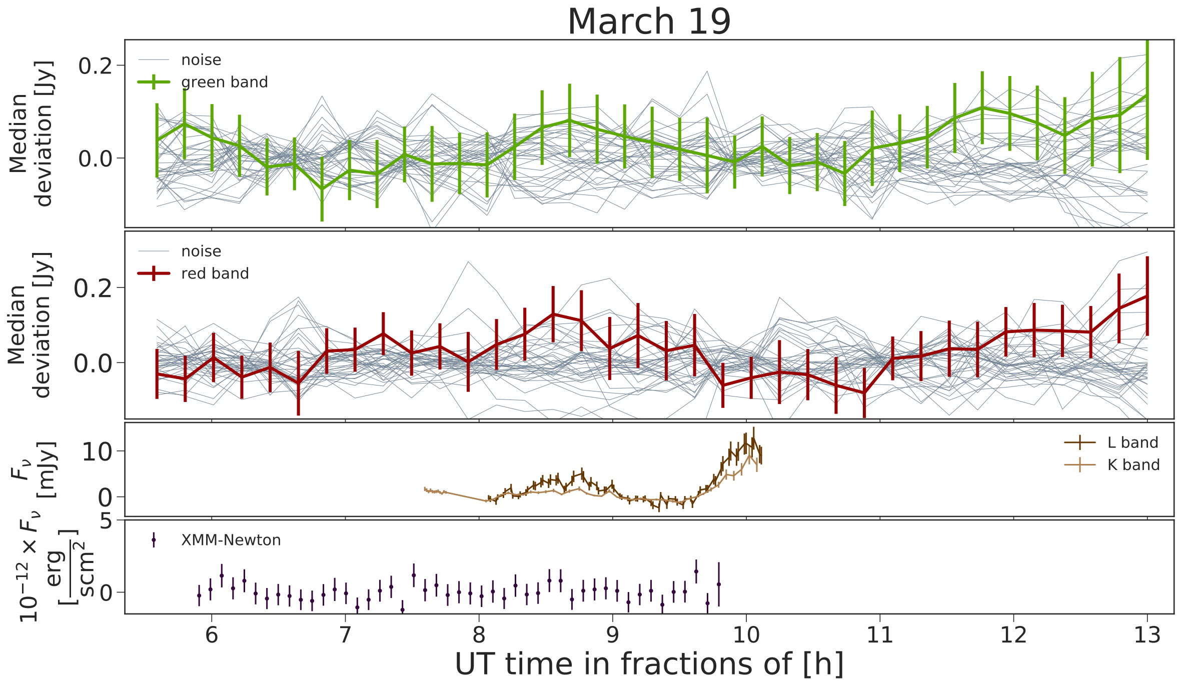

Figure 2.4: Multiwavelength observation during March 19, 2012. Same as figure 2.3 for the March 19 observation.

March 19

The light curves of the March 19 observation are shown in figure 2.4. Since the flux appears to increase at the end of the light curve, the linear drift correction is less certain for this observation. In consequence, we do not use this observation to constrain the SED. However, the observation enhances the credibility of the detection on March 17, as the green and red FIR light curves again show a correlated increase towards the end of the observation (after 11 UT). Our best attempt at correcting the linear drifts yields a significance of 1.3σ for the red band and a significance of 0.8σ for the green band.

Comparison with parallel observations The first bump in the FIR light curve happens at 8:30 UT, during a NIR flare of intensity ~ 14 Jy. Because of the low formal significance of 1.5σ, we cannot claim a detection here. Unfortunately, there are no NIR parallel observations during the increase of flux after 11 UT. However, it is interesting that there is a bright NIR flare at around 10 UT, without an immediate FIR counter part. This hints towards that the dominant variability process cannot be a simple extension of the NIR flares. Nevertheless, this bright NIR flare occurs about an hour to two hours earlier than the onset of the FIR activity. During our observing interval there is no X-ray flare. Unfortunately there are no parallel X-ray observations for the end of the observation.

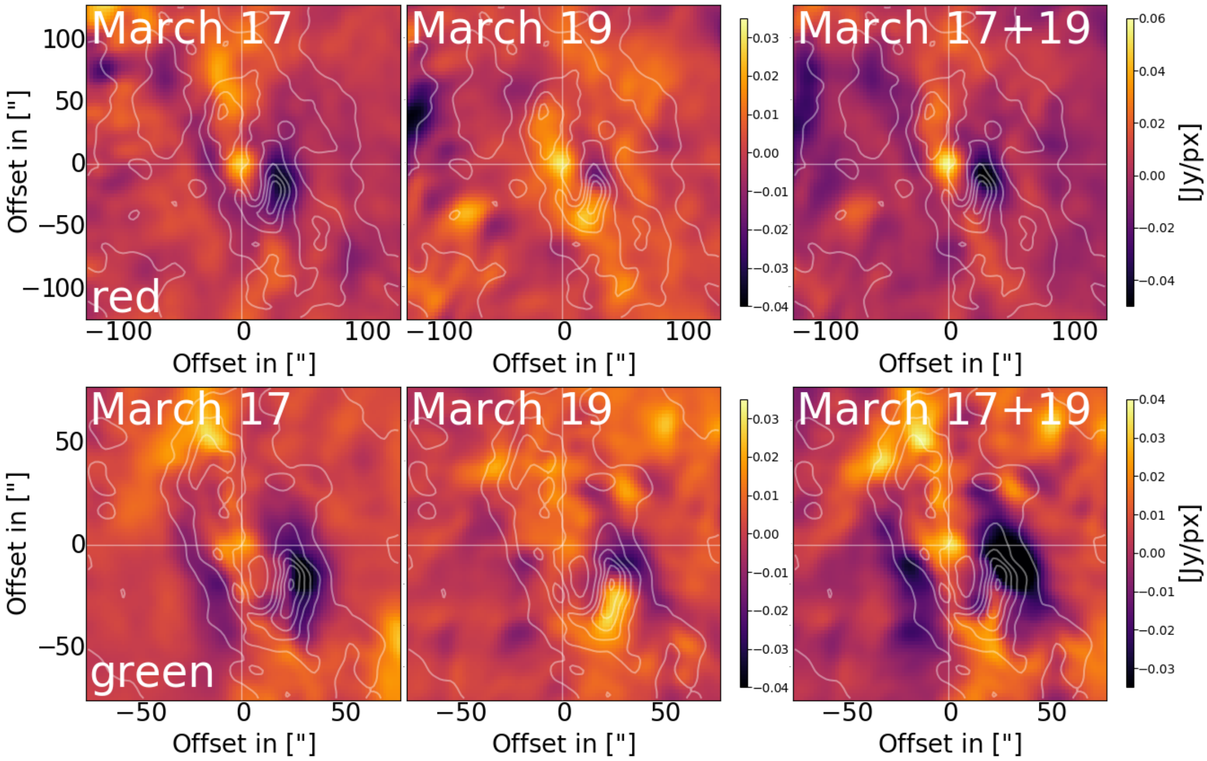

Figure 2.5: Integrated residual maps for the observations on March 17, March 19 and both nights combined. The left column shows the red and green integrated residual maps of the March 17 observation, the middle column the red and green integrated residual maps for March 19 and the right column shows the integrated residual maps of both nights.

2.3.2 Integrated residual maps

To increase statistics we sum the residual maps of each observation. The sum of the residual maps should only contain random fluctuations unless there is variable source in them, i.e. Sgr A*.

For the March 17 observation and the red band, we find a point source located at the position of Sgr A* (Figure 2.5). We also find a point source in the corresponding integrated green band residual map.

The same is true for the March 19 observation and the red band integrated residual map: a point source is discernible at the location of Sgr A*. The green excess is not strong enough to show up as a discernible point source in the corresponding integrated residual map. The integrated residual maps show large extended patches of positive and negative flux. These are spatially correlated with regions of high median intensity (and therefore not reference regions), as can be seen by comparing the patches with the contour lines. We suspect that at high fluxes, JScanam's baseline subtraction algorithm is less robust. However, especially in the red band integrated residual maps, these patches are of significantly different morphology from that of a point source (see Appendix A1.6). In the

Constraints	March 17		March 19	
	# of False Positives	Probability of Real Detection	# of False Positives	Probability of Real Detection
a 1 σ significant signal in the red band	8′203	82.7% $\hat{=}$ 1.36σ	3′102	82.7% $\hat{=}$ 1.36σ
a 2 σ significant signal in the red band	600	98.7% $\hat{=}$ 2.48σ	103	*n.a.*
a 3.8 σ significant signal in the red band	1	99.9979% $\hat{=}$ 4.25σ	1	*n.a.*
a 1.3 σ significant signal in the red band and a 0.8 σ significant signal in the green band	882	98.1% $\hat{=}$ 2.3σ	79	99.8% $\hat{=}$ 3.1σ
a 2 σ significant signal in the red band and a 1.5 σ significant signal in the green band	35	99.93% $\hat{=}$ 3.39σ	135	*n.a.*
Number of tested pixels:	47′462		45′362	

Table 2.2: False positive rate computed using the March 17 and March 19 observations.

green band the signal from Sgr A* is weaker and thus the point source less pronounced. In addition, while both observations show extended patches, the maps are, except at the position of Sgr A*, not correlated across the different observations.

2.3.3 False alarm rate

To estimate how significant our detection is, we determine the probability of measuring a signal by chance. In order to compute the false alarm rate, we measure the amplitudes at all valid reference pixels. Since the pixel scale as well as the median images are different between the two bands, we have to choose common reference regions. We apply the same criteria as before but make sure they are met in both bands.

For the 38 residual maps of size 100 px $\times$ 100 px ($= 380'000\ px$) and the March 17 observation we find 47462 pixels which are valid reference pixels in both bands. We compare the measured amplitude for each reference pixel with the error as given by equation 2.1 and compute a significance. We then count the number of reference pixels with amplitudes above a given significance threshold (Table 2.2) and compare this with our observations. The peak of the red band observation is significant at $\sim 4.5\sigma$. We find no equally significant false alarm. For a significance of 3.8σ, there is one equally significant false positive within the tested pixels of the March 17 observation. This translates into a probability of $>$ 99.998% of the detection being real. In addition we observe a simultaneous 1.6σ significant green peak. Note that we have estimated the errors conservatively, as a sum of the spatial and temporal variance. A conservative error estimate results in fewer points that have SNR of greater than one. For this reason, our 1σ constraint yields a probability of 82.2% of the detection being real, rather than the expected $\sim 68\%$.

For the March 19 observation, accounting for the systematic errors as before, we find 79 false positives that are 1.3 σ significant in the red band and 0.8 σ significant in the green band. This corresponds to a 99.8% probability of the detection being real. The number of false positives is lower than for March 17. This reflects that our estimate of the systematic error is conservative.

Summary of false alarm rate

We have found no false positives that are as significant as the measured flux increase at the position of Sgr A* for the March 17 observation. In addition:

- A point source is discernible at the proper location.
- This point source can be found in two bands.
- The flux is temporally correlated between the two bands.
- While the green and red detector sit in the same instrument, they are independent from one another, probe different physical phenomena (warmer/colder dust) and the reductions are handled independently.
- There is a second observation on March 19, for which we can detect a correlated increase of flux.
- When binning all maps together we find a discernible point source in two different observations, and two different bands.
- The residual maps for the different observations are not temporally correlated. The point source (Sgr A*) is the only reoccurring spatial structure.

We conclude, therefore, that the measured increase in flux is due to a change in brightness of Sgr A*.

2.4 Discussion

2.4.1 Implications for the SED

We now discuss these findings and compare the results to existing models of the accretion flow. The subtraction of the median in our maps precludes the possibility of absolute flux measurements. In consequence, our measurements are measurements of the variable flux components and are therefore lower limits on the total flux at the time of our measurement. In order to constrain the SED, we estimate a median flux based on the observed variable flux component. If we assume a fractional variability r, we can compute the constant component that was subtracted:

$$F_{\nu;median} = \frac{F_{\nu;variable}}{r} \tag{2.2}$$

Therefore, our detection together with a constraint on the fractional variability r allows one to estimate the median flux.

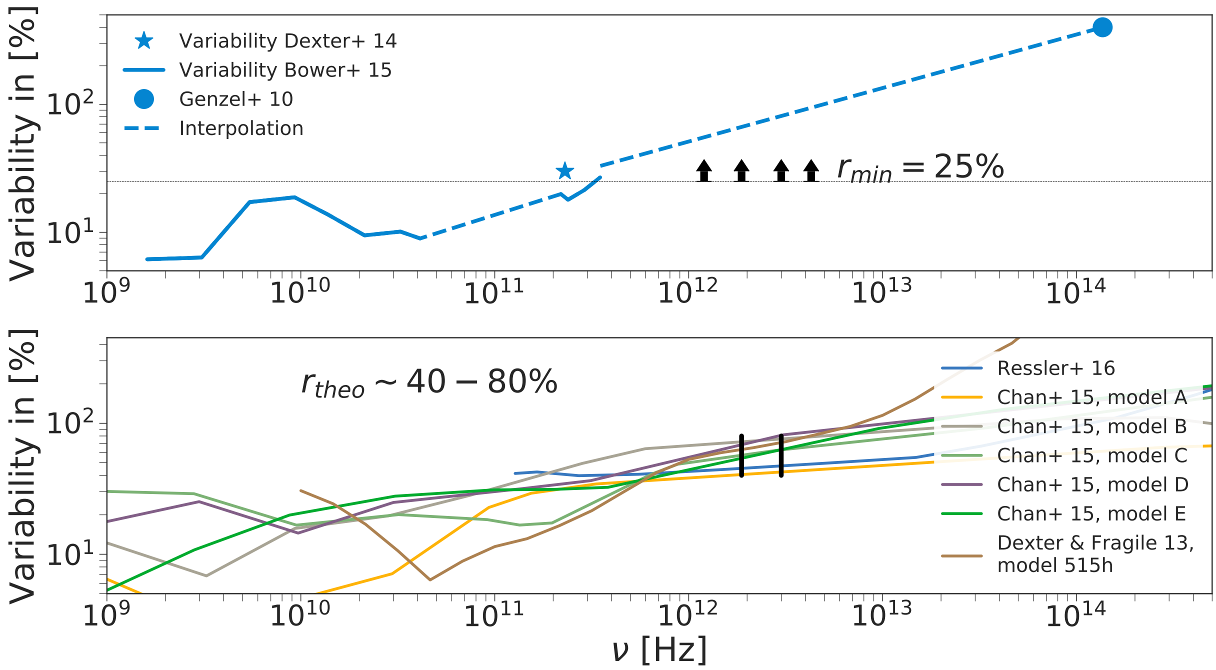

Figure 2.6: Variability of Sgr A* from observations and theory. Top: measured variability from Bower et al., 2015 (as calculated from their SED), Dexter et al., 2014 and Genzel et al., 2010. We plot our assumption of a minimal variability of $r_{min} = 25\%$ as black arrows. Bottom: Theoretical predictions of the variability from Dexter et al., 2014, Chan et al., 2015 and Ressler et al., 2017, as calculated from their SED. The range of the FIR variability is $r_{theo} = 40 - 80\%$.

2.4.2 Constraining the variability

The range of the fractional variability r can be estimated either by comparing r with the typical variability in other wavelength regimes or from theoretical arguments. When we assume a minimal fractional variability r_{min}, equation 2.2 turns into an equation for an upper limit of the flux. Thus, assuming that Sgr A* is at least as variable as a certain value leads to upper limits.

Alternatively, it is possible to obtain a value for the fractional variability from theoretical predictions. Time-dependent simulations of accretion flows can in some cases yield a prediction for typical values of the variability. This prediction can consequently be used to obtain an estimate of the median flux.

Constraints based on observations

In the following, we summarize the variability in the mm, sub-mm and the NIR regime and argue that a minimal variability of $r_{min} = 25\%$ is a reasonable assumption. Sgr A* is highly variable around the sub-mm bump, with a characteristic time scale of around

eight hours (Dexter et al., 2014). In a comprehensive study of cm and mm light curves of Sgr A*, Bower et al., 2015 calculated RMS variabilities from ALMA and VLA data. They find increasing RMS variabilities with decreasing wavelength and a variability around 30% in the sub-mm. Dexter et al., 2014 derived an RMS variability of 30% at 1.3mm.
In the NIR, Sgr A* is a highly variable source with regular faint flares and occasional bright flares. The brightest flares can easily exceed the faint flux by a factor of a few. Genzel et al., 2010 put the typical variability in the range of 300% to 400% and report a log-linear increase of variability throughout the spectrum. In both bands the variability is consistent with a red noise process (in the NIR e.g. Do et al., 2009, sub-mm e.g. Dexter et al., 2014). This implies that the fractional variability depends on the time scale of the observation.
The March 17 peak is the brightest in 40 hours of observation. This is several times the typical variability time scale in the sub-mm. Since the variability time scale is similar in the radio and mm regime ()Genzel2010, it is reasonable to assume that the FIR variability time scale is not longer than the sub-mm one. Our observation length significantly exceeds this time scale and thus equation 2.2 estimates the median flux properly. Therefore, we assume that the minimal variability r_{min} is at least as high as the long-term fractional variability observed in the sub-mm (Figure 2.6).

Upper limits in the red and green band: Conservatively setting r_{min} of the March 17 peak to 25% we obtain:

- $\langle F_{\nu \widehat{=} 160\mu\mathrm{m}} \rangle \leq (1.06 \pm 0.24)$ Jy in the red band, and
- $\langle F_{\nu \widehat{=} 100\mu\mathrm{m}} \rangle \leq (0.64 \pm 0.4)$ Jy in the green band.

Because of the higher background in the green band, the uncertainty of the green band data is higher. In addition, the observation time was only 16 hours, which makes applying eq. 2.2 less robust. We stress that these upper limits would hold even if we had not detected Sgr A*.

Upper limits for the blue band We determine the standard deviation of the light curves of the reference pixels for the blue 70 μm band. This is done for the March 15 and 21 observations. The blue March 13 observation is impaired by a signal drift of unknown origin and therefore neglected. We use the blue band standard deviation of March 21 to compute the upper limit. The 3σ limit for a non-detection is obtained by multiplying the standard deviation by a factor of three and dividing it by 0.25 as before. This yields $\langle F_{\nu \widehat{=} 100\mu\mathrm{m}} \rangle \leq 0.84$ Jy (see Appendix A1.3 and A1.5 for details).

Theoretical predictions for the FIR variability

Several time-dependent simulations of the accretion flow of Sgr A* exist which can reasonably reproduce the mm, sub-mm and/or NIR variability. As such they provide an estimate of the mean and the 1σ RMS variability. This gives a value for r, which we use to estimate

the median flux. Examples of time-dependent simulations are Dexter et al., 2009; Dolence et al., 2012, Dexter and Fragile, 2013, Chan et al., 2015 and Ressler et al., 2017.
We plot the variability prediction Dexter and Fragile, 2013; Chan et al., 2015 and Ressler et al., 2017 in Figure 2.6. The variability in these works ranges from $r_{theo} \sim 40\%$ to $r_{theo} \sim 80\%$. The mid range of these values is $r_{theo} \approx 60\%$. For the purpose of illustration, we choose this value as representative of current state of the art time-dependent simulations. Given the simplicity of equation 2.2, it is straightforward to scale our results to find median flux densities corresponding to alternative values of r_{theo}.
Alternatively, time-dependent simulations can be directly tested against our observations. The variability prediction at the FIR frequencies can be used to obtain r_{theo} and the corresponding FIR median flux ad-hoc. This allows a self-consistent test of the parameters of any time-dependent simulation. Furthermore, if the flux distribution is known, the fact that we observe the brightest peak in 40 hours can be used to estimate r_{theo} even more accurately.

Theoretical prediction for the median flux Setting the variability to $r_{theo} = 60\%$ we obtain:

- $\langle F_{\nu \widehat{=} 160\mu\text{m}} \rangle \approx 0.5 \pm 0.1$ Jy in the red band, and
- $\langle F_{\nu \widehat{=} 100\mu\text{m}} \rangle \approx 0.3 \pm 0.2$ Jy in the green band.

2.4.3 An updated SED of Sgr A*

In Figure 2.7, we plot our measurements of the FIR variable flux, the upper limits and the theoretical prediction of the median flux. For the cm, mm and sub-mm we use modern, high resolution data obtained from VLBI instruments such as ALMA and the VLA, where available.

2.4.4 The "submillimeter bump" and spherical models of the accretion flow

The model plotted in Figure 2.8 is the quiescence/median flux of the Yuan et al., 2003b RIAF model. The original model overproduces the flux throughout much of the mm and sub-mm regime and is also inconsistent with our new FIR upper limits. In fact, our data as well as modern ALMA and VLA data show that the mm and sub-mm SED is less 'bumpy' than assumed in the original model (and older single dish observations, e.g. Falcke et al., 1998). Therefore, the notion of a "sub-mm bump" may be outdated.

In 1D RIAF models, the mm and sub-mm regime luminosity is dominated by emission from a spherical bulge of hot electrons with a thermal energy distribution. We approximate such a spherical bulge of hot electrons by assuming a thermal distribution of electrons in a region with radius R with constant density, temperature, and magnetic field strength. The radius is set to be $R = 40$ μas, based on the mm-VLBI size (Doeleman et al., 2008).

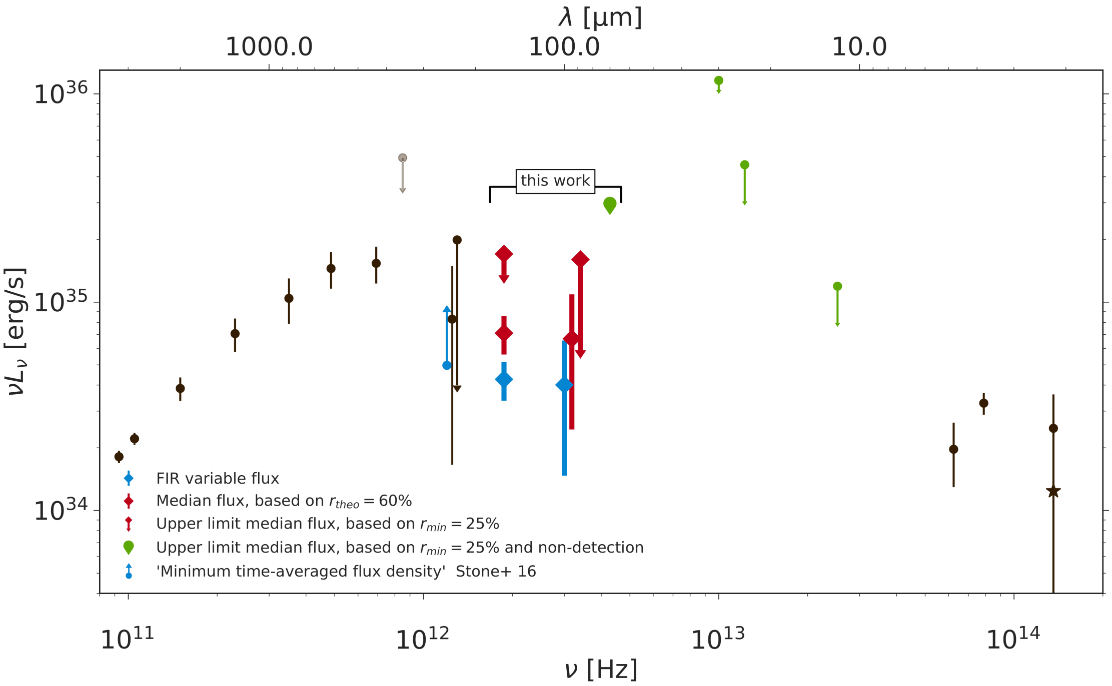

Figure 2.7: An updated SED of Sgr A*: Measured mm to sub-mm data from left to right: Brinkerink et al., 2015; Falcke et al., 1998; Bower et al., 2015; Liu et al., 2016. At $\nu = 890$ GHz, we show the measurement of Serabyn et al., 1997 as an upper limit. This is because we believe that this measurement overestimates the flux due to exceptionally high flux at the time of the measurement. The blue point at $\nu = 1.2$ THz is the "minimum time-averaged flux density" of Stone et al., 2016, where we have assigned an uncertainty of 0.4 Jy. Blue diamonds at $\nu = 1.9$ THz and $\nu = 3.0$ THz are our observed variable FIR flux. The upper limits at in the THz are based on our assumption of a minimal flux excursion of 25%. The data points below are the estimates of the median flux, based on a theoretical prediction of a 60% fractional variability. The green upper limit at $\nu = 4.3$ THz is based on the non-detection in the blue band. The MIR upper limits are taken from Melia and Falcke, 2001, Dodds-Eden et al., 2009 and Schödel et al., 2011. In the NIR, the points denote mean fluxes measured by Schödel et al., 2011, whereas the asterisk denotes the median reported by Dodds-Eden et al., 2010. We plot values and constraints of the quiescence/median flux in dark brown, and the brighter flux excursions (e.g. our FIR measurements) in blue. Upper limits based on non-detections are plotted in green.

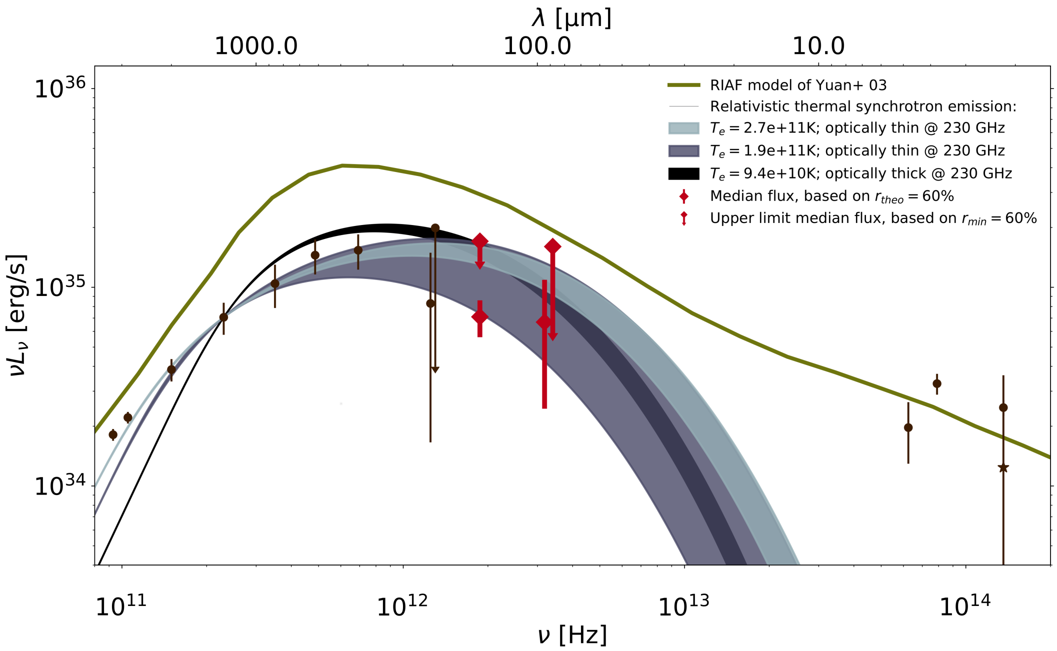

Figure 2.8: RIAF Model for Sgr A* compared to observations.
Same as Figure 2.7, without the FIR variable flux and MIR limits. Solid olive line is the 1D RIAF model of Yuan et al., 2003a. The set of spectra below are synchrotron spectra of a relativistic and thermal electron distribution. The width of the spectra demonstrate the slice through the parameter space of plasma-β which are consistent with the observations. We show the spectra with the lowest electron temperature ($T_e = 9.4 \times 10^{10}$ K) that is consistent with our limits as well as sub-mm measurements. At 230 GHz this spectrum is optically thick. The other two spectra shown are hotter and the plasma is optically thin. Here the peak is broad and set by $\nu/\nu_c \sim 1$ and not the optical depth.

Using the *symphony* code of Pandya et al., 2016 to compute the emission and absorption coefficients, we obtain the luminosity of such a configuration. We assume a wide range of values for the magnetic field strengths defined by the plasma parameter $\beta = 0.03 - 238$. To obtain the electron density, we normalize the flux to the observed value at 230 GHz. This yields a wide range of spectra from which we select the physically plausible ones and comparing them with the observed SED. We find that, a thermal distribution of electrons can describe the observed luminosity in the sub-mm and FIR regime and that the electron temperature is of the order of $T_e \sim 10^{11}$ K. Such calculations are rather sensitive to the radius of the hot bulge of electrons and the normalization flux assumed. Therefore, this electron temperature is only an estimate.
We proceed by computing the optical depth τ for our parameter grid. At 230 GHz, the accretion flow is optically thin for most valid solutions. Only for two solutions, with $T_e < 1.1 \times 10^{11}$ K, is the optical depth τ greater than 1. For the optically thin solutions, the peak is broad and the turn-over is set by $\nu/\nu_c \sim 1$ and not the optical depth.
This is interesting in the context of polarization measurements of Sgr A*. Synchrotron radiation from an optically thin, relativistic thermal distribution is expected to be highly polarized (Jones and Hardee, 1979). Faraday rotation, on the other hand, can scramble the polarization significantly, but is sensitive to both the optical depth and the electron temperature (e.g. Dexter, 2016). Models where the peak is set by synchrotron self-absorption are expected to be optically thick and depolarized by internal Faraday rotation. Higher temperatures, like the ones favored here, are more consistent with the $\sim 5 - 10\%$ linear polarization observed in Sgr A* (Jiménez-Rosales and Dexter, 2018).
In addition, we have also considered a power-law and a κ-distribution for the electron energy distribution. We find that a single power-law distribution with $\gamma_{min} \sim 350 - 500$ and $p \sim 3 - 4$ could explain both the sub-mm and the NIR emission (but not the radio spectrum). On the other hand, it is difficult to model the far- to near-infrared spectrum with the κ-distribution. For models that can successfully match the NIR median flux, the flux contribution from power-law electrons is too high.

2.5 Summary and Outlook

We have, for the first time, detected Sgr A* in the far infrared. There are four immediate conclusions from this:

- Sgr A* is a variable source at 160 μm and 100 μm. The observed peak deviation from median flux at 160 μm is $\Delta F_\nu = (0.27 \pm 0.07)$ Jy and at 100 μm $\Delta F_\nu = (0.16 \pm 0.10)$ Jy.

- The measured variability only places lower limits on the flux for the time of the measurement. Nevertheless, the measured peak variability can be used to constrain the SED by assuming a variability. Models with a prediction of the variability can be tested directly.

- Assuming a minimal flux excursion of 25% over a period of 40 hours allows us to compute upper limits in the red and green bands. At 160 μm the upper limit is $\langle F_\nu \rangle \leq (1.06 \pm 0.24)$ Jy and at 100 μm the upper limit is $\langle F_\nu \rangle \leq (0.64 \pm 0.4)$ Jy. Using the 16 hours of non-detection in the blue band we compute a 70μm upper limit of $\langle F_\nu \rangle \leq 0.84$ Jy.

- Theoretical predictions put the variability in the FIR in the range of $40 - 80\%$. Using a theoretical variability of $\sim 60\%$ yields an estimate for the FIR median flux of $\langle F_\nu \rangle \approx 0.5 \pm 0.1$ in the blue band and $\langle F_\nu \rangle \approx 0.3 \pm 0.2$ in the green band.

We find that modern VLA and ALMA data as well as our results show that the sub-mm flux of Sgr A* is lower than in older observations. In consequence, we find that the 1D RIAF model by Yuan et al., 2003b, which fitted the older sub-mm measurements well, is not consistent with the FIR upper limits and modern measurements of the sub-mm flux. In consequence, we argue that the overall shape of the sub-mm SED is less “bumpy” than previously assumed.

Assuming an isotropic and spherical bulge of relativistic and thermally distributed electrons allows a simplistic implementation of an accretion flow model. Computing several plausible spectra of such a configuration reveals that our FIR measurements, as well as the modern ALMA and VLA data, can be described by such a configuration. The electron temperature is of the order of a few 10^{12} K. This is slightly higher than older estimates. Computing the optical depth of the hot electron bulge, we find the electron plasma at 230 GHz is optically thin for most valid solutions. For those solutions, the peak in the sub-mm is broad and the turn-over is set by $\nu/\nu_c \sim 1$ and not the optical depth.

Acknowledgment GP acknowledges support by the Bundesministerium fur Wirtschaft und Technologie/Deutsches Zentrum fur Luft- und Raumfahrt (BMWI/DLR, FKZ 50 OR 1408) and the Max Planck Society. SvF, PP, IW, AJ-R and FW acknowledge support from the International Max Planck Research School (IMPRS) on Astrophysics at the Ludwig-Maximilians University, as well as funding from the Max-Planck Society.

Chapter 3

The Flux Distribution of Sagittarius A*

Original Publication: GRAVITY Collaboration &
R. Abuter, A. Amorim, M. Bauböck, J.B. Berger, H. Bonnet, W. Brandner, V. Cardoso, Y. Clénet, P.T. de Zeeu, Y. Dallilar, J. Dexter, A. Eckart, F. Eisenhauer, N.M. Förster Schreiber, P. Garcia, F. Gao, E. Gendron, R. Genzel, S. Gillessen, M. Habibi, X. Haubois, T. Henning, S. Hippler, M. Horrobin, A. Jiménez-Rosales, L. Jochum, L. Jocou, A. Kaufer, P. Kervella, S. Lacour, V. Lapeyrère, J.-B. Le Bouquin, P. Léna, M. Nowak, T. Ott, T. Paumard, K. Perraut, G. Perrin, O. Pfuhl, G. Ponti, G. Rodriguez Coira, J. Shangguan, S. Scheithauer, J. Stadler, O. Straub, C. Straubmeier, E. Sturm, L.J. Tacconi, F. Vincent, I. Waisberg, E. Wieprecht, E. Wiezorrek, J. Woillez, S. Yazici, G. Zins
Corresponding authors: S.D. von Fellenberg & F. Widmann
Published in to Astronomy and Astrophysics: GRAVITY Collaboration et al. 2020 A&A 638, A2
Abstract: The Galactic Center black hole Sagittarius A* is a variable NIR source that exhibits bright flux excursions called flares. When flux from Sgr A* is detected, the light curve has been shown to exhibit red noise characteristics and the distribution of flux densities is non-linear, non-Gaussian, and skewed to higher flux densities. However, the low-flux density turnover of the flux distribution is below the sensitivity of current single-aperture telescopes. For this reason, the median NIR flux has only been inferred indirectly from model fitting, but it has not been directly measured. In order to explore the lowest flux ranges, to measure the median flux density, and to test if the previously proposed flux distributions fit the data, we use the unprecedented resolution of the GRAVITY instrument at the VLTI. We obtain light curves using interferometric model fitting and coherent flux measurements. Our light curves are unconfused, overcoming the confusion limit of previous photometric studies. We analyze the light curves using standard statistical methods and obtain the flux distribution. We find that the flux distribution of Sgr A* turns over at a median dereddened flux density of (1.1 ± 0.3) mJy. We measure the percentiles of the flux distribution and use them to constrain the NIR K-band SED. Furthermore, we find that the flux distribution is intrinsically right-skewed to higher flux density in log space. Dereddened flux densities below 0.1 mJy are hardly ever observed.

In consequence, a single powerlaw or lognormal distribution does not suffice to describe the observed flux distribution in its entirety. However, if one takes into account a power law component at high flux densities, a lognormal distribution can describe the lower end of the observed flux distribution. We confirm the RMS-flux relation for Sgr A* and find it to be linear for all flux densities in our observation. We conclude that Sgr A* has two states: the bulk of the emission is generated in a lognormal process with a well-defined median flux density and this quiescent emission is supplemented by sporadic flares that create the observed power law extension of the flux distribution.

3.1 Introduction

The supermassive black hole at the Galactic Center, Sagittarius A* (Sgr A*) is associated with a variable radio/(sub-)mm source, a variable near-infrared (NIR) source, and a continuum source in the X-ray coupled with occasional strong X-ray flares (Genzel et al., 2010).
The NIR counterpart of Sgr A* is highly variable and not always detected in photometry of ground-based telescopes and space observatories. When the emission is detected, it shows a non-Gaussian flux distribution. The power spectral density (PSD) is best fit with a single power law slope, $\nu^{\Gamma\sim-2}$, that breaks into uncorrelated white noise for timescales longer than ~ 250 min (Witzel et al., 2018). There is no evidence for quasi-periodic oscillations if the light curve is studied in its entirety (Do et al., 2009); however, individual flares may possess periodic sub-structure (Genzel et al., 2003a). The NIR flux distribution has been modeled with a multi-component distribution function, where the fainter flux levels, if detected, are described by a lognormal distribution and the brighter so-called flare states follow a power law tail (Dodds-Eden et al., 2009). However, follow-up studies of the flux distribution have found that a power law tail is not necessary and, instead, a single power law distribution or lognormal distribution suffices to describe the observed distribution of flux densities when temporal correlations are taken into account (Witzel et al., 2012; Witzel et al., 2018). By comparing the inferred spectral slope from parallel observations in the NIR K and M band, (Witzel et al., 2018) favor a lognormal distribution for both bands.
Recently, (Do et al., 2019) reported a flare of unprecedented brightness (magnitude ~ 12 in Ks). They find that a flare of this brightness is inconsistent with the long term flux distribution published in (Witzel et al., 2018). They argue that this may indicate that the accretion flow has changed, possibly due to the pericenter passage of the star S2 or the gaseous object G2 (Gillessen et al., 2012). Alternatively, a second mechanism may be needed for the flare state.
The X-ray flares are correlated with strong NIR flares, but the converse is not true (e.g. Dodds-Eden et al., 2010; Witzel et al., 2012). While many dedicated multi-wavelength campaigns have been conducted, no clear correlation between either the X-ray or the NIR with the (sub-)mm flux could be established. This is possibly due to the roughly eight-hour timescale in the sub-mm light curve being on the order of the maximum length of ground-based observations (Dexter et al., 2014).
From a theoretical point of view, the mechanism or mechanisms that generate the NIR flux

are not well understood. Because the rise and fall time of flares is on the order of a few minutes, the emitting region is constrained by the light speed to a few Schwarzschild radii R_s. Assuming the magnetic field scales as one over the distance with respect to Sgr A*, this constrains the emitting region to be located within $\sim 10R_s$ of Sgr A* (e.g. Barrière et al., 2014).

The light curve and the slope of bright NIR/X-ray flares have been modeled quantitatively by assuming that a population of electrons is accelerated out of thermal equilibrium into a power law energy distribution. In this model, a cooling break, induced by the frequency-dependent cooling time of synchrotron radiation, explains the NIR and X-ray spectral slopes (Dodds-Eden et al., 2010; Li et al., 2015; Ponti et al., 2017). However, the mechanism that could explain such an acceleration is not understood in a quantitative fashion. Among several alternatives, previous works have proposed magnetic reconnection as a possible mechanism at work here, drawing upon analogies to solar flares or coronal mass ejections (Yuan et al., 2003b; Yusef-Zadeh et al., 2006).

Time-dependent simulations attempt to model the accretion flow more qualitatively. The plasma evolution is computed by solving the magnetohydrodynamic (MHD) equations, while accounting for general relativistic (GR) effects in the proximity of the black hole. Such time-dependent simulations have been able to reproduce the typical observational charactaristics of NIR light curves. Realistic light curves have been produced in simulations where the accretion flow is misaligned with the black hole spin (Dexter et al., 2014) through lensing of flux tubes (Chan et al., 2015), description of the electron thermodynamics (e.g. Ressler et al., 2017; Dexter et al., 2020), or through the introduction of non-thermal electrons (e.g. Ball et al., 2016; Mao et al., 2016). However, all of these simulations are limited by the numerical resolution, the volume size of the simulation, and the uncertainty of the initial magnetic field configuration. They have difficulties producing realistic outflows along the poles and cannot produce the observed high X-ray fluxes during flares.

Recently, the GRAVITY Collaboration et al., 2018a has reported the detection of orbital motions for three bright flares. The three flares exhibit a circular clockwise motion on the sky with typical scales of 150 μas over a few tens of minutes. This implies a hotspot velocity of around 30 % of the speed of light. The motion is correlated with an on-sky rotation of the polarization angle with about the same period as the motion. Using the relativistic ray tracing code NERO, the GRAVITY Collaboration et al. (submitted) modeled the motions with a hotspot orbiting the black hole, with a roughly face-on inclination of $i \sim 140°$. The emitting region is constrained to less than five gravitational radii in diameter.

In this paper, we build on our previous work on the flux distribution, extending the measurements beyond the detection limit of single-telescope observations using interferometric model fitting and coherent flux measurements. The high sensitivity of GRAVITY pushes the detection limit well beyond the peak of the flux distribution, which allows us to establish an empirical median flux density and variability measures. Through interferometric model fitting, we obtain the un-confused source flux densities of Sgr A* and thereby overcome a fundamental limitation of single telescope observations. Furthermore, we test the paradigm of a single probability distribution for the flux distribution and test different probability density functions (PDFs).

3.2 Data

There are two independent methods for extracting the flux from our interferometric data. The first method is similar to traditional photometry where we measure the integrated coherent flux. The coherent flux is computed as the flux product of each baseline consisting of a pair of telescopes, normalized by the visibility on this baseline. The coherent flux is blind to incoherent light, that is, speckle noise from bright nearby stars is suppressed. Explicitly, we compute the coherent flux as:

$$\langle F_{coherent} \rangle = | \ \langle A_{vis} \cdot \exp\left(-i\phi_{vis}\right) \rangle_B \cdot \langle F \rangle_B \ |, \tag{3.1}$$

where A_{vis} is the visibility amplitude, ϕ_{vis} is the visibility phase, F is the detector flux and $\langle \circ \rangle_B$ denotes the average over all baselines. To calibrate the flux density, we compute the coherent flux of observations centered on S2. We interpolate the flux in the time gaps between calibration observations using polynomial fits. We use a zeroth order polynomial if there are fewer then three calibrator measurements, a first order polynomial if there are fewer than five calibrator measurements, and a second order polynomial if there are five or more measurements. The coherent flux of S2 is closely correlated with airmass. If extrapolation is necessary, we check that it is reasonable. Explicitly, we checked that the extrapolation does not diverge and that it resembles the air mass trend. To account for the fact that S2 may not be perfectly centered with respect to the actual fiber position, we calibrate the visibility phase to 0°.
The second method to measure the flux density uses a model fitting applied to the observed interferometric quantities: the visibility modulus, the visibility squared, and the closure phase. We can model the GRAVITY Galactic Center observations with an interferometric binary consisting of Sgr A* and the orbiting star S2. According to the van Cittert-Zernicke theorem, the visibility of an image is given by the Fourier transform of the image. In the simple binary case, where S2 and Sgr A* are modeled as two point sources of a given flux ratio f, separated by a certain distance $s = \vec{B} \cdot \delta\vec{D}$, the complex visibility is given by:

$$V(s, f) = \frac{1 + f e^{(-2\pi i s)/\lambda}}{1 + f}, \tag{3.2}$$

for a given baseline vector $\vec{B}$, separation vector $\delta\vec{D}$ and wavelength λ.
For real observations, this formula needs to be extended to account for various different parameters such as the source spectral slopes, potentially varying flux ratios for different baselines, pixel response functions, etc. The full derivation of the fitting formula can be found in Waisberg, 2019.
Figure 3.1 shows an example of the full binary model fit to the observed visibilities and closure phases for the night of July 28, 2018. The angular separation of S2 and Sgr A* was ~ 24.7 mas. Moreover, during the observation, a bright flare occurred for which an orbital motion close to the innermost stable orbit was reported in GRAVITY Collaboration et al., 2018a. The flux density of Sgr A* is (9.1 ± 1.3) mJy.
We chose either the coherent flux or the binary fit to measure the flux density depending on the separation of S2 and Sgr A*. For 2017 and 2018, strong binary signatures are present

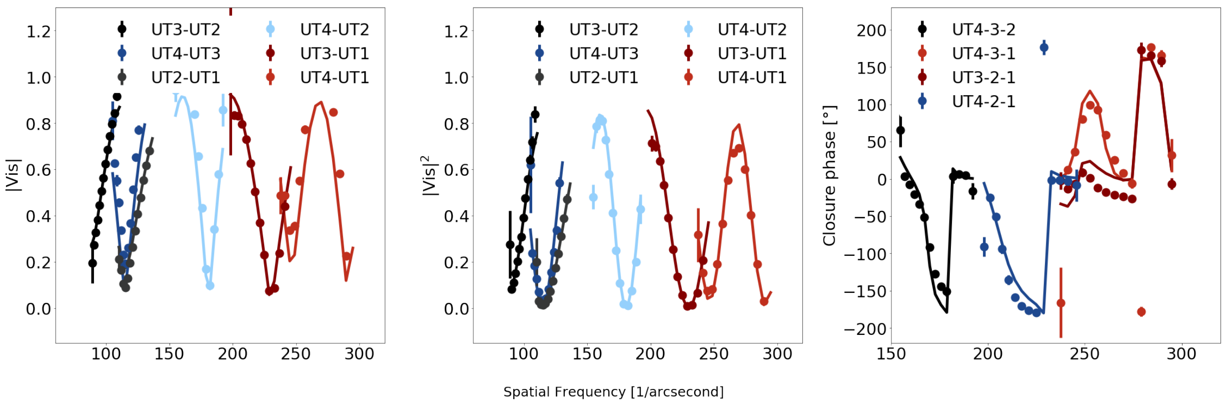

Figure 3.1: Binary fit to interferometric quantities for the night of July 28, 2018. The three panels show the best-fit binary model to the visibility modulus, the visibility squared, and the closure phase.

in the data. We can therefore make use of the model fitting where the flux ratio is a direct, absolute and un-confused measurement of the flux of Sgr A*. In 2019, S2 moved to the edge of the interferometric field of view (IFOV), and thus fitting a binary model becomes more difficult. Consequently, we use the integrated coherent flux for 2019.

The binary flux ratios measure the un-confused flux ratio of the two sources. This assumes that there is no third source hidden near Sgr A* or S2 within the $\sim (2 \times 4)$ mas interferometric beam of GRAVITY. The 2017 and 2018 light curves of Sgr A* are unaffected by the contribution of nearby stars overcoming the confusion limit of previous studies. In contrast, the coherent flux includes any possible coherent sources within the IFOV of GRAVITY, corresponding to FWHM $=\sim 70$ mas.

In total, our data set comprises 47 nights in 2017 to 2018 and an additional 27 nights in 2019. Prior to 2019, there are 650 exposures centered on Sgr A*, totaling to ~ 54.2 hours. After bad data rejection, 461 exposures remain totaling to ~ 38.4 hours. In 2019 there are 324 observations, out of which 268 pass the rejection totaling to 26.3 hours.

The reduction of the individual exposures is largely unchanged compared to the reduction used in GRAVITY Collaboration et al., 2018b; GRAVITY Collaboration et al., 2019a. For the 2017 and 2018 data, we bin the data to five-minute exposures in order to ensure a robust binary fit at the lowest fluxes. For the 2019 data, where we can measure the coherent flux directly, we use sub-exposures binned to 40 seconds.

We report the dereddend flux density at 2.2 μm. To obtain absolute, dereddened fluxes, we use the extinction coefficient $A_{Ks} = 2.43 \pm 0.07$ from Schödel et al., 2010 and Fritz et al., 2011. We derive the flux density of S2 from the long-term photometry with NACO, yielding $mag_{K_s} = 14.12 \pm 0.076$. Throughout this work we assume that the S2 flux density is constant in time (Habibi et al., 2017). Combining this measurement with the extinction coefficient above, we find the dereddened S2 flux density at 2.18 μm to be 15.8 ± 1.5mJy. The uncertainty is dominated by the S2 photometry and the extinction uncertainty. Therefore, we neglect the difference in central wavelength of the NACO and GRAVITY bands

($\sim$ 0.02 μm). Both methods described above have several peculiarities which must be tuned in the data reduction before we can produce a final light curve. The details are given in the next two sections.

3.2.1 Tuning of binary flux ratios

Outlier contamination

Bad fits must be flagged and removed. This is critical in the context of estimating the flux distribution: The quality of the fit is a function of the brightness of Sgr A* and any selection bias may affect the results. In order to minimize the flux dependent bias, we reject data only based on bad observing conditions or data with obvious telescope, facility or instrument problems. These classifiers are flux independent, and therefore the rejection is less critical. However, even such a blind approach may bias the flux distribution if too many bad fits contaminate the light curve. In order to rule out that bad fits significantly contaminate the flux distribution, we tested different flagging schemes. We find that our results are robust against outlier contamination (see Appendix A2.1).

Coupling correction

The flux from the different telescopes is coupled into optical fibers. Therefore, the flux ratio in the binary fits is not only a function of the intrinsic flux ratio but also of the fiber coupling response function. We approximate the fiber coupling response function as a two-dimensional Gaussian in the field, centered on the fiber center (Perrin and Woillez, 2019; GRAVITY Collaboration et al., 2018b). We have chosen files in which the fiber is centered on Sgr A*. Since the distance between S2 and Sgr A* changes with time, the flux ratio is modulated by this movement. We correct for this modulation by multiplying the flux ratio by the response function. To account for positioning errors of the fiber, we compute the coupling factor using the measured fiber position with respect to S2.
In 2017, for each telescope, the respective fiber position was often offset by a few mas. This complicates the correction and makes the 2017 light curve sensitive to this effect. In 2018, the fiber positioning was optimized. Furthermore, S2 was closer to Sgr A* and the binary separation changes less. As a consequence, the fiber coupling correction is less critical in this year.

3.2.2 Tuning of coherent flux measurement

In 2019, S2 moved to the edge of the $\sim$ 70 mas IFOV of GRAVITY. However, throughout 2019, the S2 contribution was on the order of a few percent. It is thus necessary to subtract S2's contribution.
We can model the flux that is coupled into the fiber using the fiber coupling response function used for the binary. However, at the edge of the IFOV, the relation starts to break down. This is especially critical for low fluxes of Sgr A* for which the contribution of S2 is comparably large.

To improve the coupling correction, we use the measured binary flux ratio: We fit the flux ratio for each file and divide the fitted flux through the coherent flux of that file. Since S2's contribution is constant during the night, its contribution can be estimated by dividing the binary flux ratio by the coherent flux and averaging this ratio. The median S2 contribution is around 4% or ≈ 0.4 mJy. We correct the coherent flux by subtracting each night's median S2 flux from the individual exposures.

3.2.3 Determination of noise

The uncertainty of the binary flux ratios includes the fit uncertainty. However, systematics dominate the errors. Consequently, to determine the noise in our light curve, we use two proxy methods. We use the 2019 light curve which has a higher temporal sampling of eight times 40 seconds per five-minute exposure. We subtract a polynomial fit from each five minute exposure. We determine the noise from the standard deviation of the residuals. The second approach uses the difference between the 0° and the 90° polarization for each exposure. We find a consistent power law dependency between the RMS and the dereddened flux density for both methods:

$$\sigma(F) = 0.3 \times F^{0.67}. \tag{3.3}$$

We find that a single power law slope suffices to describe the noise. We do not find evidence for a flattening of the noise towards lower fluxes, which would indicate a transition to detector read-out noise. The details of this analysis are presented in Appendix A2.2.

3.3 Results

Figure 3.2 shows the light curve observed in the years 2017, 2018, and 2019. Figure 3.3 shows the derived flux distribution for the respective years. We choose our histogram bin width and the bin number using Scott's normal reference rule (Scott, 2015). This choice is motivated by the fact that the data was well described by a lognormal parameterization in previous studies and our choice of log bins.
For correlated data, as in our light curve, the $\sigma = 1/\sqrt{N}$ estimator for the bin uncertainty underestimates the errors (e.g., Vaughan et al., 2003). For this reason, we chose block bootstrapping to estimate the histogram uncertainty. We created 100 surrogate light curves by copying the original data and dropping 50% of the observation nights. We redrew the observations nights with replacement from the original data. The choice for blocks of observation nights ensures that the light curve is uncorrelated. We estimate the uncertainty of each histogram bin from the standard deviation of the histogram created from the bootstrapped light curves and quadratically add the $1/\sqrt{N}$ estimate. For 2017 and 2018 we have defined a formal detection significance ratio based on the ratio of significance of a single source model compared to the binary model. If this ratio is below 1, we count the flux density point in the flux density bin where it is observed, but we quadratically add its density contribution to the bin's error.

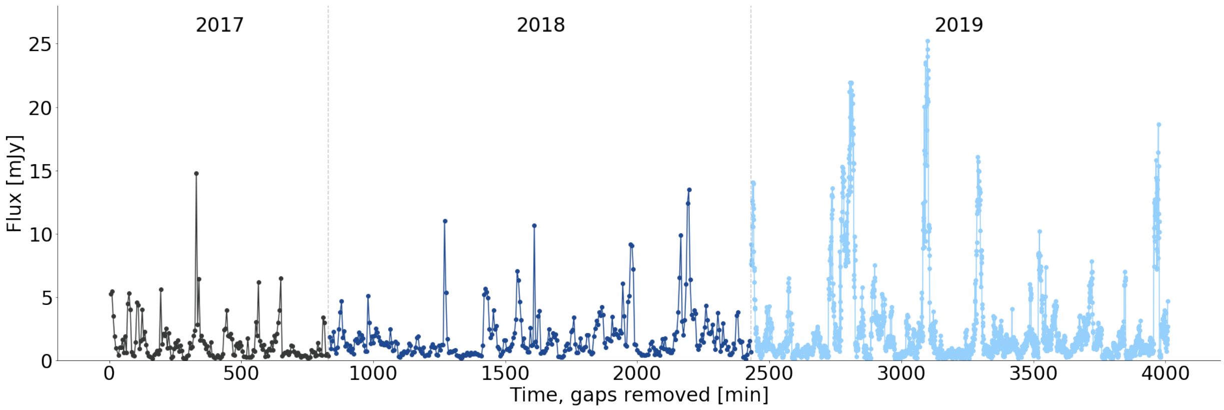

Figure 3.2: Light curve of Sgr A* as observed by GRAVITY in the years 2017, 2018, and 2019 with time gaps removed.

Sgr A*'s light curve is correlated and, thus, the flux density histogram is not strictly a measure of the averaged probability density. As a consequence, if Sgr A* spends less than a correlation time in a certain flux density bin, it is expected that the detection frequency is biased. Because adjacent points in the light curve are correlated, a single high flux density value is likely to be preceded and followed by additional high flux densities. A histogram of such a section of the light curve would overestimate the detection frequency of these high flux densities. Conversely, a section of the light curve containing no high-flux density excursions would lead to an underestimated detection frequency of high flux densities. For observations that last much longer than the correlation timescale, the observed detection frequency converges to the true value.

While we expect that the block bootstrap captures this effect to some extent. However, it is not clear if it can estimate the errors if more than one physical process in the source is present which may be on or off in different observations. As a consequence, for flux density bins above a dereddened flux of 3 mJy, we conservatively increase the histogram errors by multiplying them by a weight factor. The weight factor is computed by dividing the total observation time for a given flux density bin by a correlation time guess of 120 minutes. While this is shorter than the correlation time estimate in, for instance, Witzel et al., 2018, it is longer than the usual length of the perceived flares and, consequently, a conservative estimate for a two-process scenario.

It is noteworthy to add that we almost always detect Sgr A* for all three years. Using our most conservative estimate, we find 17 ($> 3\sigma$) or 6 ($> 1\sigma$) non-detections in 2017 and 2018 (See Appendix A2.1 for details). Furthermore, despite the large separation, and consequently the minimal flux coupling of S2, we can almost always fit a binary in 2019. Using reconstructed images we find that Sgr A* is always detected in 2019 (GRAVITY Collaboration in prep.). This illustrates that the flux distribution is right-skewed in log space, and flux densities below 0.1 mJy occur only very infrequently.

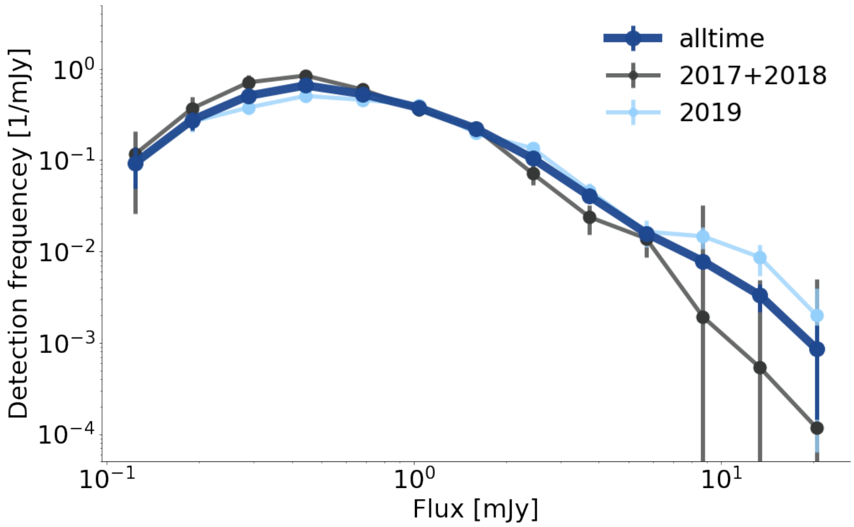

Figure 3.3: Dereddened flux distribution of Sgr A*: The thick blue line is the flux distribution combining all three observation years. The grey line combines the flux distribution of 2017 and 2018, while the light blue line is the flux distribution of 2019.

3.3.1 The empirical flux distribution

Since we almost always have a detection of Sgr A*, the empirical percentiles can serve as an assumption-free description of the flux distribution. Using the percentiles shown in Table 3.1, we updated the SED of Sgr A* as shown in Figure 3.4. The uncertainty on the flux density percentile is computed from the difference in the two polarizations, which is believed to be largely instrumental.

Comparing the polarization-averaged flux density percentiles, the 2017 and 2018 50%, 86%, and 95% percentiles are consistent. Because the 2017 light curve is limited by the fiber coupling correction (see Section 3.2.1), the low percentiles of 2017 cannot be compared with those of the following years. On the other hand, the low flux density percentiles (5% and 14%) of 2018 and 2019 are consistent with each other. The 50% percentile for 2019 is marginally consistent with its 2017 and 2018 counterpart.

This is consistent with an unchanged low and median flux distribution in all years covered by GRAVITY observations. The high flux density percentiles (86% and 95%) of the 2019 data are not consistent with their counter parts from the previous years. This increase in observed flux density is caused by the detection of six bright flares ($F_{SgrA} \sim F_{S2}$) in 2019. The increase in the flux density percentiles is significant with respect to the measurement uncertainty. In the flux distribution we have estimated the bin uncertainty conservatively to account for the correlation in the light curve and the effect of two potential states. In consequence, the flux distribution of 2017 and 2018 is consistent with the 2019 flux distribution.

Table 3.1 lists separately the percentiles for both 0° and 90° polarizations as well as the average. It is not clear if the apparent differences between the two polarization are of

Percentiles [mJy]: 2017	5 %	14 %	50%	86%	95%
0° Polarization	~~0.21~~	~~0.29~~	1.0	2.5	5.0
90° Polarization	~~0.20~~	~~0.26~~	0.6	1.7	3.0
Average	$\cancel{0.21 \pm 0.01}$	$\cancel{0.28 \pm 0.02}$	0.8 ± 0.3	2.1 ± 0.6	4.0 ± 1.4
Percentiles [mJy]: 2018	5 %	14 %	50%	86%	95%
0° Polarization	0.35	0.48	1.2	2.8	5.0
90° Polarization	0.31	0.43	0.9	2.3	5.1
Average	0.33 ± 0.03	0.46 ± 0.04	1.1 ± 0.2	2.6 ± 0.4	5.0 ± 0.1
Percentiles [mJy]: 2019	5 %	14 %	50%	86%	95%
0° Polarization	0.26	0.43	1.2	5.3	12.1
90° Polarization	0.34	0.60	1.6	5.6	11.4
Average	0.30 ± 0.06	0.5 ± 0.12	1.4 ± 0.3	5.5 ± 0.2	11.8 ± 1.3
2017, 2018 & 2019 average	0.28 ± 0.07	0.4 ± 0.1	1.1 ± 0.3	3.4 ± 1.7	6.9 ± 3.8

Table 3.1: Percentiles of the flux distribution: Empirical dereddened flux density percentiles of the light curve for the two measured polarizations. The averages reported are the mean of the polarization, the error is computed from the difference of the polarizations. The 5% and 14% quantiles of 2017 are affected by instrument systematics and thus are given only for completeness. We note that the polarization angle is with respect to the instrument and is not de-rotated to reflect the on-sky polarization.

physical origin, since the polarization angle is measured with respect to the instrument and not the on-sky orientation. In consequence, the differences may reflect additional systematic uncertainties rather than the intrinsic polarization of the source.

3.3.2 Analytic Distribution Function

We fit the flux distribution histogram with several analytic probability density functions (PDFs). These distributions have been selected according to four criteria: non-Gaussianity, right skewedness, historical usage, and physical motivation. These can be grouped into four families of PDFs:

1. The lognormal distribution: This distribution is frequently used in active galactic nuclei (AGN) and X-ray binaries: The lognormal distribution results from many unresolved subprocesses which are Gaussian and amplify each other into a single observable. Thus the lognormal distribution results from the product of the Gaussian subprocesses (e.g., Uttley et al., 2005). This model has been applied to Sgr A* in all past studies of the NIR flux distribution (e.g., Dodds-Eden et al., 2009; Witzel et al., 2012; Hora et al., 2014; Witzel et al., 2018).

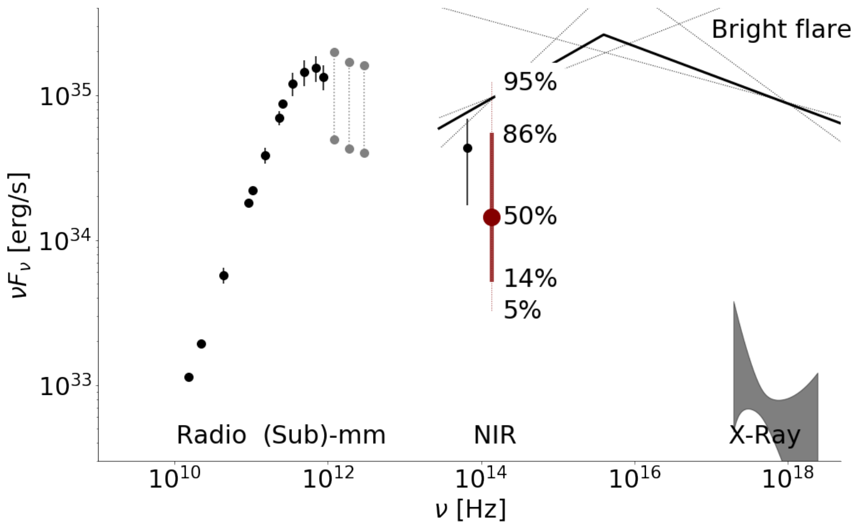

Figure 3.4: SED of Sgr A*: the radio and sub-mm data are from Falcke et al., 1998; Bower et al., 2015; Brinkerink et al., 2015; Liu et al., 2016; Bower et al., 2019. The far infrared data is from Stone et al., 2016 and Fellenberg et al., 2018. The NIR M-band data is the median dereddened flux density inferred from the lognormal model of Witzel et al., 2018. The NIR K-band data is the GRAVITY dereddened flux density: the thick point is the median flux density, and further flux density percentiles are annotated. Also shown are the NIR and X-ray flux density spectrum of a bright simultaneous flare observed by Ponti et al., 2017, the quiescent X-ray flux density is determined from Baganoff et al., 2003b.

2. The power law distribution: power law distributions are commonly observed in nature and find a possible explanation in the frame work of self-organized criticality: Self-organized critical systems are systems in which a constant influx of energy breaks down to smaller scales; the power is sometimes associated with the dimensionality of the system or the degrees of freedom (Aschwanden et al., 2016). Such distributions have been discussed in the context of Sgr A* to explain a possible flare state, the distribution of NIR emission as a whole and the distribution of X-ray flares (Dodds-Eden et al., 2009; Witzel et al., 2012; Li et al., 2015).

3. The family of exponential distributions: Exponential distribution functions such as the Gamma distribution are a generalization of the Poisson process, in which a waiting time between two events is relevant. Such distribution functions have not previously been used to describe the flux distribution of Sgr A*. However, they are conceptually attractive for accretion flows since the flux density at any time depends on the influx of energy and on the intensity of the flares that had come before.

4. Composite distributions: If there are two processes creating the flux, the observed PDF is the convolution of the PDF of each process. Such a two state scenario has been proposed by Dodds-Eden et al., 2009 to overcome the apparent tension of a single lognormal and the high flux flares. In their scenario, the bulk of the emission is created from a lognormal process, and a power law tail is allowed to explain the high flux flares. We adopt this parameterization, but we note that, in principle, many combinations of PDFs could be imagined to explain such a two state scenario.

Before these model PDFs can be fitted to the flux distribution, the effects of measurement noise have to be taken into account. In contrast to single telescope photometric studies, the light curve measured by GRAVITY is unconfused. Prior to 2019, the flux density reported is the direct ratio of S2 and Sgr A* and is thus unconfused. This assume that there is no third source within the GRAVITY beam (FWHM $\sim$ (2×4) mas). In 2019 we have measured the integrated coherent flux density in the IFOV, which is blind to the background contribution of bright nearby stars and the galaxy. Furthermore we have subtracted the contribution from S2, which is the closest and brightest star in the IFOV. Using deep images obtained from stacking several observation nights yields an upper limit for the brightness of a potential third source of $\sim$ 0.3 mJy. We therefore assume that Sgr A* is the only flux contributor in 2019. This assumption is assessed in further detail in appendix A2.1. Consequently, we can model the flux distribution without the assumption of a Gaussian background.

In the presence of observational noise, the intrinsic PDF of Sgr A* will be affected by the PDF of the noise, that is, the intrinsic distribution function is convolved with the noise distribution. In order to compare our data to a model PDF, we bin the model PDF to match the flux density bins of the observed flux distribution. To address this mathematically, we

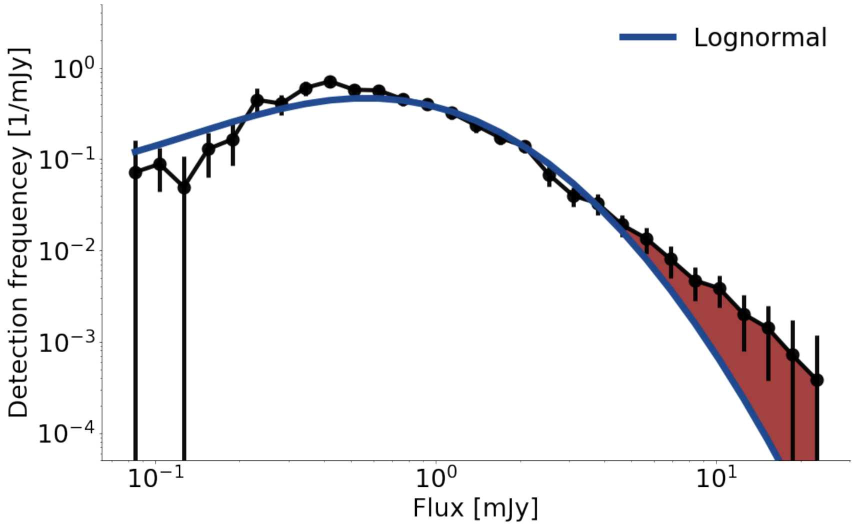

Figure 3.5: Distribution fits: The observed dereddened flux distribution is fitted with a lognormal PDF. The blue line shows the disfavored single lognormal distribution, the red region line indicates the excess flux density compared to the best-fit distribution. We chose the bin number according to Scott's rule and we chose a logarithmic binning. The error bars are computed from Poisson statistics and a block boot strap: see Section 3.2 for details.

integrate the noise smoothed model PDF over each histogram bin:

$$P(F) = \frac{1}{F_{max} - F_{min}} \int\limits_{F_{min}}^{F_{max}} \int\limits_{0}^{\infty} \mathrm{P}_{\mathrm{int}}(t, \dots) \cdot \mathcal{N}(\tau, F', \sigma(\tau)) \; d\tau \; dF', \tag{3.4}$$

where F is the flux density of the bin center, and ... substitutes for the intrinsic parameters of the PDF. Since the histogram is normalized to 1, but not all possible flux density states have been observed, we renormalize the observed distribution function. Assuming the empirical noise relation obtained for the 2019 observations holds for the other years as well, we can model the noise as a Gaussian $\mathcal{N}(F_{obs}, \sigma(F_{obs}))$, where $\sigma = 0.3 \times F^{0.67}$.

Lognormal and power law flux distributions

We find that a single lognormal distribution is not sufficient to describe the data. The flux distribution is log-right skewed. Consequently the log-symmetric lognormal distribution cannot fit the tail of the distribution at high flux densities. A lognormal fit to the noise-convoluted distribution function is given in Figure 3.5.
Similarly, the detection of the mode of the flux distribution rules out a simplistic power law model with $P(F > F_{min}) = (\alpha + 1)/F_{min} \cdot F^{-\alpha}$ and $P(F < F_{min}) = 0$. Nevertheless, the power- law-like tail for flux densities larger than the mode of the flux distribution allows for a variety of models in which high flux densities are described by a power law

and the flux densities beyond the mode of the distribution are described by a different parameterization. One such model, the tailed lognormal model proposed by Dodds-Eden et al., 2011 will be discussed in the following subsection.

Exponential distribution functions

We test the Gamma distribution and the Weibull distribution as model distributions for Sgr A*. We find that neither distribution can describe the observed flux distribution. However, when taking their inverse form (i.e., $P(F) = \Gamma(1/F)$) both distribution functions give a good fit to the observed flux distribution. The grey and the dark blue curves in Figure 3.6 show the best-fit inverse Gamma and inverse Weibull PDFs to the flux distribution.

The Gamma function arises from Poisson processes with a distribution of wait times between successive events. This picture makes them initially attractive for modeling the infrared variability as a recurrent flaring process. However, the inverse Gamma function is the same distribution with a random variable corresponding to the reciprocal of the flux density. This quantity can be understood as a timescale with units [s/erg], that is, the time it takes for a certain amount of energy to be released. It is difficult to imagine a physical scenario in which the flux from Sgr A* can be explained by a succession of events corresponding to an increase in the characteristic emission timescale of the accreting material. We are not aware of any discussion in the literature of such a process. In the absence of a physically motivated model, we do not therefore consider the inverse exponential description of the flux distribution.

Composite distribution functions

We find that a piecewise function consisting of a lognormal distribution joined to a power law tail for flux densities greater than a transition flux density yields a good fit to the flux distribution. Such a distribution function has been proposed by Dodds-Eden et al., 2010 and has been interpreted in the following sense: The quiescent low flux density states are associated with a lognormal distribution. The lognormal flux distribution is motivated in analogy to the flux distribution of many accreting compact objects such as X-ray binaries or AGN ()Uttley2005. On top of the quiescent phase, there exists a secondary process which creates the flux density tail responsible for the highest flux densities, which coincide with the observed flaring events. The transition flux density marks the flux density at which the observed fluxes are dominated by the secondary process. We fit the distribution function with the parametrization proposed by Dodds-Eden et al., 2010 and find that such a prescription yields a very good fit to the data (see the light blue curve in Figure 3.6). Such a parametrization is useful to illustrate a flux distribution composed of multiple components; however it is not rigorous in a statistical sense: A two-process scenario would be described by the convolution of the individual processes. However, we include it here as a proxy for models in which the flares are described by a separate physical process from the low-flux density state.

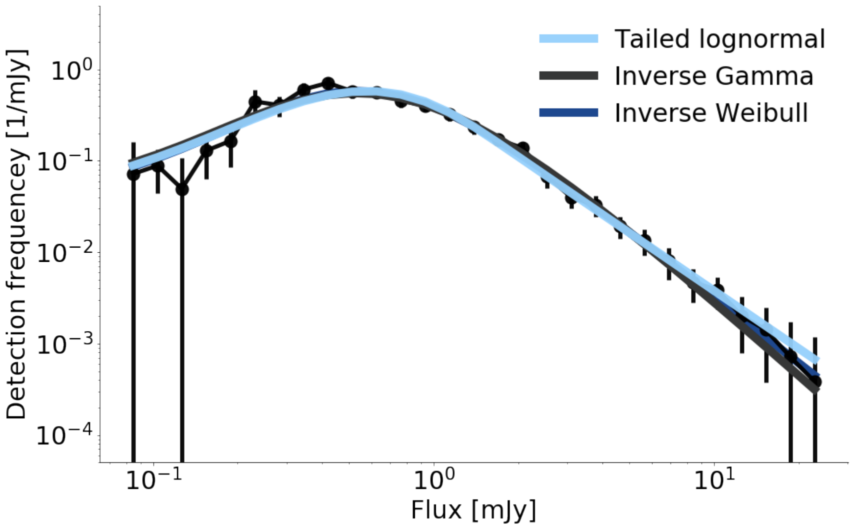

Figure 3.6: Same as Figure 3.5, for distribution functions which describe the observed distribution well.

Distribution name	Functional	best fit values	χ^2_{red}	BIC	AICc
LogNormal	$\frac{1}{\sqrt{2\pi}}\frac{1}{x\sigma_{ln}} \times \exp\frac{-(\log x - \mu_{ln})^2}{(2\sigma_{ln})^2}$	$\mu_{ln} = (0.08 \pm 0.04)$ $\sigma_{ln} = (0.77 \pm 0.03)$	1.69	52.4	46.1
LogNormal + Tail	$\begin{cases} \mathcal{LN}(x) & x \leq x_{min} \\ c\mathcal{LN}(x_{min})F^{-\alpha}/x_{min}^{-\alpha} & x > x_{min} \end{cases}$	$\mu_{ln} = (-0.21 \pm 0.23)$ $\sigma_{ln} = (0.53 \pm 0.13)$ $\alpha = (2.08 \pm 0.12)$ $x_{min} = (1.1 \pm 1.9)$	0.63	29.2	17.4
Inverse Gamma	$\frac{\beta^\alpha}{\Gamma(\alpha)x^{(\alpha+1)}}e^{(-\beta/x)}$	$\alpha = (1.76 \pm 0.14)$ $\beta = (1.49 \pm 0.14)$	0.57	22.1	15.8
Inverse Weibull	$\beta\ \alpha^\beta x^{(\beta+1)} e^{(-(\alpha/x)^\beta)}$	$\alpha = (0.78 \pm 0.03)$ $\beta = (1.41 \pm 0.07)$	0.44	18.7	12.4

Table 3.2: Comparison of a lognormal, tailed lognormal, inverse Gamma and Weibull distribution: Name, functional, best fit values, χ^2, Bayesian Information Criterion (BIC) and the small sample corrected Akaike Information Criterion (AICc). The dimensionless parameters describing dereddened flux densities are in mJy.

Comparison of the distribution fits

Table 3.2 summarizes the least squares distribution fits presented in Figures 3.5 and 3.6. We assess the four competing models using different standard model comparison formulae. We have disfavored the inverse exponential distribution functions, because we do not find a straight forward physical model.
In all model comparisons, the visual perception that the lognormal distribution fails to produce the high flux density tail is reflected, despite the larger number of parameters of the tailed lognormal model. For instance, the difference in the small-sample corrected Akaike Information criterion[1] (AICc) between lognormal and the tailed lognormal model is $\Delta AICc = 46.1 - 17.4 = 28.7$, indicating a very strong evidence in favor of the tailed model.

3.3.3 The RMS-flux relation

Using the mean and the standard deviation of the 40 second bins of each five minute exposure, we establish the RMS-flux relation for this time scale range. We do not use the integrated power spectrum to determine the RMS, but compute the RMS as $RMS = 1/(N-1)\sum^{N}(x_n - \langle x \rangle)^2$. The relation is plotted in Figure 3.7. In order to correct the RMS for the noise in the measurements, we subtract in quadrature the standard deviation σ of the polynomial subtracted light curve to account for the observational errors.
Every time series generated from a skewed distribution exhibits a relation between the RMS and the mean flux density of a subset of the series (e.g. Witzel et al., 2012). Since the RMS of a time series is related to its power spectrum through Parceval's theorem, the RMS-flux relation allows to probe the power spectrum at different mean flux density levels (in the time domain).
Vaughan et al., 2003 and Uttley et al., 2005 have argued that in the case of a multiplicative lognormal process creating the light curve, the RMS-flux relation is linear on all relevant time scales. Witzel et al., 2012 have reported that Sgr A* exhibits an RMS-flux relation which is linear to first order. The NACO instrument used by Witzel et al., 2012 is sensitive to timescales on the order of minutes to a few hours.This is too short a time span to effectively probe the variability of Sgr A* at all relevant time scales; it is shorter than the typical NIR quiescent state correlation time measurements, for instance of 423^{+82}_{-57} minutes (Witzel et al., 2018). The same of course applies to GRAVITY, since it is also a ground-based instrument. Consequently, the line of argument used for X-ray binaries, for example, by Uttley et al., 2005 cannot be repeated for Sgr A* to show a multiplicative process and a lognormal flux distribution. Furthermore, this interpretation has recently been challenged by Scargle, 2020, who argues that both a lognormal and a RMS-flux relation can be created in a shot noise scenario.
Nevertheless, if the power spectrum were different for the higher flux flares, the RMS-flux relation could serve as a tool to disentangle low and high flux density states. We find that

[1]For correlated data, the model selection criteria are expected to be over or underestimated. We have ignored this effect.

the RMS-flux relation is approximately linear. The best-fit linear function has a slope of 1.0 ± 0.05 and an abscissa offset of 0.15 ± 0.01 [mJy]. The red points in Figure 3.7 are RMS estimates for the six nights for which a bright flare occurred. These points follow the same RMS-flux relation as the low flux density points. Consequently, we find no significant evidence for changed variability during flares. Furthermore we find no flattening of the RMS-flux relation towards the lowest fluxes. This rules out a scenario in which the lowest fluxes are dominated by a second Gaussian source or instrumental limitations.
The RMS-flux relation can serve as a powerful tool to quantify the variability. It is easily obtained from computing RMS in time domain. This avoids the biases introduced by gaps in the light curve inherent to variability studies in frequency domain. To demonstrate this we compare the observed RMS-flux relation to the relations obtained from two simulations from Dexter et al., 2020 The simulations describe the SED of Sgr A* well. Both have a duration of roughly 27 hours, assume a black hole spin of $a = 0.5$ and an inclination of $i = 25°$ with respect to the observer. They differ in the ratio of magnetic to gas pressure. For the SANE (Standard And Normal Evolution) simulation the gas pressure dominates. In the MAD (Magnetically Arrested Disk) simulation the magnetic pressure dominates. Furthermore they differ in the description of sub-grid electron heating: The first simulation uses a turbulence-like description and the second simulation uses a description based on magnetic reconnection description. The details of both simulations are described in Dexter et al. (2020, submitted).
We find that both simulations describe the overall variability of Sgr A* well. The SANE / Turbulence simulation matches the observed variability better, whereas the MAD / Reconnection simulation slightly under-produces the observed mean flux density and variability. This is of course a consequence of the chosen parameters, but demonstrates the use of the RMS-flux relation as an observationally very simple, yet very powerful, tool to constrain models of Sgr A*.

3.4 Discussion

We find that the flux distribution of Sgr A* turns over at a dereddened flux density of around 0.6 mJy and the empirical median dereddened flux density is approximately 1 mJy. This bulk of the emission, in the quiescent state, is consistent with remaining through the years of 2017, 2018, and 2019, indicating no immediate effect of the pericenter passage of S2.
In 2019, we observed six bright flares from Sgr A*. These bright flares cause the flux distribution to extend in a power-law-like fashion for dereddened flux densities above $\sim$ 2 mJy. We fit the flux distribution with different model PDFs taking into account the effect of observational noise and the binning of the data. Here, the analysis is supported by the fact that our light curves are unconfused. This makes statistical modeling of the background unnecessary. A single power law PDF model is not favored because the flux distribution turns over. It is clear that a bent or broken power law can describe the observed flux distribution. However, without a physically motivated statistical model for

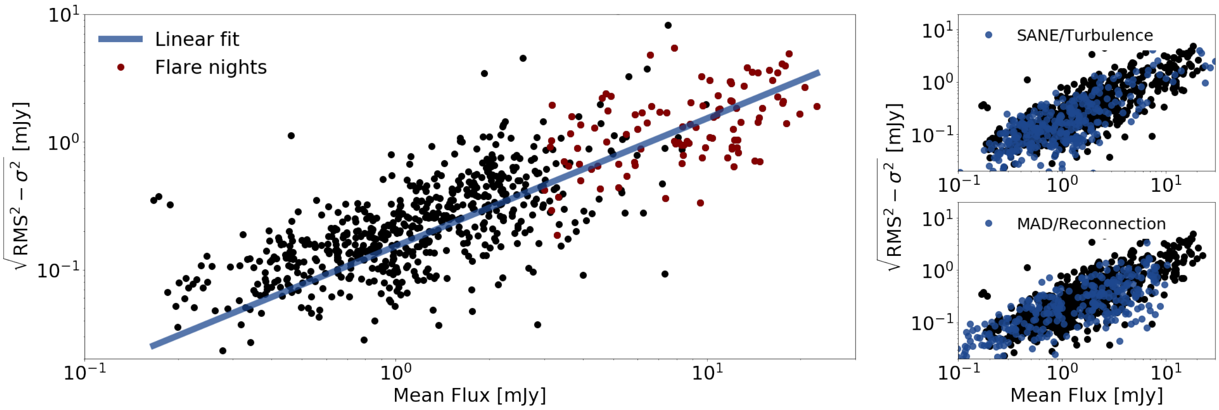

Figure 3.7: Left: RMS-flux relation of Sgr A*: The RMS variability of five minute segments of the light curve as a function of the mean dereddened flux density in the time bin. The light curve has a data point every 40 seconds, the RMS is computed in the time domain and corrected for the measurement noise σ. The red points show the relation for mean flux densities above 3 mJy for the six nights with bright flares. The dark blue line is a linear fit, where the RMS values have been weighted using the noise flux density relation determined in section 3.2.3. This accounts for the increasing noise at higher flux densities. Right: Comparison of the observed RMS-flux relation to the relation computed from two GRMHD simulations presented in Dexter et al. 2020 (submitted). The top plot compares the observed relation (black points) to a simulation with a SANE disk (gas pressure dominated) in which electron heating is achieved through a turbulence-like description (dark blue points); bottom plot compares the observations (black points) to MAD disk simulation (dynamically important magnetic fields) in which electron heating is achieved through magnetic-reconnection-like description (dark blue points).

the emission of Sgr A*, such a bent power law does not offer any valuable information. Similarly, we find that distributions of inverse exponential type can describe the log-right skewed flux distribution. However, the inverse form of the distribution function implies a inverse dependence of the flux density to the intrinsic random variable. We associate the inverse flux density to a process-inherent time scale, however we cannot identify such a process. Recently, Scargle, 2020 has reviewed a family of flare-like models for astronomical light curves. These models are seemingly able to create arbitrarily shaped flux distributions and linear RMS-flux relations. However, a detailed analysis of the implication of such models is beyond the scope of this paper.
An alternative to intrinsically log-right-skewed distributions are composite flux distributions. To account for the excess flux density, we allow for an additional power law tail at high flux densities. The tailed lognormal distribution represents a two-state system in which the quiescent emission is created in the first process and the flares cause the power law tail.
We study the variability of the light curve using the RMS-flux relation. We find the RMS-flux relation to be linear for the probed time scale of 40 seconds to five minutes. Intriguingly, we do not observe a change in the RMS-flux relation during the flares.
Based on our finding of a tailed lognormal flux distribution we favor a NIR emission scenario which consists of two components: A quiescent lognormal mechanism that is usually dominant and a separate flare mechanism. Besides the evidence brought forward in this work and previous works on the flux distribution, there are several additional arguments favoring two distinct NIR states for Sgr A*.

1. X-ray flares and NIR flares are coupled. The converse is not true (e.g. Dodds-Eden et al., 2009).

2. There is no detectable X-ray quiescent state, which would be clearly associated with the NIR counterpart (e.g., Genzel et al., 2010).

3. Strong NIR flares are polarized. The degree of polarization increases with flux density (e.g., Eckart et al., 2006)).

4. The spectral index of the flares changes with observed brightness. For flares, the spectral index is $\alpha_{\nu F_\nu} \sim 0.5$, but this value decreases to $\alpha_{\nu F_\nu} \sim -2$ during the quiescent phase (Gillessen et al., 2006).

5. Do et al., 2019 detect a 70 mJy flare which is inconsistent with the lognormal flux distribution model of Witzel et al., 2018, but consistent with a power law tail (G. Witzel, private communication).

6. Three bright NIR flares have been observed with GRAVITY which show orbital motions. The timescale of the motion is on the same order as the flare duration. Similarly, the observed polarization degree and orientation are correlated with the flare duration and astrometric motion (GRAVITY Collaboration et al., 2018a).

3.5 Summary

In this paper, we build on our previous work on the flux distribution into the lowest and highest flux density domains. We detected Sgr A* in more than 95% of our observations and we conclude that:

1. The median dereddened flux density (1.1 ± 0.3 mJy) as well as the flux density percentiles are robustly measured.

2. The Sgr A* SED is constrained by using the measured flux density percentiles. Because we measure flux densities beyond the peak of the flux distribution, we do not have to assume an analytic model for the flux distribution as in previous works ()Dodds-Eden2010, Witzel2018.

3. The lower percentiles and the median of the flux distribution are stationary within our error estimates and systematic limitations. However, in 2019, we find an increase for the higher percentiles of the light curve. This is due to the observation of six bright flares.

4. A single lognormal or power-law-like flux distribution is ruled out. This is because the flux distribution turns over and is log right skewed with a powerl-law-like fall off at dereddened flux densities higher than ~ 2 mJy.

5. The flux distribution is well described by composite distribution functions, such as the tailed lognormal parameterization proposed by Dodds-Eden et al., 2010.

6. GRAVITY is the first instrument that allows the study of the variability of the light curve both at fluxes beyond the mode of the flux distribution, as well as the variability of the bright flares. Using the RMS-flux relation, we search for a change in variability during flares. We find a linear RMS-flux relation that holds for both quiescent and flare states.

7. We conclude that a tailed lognormal PDF describes both the flux distribution and the RMS-flux relation. The two-stated model implied by this parameterization is consistent with all other observational characteristics of the light curve. We thus favor this model over other single-state, right-skewed distribution functions that lack physical motivation.

Ultimately, the detection of an extreme and unprecedentedly bright flare by Do et al., 2019 and our observations of six additional bright flares in 2019 may indicate that the accretion flow has been altered by the pericenter passage of S2 and/or G2. However, we do not find evidence that the median or mode of the flux distribution has significantly changed in 2019. In consequence, if there are indeed two processes generating the faint quiescent and flaring states, the pericenter passage of S2 or G2 can only have affected the process generating the flares. In light of this constraint, it would be highly interesting to

study the sub-mm light curve of Sgr A*: Since the sub-mm emission is dominated by a population of thermal electrons it measures the particle density and the magnetic properties of the innermost region. Consequently any change in the sub-mm flux distribution in 2019 compared to the previous years may help in understanding the NIR emission scenario.
GRAVITY will continue observing Sgr A* in the years to come, which will allow for a long-term analysis of the light curve at all flux density levels. This will make it possible to test the long term stationarity of the light curve and possibly yield insights into the changes of the accretion rate.

Acknowledgements SvF, FW, AJ-R & IW acknowledge support by the Max Planck International Research School. GP is supported by the H2020 ERC Consolidator Grant Hot Milk under grant agreement Nr. 865637. A.A. and P.G. were supported by Fundação para a Ciência e a Tecnologia, with grants reference UIDB/00099/2020 and SFRH/BSAB/142940/2018.

Chapter 4

Constraining Particle Acceleration in Sgr A* with Simultaneous GRAVITY, Spitzer, NuSTAR, and Chandra Observations

Original Publication: GRAVITY Collaboration &
R. Abuter, A. Amorim, M. Bauböck, F. Baganoff, J.P. Berger, H. Boyce, H. Bonnet, W. Brandner, Y. Clénet, R. Davies, P.T. de Zeeuw, J. Dexter, A. Drescher, A. Eckart, F. Eisenhauer, G.G. Fazio, N.M. Förster Schreiber, K. Foster, C. Gammie, P. Garcia, F. Gao, E. Gendron, R. Genzel, G. Ghisellini, S. Gillessen, M.A. Gurwell, M. Habibi, D. Haggard, C. Hailey, F. A. Harrison, X. Haubois, G. Heißel, T. Henning, S. Hippler, J.L. Hora, M. Horrobin, A. Jiménez-Rosales, L. Jochum, L. Jocou, A. Kaufer, P. Kervella, S. Lacour, V. Lapeyrère, J.-B. Le Bouquin, P. Léna, P.J. Lowrance, D. Lutz, S. Markoff, K. Mori, M.R. Morris, J. Neilsen, M. Nowak, T. Ott, T. Paumard, K. Perraut, G. Perrin, O. Pfuhl, S. Rabien, G. Rodríguez-Coira, J. Shangguan, T. Shimizu, S. Scheithauer, H.A. Smith, J. Stadler, D. K. Stern, O. Straub, C. Straubmeier, E. Sturm, L.J. Tacconi, F. Vincent, I. Waisberg, F. Widmann, E. Wieprecht, E. Wiezorrek, S.P. Willner, J. Woillez, S. Yazici, A. Young, S. Zhang, G. Zins
Corresponding authors: S.D. von Fellenberg, G. Ponti, Y. Dallilar & G. Witzel
Published in Astronomy and Astrophysics: GRAVITY Collaboration et al. 2021 A&A Volume 654
Abstract: We obtained light curves in the M, K, and H bands in the mid- and near-infrared and in the $2-8$ keV and $2-70$ keV bands in the X-ray. The observed spectral slope in the near-infrared band is $\nu L_\nu \propto \nu^{0.5\pm0.2}$; the spectral slope observed in the X-ray band is $\nu L_\nu \propto \nu^{-0.7\pm0.5}$.

Using a fast numerical implementation of a synchrotron sphere with a constant radius, magnetic field, and electron density (i.e., a one-zone model), we tested various synchrotron and synchrotron self-Compton scenarios. The observed near-infrared brightness and X-ray faintness, together with the observed spectral slopes, pose challenges for all models explored. We rule out a scenario in which the near-infrared emission is synchrotron emission and the X-ray emission is synchrotron self-Compton. Two realizations of the one-zone model can explain the observed flare and its temporal correlation: one-zone model in which the near-infrared and X-ray luminosity are produced by synchrotron self-Compton and a model in which the luminosity stems from a cooled synchrotron spectrum. Both models can describe the mean spectral energy distribution (SED) and temporal evolution similarly well. In order to describe the mean SED, both models require specific values of the maximum Lorentz factor γ_{max}, which differ by roughly two orders of magnitude. The synchrotron self-Compton model suggests that electrons are accelerated to $\gamma_{max} \sim 500$, while cooled synchrotron model requires acceleration up to $\gamma_{max} \sim 5 \times 10^4$. The synchrotron self-Compton scenario requires electron densities of 10^{10} cm^{-3} that are much larger than typical ambient densities in the accretion flow. Furthermore, it requires a variation of the particle density that is inconsistent with the average mass-flow rate inferred from polarization measurements and can therefore only be realized in an extraordinary accretion event. In contrast, assuming a source size of $1R_s$, the cooled synchrotron scenario can be realized with densities and magnetic fields comparable with the ambient accretion flow. For both models, the temporal evolution is regulated through the maximum acceleration factor γ_{max}, implying that sustained particle acceleration is required to explain at least a part of the temporal evolution of the flare.

4.1 Introduction

It is believed that most galaxies harbor at least one supermassive black hole (BH) at their center (Kormendy & Ho 2013). However, only a small fraction are accreting at a high rate and appear as active galactic nuclei. The vast majority are quiescent and therefore inaccessible to us. One exception is Sgr A*. Located only 8.27 kpc from us (GRAVITY Collaboration et al., 2019a; Do et al., 2019; Gravity Collaboration et al., 2021a), Sgr A* is the closest supermassive BH, and has a mass of (4.297 ± 0.013) M$_\odot$ and a corresponding Schwarzschild radius of $R_S = 2GM_{BH}/c^2 {\sim} 1.3 \times 10^{10}$ m. Because it is so close, Sgr A* appears orders of magnitudes brighter than any other supermassive BH in quiescence despite its faint X-ray flux of $\sim 2 \times 10^{33}$ erg s^{-1} (Baganoff et al., 2003b). Therefore, Sgr A* offers a unique opportunity to study the physics of accretion in quiescent systems.

The majority of the steady radiation from Sgr A* is emitted at submillimeter frequencies. This radiation is most likely produced by optically thick synchrotron emission originating from relativistic thermal electrons in the central $\sim$10 Schwarzschild radii (R_S) at temperatures of $T_e \sim$ a few 10^{11} K and densities $n_e {\sim} 10^7$ cm^{-3}, embedded in a magnetic field with a strength of $\sim 10 - 50$ G (Loeb and Waxman, 2007; Fellenberg et al., 2018;

Bower et al., 2019). This implies that the accretion flow at a few Schwarzschild radii from the BH is strongly magnetized. For an ambient magnetic field strength of $B{\sim}40$ G and ambient $n_e \sim 10^6$ cm^{-3}, we estimate a plasma parameter β of $\sim$0.04 (comparing the thermal pressure of the gas with the magnetic pressure), and $\sigma_{th}{\sim}15$ (comparing the magnetic field energy with the thermal energy).

In the X-ray band, Sgr A* appears as a faint ($L_{2-10\ keV} \sim 2 \times 10^{33}$ erg s^{-1}) extended source with a size, $\sim 1''$, comparable to the Bondi radius, emitting via bremsstrahlung emission from a hot plasma with $T_e \sim 7 \times 10^7$ K and $n_e \sim 100$ cm^{-3} (Quataert, 2002; Baganoff et al., 2003b; Xu et al., 2006). In the X-ray band, Sgr A* occasionally shows sudden rises (flares) of up to 1-2 orders of magnitudes, suggesting individual and distinct events, randomly punctuating an otherwise quiescent source (Baganoff et al., 2001b; Porquet et al., 2003; Porquet et al., 2008; Neilsen et al., 2013; Ponti et al., 2015; Bouffard et al., 2019). X-ray flares are associated with bright flux excursions in the near-infrared (NIR) band, which also led to the definition of the latter as flares (Genzel et al., 2003a; Ghez et al., 2004). However, the IR emission is continuously varying (Do et al., 2009; Meyer et al., 2009; Witzel et al., 2018).

In 2018, GRAVITY Collaboration et al., 2018a reported the first detection of an orbital signature in the centroid motion of three Sgr A* flares. The centroid motion of the three flares is consistent with a source on a relativistic orbit around the BH. Using a fully general relativistic model of a "hot spot", the authors derived a typical orbital radius of around $\sim$4.5 R_s, constrained the emission regions to $\sim$2.5 R_s, and a viewing angle of $i{\sim}140$ deg (the inclination of the orbital plane to the line of sight). This model was extended by Gravity Collaboration et al., 2020e, who showed that the flare light curves may be modulated by Doppler boosting on the order a few tens of percent. The polarimetric analysis of these flares showed consistent results (Gravity Collaboration et al., 2020c). These findings further cement the picture of flares originating from localized regions of the accretion flow in which particles are heated or accelerated.

However, the radiative mechanism powering flares is still disputed. The most common proposed mechanisms are as follows: synchrotron with a cooling break, synchrotron self-Compton (SSC), inverse Compton (IC), and synchrotron (Markoff et al., 2001; Yuan et al., 2003b; Eckart et al., 2004; Eckart et al., 2006; Eckart et al., 2008; Eckart et al., 2009; Eckart et al., 2012; Yusef-Zadeh et al., 2006; Yusef-Zadeh et al., 2008; Yusef-Zadeh et al., 2009b; Hornstein et al., 2007; Marrone et al., 2008; Dodds-Eden et al., 2009; Dodds-Eden et al., 2010; Trap et al., 2011; Dibi et al., 2014; Barrière et al., 2014). Simultaneous determination during an X-ray flare of the photon index (Γ) in the NIR ($\Gamma_{\rm IR}$) and X-ray ($\Gamma_{\rm X}$) bands allows us to discriminate synchrotron and synchrotron with a cooling break from the other radiative mechanisms. It is expected that $\Gamma_{\rm X} = \Gamma_{\rm IR}$ or $\Gamma_{\rm X} = \Gamma_{\rm IR} + 0.5$ for the synchrotron and synchrotron with a cooling break model, respectively (Kardashev, 1962; Pacholczyk, 1970; Dodds-Eden et al., 2010; Ponti et al., 2017). Any other value would favor either SSC or IC scenarios.

Thanks to an extensive multiwavelength monitoring campaign covering from the IR (with *SINFONI*) to X-ray (with *XMM-Newton+NuSTAR*), Ponti et al., 2017 observed a very bright NIR and X-ray flare in August 2014. The radiative mechanism was consistent with synchrotron emission all the way from IR to X-ray, therefore implying the presence of a powerful accelerator (with $\gamma_{max} > 10^{5-6}$) and an evolving cooling break and high-energy cutoff in the distribution of accelerated particles. This demonstrated that, at least for that flare, synchrotron emission with a cooling break and a varying high-energy cutoff is a viable mechanism.

To obtain a better insight into the flaring activity of Sgr A*, we deployed a large multi-wavelength campaign in July 2019. The campaign was built around a core of three strictly simultaneous 16 hr *Chandra* and *Spitzer* observations covering emission from Sgr A* in the soft X-ray and M band (PI G.G. Fazio). In addition, two long *NuSTAR* exposures were performed to simultaneously cover the entire campaign in the hard X-ray band. Finally, a ~6.5 hr observation with the VLTI-GRAVITY interferometer was performed in the night between July 17 and 18, expanding the campaign to the K and H bands. For simplicity, we refer to the IR observations by the observing band most similar with the effective wavelength of the observations throughout the paper. Table 4.1 reports the effective wavelength. Observations with the Submillimeter Array (Witzel et al. 2021) were approved but not executed, owing to a number of factors including weather and limited access to the array during the summer of 2019. During the time window when all instruments were active, we caught a bright IR and moderate X-ray flare. We report in this work the characterization and evolution of the IR to X-ray spectral energy distribution (SED) during the flare and the implications for our understanding of particle acceleration during the Sgr A* flares.

4.2 Data reduction

4.2.1 Basic assumptions

Throughout this paper we assume a distance to Sgr A* of 8.249 kpc and a mass $M_{\rm BH} = 4.26 \times 10^6 M_\odot$ (Gravity Collaboration 2020). The quoted errors and upper limits are at the 1σ and 90% confidence level, respectively. The X-ray data were initially fitted with XSPEC v. 12.10.1f, employing the Cash statistics in spectral fits (Cash 1979). Throughout our analysis and discussion we make the following assumptions:

- Effects of beaming are negligible.
- Emission is dominated by a single emitting zone.
- Unless otherwise stated, we follow Do et al., 2009 and assume a constant escape time of the synchrotron emitting electrons equal to $t_{esc} = 120$ s.

4.2.2 *Chandra*

A series of three *Chandra* (Weisskopf et al., 2000) observations was analyzed (see Tab. 4.1). To enhance sensitivity and reduce the effects of pile-up during flares of Sgr A*, the

Instrument	OBSID	Start (UTC)	Start (MJD)	Exp (ks)	Energy	Wavelength
Chandra	22230	2019-07-17 22:51:26	58681.9524	57.6	2–8keV	6.2–1.6Å
	20446	2019-07-21 00:00:14	58685.0002	57.6	2–8keV	6.2–1.6Å
	20447	2019-07-26 01:32:40	58690.0639	57.6	2–8keV	6.2–1.6Å
NuSTAR	30502006002	2019-07-17 21:51:09	58681.9105	38.6	2–70keV	6.2–0.2Å
	30502006004	2019-07-26 00:41:09	58690.0286	34.8	2–70keV	6.2–0.2Å
GRAVITY	0103.B-0032(D)	2019-07-17 23:32:55	58681.9812	21.6	0.7–0.8eV	2.2–1.65 μm
Spitzer	69965312	2019-07-17 23:21:33	58681.9733	17.6	0.3eV	4.5 μm
	69965568	2019-07-18 07:25:02	58682.3091	17.6	0.3eV	4.5 μm

Table 4.1: Datasets analyzed in this work. The table reports the instrument used, the identification number of the dataset, the start time of the observation, the total exposure, energy bands, and effective wavelengths of the different instruments

.

observations were taken with ACIS-S at the focus (Garmire et al., 2003). Only one CCD was active (S3) with a one-eighth subarray (i.e., 128 rows) and no grating applied. The data were reduced with standard tools from the CIAO analysis suite, version 4.12 (Fruscione et al., 2006) and calibration database v4.9.3, released on October 16, 2020. The data from each observation were reprocessed applying the CHANDRA_REPRO script with standard settings. Barycentric corrections with the task AXBARY were applied to the events files, the aspect solution, and all products. To match the exposure of the GRAVITY light curves, we computed light curves in the 2–8 keV, 2–4 keV, and 4–8 keV bands with 380 s time bins, following the GRAVITY exposure time of 320 s plus a dead time of approximately 60 s. Considering the small number of events during quiescence, we represent the count rates following the Gehrels approximation ($\sqrt{(N+0.75)}+1$ Gehrels, 1986).

During OBSID 22230, we observed a peak count rate of 0.09 ph s^{-1} in the 2–8 keV band. Given the instrumental setup, pile-up effects are negligible even at the peak (e.g. Ponti et al., 2015). By using the Ponti et al., 2015 conversion factors, we estimate a total observed (absorbed) energy of $\sim 3.2 \times 10^9$ erg released during the flare in the 2–8 keV band. Following the classification of Ponti et al., 2015, this flare belongs to the group of moderate flares in the X-ray band.

Photons from Sgr A* were extracted from a circular region of 1.25″ radius. The spectrum of the flare was extracted with SPECEXTRACT within the time interval MJD = 58682.134:58682.148 (see dotted lines in Figure 4.2) and contains a total of 72 photons in the 2-10 keV band. The background spectrum was extracted from the same source region but from the events file accumulated during OBSID 20447, during which no flare of Sgr A* was detected.

4.2.3 *NuSTAR*

To study the flare characteristics in the hard X-ray band, we analyzed the two NuSTAR (Harrison et al., 2013) observations taken in July 2019 in coordination with GRAVITY, *Chandra*, and *Spitzer* (Table 4.1). We processed the data using the *NuSTAR* Data Analysis Software *NUSTARDAS* and HEASOFT v. 6.28, and CALDB v20200912, filtered for periods of high instrumental background due to South Atlantic Anomaly passages and known bad detector pixels. The data were barycenter corrected. Products were extracted from a region of radius 20″ centered on the position of Sgr A* using the tool NUPRODUCTS within the intervals shown in Fig. 4.2. The background spectra were extracted from the same region in the off-flare intervals within the same observation. In particular, the background spectrum was integrated for each orbit during which no X-ray flares nor bright IR flux excursions were observed in the *NuSTAR* and *Chandra* as well as the GRAVITYand *Spitzer* light curves (Boyce et al. in prep.), resulting in a net exposure time of ∼30 ks. Because part of the FPMB instrument is affected by stray light as a result of a Galactic Center X-ray transient outside of the field of view, we only present the analysis of the FPMA data. The results from FPMB are consistent with those presented in this work. The light curves were accumulated in the 3–10 keV band and with 380 s time bins for comparison with the GRAVITY data. Bins with small fractional exposures were removed.

4.2.4 *Spitzer/IRAC*

The observations were obtained using the IRAC instrument (Fazio et al., 2004) on the *Spitzer* Space Telescope (Werner et al., 2004). The observations were part of the *Spitzer* program 14026 (Fazio et al., 2018), which observed Sgr A* at 4.5 μm during three epochs of ∼16 hours each in 2019 July. The observing sequence included an initial mapping operation and then two successive eight-hour staring-mode observations, each using the "PCRS peak-up" to center Sgr A* on pixel (16,16) of the subarray. We used a similar data pipeline as described by Hora et al., 2014, Witzel et al., 2018, and Boyce et al., 2019 to derive differential flux measurements. Modifications to the procedure for reduction and calibration of the light curves were necessary because of the larger pointing drift compared to previous observations (about one full pixel over the first three hours of the staring observation). The procedure was modified to transition to the neighboring pixel for the flux measurement when the drift moved Sgr A* into that pixel, roughly one hour after the start of the stare. Also because of the large drift, we derived a new calibration curve that would be valid over the larger range. We used observations of standard stars previously obtained for the subarray "sweet spot" calibration (Ingalls et al., 2012), and found that a fifth-degree polynomial using the distance from the center of the pixel and central pixel flux density provided an acceptable fit to the total flux density of a point source with a standard deviation consistent with the signal-to-noise ratio (S/N) of the observations.

The uncertainty of the *Spitzer* light curve was estimated by computing the standard deviation of the light curve sections where the GRAVITY K-band flux was low. Because the light curve shows residual artifacts from the imperfect background subtraction, we scaled the standard deviation such that low-flux parts of the light curve have $\chi^2_{red} = 1$ with respect to zero mean flux. The flux was de-reddened using the Fritz et al., 2011 extinction values reported in Table 4.2. Because the *Spitzer* light curve was derived through differential photometry, we needed to add a flux offset. We used the method described by Witzel et al., 2018 to account for the flux offset but used the median K-band flux derived by Gravity Collaboration et al., 2020f. Explicitly, we added 1.8 ± 0.3 mJy to all differential flux measurements of *Spitzer*.

4.2.5 *GRAVITY*

The interferometric K-band flux density was determined in the same way as by Gravity Collaboration et al., 2020f. The values reported are the coherent flux values corrected for the contribution of the star S2. We neglected the contribution of the star S62, which amounts to a constant flux of ∼0.1 mJy. For the details of the flux determination, see Gravity Collaboration et al., 2020f.

The H-band flux was determined from aperture photometry of the deconvolved acquisition camera images. The acquisition camera of GRAVITY is normally used for the acquisition of the observation as well as the field and pupil tracking for each of the four unit telescopes. In order to use the aquistion camera images for science, we averaged the four images[1]. The images were bad-pixel-corrected and dark-subtracted. We approximated the point spread function (PSF) of the images by a Gaussian. The parameters of the Gaussian were determined by fitting a Gaussian model to the bright star S10, and we used this PSF model to deconvolve the images using the Lucy-Richardson algorithm implemented in dpuser[2].

In the K and H bands we measured the flux ratio of Sgr A* relative to S2. Because Sgr A* is a much redder source than S2 (Genzel et al., 2010), we had to take the difference in spectral index into account. For the K band this was achieved by fitting a power-law spectrum to both sources and determining the flux at 2.2 μm. For the H band, we accounted for this difference in spectral index by assuming that the reddened flux from both sources is described by a power law. We used NACO photometry of S2 to determine the reddened spectral slope of S2. By using the observed flux ratio in the H and K bands and the transmission curve of the acquisition camera detector, we derived the effective wavelength of Sgr A* in the H band: $\lambda_{\mathrm{Sgr\ A*}} \sim 1.63$ μm. Once the effective wavelength was determined, we used the observed flux ratio in the H and K band to determine the flux density of Sgr A* in the H band. The details of this are outlined in subsection A3.2.

4.2.6 Extinction

The Galactic Center is a highly extincted region, which has an approximately broken-power-law extinction $A(\lambda)$ between 1.2 μm and 8 μm (Fritz et al., 2011). The extinction

[1]The aquistion camera pipeline will be made available under `https://github.com/Sebastiano-von-Fellenberg/AquisitionCamera`. It has been written by SvF and Giuila Folchi.

[2]https://www.mpe.mpg.de/ ott/dpuser/

Band	Fritz et al., 2011
A_H	4.21 ± 0.08
A_{Ks}	2.42 ± 0.002
A_M	0.97 ± 0.03

Table 4.2: Extinction values of Fritz et al., 2011 in magnitudes. The uncertainties of Fritz et al., 2011 have been propagated only taking the uncertainty of the spectral slope into account.

is a major source of uncertainty for our analysis because even a small variation in the power-law extinction slope leads to a large change in our measured IR spectral slope. The hydrogen column density is similarly a key ingredient in the derivation of the X-ray absorption and thus the modeling of the X-ray spectral slope. Moreover, the hydrogen column density and the IR extinction are related but independently determined. This may therefore lead to a systematic offset between NIR and X-ray observations.

Infrared extinction

We used the extinction model from Fritz et al., 2011, who used the hydrogen emission lines observed with SINFONI at the VLT to derive a broken-power-law extinction curve. This allows us to drop the uncertainty on the absolute calibration and only propagate the uncertainty on the power law exponents. The authors also provided extinction values for NACO and *Spitzer*, tabulated in Table 4.2. We neglected the uncertainty owing to the difference in filter response between NACO and the two GRAVITY bands.

X-ray extinction

The observed X-ray spectrum is distorted by the combination of absorption and dust scattering. The latter effect produces a halo of emission, which is typically partially included within the limited extraction region used to compute the spectrum of Sgr A*. We fitted the scattering halo of the dust with the model FGCDUST in XSPEC (Jin et al., 2017; Jin et al., 2018), and it was assumed to be the same as the foreground component along the line of sight toward AX J1745.6-2901 (Jin et al., 2017; Jin et al., 2018).

We fit the absorption affecting the X-ray spectra with the model TBABS (see Wilms et al., 2000a) with the cross sections of Verner et al., 1996 and abundances from Wilms et al., 2000b. Figure 4.5 shows the impact of the different assumptions for the column density on the X-ray spectral slope. As Ponti et al., 2017, we assumed a column density of $N_{\rm H} = 1.6 \times 10^{23}$ cm^{-2}.

4.3 Light curves

Fig. 4.1 shows the full duration of the multiwavelength campaign performed on July 17-18, 2019. The *Spitzer* and GRAVITY light curves follow each other very well. The *Spitzer* light

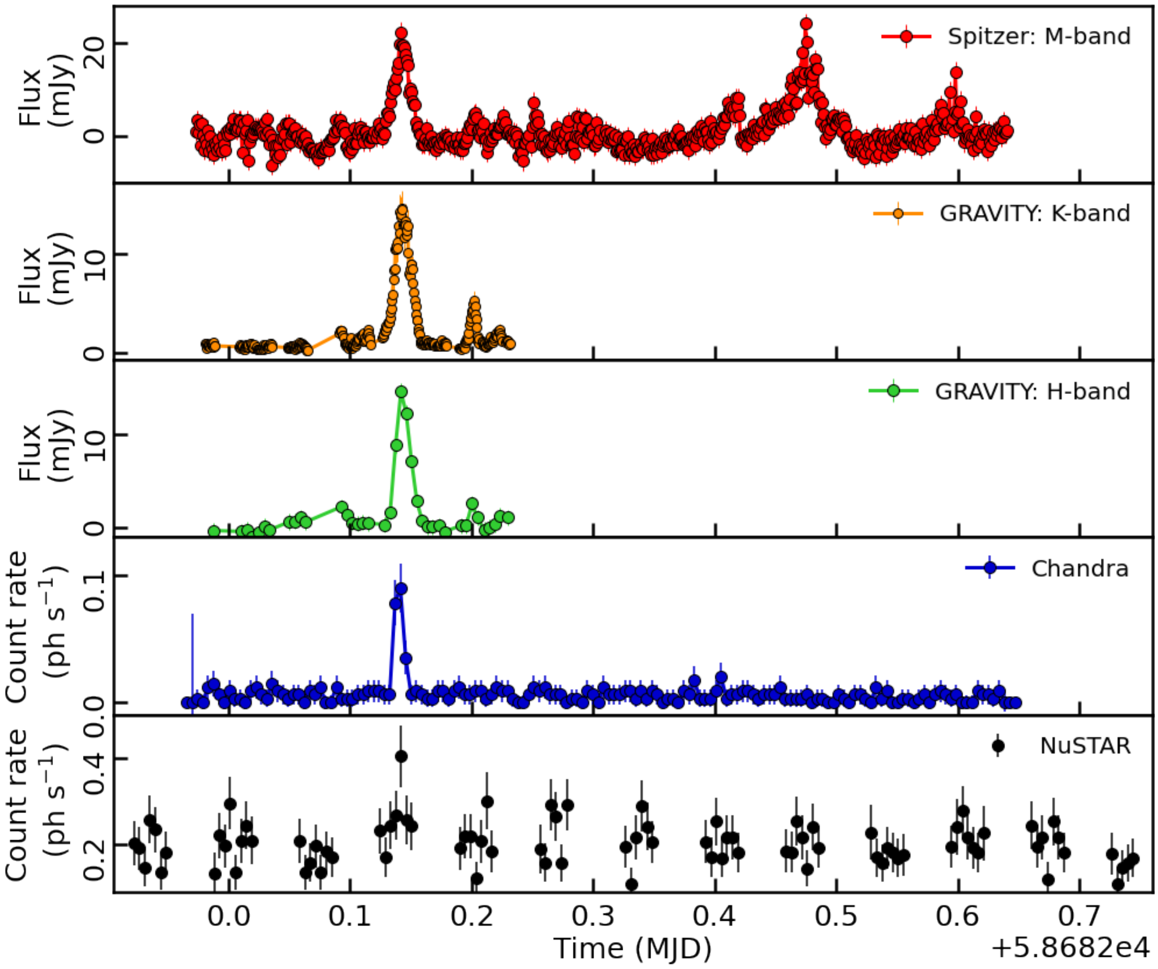

Figure 4.1: X-ray and IR light curves of the multiwavelength observations performed on July 18, 2019. The *Spitzer* (red), GRAVITY K (orange) and H band (green), *Chandra* (blue), and *NuSTAR*(black) data. The *Spitzer* light curves show the differential flux density. The NIR flux densities have been corrected for extinction using the values in Table 4.2.

curve shows IR flares in excess of 5 mJy. In particular, two $F_M \gtrsim 15$ mJy and $t \gtrsim 30$ min IR flares are observed by *Spitzer* at $MJD \sim 58682.14$ and ~ 58682.47. However, only the first IR flare has a detectable X-ray counterpart (Fig. 4.1), which suggests that one or more additional parameters are required to control the X-ray loudness of the IR flares.

Figure 4.2 shows a zoom-in of the light curves of the bright IR flare with X-ray counterpart detected on July 18, 2019. As discussed by Boyce et al. (in prep.), the flare occurred nearly simultaneously in the two bands, with the X-ray peak occurring at the maximum of the IR emission. The X-ray flare, as observed by *Chandra*, was shorter ($\sim$19 min duration) than its IR counterpart ($\sim$38 min duration). A shorter duration of the X-ray flare has been observed before (Dodds-Eden et al., 2010; Dodds-Eden et al., 2011).

At the start of the flare (T1[3] $\sim$58682.133) emission was observed in the K and M bands ($\sim$5 mJy) with simultaneous H-band emission but no excess above quiescence in the X-ray band. Soon after, the X-ray band rose very rapidly (T2). It then decayed quickly back to quiescence, while the IR flux rose and decayed more gently (Fig. 4.2). Indeed, when the X-ray emission reached quiescence, the IR flux density was still above $\sim$8 mJy in every IR band (Fig. 4.2; T5 and T6).

4.4 The multiwavelength flare in context

The IR flare reported in this paper is among the brightest ever observed. It is the third brightest flare observed with GRAVITY, although it is significantly shorter than the flares observed in 2019. The left panel of Figure 4.3 shows the flux distribution of Sgr A* (Gravity Collaboration et al., 2020f) and compares the peak fluxes of three flares possessing an X-ray counterpart. The flare under investigation in this work is almost an order of magnitude fainter and a factor of $\sim 2-3$ shorter than previously analyzed very bright X-ray flares (Dodds-Eden et al., 2009; Ponti et al., 2017). Thanks to the frequent observations of X-ray emission from Sgr A* , more than 100 X-ray flares of Sgr A* have been detected so far by *Chandra* and *XMM-Newton* (Neilsen et al., 2013; Ponti et al., 2015; Mossoux et al., 2016; Li et al., 2017; Bouffard et al., 2019)). Figure 4.3 highlights the fluence and duration of the X-ray flare detected in this work and compared to previously detected flares.

The July 18 flare shows only moderate emission in the X-ray band. This flare is almost an order of magnitude fainter and a factor of $\sim 2-3$ shorter than the very bright X-ray flares for which the IR to X-ray SED has been investigated in detail in previous works (Dodds-Eden et al., 2009; Ponti et al., 2017). The relative X-ray faintness is unexpected, considering that the flare is one of the brightest flares in the IR band.

[3]T1 stands for the first time interval of the time resolved analysis.

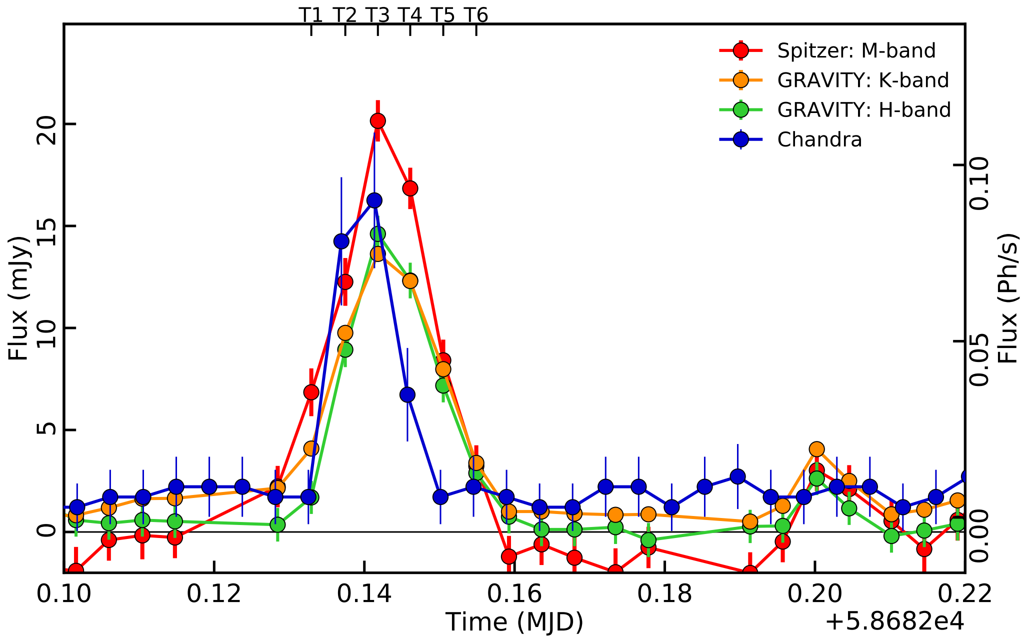

Figure 4.2: X-ray and IR light curves of the flare detected on July 18, 2019. The blue points show the *Chandra* light curve in the 2–8 keV band. The red, orange, and green points show *Spitzer* (M-band), the GRAVITY K-band, and H-band light curves corrected for extinction, respectively. The bold ticks on the top abscissa labeled T1, T2, T3, T4, T5, and T6 mark the times that will be used in the subsequent analysis.

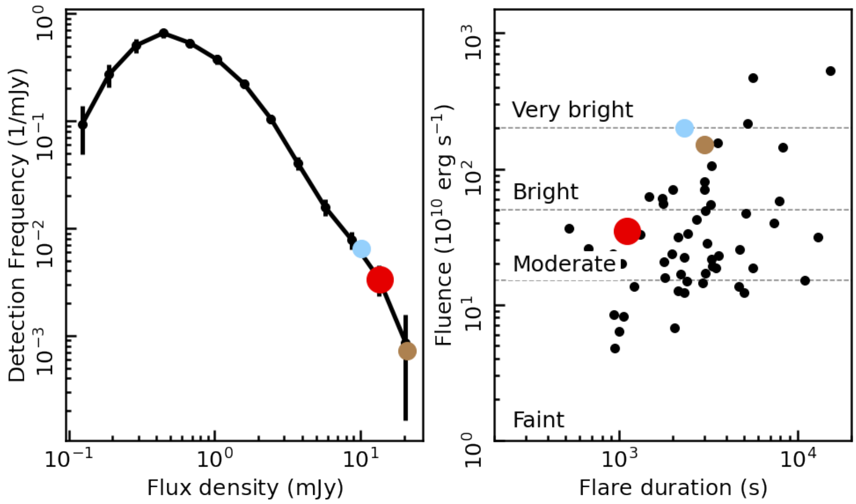

Figure 4.3: Left: GRAVITY K-band flux density distribution as reported in Gravity Collaboration et al., 2020f and the peak flux densities of three bright flares. The red point indicates the peak flux density of the flare analyzed in this paper. The light blue point indicates the peak flux reported by Ponti et al., 2017 observed with SINFONI. The light brown point represents the peak L'-band flux density scaled to 2.2 μm, assuming a flux density scale $F_{Kband} = F_{L'band} \cdot (\nu_K/\nu_{L'})^{-0.5}$. Right: Duration and fluence of all flares of Sgr A* detected by *XMM-Newton* and *Chandra* before 2015 (see Neilsen et al., 2013; Ponti et al., 2015). Partial (i.e., only partially covered) and dubious flares have been omitted. As in the left plot, the red, light blue, and dark blue circles show the duration and fluence of the X-ray flares investigated in this work, by Ponti et al., 2017, and by Dodds-Eden et al., 2009.

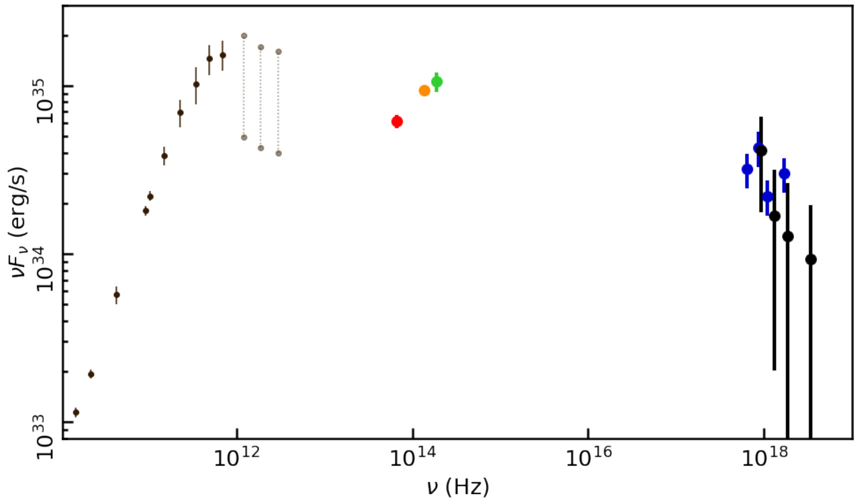

Figure 4.4: Mean SED plotted together with the best-fit power-law slope. The submillimeter SED is plotted for orientation; the radio and submillimeter data are from Falcke et al., 1998; Bower et al., 2015; Brinkerink et al., 2015; Liu et al., 2016; Bower et al., 2019. The far-infrared data are from Stone et al., 2016 and Fellenberg et al., 2018.

4.5 Analysis of the mean spectrum

4.5.1 Infrared spectrum

To obtain the mean spectrum, we binned all six exposures with significant IR flux to find the average flux density in the M, K, and H bands. These flux densities were converted to luminosities and are shown in Figure 4.4.

4.5.2 *Chandra*

Dust extinction and absorption due to neutral material along the line of sight are a major source of systematic uncertainty for all observations of the Galactic Center. A fit of the original *Chandra* spectrum with an absorbed power law, corrected for the distortions introduced by dust scattering, provides a best-fit photon index $\Gamma = 2.7 \pm 0.5$ (C-stat = 238.1 for 545 dof). The best-fit 2–10 keV observed flux is $F_{\mathrm{Abs}\ 2-10} = 2.3 \times 10^{-12}$ erg cm^{-2} s^{-1}. Once de-absorbed and corrected for the effects of dust scattering, this corresponds to $F_{\mathrm{Deabs}\ 2-10} = 6.9 \times 10^{-12}$ erg cm^{-2} s^{-1}. To fit the temporal evolution of the spectrum together with the NIR data, we rebinned the observed spectrum to have four bins in energy each containing 18 photons. For the time-resolved spectra, we binned our spectra in 2, 2, and 1 bins containing 16, 14, and 12 photons for T2, T3, and T4, respectively. Starting from the best-fit model of the original data, we computed the ratio of the absorbed to scattered model and the de-absorbed and dust-scattering-corrected model. We then applied this model ratio to the rebinned spectrum to derive the corrected spectrum of the Sgr A* flare.

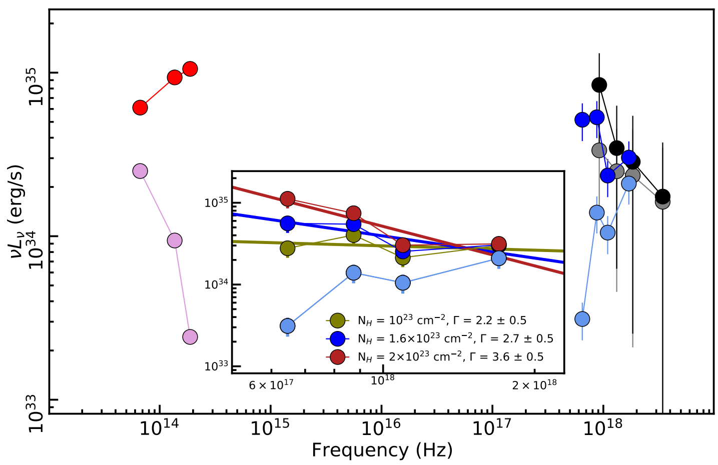

Figure 4.5: *Main panel:* Comparison between observed and corrected spectra. The cyan, gray, and pink points show the spectra as observed by *Chandra*, *NuSTAR*, and in the IR band, respectively. The blue, black, and red points show the same data corrected for absorption and the effects of dust scattering. The correction amounts to more than one order of magnitude in K and H as well as in the soft X-ray band. *Inset:* As in the main panel, the cyan points show the spectrum as observed by *Chandra*. The olive, blue, and dark red points show the *Chandra* spectrum after correction assuming $N_{\mathrm{H}} = 10^{23}$, 1.6×10^{23}, and $2 \times 10^{23}\mathrm{cm}^{-2}$, respectively.

The effects of absorption and dust scattering are very significant in the soft X-ray band. A comparison between the observed and de-absorbed spectra shown in Fig. 4.5 shows a ratio in excess of one order of magnitude below ∼3 keV. The soft X-ray flux and X-ray photon index are strongly correlated dependent on the assumed column density of absorbing material (see of Figure 4.5). By assuming column densities of $N_H = 10^{23}$, 1.6×10^{23} and 2×10^{23} cm^{-2} (all values which are consistent with the spectrum of this moderate X-ray flare), the best-fit photon index is $\Gamma = 2.2 \pm 0.5$, 2.7 ± 0.5, and 3.6 ± 0.5, respectively. These values are consistent with the allowed range of values reported in works compiling several X-ray flares (Porquet et al., 2008; Nowak et al., 2012). To allow a better comparison with previous multiwavelength flares of Sgr A*, we assume $N_H = 1.6 \times 10^{23}$ cm^{-2} (Ponti et al., 2017). We discuss the implications of this choice in Appendix A3.3.

4.5.3 ***NuSTAR***

As a consequence of the larger PSF of the *NuSTAR* mirrors, a larger fraction of diffuse emission contaminates the *NuSTAR* spectra of Sgr A* compared to *Chandra*. The Sgr A* photons amount to about 30 % of the total flux in the 3–20 keV band. We fitted the background spectrum simultaneously with the source plus background to reduce the uncertainties associated with background subtraction, thereby adopting the same background model components in both cases.

We parameterized the *NuSTAR* background spectrum in the 3–50 keV band with a collisionally ionized diffuse plasma component (APEC in XSPEC) plus a power law, all absorbed by neutral material. This model provides a good description of the background spectrum (see Tab. 4.3). We simultaneously fitted the source plus background spectrum by adding an absorbed power-law component to this model to fit the emission from Sgr A*. The best-fit photon index of Sgr A* emission is $\Gamma = 2.6 \pm 1.0$ with an absorbed 3–20 keV flux of $F_{\mathrm{Abs}\ 3-2\mathrm{Y}0} = 3.1 \times 10^{-12}$ erg cm^{-2} s^{-1} ($F_{\mathrm{Deabs}\ 3-20} = 4.5 \times 10^{-12}$ erg cm^{-2} s^{-1}).

4.5.4 Combined fit of *Chandra+NuSTAR* spectra

Finally, we simultaneously fitted the background subtracted *Chandra* as well as the source plus background and background *NuSTAR* spectra. This provides a good fit to the data, with a best-fit $\Gamma = 2.7 \pm 0.5$ (see Tab. 4.3). To perform multiwavelength fits with models not yet implemented in XSPEC (e.g., synchrotron cooling break and high-energy cutoff SSC models), we corrected the binned *Chandra* and the binned[4] background-subtracted *NuSTAR* spectrum for the effects of absorption and dust scattering and then fit the corrected spectrum with a least-squares fit. This step might introduce biases in the corrected spectrum. However, we verified that such distortions are negligible compared to the statistical uncertainties of the X-ray spectra.

[4] The *NuSTAR* spectrum has been rebinned to have 21 photons per bin in the 3–40 keV energy band.

X-ray spectral analysis	*Chandra*	*NuSTAR*	*Chandra*+ *NuSTAR*
Sgr A*			
Γ	2.7 ± 0.5	2.6 ± 1.0	2.7 ± 0.5
N_{pl}	87^{+90}_{-45}	50^{+300}_{-40}	67^{+90}_{-40}
Background			
kT_a		1.8 ± 0.2	1.8 ± 0.2
N_H		2.4 ± 0.4	2.6 ± 0.4
Γ		1.7 ± 0.1	1.7 ± 0.1
N_{pl}		12 ± 4	13 ± 4
C-S/dof	238.1/547	1046.6/1717	1284.6/2264

Table 4.3: Parameters of the best fit to the *Chandra*, *NuSTAR*, and combined source and background spectra. The quantity N_H: the column density of the neutral material (10^{22} atoms cm^{-2}); Γ: the photon index of the power-law component; N_{pl} normalization (10^{-4} photons keV^{-1} cm^{-2} s^{-1} at 1 keV) of the power-law component; kT_a plasma temperature (keV) of the APEC component; N_a normalization (10^{-2}) of the APEC component; and C-S: value of Cash statistic.

4.6 Temporal evolution of the SED

We can determine a spectral index for each of the six exposures with significant IR flux. In this section, we report the spectral slope of the flux density $F_\nu \propto \nu^\alpha$. The spectral slope of the luminosity is $\nu F_\nu \propto \nu^\beta$, where $\beta = \alpha + 1$. In order to compare the spectrum of the M band to the K band and the K band to the H band, we analytically computed the spectral slope as follows:

$$\alpha_{\text{Band1}-\text{Band2}} = \log_{(F_{\text{Band1}}/F_{\text{Band2}})}(\nu_{\text{Band1}}/\nu_{\text{Band2}}), \tag{4.1}$$

and we propagated the uncertainty of the observed flux densities (Figure 4.6).

During the onset of the flare, Sgr A* was faint in the H band, while there is already substantial flux measured in the M and K bands. This resulted in a very red $H-K$ slope ~ -3, while the $K-M$ slope was ~ -0.7. After the first data point, the $H-K$ slope jumped to ~ -1. For the next two data points, the spectral slope increased from $\alpha_{H-K}{\sim}-1$ to $\alpha_{H-K}{\sim}0$ at the peak of the flare. After the peak α_{H-K} decreased, with $\alpha_{H-K}{\sim}-1$ at the end of the flare. This indicates a correlation between the $H-K$ spectral slope and the flux density. Conversely, there was no strict correlation of the spectral slope with flux density for α_{H-K}. The $K-M$ slope varied in the range $\alpha_{K-M} = [-0.8, 0.0]$ and increased toward the end of the flare. However, this might be indicative of a correlated error owing to a telescope slew of the *Spitzer* spacecraft. The temporal evolution of the flare SED is shown in Figure 4.7.

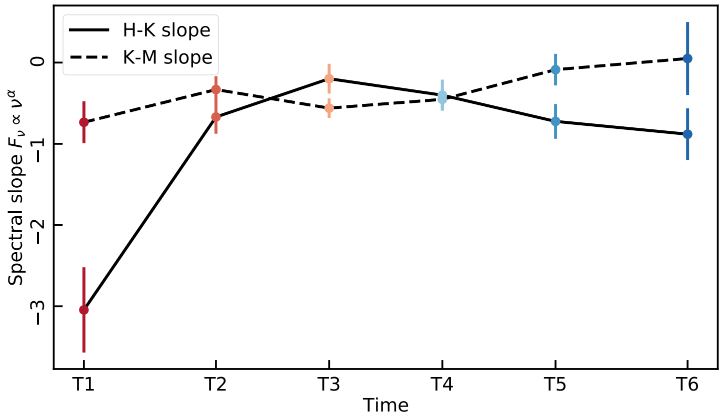

Figure 4.6: Infrared spectral slopes α for the six times T1 to T6. The color encodes the time, dark red to dark blue. The black solid line shows the $H - K$ slope; the black dashed line shows the $K - M$ slope.

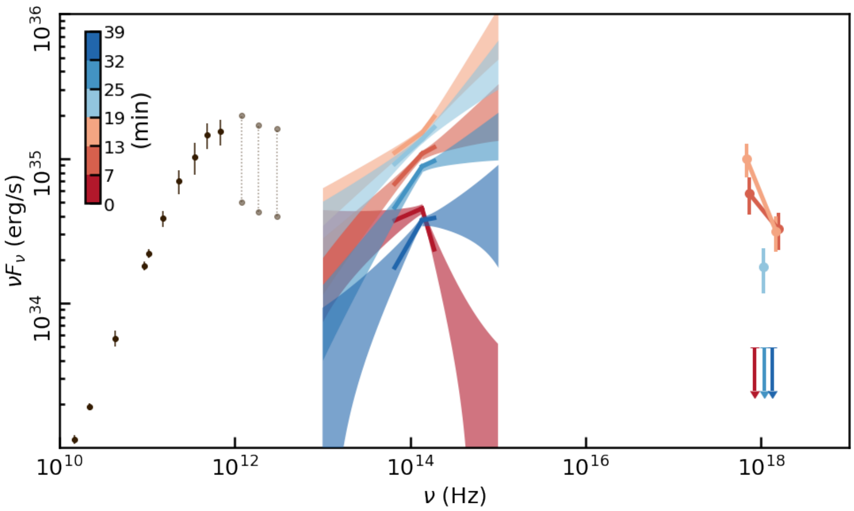

Figure 4.7: Temporal evolution of the SED. The color encodes the time: dark red to dark blue as indicated in the color bar. For two time steps, the X-ray spectrum can be split up into two points (T2 and T3). For T4, only one X-ray flux measurement is possible. The upper limits are plotted for T1, T5, and T6. The measurements in the NIR are indicated by thick lines, with the uncertainties indicated and extrapolated by the shaded area. The submillimeter data shown are the same as in Figure 4.4.

4.7 One zone SED model

To model the IR to X-ray SED of Sgr A*, we developed a dedicated Python package (Dallilar et al. in prep.). The code implements robust calculation of synchrotron emission or IC scattering from a given underlying electron distribution in a single zone. We also provide a convenient SED fitting interface built on top of the general purpose Python fitting package LMFIT[5]. For testing and convenience, the code includes theoretical solutions to synchrotron emission and absorption coefficients of a thermal, power law, or kappa distribution based on the formalism presented by Pandya et al., 2016. Furthermore, we implemented a fast numerical calculation of the emission and absorption coefficients for a given arbitrary electron distribution. With this feature, we are able to explore more complex electron distributions. This is especially important in the context of including "cooling break" types of models (Dodds-Eden et al., 2009; Ponti et al., 2017) and more realistic cut-off shapes of the electron distribution. Our approach is an improvement compared to similar attempts in the aforementioned works in terms of self-consistent determination of electron distribution parameters from SED fitting. The IC scattering formalism of the code follows the concepts presented by Dodds-Eden et al., 2009. As with synchrotron emission, we can take advantage of arbitrary electron distributions as the scattering medium. Seed photons can be either an external (arbitrary) photon field or synchrotron emission from an underlying electron population, namely, SSC emission. The details of the code will discussed by Dallilar et al. (in prep.)

The philosophy of the code is to provide emission scenarios that are as simple as possible. This is achieved by modeling the flares in a scenario in which the emission is dominated by a single localized region in the accretion flow and by a single population of electrons, reducing the number of free parameters. For instance, if the emission is modeled using a power-law distribution of electrons, the number of free parameters is six. Keeping the number of free parameters small is necessary because our limited spectral coverage does not warrant a more complex fit (i.e the number of model parameters should be smaller than the number of observables). Therefore, the luminosity is computed for a homogeneous and spherical geometry of electrons. Ultimately, we can fit the model SED to the data, either through χ^2 minimization or through MCMC modeling.

4.8 Reproducing the mean SED of the flare

4.8.1 Synchrotron with a cooling break

We began by fitting the mean spectrum of the flare with a simple synchrotron model with a cooling break (see Fig. 4.8). We call this model the PLCool model. Although the difference in photon indices between the IR ($\Gamma_{\rm IR} = 1.5 \pm 0.2$) and X-ray ($\Gamma_{\rm X} = 2.7 \pm 0.5$) bands is consistent with the expectations of the synchrotron model with cooling break ($\Delta\Gamma = 0.5$), it is not possible to fit the mean SED of the flare with this model. Indeed, the

[5] `https://github.com/lmfit/lmfit-py/`

	Mean SED			Time Resolved					
	PLCool	PLCoolγ_{max}sharp	PLCoolγ_{max}	T1	T2	T3	T4	T5	T6
$\log(n_e \times 1\mathrm{cm}^{-3})$	6.7±0.2	6.3±0.2	5.52 ± 0.01	5.5 ± 0.2	5.6 ± 0.1	5.8 ± 0.1	5.8 ± 0.1	5.7 ± 0.1	5.3 ± 0.1
R [R$_S$]	1†	1†	1†	1†	1†	1†	1†	1†	1†
B [G]	38±6	30†	30†	30†	30†	30†	30†	30†	30†
p	2.4±0.1	2.0±0.1	2†	2†	2†	2†	2†	2†	2†
γ_{max}	$> 10^3$	68±13	48 ± 4	1.5 ± 1.4	52 ± 0.7	43 ± 5	29 ± 4	5†	5†
χ^2_{red} / DOF	5.0 / 3	2.2 / 4	1.1 / 2	4.9 / 2	0.6 / 2	0.8 / 2	0.7 / 2	5.7 / 1	2.0 / 1

Table 4.4: Best-fit parameters of the fit of the SED with the PLCoolgamma model. The quantity n_e: the electron density within the source; p: the power-law index of the electron distribution; R: the projected radius, in Schwarzschild radii, of the emitting source; B: the magnetic field intensity (G); γ_{max}: the maximum Lorentz factor of the accelerated electrons in units of 10^3; χ^2_{red}; DOF: the reduced χ^2 of the best fit, the number of free parameters †: value fixed. The uncertainties reported correspond to the 1σ confidence limits determined through MCMC sampling.

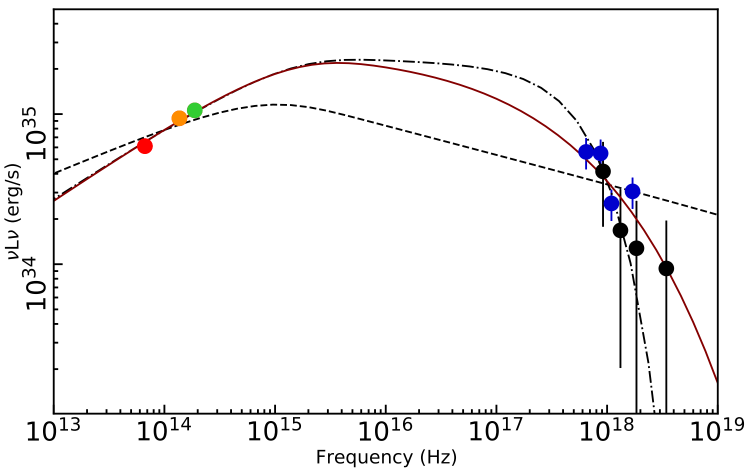

Figure 4.8: Mean SED of Sgr A* during the flare as in Figure 4.4, including the best-fit synchrotron models. The black dashed line shows the best-fit PLCool model (synchrotron with cooling break model with no high-energy cutoff). This model is ruled out because it cannot fit the difference in X-ray vs. IR spectral slopes due to the X-ray vs. IR flux ratio. The dashed-dotted black lines shows the best fit PLCoolγ_{max}sharp model (synchrotron with cooling break plus a sharp γ_{max} cutoff). The line cuts off too sharply in the X-ray and fails to reproduce the high-energy *NuSTAR* data. The dark red line shows the best-fit PLCoolγ_{max} model (synchrotron with cooling break plus an exponential high energy cutoff). For this model, the SSC component, which peaks at $\nu \sim 10^{23}$ Hz, is also computed (not shown here, see Figure 12).

high luminosity in the IR band combined with the rather flat IR spectrum would imply a very high luminosity in the X-ray band. As a consequence of this tension, the PLCool model settles to a less blue IR slope than observed, failing to satisfactorily fit the data (Figure 4.8 and Table 4.4).

4.8.2 Synchrotron with a cooling break and sharp high-energy cutoff

The acceleration mechanism generating the flare may not be powerful enough to accelerate particles to $\gamma_{max} \gg 10^5$ at all times (Ponti et al., 2017). If this is true, we expect to observe a high-energy cutoff between the IR and X-ray bands. Hence, we fit the mean SED with a synchrotron model with cooling break and a high-energy cutoff in the electron distribution. We call this model the PLCool$\gamma_{max\mathrm{sharp}}$. In particular, we assumed that the high-energy cutoff is a step function with no electrons having $\gamma > \gamma_{max}$. We assumed that the electrons are accelerated from the thermal pool that is producing the submillimeter emission, and therefore we fixed $\gamma_{min} = 50$. We assume a source with 1 R_s radius, a magnetic field strength of $B = 30$ G, and a cooling time of two minutes (Tab. 4.4). A fixed cooling timescale of two minutes was motivated by the light travel time for a source with radius 1 R_s: the cooling-break model assumes an equilibrium of particle acceleration and particle losses due to particle escape, and thus particles at low-energy escape the flare region before they cool. In consequence, the position of the cooling break in the spectrum corresponds to the electron energy at which the escape time is equal to the cooling time (Kardashev, 1962; Yuan et al., 2003b). Following Dodds-Eden et al., 2009, we assume that the escape from the system can be approximated by the dynamical timescale. This assumption, together with our assumption of a magnetic field strength of $B = 30$ G, fixes the cooling break as follows:

$$\begin{aligned} \nu_B &= 64 \cdot (B/30[\mathrm{G}])^{-3} \times 10^{14}/t_{cool}^2 \\ &= 1.6 \times 10^{15} \text{ Hz}. \end{aligned} \tag{4.2}$$

This model provides a decent description of the data with acceptable physical parameters, as shown in Fig. 4.8. The best-fit $\log(n_e) = 6.3 \pm 0.2$ and slope of the electron distribution, $p = 2.0 \pm 0.1$ are in line with the density expected in the hot accretion flow of Sgr A* and the electron distribution undergoing synchrotron cooling $p \geq 2$ (Kardashev, 1962; Ghisellini, 2013). On the other hand, the model predicts a significantly softer X-ray emission than observed. Large residuals are observed at high energy, where the model decays quickly with frequency, while the data indicate a clear excess of emission associated with the flare all the way from ~2 to ~8 keV. Therefore, this model is also unsatisfactory.

4.8.3 Synchrotron with a cooling break and exponential high-energy cutoff

A more realistic model is an exponential decay of the electron distribution above a certain cutoff energy. This induces a shallower spectrum at high energy. A synchrotron model with a cooling break and exponential high-energy cutoff can fit the data in an acceptable way. We call this model the PLCoolγ_{max}. The slope of the electron distribution is $p = 2.0 \pm 0.2$, which is consistent with the cooling break scenario (Kardashev, 1962; Ghisellini, 2013). The density $n_e = 10^{5.5\pm0.1}$ cm^{-3} of accelerated electrons suggests that only a fraction of the electrons in the hot accretion flow are involved in the acceleration process. Finally, the best-fit $\gamma_{max} = (4.8 \pm 4.0) \times 10^4$ induces a cutoff in the X-ray band explaining the observed X-ray faintness.

4.9 Time-resolved evolution of Sgr A* SED during the flare

4.9.1 Synchrotron with a cooling break and high-energy cutoff

Figure 4.9 shows the Sgr A* SED temporal evolution during the flare fitted with the PLCoolγ_{max} model. Table 4.4 reports the maximum-likelihood fit parameters and their uncertainties from the 1σ posterior contours of the Markov chain Monte Carlo (MCMC) sampling. For T1, T5, and T6, no X-ray flux was detected. For these three time steps, therefore, the spectrum is composed of only three data points. For T2 and T3, significant X-ray flux was observed, which allows us to determine the flux of Sgr A* in two energy bins. For T4, we binned the high-energy band to one data point. Because of the limited number of free parameters in this time-resolved analysis and in the interest of reducing the number of free parameters in our model, we fixed the magnetic field strength B and the source radius R to $B = 30$ G and $R = 1$ R$_\mathrm{S}$. However, we left the particle density n_e free. The particle density primarily drives the normalization of the spectrum. The magnetic field strength, radius, and particle density are degenerate in the model. Therefore an error in our assumed values of the magnetic field strength and source radius would be compensated by the electron density.

We did not attempt to model the evolution of the electron distribution self-consistently. This would require assuming an emission zone expansion, an electron injection, and an electron cooling scenario. While informative, such scenarios have been explored in one-zone models of flares before (e.g., Dodds-Eden et al., 2010; Dibi et al., 2014) and we assume that the conclusions found in these studies are applicable. The analysis of the mean SED of this flare requires a maximum acceleration $\gamma_{max} \sim 10^4$, and we focused our modeling on the evolution of this parameter.

The minimum acceleration of the electrons is based on the submillimeter emission and fixed at $\gamma_{min} = 50$. Motivated by the fit to the mean SED, we fixed the slope of the electron distribution to $p = 2$. Therefore, the free parameters in the model are n_e and γ_{max}. Fixing the electron distribution slope precludes the possibility to explore the changes of spectral slope shown in Figure 4.6. These choices and assuming that the cooling timescale is set by the escape time of particles escaping the emission region fixes the cooling break at $\nu = 1.6 \times 10^{15}$ Hz.

At the start of the flare during T1 (Figure 4.9), relatively bright emission was observed in the M and K bands, while fainter emission was observed in the H band and no excess emission was detected in the X-ray band. If the IR emission is produced by nonthermal synchrotron emission with a positive IR spectral slope (in νF_ν), then the lack of X-ray emission implies that the distribution of relativistic electrons must have a cutoff at high energy. The flare was bright in the M and K bands during T1, but it was barely detected in the H band, which can be understood in the framework of the PLCoolγ_{max} model. If the maximum acceleration of the electrons (γ_{max}) happens to be located within the K or H band, then the flux drops in the H band and no X-ray emission is expected, in line with the observational results. However, this does not explain the drop in flux between the K and H bands. The PLCoolγ_{max} model only marginally matches the data, with the H-band flux being too faint compared to the K and M bands. This might be a consequence of an underestimated uncertainty for the marginal H-band detection.

In T2, the IR flux increases and the slope was consistent with a power law from the M to the H band, and significant X-ray flux was detected. The data are well-fit by the PLCoolγ_{max} model, and the maximum acceleration is at frequencies slightly higher than the X-ray band. For T2 (shown by the red SED in Figure 4.9), the fitted acceleration reaches its maximal value $\gamma_{max} = (52 \pm 1) \times 10^3$. During the following interval (T3, shown by the light red SED in Figure 4.9), the IR and X-ray emission are at their peaks. However, although little variation in the spectral slope was observed in the IR band, the simultaneous X-ray spectrum appears softer. Our model ascribes this to the maximum acceleration of the electrons having decreased to $\gamma_{max} = (43 \pm 5) \times 10^3$. Subsequently, in T4, the flux starts to drop in both bands (shown by the light blue SED in Figure 4.9). However, although the drop in the IR band is on the order ∼20 % (Figure 4.9 and Table 4.4), again with little variation in the spectral slope, the flux in the X-ray band dropped by more than a factor of 3. Within the framework of the PLCoolγ_{max} model, this can be ascribed to the acceleration mechanism continuing to lose the capability to accelerate electrons to the highest energies, therefore moving γ_{max} to $(29 \pm 4) \times 10^3$. This puts the high-energy cutoff in the electron distribution between the IR and X-ray bands, and the X-ray emission at this time would be produced mainly by electrons above the cutoff.

No X-ray emission was observed during the subsequent intervals T5 and T6 (shown by the blue and dark blue in Figure 4.9). As in T1, the IR was still bright ($\sim 5 - 10$ mJy) and flat. The PLCoolγ_{max} model reproduces this by placing the high-energy cutoff somewhere between the IR and X-ray band. We thus obtain an upper limit on $\gamma_{max} < 5000$.

During these last two intervals, the M-band flux dropped faster than the K- and H-band fluxes. This resulted in a blue $K - M$ slope, which would imply a decrease of p to $p \sim 1.4$, while the $H - K$ slope was consistent with $p \sim 2$. If taken at face value, the observed M-band flux was inconsistent with a fixed slope of $p = 2$ and is responsible for the worse χ^2 for T5 and T6. However, this may be attributable to a correlated error in the relative flux measurement resulting from a telescope slew (Section 4.6)

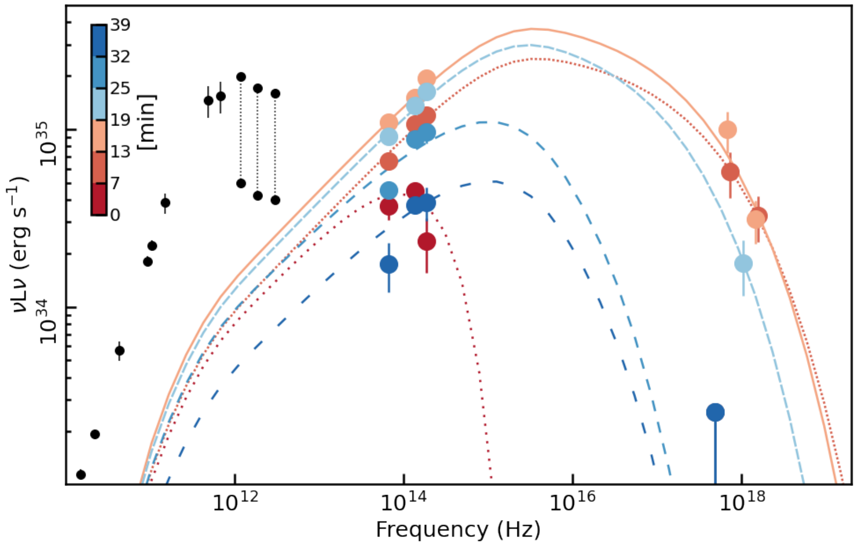

Figure 4.9: Data points show the *Spitzer* + GRAVITY, and *Chandra* photometry during T1 to T6, respectively (dark red to dark blue lines). The data are corrected for the effects of absorption and dust scattering. The lines show the best-fit synchrotron with cooling break and high-energy cutoff models. During the early phases of the flare, the high-energy cutoff appears to be at low energy. During the peak of the flare, the cutoff moves to the X-ray band and then drops again to low energies toward the end of the flare. The submillimeter data shown are the same as in Figure 4.4, and the color bar indicates the time and color progression.

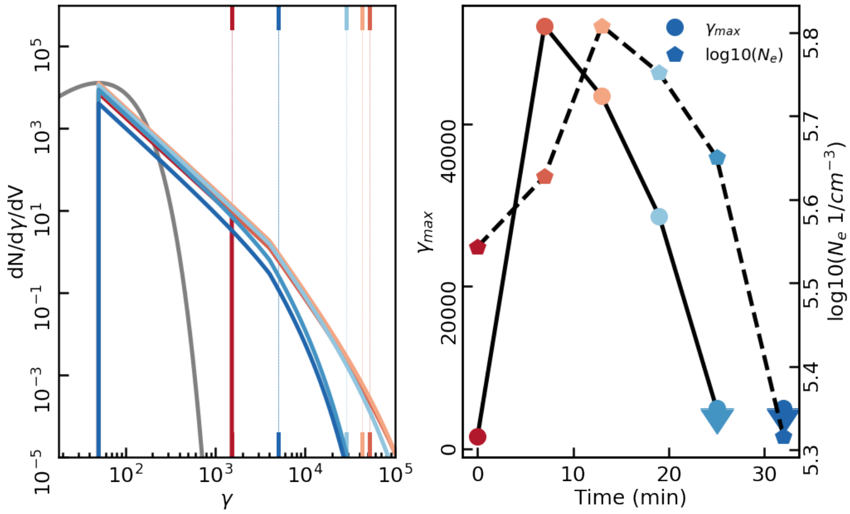

Figure 4.10: Left: Evolution of the electron distribution during the flare. The different temporal steps are plotted dark red (T1), progressing to lighter reds (T3), to light blue (T4), to dark blue (T6). The dotted lines indicate the location of γ_{max}. The gray line shows a thermal distribution of electrons, peaking at $\gamma \sim 50$, which set the minimum acceleration of the electrons for the flare. Right: Evolution of the distribution parameters γ_{max} (shown by the solid line) and n_e (shown by the dashed line).

4.9.2 Temporal evolution of the electron distribution

Figure 4.10 reports the energy distribution of the accelerated electrons for each of the time bins during the flare. It also we shows the energy distribution of the electrons responsible for the submillimeter emission. To match the submillimeter SED of Sgr A*, we computed the spectrum assuming values within the range of parameters reported by Bower et al., 2019. For the submillimeter emission, we assumed an ambient magnetic field strength $B = 30$ G, as for the flare, and a size of 4 R_S, which is consistent with the observed submillimeter size (Issaoun et al., 2019). We chose an ambient particle density $\log(n_e) = 1.7 \times 10^5$ such that the distribution peaks at $\gamma_{min} = 50$. The right panel of Figure 4.10 shows that within 380 s, γ_{max} reaches its maximum value of $\gamma_{max} \sim 5 \times 10^4$, indicating that the most energetic electrons are accelerated during T2. In the following intervals, the maximum Γ steadily decreases, and we can only constrain it to values below 4×10^3 once the X-ray flux has dropped below the detection limit. The electron density, plotted in the right panel of Figure 4.10, reaches its maximum when the flux is the highest (T3), after which it steadily decreases.

Figure 4.11 shows the evolution of the time-resolved SED fitted with the PLCoolγ_{max}model along with the respective electron distributions as inferred from the best fit.

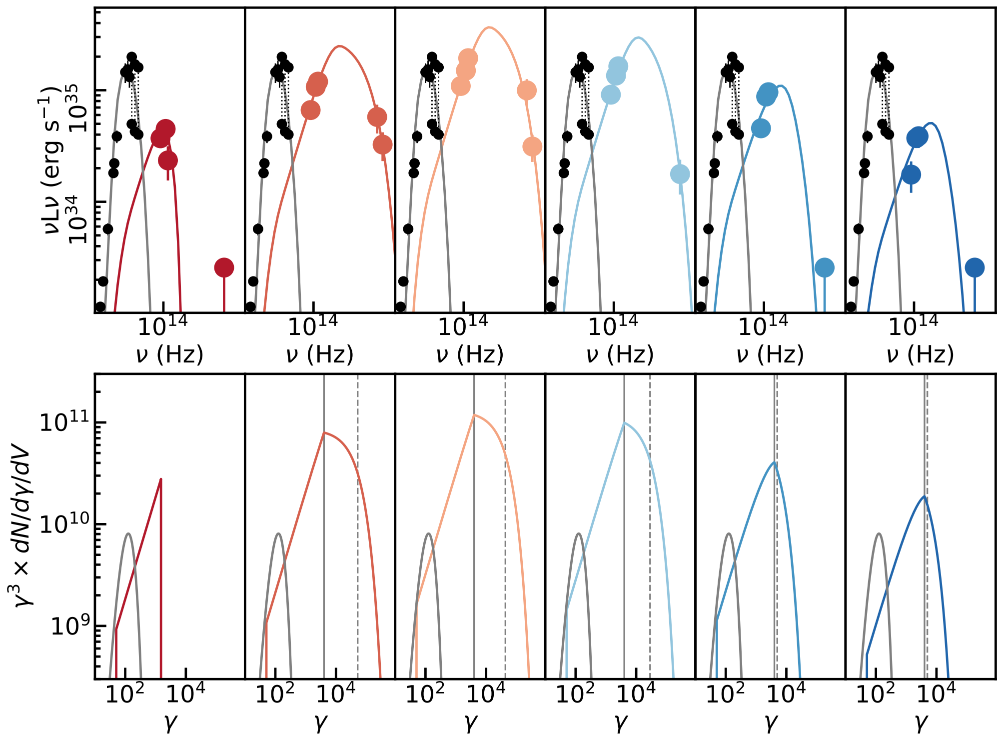

Figure 4.11: Temporal evolution of the flare SED and the temporal evolution of the electron energy distribution. Panels (left to right) show the temporal evolution from T1 to T6. Top row: The observed SED of the flare (colored points) and the best-fit PLCoolγ_{max} model (colored lines). The black points indicate the submillimeter SED of Sgr A*, with the same data as in Figure 4.4. The thin gray line shows a thermal synchrotron spectrum matching the submillimeter data. Bottom row: The electron energy distribution of the respective synchrotron spectra in the top row. Colored lines show the best-fit PLCoolγ_{max} models; the thin gray line shows the electron energy distribution of the thermal spectrum. The positions of the cooling break and γ_{max} are indicated with solid and dashed gray lines, respectively. To highlight the location of the breaks in the distributions, the cooling break, and the maximum acceleration the electron distribution is multiplied by a factor γ^3.

4.9.3 Alternative model: Synchrotron self-Compton scattering of submillimeter photons

An alternative scenario to explain the temporal evolution of Sgr A* variability is proposed by Witzel et al. (2021). Using a comprehensive statistical sample of variability data at submillimeter, IR, and X-ray wavelengths, the authors discussed a strongly variable one-zone synchrotron model[6] at submillimeter to NIR wavelengths that explains the X-ray emission by IC emission. More precisely, submillimeter synchrotron photons are up-scattered to the X-ray regime by the same electron population that is responsible for the synchrotron emission. This model was motivated by the following two facts: First, a compact, self-absorbed synchrotron source has the conditions necessary for the scattering efficiency to be significant. Second, the mechanism can explain the observed flux densities in the submillimeter, IR, and X-ray; the respective power spectral densities; and the cross-correlation properties between these bands.

One shortcoming of the analysis of Witzel et al. (2021) is its inability to explain the IR spectral indices $\alpha > -0.8$ as observed for several bright flares, among which is the flare discussed in this work. This is a consequence of relating the amplitude of the variable flux densities at IR and submillimeter wavelengths. In this model, the IR and submillimeter flux densities have been related to explain the strong correlation of X-ray photons (which are up-scattered from the submillimeter) with the IR. While this model was proposed as a baseline model that works for moderate flares at flux densities where the IR spectral indices are also described properly, Witzel et al. (2021) speculate that brighter flares with blue spectral indices are states in which up-scattered photons contribute to the SED even in the IR.

We implemented an SSC model based on a nonthermal, power-law-distributed electron energy distribution to fit the time-resolved data of July 18, 2019. This model was determined by the same parameters as the PLCoolγ_{max} model, but it differs fundamentally from the synchrotron models above: the synchrotron part of the spectrum is located in the submillimeter (i.e., the SSC model predicts correlated submillimeter variability during this IR and X-ray flaring episode), and the IR and X-ray emission is explained through IC up-scattered photons.

In this case the parameters are also degenerate: at different electron densities n_e the source parameters B, R, and the energy range γ_{min} to γ_{max} can be chosen such that the IR to X-ray IC spectrum is reproduced as measured. However, for $n_e < 10^9$ cm^{-3} the synchrotron component significantly exceeds observed submillimeter emission levels. Therefore, we fixed the slope of the electron energy distribution to $p = 3.1$, which is consistent with the posterior of the analysis by Witzel et al. (2021). We then chose initial conditions with tight bounds such that the submillimeter luminosity remains within the range of observed submillimeter flares, and all the parameters show a continuous progression in

[6] In this scenario, this highly variable component contributes to the submillimeter, but cannot entirely explain the observed submillimeter flux density levels. A second electron population is required to explain the SED at radio to submillimeter wavelengths, and the observed submillimeter flux density is the result of the superposition of both components.

	Time resolved					
	T1	T2	T3	T4	T5	T6
$log(n_e \times\ 1\mathrm{cm}^{-3}))$	10.0	10.0± 0.5	10.1±0.4	10.0±0.2	10.0	9.8
R μas	15†	15±8	16±8	16†	12	12†
B G	8.2	8±6	8±5	7±10	8.0†	8.0†
p	3.1†	3.1†	3.1†	3.1†	3.1†	3.1†
γ_{max}	180†	500±100	470±80	360±70	230†	243
γ_{min}	5.2	6.1±1.8	5.4±1.1	6.1±0.9	7.4	7.8
χ^2_{red}; DOF	6.7	0.1	2.7	0.9	0.2	0.4

Table 4.5: Best-fit parameters of the fit of the SED with the SSC model. The quantity n_e: the electron density within the source; p: the power-law index of the electron distribution; R: the projected radius, in μas, of the emitting source; B: the magnetic field intensity (G); γ_{max}: the maximum Lorentz factor of the accelerated electrons; γ_{min}: the minimum Lorentz factor of the accelerated electrons; χ^2_{red}; DOF: the reduced χ^2 and number of free parameters of the best-fit †: value fixed.

time.

In T2–T4, where X-ray emission was detected, all other parameters besides p were left free in the fits of the SEDs. We additionally fixed γ_{max} in T1 and T5, R for T1, T4, and T6, and B for T5 and T6. To derive reliable uncertainties for T2–T4, we probed the parameter space with an MCMC sampler after lifting the bounds. The results are listed in Table 4.5, and the resulting SEDs and time series of parameters are shown in Figures 4.12 and 4.13.

4.10 Discussion

This paper discusses the first Sgr A* flare that has been continuously observed from 4.5 μm to 1.65 μm in the NIR and from 2 keV to 70 keV in the X-ray band. Compared to previously studied flares simultaneously observed in the X-ray and IR bands, this flare is exceptional for its remarkable IR brightness, relative X-ray faintness, and short duration.

4.10.1 Slope variability in the IR band during the flare

The IR spectrum of the flare showed an increasing spectral index with increasing flux density. During the onset of the flare, the ratio of the H-band flux to the M- and K-band fluxes was low. This resulted in a kink in the intra-IR spectrum. The $H - K$ slope seemed to increase with flux density, being the bluest when the flare was the brightest and decreased again toward the end of the flare. Such a flux correlation has been discussed in previous works. While Hornstein et al., 2007 measured a constant spectral slope $\nu F_\nu \propto \nu^{0.5}$ independent of flux density, Eisenhauer et al., 2005, Gillessen et al., 2006, and Genzel

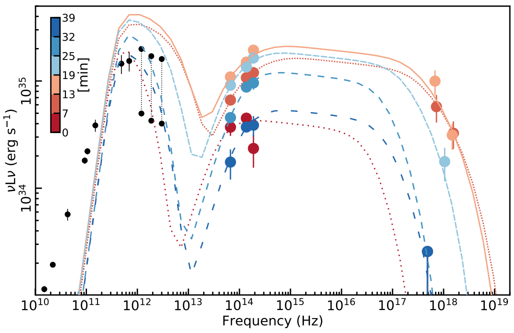

Figure 4.12: SEDs of the best-fit SSC models. The colors correspond to T1 to T6 as shown in the color bar. The colored point show the observed data for each time. The dark points show the submillimeter SED of Sgr A* with the same data as in Figure 4.4. As in the models involving only synchrotron emission, the flare evolution can largely be explained by progression of the electron density n_e and high-energy cutoff $\gamma_{\max}$.

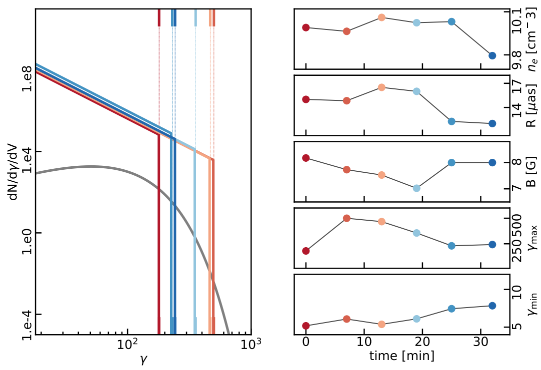

Figure 4.13: SSC parameter evolution during flare, analogous to Figure 4.10. Left: The evolution of the electron distribution during the flare. The dash-dotted lines indicate the location of γ_{max}. The gray line shows the thermal distribution of electrons, peaking at $\gamma \sim 50$, which sets the minimum acceleration of the electrons for the flare. Right: Evolution of the model parameters n_e, R, B, γ_{max}, and γ_{min}. For the SSC models $\gamma_{\max}$ is significantly lower and n_e significantly higher than for the PLCoolγ_{max} model.

et al., 2010 confirmed $\nu F_\nu \propto \nu^{0.5}$ at high flux density but argued for a flux-dependent $\nu F_\nu \propto \nu^{-1\cdots-3}$ at lower flux density. The statistical analysis of the M- and K-band flux distributions presented in Witzel et al., 2018 favored a variable, flux-dependent spectral index. Our work adds further evidence for a flux-dependent spectral index. Small changes in the spectral slope that be explained either by stochastic fluctuation or a flux-dependent scaling. We also found a kink in the intra-IR spectral slope during T1. Despite the difficulty of obtaining reliable flux measurements at very low flux from AO photometry, the variation is formally significant (>1 σ, Figure 4.7).

4.10.2 Single zone emission model for Sgr A*

Using our fast numerical implementation of a one-zone emitting source, we explored a variety of models, at first regardless of their physicality in the context of the Sgr A* accretion flow. All our models require a set of parameters describing the ambient conditions as follows: i) electron density n_e; ii) magnetic field strength B; iii) radius R of the emitting source, assumed to be spherical; and iv) an energy distribution of accelerated electrons described by a set of parameters. For a thermal scenario, the distribution is characterized by a single parameter: the temperature of the electrons. For a power-law distribution, at least two parameters are required: the slope of the distribution and one or two normalization constants (γ_{min}, γ_{max}). The normalization constants can be interpreted in a physical sense: if the distribution is generated from a process which accelerates particles, then the minimum Lorentz factor γ_{min} can be interpreted as the ambient Lorentz factor of the particles. Similarly, the maximum Lorentz factor γ_{max} can be interpreted as a maximum length scale on which the particles are accelerated. Furthermore, the power-law distribution can have more than one slope. Such a broken power-law distribution is for instance assumed in the PLCoolγ_{max} model, where synchrotron cooling is expected to induce a change of $p_2 = p_1 - 1$ at the cooling break.

Before reaching the observer, the synchrotron radiation can be up-scattered by a population of relativistic electrons and produce an IC component. For example, for synchrotron one-zone models that take into account the respective SSC component, there are three different ways of obtaining simultaneous IR and X-ray emission.

1. The emission in both bands is entirely dominated by synchrotron emission. We refer to scenarios of this type as SYN–SYN scenario. In such scenarios, the photon index observed in the X-ray band should be steeper by 0.5 than the simultaneous IR value (as a consequence of the cooling break).

2. The emission in the IR is synchrotron emission, and the X-ray emission is SSC emission. We refer to these scenarios as SYN–SSC scenario.

3. The emission in both bands is entirely dominated by the IC component of the SSC emission. We refer to such a scenario as SSC–SSC scenario.

4.10.3 Constraints from the simultaneous IR and X-ray photon indices and flux ratios

A major problem for the SYN–SYN and the SSC models is the combination of i) the observed positive IR slope, ii) the observed negative X-ray slope, and iii) the large flux ratio of IR to X-ray.

Taken at face value, the difference in X-ray to IR slopes would be perfectly consistent with a synchrotron model with a cooling break in the electron distribution (Dodds-Eden et al., 2009). However, such a model cannot at the same time reproduce the flux ratio of the IR to X-ray (§8.1).

The observed luminosity in both bands sets parameter regimes for which the three scenarios match the observed spectrum:

- To be dominated by synchrotron emission in both bands, the maximum Lorentz factor γ_{max} is required to be $\gg 10^4$.
- To be dominated by synchrotron emission in the IR and by SSC in the X-ray, γ_{max} must be rather low. The frequency at which the synchrotron emission peaks scales $\nu_c(B) \times \gamma_{max}^2$. Therefore a large magnetic field $\gg 10^3$ G is needed to shift the synchrotron peak into the IR.
- Similarly, to be dominated by SSC in both bands, γ_{max} cannot be too large. However, because the synchrotron emission does not need to be shifted into the NIR, the constraints on the magnetic field can be relaxed. Nevertheless, to sustain high SSC flux from IR to X-ray, the particle density has to be $\gg 10^9$ cm^{-3}.

The SYN–SSC scenario:

The SYN–SSC scenario has severe problems: First, it requires magnetic fields of $\sim 10^4$ G, source regions around $\sim 0.001 R_s$, and densities $\sim 10^{12}$ cm^{-3}. These parameters are extreme compared to the submillimeter ambient conditions. Even ignoring this, the synchrotron cooling timescale in such a strong magnetic field is on the order of 0.1 seconds in the IR and on the order of 1 millisecond in the X-ray. Even though flares of Sgr A* are highly variable, spikes on timescales shorter than tens of seconds have never been observed in the IR band. We attribute this lack of short timescale, IR variability to the effects of the cooling time of the electrons, which smooth out any variation shorter than a few seconds. We rule out Dodds-Eden et al., 2009 and Dibi et al., 2014, that is, the scenario in which the IR flare is generated from synchrotron emission with a thermal distribution and the X-ray flare is SSC. This is a direct consequence of the negative X-ray spectral slope. If the observed X-ray slope were flat or positive, the requirement of a $\gamma_{max} < 10^2$ would be relaxed. This is because for a positive or flat spectral slopes the emission can stem from the rising or flat part of SSC spectrum. In turn, this relaxes the requirement for very large magnetic fields because the peak of the synchrotron component at $\nu_{max,syn}$ can be shifted by γ_{max} as well and not only by the magnetic field.

The SSC–SSC scenario:

In the picture of the time-dependent model of Witzel et al. (2021), which can successfully describe the flux density distributions and the auto-correlation and cross-correlation properties of the light curves, the fast IR variability is the result of a quickly varying γ_{max} that truncates the synchrotron spectrum. In order to link the IR variability amplitudes at longer timescales with the submillimeter and X-ray regimes, an overall $\alpha = -1$ is required that—depending on the brightness—steepens toward the IR owing to the γ_{max} cutoff. Flatter IR spectral indices of $\alpha > -0.8$ as reported here are not possible without the up-scattered spectrum contributing to the IR.

The 2019-07-17 flare requires an even more extreme scenario in that it shows a very bright IR flare in combination with moderate X-ray luminosity. This particular configuration requires the range of the SSC component of the spectrum to be limited such that its decreasing flank falls into the 2–8 keV range. For the fit, this is achieved by restricting γ_{max} to lower values such that the IR is not a superposition of direct synchrotron and scattered photons anymore but is dominated by the SSC component entirely. To then reach the high IR flux density of this flare while keeping B and R at levels that do not lead to unobserved, high submillimeter luminosities, $n_e > 10^{10}$ cm^{-3} is required. While much higher than the typical, average electron densities derived from modeling the radio to submillimeter SED of Sgr A* with synchrotron emission from a thermal electron distribution (ambient $n_e < 10^7$ cm^{-3} Bower et al., 2019), $n_e > 10^{10}$ cm^{-3} is not out of the question: Mościbrodzka and Falcke, 2013 discussed mid-plane densities of $n_e = 10^9$ cm^{-3}, and Yoon et al., 2020 used 10^{-13} gcm^{-3}, which corresponds to $5.9 \cdot 10^{10}$ cm^{-3}.

The SYN–SYN scenario

The SYN–SYN scenario realized via the PLCoolγ_{max} model requires $\gamma_{max} \sim 50\,000$ and an exponential decay rather than a sharp cutoff (see Figure 4.11). Because our data constrains the fit in the optically thin part of the spectrum, we can infer only the total number of electrons rather than the radius and electron density independently. Fixing the source radius to $1R_S$, we obtained an estimate of the electron density. By assuming a cooling timescale of two minutes and by requiring a cooling break between the IR and the X-ray, the magnetic field is constrained to $B \sim 1$ to 100 G[7]. Under these assumptions, the plasma parameters required are comparable to the submillimeter ambient parameters inferred from the submillimeter SED (Yuan et al., 2003b; Bower et al., 2019, e.g.:). This model requires that the process accelerating the electrons generates Lorentz factors increased from ambient conditions by a factor $> 10^3$ and does so without alteration of the ambient plasma parameters on large scales. The best-fit model for the mean SED sets a direct constraint on γ_{max}. As discussed in section 4.8.2, this is a consequence of the high flux in the IR together with moderate flux in X-ray. Under the model assumptions, our observations place limits on the maximum acceleration of the flare-generating process (as

[7]This is sensitive to our choice of the cooling timescale because the break frequency scales as $\nu_{break} \propto 1/t^2_{cool}$.

done by Ponti et al., 2017). Notably, this flare mechanism does not produce any relevant submillimeter flux. Therefore, it does not predict any direct effect on the submillimeter light curve and observable accretion flow[8]. For our choice of $R = 1\ R_s$, the SSC component of the flare peaks at around 10^{23} Hz (corresponding to GeV energy band), with a peak luminosity of $\sim 10^{34}$ erg s^{-1} (Figure 12). Unfortunately, this implies that the expected SSC luminosity is too faint to be observable by, for instance, the *Fermi* satellite (Malyshev et al., 2015).

4.10.4 Temporal evolution of the flare

Temporal evolution in the SSC–SSC scenario

The Compton component of the SSC–SSC model is sensitive to where the synchrotron emission becomes optically thick. Therefore, such a model places strong constraints on the synchrotron part of the spectrum, which is expected to reproduce the emission in the submillimeter band. Unfortunately, our campaign has no coverage of the submillimeter band. Therefore, we cannot uniquely derive the best-fit solution, but instead can only constrain the parameters by assuming typical values for the submillimeter emission. Keeping the magnetic field, the electron density and the radius thus constrained, we modeled the light curve of the flare by selecting a suitable local minimum. The temporal evolution of flux densities is then mostly driven by the variation of γ_{max}, which determines the width of the synchrotron spectrum and, as a consequence, scales the X-ray flux.

The SSC–SSC scenario predicts that a high submillimeter flux density excursion is associated with the flare of 2019-07-17, that is, that the submillimeter exhibits temporal correlation with the IR light curve. Depending on the exact combination of parameters, the submillimeter light curve may lag slightly behind the IR and X-ray, comparable to the effects of source expansion discussed by Witzel et al. (2021).

The "kink" in the X-ray spectrum of the first data point cannot be explained by SSC-SSC scenario because it either requires a SSC component that is too narrow, or an extension of the synchrotron component into the IR for only the first data point. Except for this cutoff between the K and H band of T1, the model can closely fit the measurements. In particular, it reproduces the frequency-dependent spectral index in the IR that changes from the very blue index between the M and K band to a flatter $K - H$ index.

Bower et al., 2018 showed in a study of ALMA polarization data that the observed Faraday rotation is consistent with the rotation measure expected from a radiatively inefficient accretion flow (RIAF) with $\dot{\mathrm{M}} = 10^{-8}\mathrm{M}_{\odot}\mathrm{y}^{-1}$, or $\dot{\mathrm{M}} = 3 \cdot 10^{-16}\mathrm{M}_{\odot}\mathrm{s}^{-1}$. Assuming a proton to electron ratio of unity, the changes in electron density as suggested by the

[8] This is strictly true only if the assumptions made here are valid. Ponti et al., 2017 discussed a brighter X-ray flare, where the magnetic field strength was consistent with the ambient value before and after the flare, while it significantly drops at the peak of the flare. If the magnetic field strength dropped at the peak of the flare (possibly as a consequence of magnetic reconnection) in a significant fraction of the volume producing the emission in the submillimeter band, then a drop in the submillimeter emission might be expected to be observed at the peak of the flare as a consequence of the smaller magnetic field strength (Dodds-Eden et al., 2010).

temporal evolution described in this work of $\Delta n_e \approx 6.3 \cdot 10^9$ cm^{-3} over a region of $\sim$1.5 R_S require an additional mass $\Delta M \approx 1.3 \cdot 10^{-10}$ M$_\odot$. The average accretion flow would require >100 hours to provide this much mass, but in this scenario the density evolves within less than 30 min. This suggests that interpreting the flare in the context of the SSC–SSC model makes the implicit assumption of moments of extraordinary accretion far exceeding the average accretion flow.

Temporal evolution of the SYN–SYN scenario

The time-resolved spectra were fitted assuming a constant magnetic field strength and source size because of the degeneracy with the electron density. Therefore, in our modeling, the normalization of the spectrum is mainly determined by the electron density. Similar to the model discussed by Dodds-Eden et al., 2010 and Ponti et al., 2017, this scenario assumes an episode of particle injection with large γ_{max}, which sustains the X-ray emission against the very short cooling timescales. The quality of the data and the degeneracy of the model parameters do not allow us to explicitly model the evolution of the radius and magnetic field intensity in addition to the electron density (e.g., Dodds-Eden et al., 2010; Ponti et al., 2017). Therefore, it remains to be verified whether the findings of Dodds-Eden et al., 2010 and Ponti et al., 2017 hold and are applicable here as well.

Although it appears sharper than the model predicts, the apparent kink in the IR spectrum at T1 is attributed to the truncated electron distribution function at $\gamma_{max} \sim$ 500. These observations place strong constraints on the timescales under which electron acceleration has to be maintained and on how fast it needs to vary (see Figure 4.10 Ponti et al., 2017).

4.10.5 Concluding remarks

For both the SYN–SYN and SSC–SSC models, this flare sets strong requirements on the mechanism responsible for its emission. Either the flare requires acceleration of electrons by a factor of $>10^3$, or it requires electron densities increased by a factor of $10^{2\ldots3}$ ecm^{-3} and electron density changes with respect to the submillimeter ambient conditions that cannot be explained from the average accretion flow. Furthermore, it is remarkable that in both cases, the maximum Lorentz factor plays a very important role for the temporal evolution of the flare. For the SSC–SSC scenario, γ_{max} regulates the width of the synchrotron spectrum, which in turn sets the width of the Compton component. Similarly, for the SYN–SYN scenario, the kink of the IR spectrum for T1, the high IR-to-X-ray flux ratio, and the X-ray slope are dictated by the evolution of γ_{max}. A similar evolution of the SED was observed during another flare detected simultaneously in the IR and X-ray band (Ponti et al., 2017). Both models make strong predictions about the presence of a direct submillimeter counterpart. The SSC–SSC scenario would be ruled out in the absence of a strong flux increase by a factor of 2 to 3, while the extrapolation to the submillimeter band of the SYN–SYN model predicts no significant contribution to the submillimeter emission; a possible variation of the magnetic field however might induce some degree of correlated variations in the submillimeter band (Dodds-Eden et al., 2010; Ponti et al., 2017). All of our modeling has ignored the expected modulation of the light curve from the relativistic motion of the flare itself and other relativistic effects expected in the proximity of the BH (GRAVITY Collaboration et al., 2018a; Gravity Collaboration et al., 2020e). For the SYN–SYN scenario, the modulation of the light curve by relativistic boosting does merely translate into a variation of the assumed parameters. The same is not true for the SSC–SSC scenario: the Compton scattering occurs in the flare rest frame, while the synchrotron emission is observed from outside. Consequently, the SSC component of a relativistic hot spot may be lowered while the synchrotron component may be increased (or vice versa). Future modeling of such a scenario should take this effect into account.

In light of the new data, we rule out the SYN–SSC scenario for this flare because it requires nonphysical model parameters and would imply NIR variability on timescales not observed. We consider that neither the SYN–SYN nor the SSC–SSC models can be strictly ruled out. However, the SSC–SSC scenarios requires very high local over-densities in the accretion flow and a density variation that cannot be explained with the average mass accretion. It therefore requires an extraordinary accretion event together with moderate particle acceleration.

The SYN–SYN model does not require extraordinary accretion, but requires particle acceleration from Lorentz factors of the ambient electrons of $\gamma \sim 10$ to $\gamma \sim 10^4$. Typically discussed candidate mechanisms are either electron acceleration through magnetic reconnection, turbulent heating in shocks induced by a misalignment of BH spin and accretion flow or in shocks along an outflow/jet (Dodds-Eden et al., 2009; Dexter and Fragile, 2012). Large-scale simulations of the accretion flow do not have the resolution to trace individual reconnection events, but several strategies have been developed to try to account for this (Dexter et al., 2020; Chatterjee et al., 2020). Particles in cell simulations of plasmas show that turbulence heating and magnetic reconnection can create significantly nonthermal, power-law electron distributions (Sironi and Beloborodov, 2020; Wong et al., 2020; Werner and Uzdensky, 2021). Interestingly, the arge-scale simulation presented by Ripperda et al., 2020 shows flare regions of a size of around 1 to $2R_S$ formed through magnetic reconnection with comparable field strengths to those in the toy models discussed in this work. In the SYN–SYN model, this flare places tight constraints on the maximum allowed acceleration. If no rigorous theoretical motivation for such a specific value of the maximum acceleration value is found[9], it may ultimately be viewed as too constraining to uphold the simple SYN–SYN model and it may need to be discarded in favor of more complicated models. Conversely, if the maximum acceleration of an acceleration process is rooted in a sound theoretical framework, future observations of IR bright and X-ray faint flares may provide a powerful tool to constrain the underlying acceleration physics.

Currently, there are no models that can correctly match the observed spectrum, variability, and orbital motions of the emission at the Galactic Center. Our two models shown

[9]For instance, assuming the particles are accelerated for $1R_S$ with a fraction of the speed of light would yield a Lorentz factor of $\gamma(v) = eBR_S/m_e c^2 \times v/c \sim 1 \times 10^{10} \times v/c$, implying that the acceleration happens on much smaller scales.

above reproduce the SED during flares, but do not include enough physics to account for variability or orbital motions. More physically motivated GRMHD simulations show more complexity but are also not able to fully explain observations. However, in GRMHD models the NIR synchrotron photons and IC scattering are associated with spatially separate populations of electrons, an effect that is not captured in our simple one-zone models. More work is needed to combine these approaches or develop new methods to understand the emission mechanism and dynamical properties of the accretion flow at the smallest scales.

Acknowledgements SvF thanks Giulia Focchi for her contribution to the H-band acquisition camera pipeline. SvF, & FW acknowledge support by the Max Planck International Research School. GP is supported by the H2020 ERC Consolidator Grant Hot Milk under grant agreement Nr. 865637. A.A. and P.G. were supported by Fundação para a Ciência e a Tecnologia, with grants reference UIDB/00099/2020 and SFRH/BSAB/142940/2018. This work is based in part on observations made with the Spitzer Space Telescope, which was operated by the Jet Propulsion Laboratory, California Institute of Technology under a contract with NASA. Support for this work was provided by NASA. The scientific results reported in this article are based in part on observations made by the Chandra X-ray Observatory. This work is based in part on observations made with NuSTAR, which is operated by NASA/JPL-Caltech. GGF, JLH, HAS, & SPW acknowledge support for this work from the NASA ADAP program under NASA grant 80NSSC18K0416.

Chapter 5

The Young Stars in the Galactic Center

5.1 Introduction

The first infrared observations of the Galactic Center (GC) revealed that the central region of the Milky Way is surprisingly bright (Becklin and Neugebauer, 1968; Becklin and Neugebauer, 1975). Due to the advent of ever higher resolution observations we now know that this light originates from a cluster of young, massive stars, many of them O-type or Wolf-Rayet stars, residing in the central parsec (Genzel et al., 1994; Simons and Becklin, 1996; Blum et al., 1996). The presence of young stars close to the massive black hole is puzzling, since star formation should be suppressed in the tidal field of the large mass. At the same time, the lifetimes of such stars is so short that they cannot have migrated from far.

The most important clue to solving this puzzle came from resolved stellar kinematics (Genzel et al., 2000; Genzel et al., 2003b; Levin and Beloborodov, 2003; Beloborodov et al., 2006; Lu et al., 2006; Paumard et al., 2006; Lu et al., 2009). The young stars to a large extent reside in two counter-rotating disks/streamers. This is now understood as a result of their formation from a massive ($\sim$1 $\times$ $10^5\,M_\odot$) gaseous disks a few Myr ago (Bonnell and Rice, 2008; Hobbs and Nayakshin, 2009). This picture is supported by the fact that the observed (and hence also initial) mass function is very top-heavy (Bartko et al., 2010) and the surface radial density follows a powerlaw profile $\sim r^{-2}$. Further, the dynamical structure shows a warp for the clockwise disk (Bartko et al., 2010), which might be a natural consequence of resonant relaxation (Kocsis and Tremaine, 2011).

While the basic findings and physical picture are agreed upon in the scientific community, there are several details which are not fully settled: Do et al. (2013) and Lu et al. (2013) find a less top-heavy mass function than Bartko et al. (2010). The statistical significance of the presence of the counter-clockwise disk is low, owed to the small number of stars, and has been disputed in Yelda et al. (2014). The same authors also do not find the clockwise disks' warp.

Since these studies, the underlying data base has grown further. More stars in the GC field have been observed spectroscopically which is the key for spectral typing and being able to include them into the kinematic analysis. Further, the number of stars for which we can report full orbital solutions has increased due to the longer time coverage. Given these advances and the open questions, we here present a re-analysis of the dynamics of the young stars in the GC.

5.2 Observations and data reduction

5.2.1 Observations

In this analysis we have compiled a unique set of spectroscopic GC observations spanning almost two decades. Our observations consist of AO-assisted SINFONI observations, most of which were obtained in the combined H+K band, with a pixel scale of 100 mas. We re-reduced and analysed all GC SINFONI pointings. A considerable fraction of these data were analysed in previous publications, e.g. Paumard et al., 2006; Bartko et al., 2009; Bartko et al., 2010; Pfuhl et al., 2011; Pfuhl et al., 2014. In addition, we analysed previously unpublished observations of the GC, obtained as back-up during the continuous monitoring of the motions of the stars in the GC (Gillessen et al., 2009; Gillessen et al., 2017; Gravity Collaboration et al., 2021b).
For stars closer than 2 $''$ to the black hole, our astrometry is determined from the same continuous observing program, while for stars at larger projected distances, we rely on the astrometry presented by Trippe et al., 2008. Figure 5.1 shows an overview of the SINFONI exposures. Our spectroscopic coverage increased substantially compared to previous studies (e.g. Pfuhl et al. 2011 and Yelda et al. 2014). While we have reduced the gaps in our coverage, our observation coverage is biased towards the natural guide star used by the SINFONI AO system in the North-East, which prohibits Southern and North-Western observations. We covered a square spanning $\sim -20''$ to $\sim 10''$ offset from Sgr A* in right ascension and $\sim -10''$ to $\sim 20''$ in declination. The integration depth across this square is however not homogeneous, with some patches suffering from poor quality. Further, bright sources outshine near-by fainter stars in some patches. Only few Southern or North-Western exposures exist which rely on the laser guide star system (Bonnet et al., 2004). We stacked exposures from different epochs if multiple exposures exist. We accounted for Earths motion around the Sun by shifting the wavelength axis of each exposure to the local standard of rest before combination.
We tried to classify all stars photometrically discernible in the exposures into either young or old type. We did so by taking a spectrum using aperture photometry of each star. Once the optimal spectra was extracted from the combined data cube, we classified the star by the emission and absorption lines in the spectrum. We classified stars as old stars if the CO band heads around $\sim 2.3\ \mu$m are detected. Young stars are classified by the detection of the Bracket γ (Brγ) line at 2.166 μm (and other lines). Because our observations seldomly allowed for the detection of stars fainter than $K_{mag} = 15$, such a simple classification

scheme suffices to determine the age of the stars (e.g. Do et al., 2013). The classification of young stars is complicated by the Brγ emission of the ionized gas in the Galactic Center, which can mimic young star features if the background subtraction is poor. Thus we allow for stars to remain un-classified, if the stars do not show CO-band heads, but the Brγ line is also not credibly detected.
All in all, we classified over 2800 stars into un-classifiable, old, candidate young or young star. For all classifiable stars, we determine the radial velocity. Here, we only investigate the young stars. The old stars will be investigated in a future publication.

5.2.2 Radial velocity measurement of young stars

The radial velocity measurement of young stars gets complicated by the presence of multiple gas emission clouds that contaminate the Brγ absorption line of the stars (e.g. Paumard et al., 2006). By selecting a suitable background we tried to minimize the effect ionized gas emission. However, this approach is limited. For stars with difficult background subtraction, we reverted to the Helium absorption line at 2.13 µm, which is much less affected by background emission but is significantly harder to detect. This led to low SNR in the line detections for many stars. We used line-maps to confirm stars with faint lines, as well as the consistency of Brγ and Helium velocities.
For each star we obtained three different spectra using three different background aperture masks and determined the radial velocity for each. This allows us to estimate the uncertainty from the spectral extraction and the gas emission contamination. The mean radial velocity uncertainty of our data is 58 km/s, with many stars having radial velocity uncertainties larger than 100 km/s.

5.2.3 Spectroscopic completeness

Estimating the spectroscopic completeness is notoriously difficult. This study focuses on the dynamical properties of the young stars. Nevertheless, we tried to estimate the fraction of stars we are able to detect. Typically this is done by planting point sources of different brightness in the images and estimating their detectablilty. Because our coverage is very patchy, and the integration depth is different for each pointing, we reverted to a simpler technique: we assumed that the catalogue by Trippe et al., 2008 is photometrically complete up to stars of $K_{mag} = 16$. Under this assumption we cross-referenced all stars which we were able to classify as either young or old to this catalogue. By binning the catalog stars in steps of 0.5 magnitudes, we can count the fraction of stars we were able to classify spectroscopically. Figure 5.2 shows the resulting completeness maps. Unlike planting point sources, our method can account for the effect of bright stars outshining fainter ones. We nevertheless assume that many stars are not caught, and estimate that our completeness estimate is uncertain by $\sim$1 magnitude. Remarkably, we detect stars up to $K_{mag} = 14.5$ for most of our covered area, despite the integration time per pointing is typically less the further the pointing is from Sgr A*. Furthermore, the central region which has been observed most frequently, is typically less complete than the outer regions. This is a

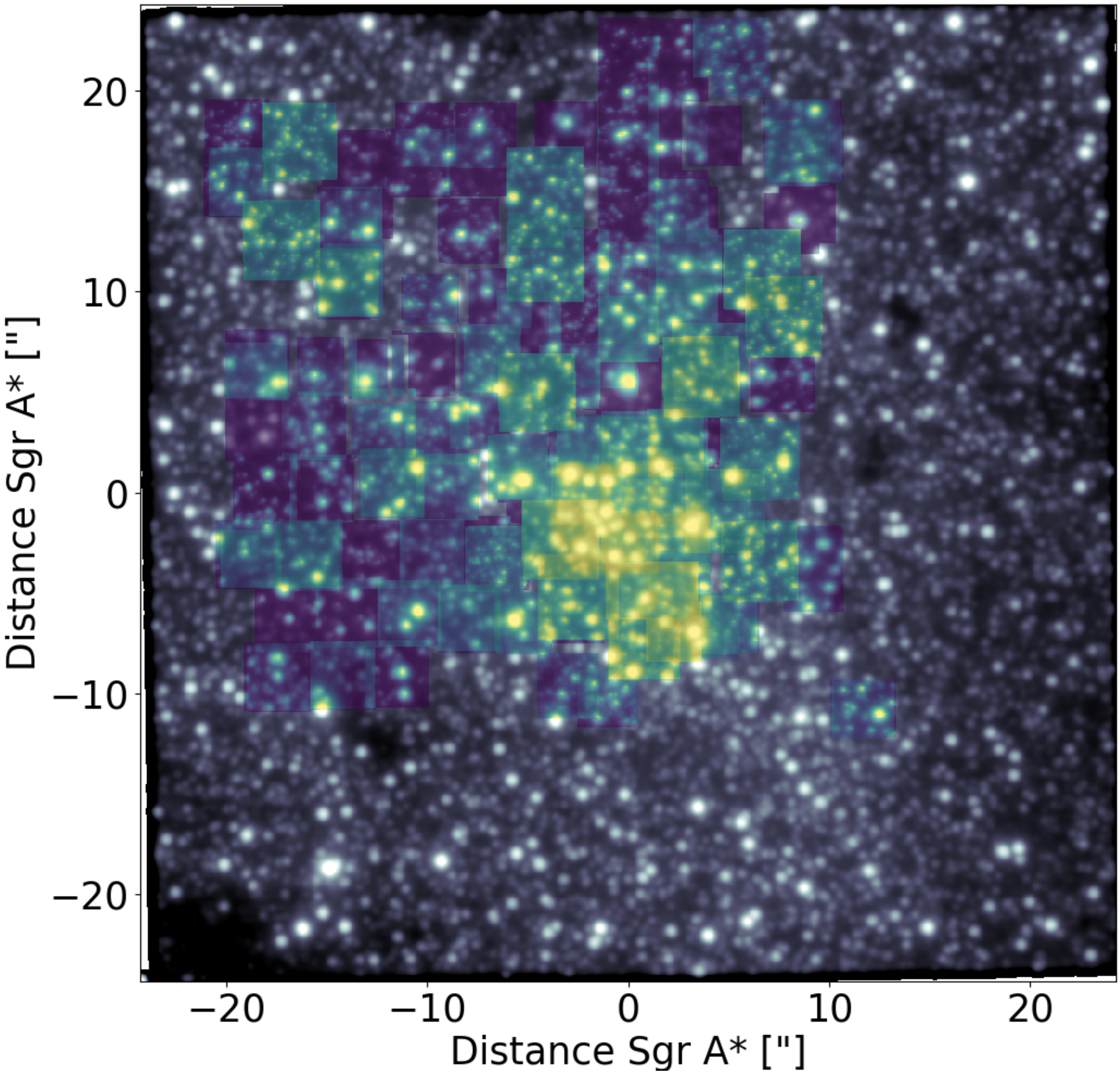

Figure 5.1: The SINFONI Galactic Center exposure map. The image in grey-scale is a large NACO mosaic which has been re-scaled to match the SINFONI 100 mas plate scale. The SINFONI exposures have been aligned with the NACO mosaic, and over-plotted using the green-blue color scale.

consequence of the increasing number of (bright) stars towards the center which complicate the identification of close by fainter stars. In other words, the decreasing number of stars at larger projected distances compensates for the shorter integration time. Other than the decreasing completeness in the central region there is no substantial bias in neither Norther, North-Eastern nor Eastern direction. Furthermore, our completeness estimate is comparable with that found in Pfuhl et al., 2011.

5.3 Young star data set

5.3.1 Stars with full orbits

Overall 35 young stars have known full orbital solutions. We give them and the associated uncertainties in Table 2 in subsection A4.1. Figure 5.3 shows the inferred orbits. The track of astrometric measurements is over-plotted as darkened points. Of these orbits, 30 have been presented in previous studies (Gillessen et al., 2009; Gillessen et al., 2017), but we have updated their orbital estimates. 5 stars have new orbital solutions that we have added here.

5.3.2 Stars without orbits

For 195 young stars we are able to determine five of the six phase space coordinates (x,y, v_x, v_y, v_z), which are given in Table 3 in subsection A4.2. We plot the astrometric positions of these stars on top of a large NACO mosaic in Figure 5.4, labeled by the row number in Table 3. In the following we will describe our star list and compare it with previously published star lists. The source of the radial velocity is given in the column “Source of radial velocity” of Table 3 for all stars.

Newly identified stars and consolidated radial velocities of known young stars

Compared to the latest published list of known young stars in the GC by Yelda et al., 2014 we have identified 54 new young stars. Furthermore, we’ve updated the radial velocities of 74 young stars.

Stars from the literature

For the remaining stars in Table 3, we’ve resorted to previously published values. For instance, we have not reanalysed the radial velocities of any of the Wolf-Rayet stars, for which the radial velocities need to be derived from a stellar atmosphere model, and the uncertainty is dominated by the modeling. Thus, re-derived spectra would not improve the radial velocity (F. Martins, private comm.). Furthermore, we’ve adopted the radial velocities reported in Yelda et al., 2014 for stars which we either did not observe, or when our spectrum is too poor to derive a radial velocity, but does not contradict the classification. Stars that are part of the continuous monitoring of the central arcseconds

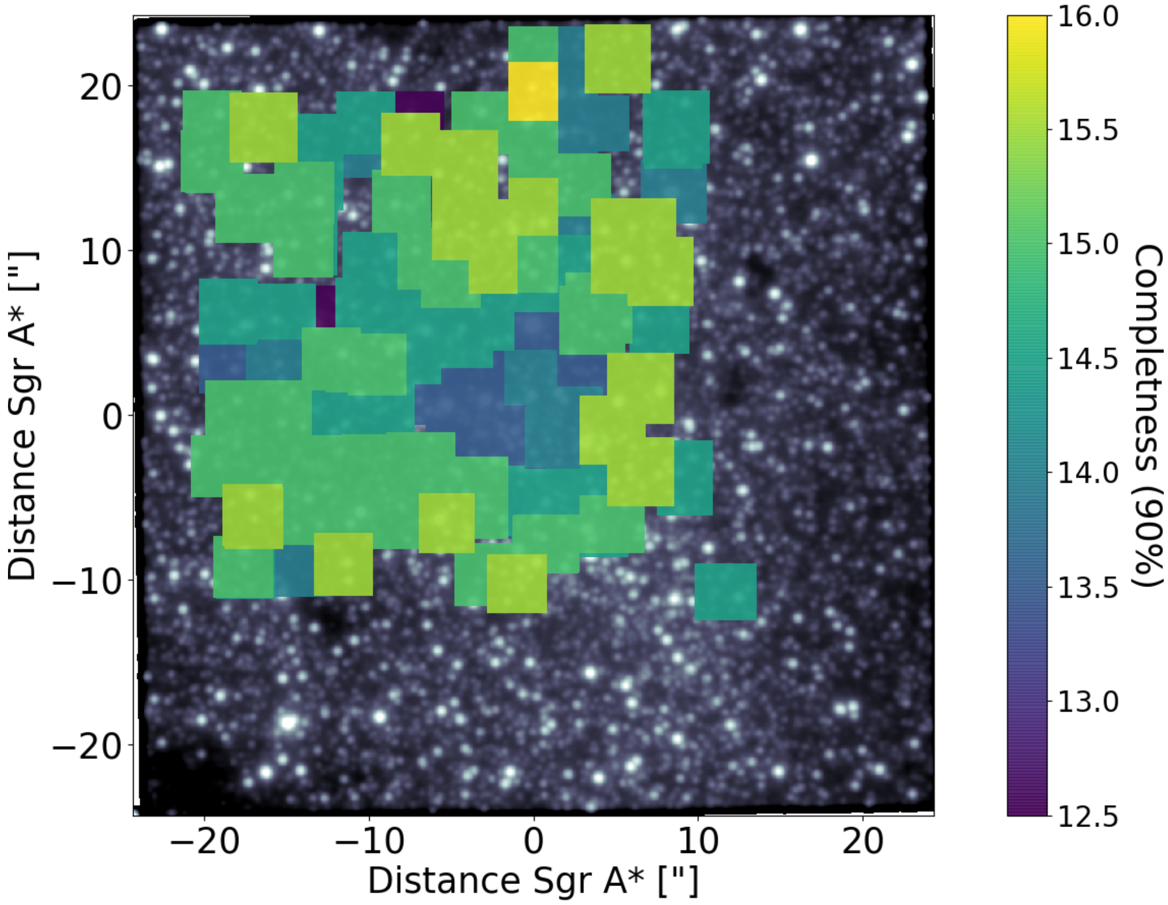

Figure 5.2: 90% Completeness estimate based on cross-referencing spectropically identified stars with the catalogue by Trippe et al., 2008. We very conservatively assume that our completeness estimate is uncertain by ∼1 magnitude. See text for details.

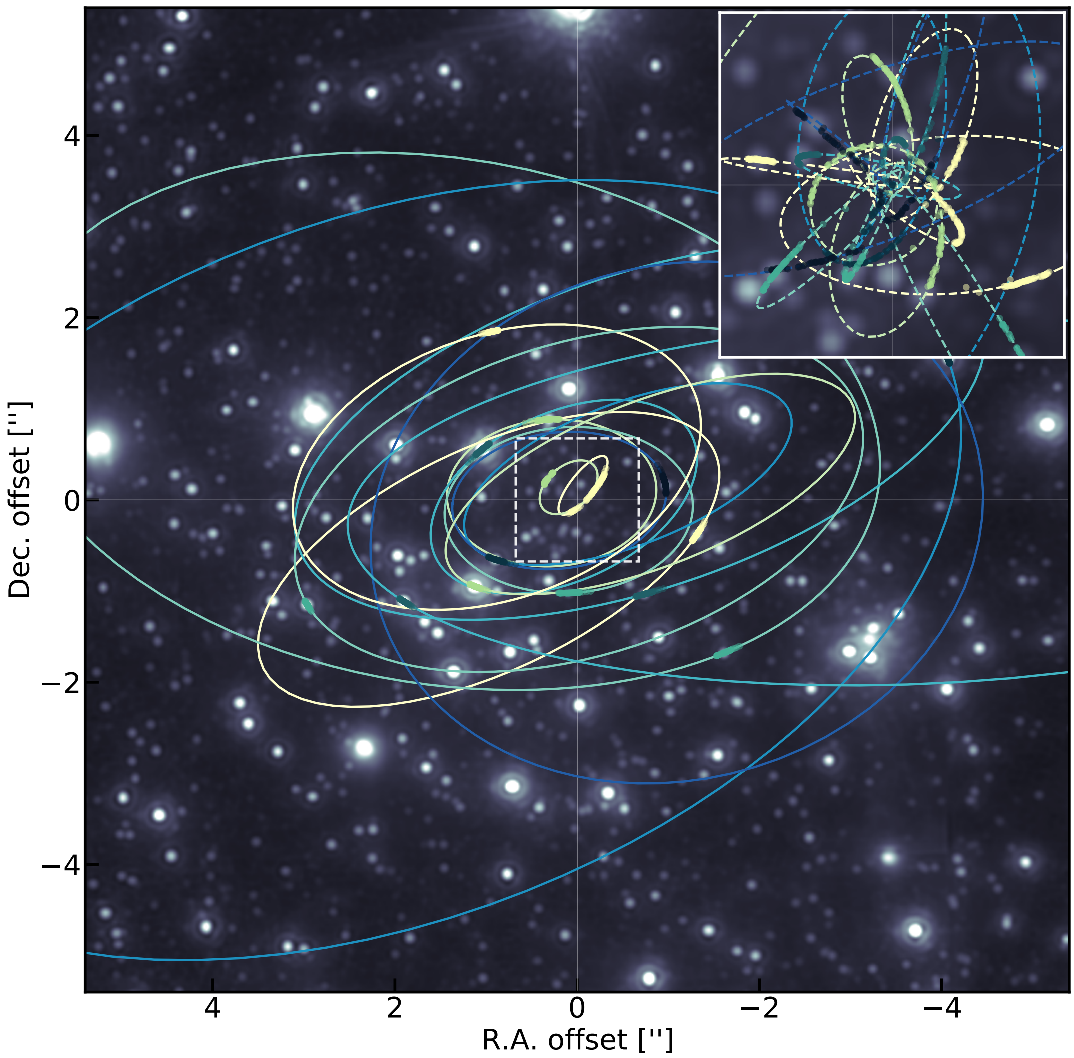

Figure 5.3: Orbits and astrometric measurements of the 35 young stars in the Galactic Center. The large figure shows the orbits of the outer young stars. The outer stars belong to the clockwise disk. The inset shows the “Sgr A* star cluster” of the inner most young stars which are on preferentially eccentric, and random distributions.

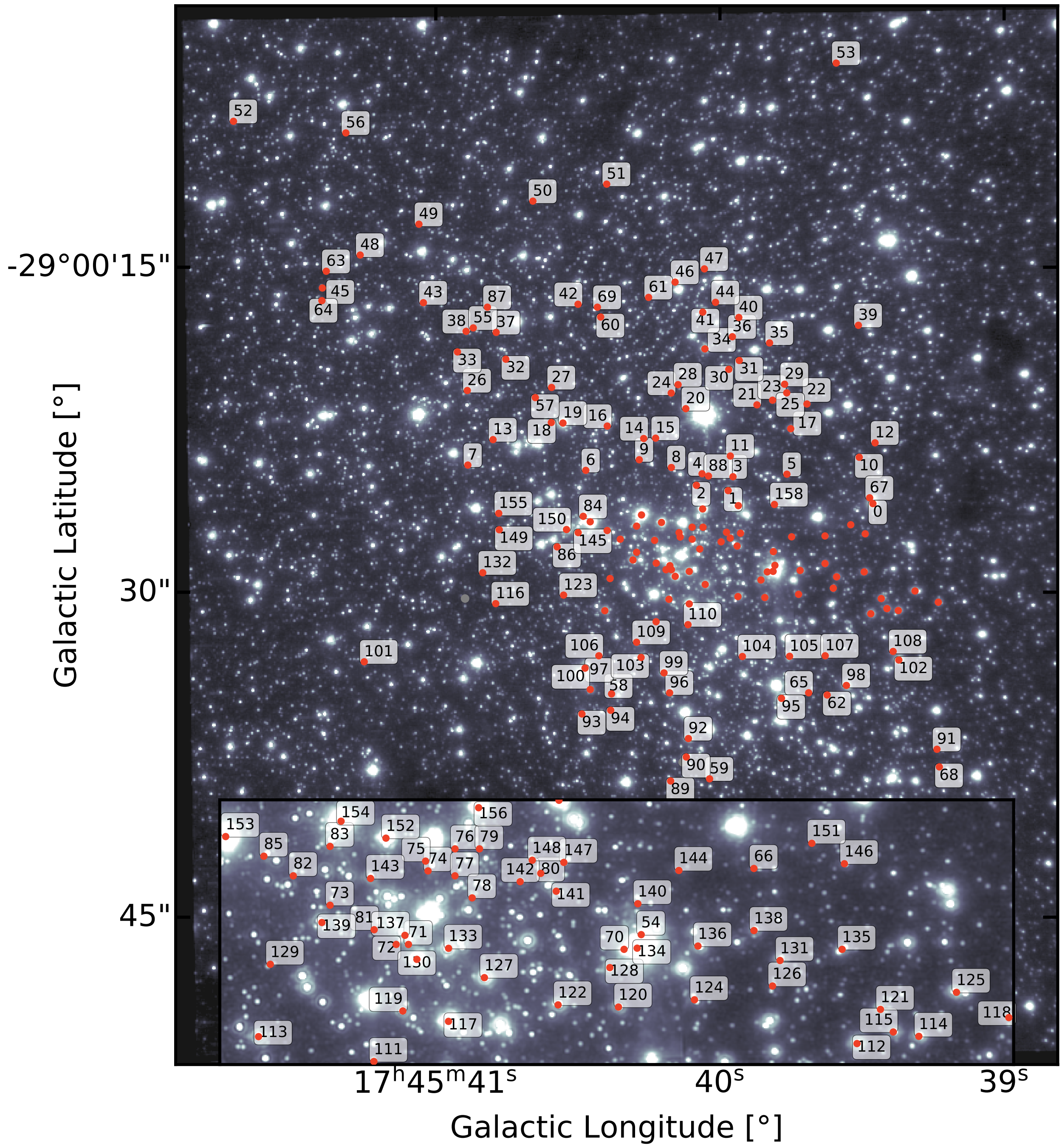

Figure 5.4: Lookup map of young stars without accelerations: Young stars used in this study. The number indicated next to star corresponds to the row index in column # in Table 3.

of the Galactic Center and we either use the radial velocity published in Gillessen et al., 2009, Gillessen et al., 2017 or an updated value.

5.3.3 Stars in the literature removed from star list

For five stars reported in Yelda et al., 2014 we identified CO-bandheads in the spectra. This may be the result of confusion, for instance our spatial resolution may not suffice to disentangle a young star next to a bright old one. Nevertheless, we've removed the stars from our list. These are: S1-19, S4-287, S7-36, S10-34, and S13-3.

5.4 Analysis: Theory and numerical experiments

The initial conditions of a test particle in a fixed gravitational potential have six degrees of freedom, corresponding to the initial position and velocity of the particle. It is standard practice to express those in terms of orbital elements. One choice are the classical Keplerian parameters: the semi-major axis a, the eccentricity e, the inclination i, the longitude of the pericenter ω, the position angle of the ascending node Ω, and the epoch of pericenter passage t_P.

In order to determine these six numbers, one needs to measure six dynamical quantities. From multi-epoch astrometry in the GC, one can determine the on-sky position (x, y) and proper motion (v_x, v_y) of the object. Thus, one needs two more dynamical quantities in order to determine an orbit. From spectroscopy one can get the radial velocity of a star (v_z). The missing z-coordinate is not accessible directly at the GC distance of $\sim$8.25 kpc (GRAVITY Collaboration et al., 2019b), but it can be determined by measuring an acceleration, either by detecting curvature in the on-sky orbital trace, or by a change in radial velocity.

For stars with (at least) six dynamical quantities measured, standard fitting techniques uniquely determine the orbital elements, see for example Gillessen et al., 2009; Gillessen et al., 2017. If only five dynamical quantities are known, in almost all cases one lacks an acceleration measurement, i.e. information on z. Yet, some constraints on the orbital parameters can be constructed. For example the angular momentum vector direction can be limited to lie within a one-dimensional half large-circle across the sphere of possible orientations (Paumard et al., 2006; Lu et al., 2009). We call such stars "5D-constrained".

The key finding of these earlier works was that one can find a specific direction of the orbital angular momentum vector, which is compatible with a large number of the 5D-constrained young stars in the GC. The simplest explanation for that finding is that these stars rotate in a common disk. This interpretation was independently confirmed by stars in the young star sample, for which full orbits have been determined (Gillessen et al., 2009; Yelda et al., 2014; Gillessen et al., 2017).

The probability distribution of the orbital angular momentum vector for a given star depends on the assumptions one makes on the missing information, i.e. the z-coordinate.

Hence the exact dynamical structure (and thus the significance of certain features such as disks and warps) of the young star sample depends on the choice of the z-prior.

In the following section we first discuss the method used in this paper (subsection 5.4.1), after which we discuss how the significance of a kinematic feature is assessed (subsection 5.4.2). Than we discuss different priors that were used in the past and introduce a new z-prior (subsection 5.4.3). In subsection 5.4.4 we compare the different z-priors.

5.4.1 Determining the distribution of angular momentum vectors of the 5D-constrained stars

In order to estimate the smoothed distribution of angular momentum vectors of the 5D-constrained stars, we use the following procedure:

1. Generate 10000 realizations of each star, where the x, y, v_x, v_y and v_z coordinates are sampled from the respective measured values and errors, assuming Gaussian distributions. The z coordinate is sampled from the chosen z-prior distribution, see subsection 5.4.3.

2. Compute the orbital elements corresponding the phase space coordinates for each of the 10000 realizations of each observed star.

3. Like in Yelda et al., 2014, we compute the 3^{rd}-neighbour density of angular momentum vector directions at the desired grid points over the unit sphere spanned by (i, Ω) for each of the 10000 realizations of the sample stars.

4. The mean and standard deviation at each grid point define the measured density and uncertainty of the angular momentum vector direction.

The 3^{rd}-neighbour density was introduced by Yelda et al. (2014) as a computationally efficient way to obtain a smooth map from a discrete distribution. For its calculation one needs to find at each map point the smallest radius which contains seven stars.

5.4.2 Determining the null hypothesis distributions

The null hypothesis we test is an isotropic cluster, since an old, relaxed distribution should reach asymptotically that state (Bahcall and Wolf, 1976; Pfuhl et al., 2011).
The procedure to generate an isotropic cluster is described in Schödel et al. (2003):

1. Sample the inclination i and the longitude of the ascending node Ω isotropically on a sphere.

2. Sample the argument of pericenter uniformly from $\omega \in [0°, 360°[$.

3. Draw the semi-major axis from a power law distribution $\frac{dN}{da} \propto a^{-\beta}$. We choose $\beta = 2$ to resemble the observed distribution of stars. We sample a from 0.2 arcseconds to 40 arcseconds, in order to match the observed scales.

4. Sample the eccentricity such that $\frac{dN}{de} \propto e$, i.e. a thermal distribution of eccentricities.
5. Compute the true anomaly by assuming a uniform distribution of time points along the orbit: $t_{orbit} \in [0, P_{orbit}[$. This corresponds to a uniform mean anomolay distribution.

With this recipe, we generate a cluster containing 100′000 stars and calculate the phase space coordinates. We then discard the z coordinates and redraw them from the z-prior distribution. From this cluster we choose N stars, as many as our data sample contains, taking into account the observational biases from the fields covered. This yields a mock data set that we analyze the same way as the real data in subsection 5.4.1. This procedure is repeated 10000 times, creating 10000 mock data sets from which we calcuate the mean and standard deviation in each pixel.

5.4.3 Constraining the z-values

In the above analysis, one needs to choose what to assume for the distribution of z-values. A natural upper limit on $|z|$ is obtained by imposing that the orbits need to be bound. This yields a maximum z-value as a function of projected 2D distance from the massive black hole:

$$|z_{\max}| = \sqrt{\left(\frac{2GM_\bullet}{v_x^2 + v_y^2 + v_z^2}\right)^2 - R^2}, \tag{5.1}$$

where $R = \sqrt{x^2 + y^2}$ is the 2D projected radius and $M_\bullet$ the mass of the MBH. We use this upper limit when sampling the z coordinate and redraw the coordinate in case z was sampled outside the allowed bounds.
Further, 5D-constrained stars yield an upper limit on the acceleration $a_{\max}$. This corresponds to a minimum $|z|$ value

$$|z_{\min}| = \sqrt{\frac{GM_\bullet}{a_{\max}} - R^2}. \tag{5.2}$$

For the distribution of z-values between the extreme values two choices have been made in the past:

- The so-called "stellar cusp prior" (Bartko et al., 2009), which assumes a power-law distribution of z-values, based on the observed power-law density profile of the stellar cusp in the GC (Genzel et al., 2003b; Schödel et al., 2009).
- A "uniform acceleration prior" (Lu et al., 2009; Yelda et al., 2014), where the z-values are computed from a uniform distribution of accelerations up to the maximum allowed acceleration for the given projected distance of the star.

In the following we show that both these priors are not ideal and the inferred cluster structure does not recover with simulated isotropic one. We propose a third prior that mitigates the problems of the other two priors:

- The "isotropic cluster prior" which directly evaluates the probability distribution function of an isotropic cluster for each star. Since the probability distribution functions for isotropic cluster are analytically defined, they can be evaluated using the available observational data of each star. The difficulty lies in expressing the distribution function which are given in orbital elements, in phase space coordinates, in which our observations are obtained. We derive a procedure in section 5.4.3.

The choice of a certain prior implies choosing the corresponding null hypothesis against which the dynamical structure can be tested. Thus, the prior choice necessarily introduces some prejudice on what one believes the dynamical structure in GC is.
In the subsequent sections we present the three priors and investigate how well they reproduce an isotropic cluster, our null hypothesis. We compare the resulting cluster with the input cluster. The results are summarized in Figure 5.7.

The stellar cusp prior

Bartko et al., 2009 introduced the stellar cusp prior. The distribution of z coordinates is given by:

$$P(z|x_{obs}, y_{obs}) \propto (x_{obs}^2 + y_{obs}^2 + z^2)^{-\frac{\beta+1}{2}} \tag{5.3}$$

where $\beta = 2$ the power-law index of projected density profile of the cusp in the GC $dN/dR \propto R^{-\beta}$ (Genzel et al., 2003b) and x_{obs}/y_{obs} stand for the observed star positions.
The simulated cluster generated with the stellar cusp prior correctly captures the input distribution of eccentricities and also the distribution of semi-major axes is reproduced closely. However, the argument of pericenter ω does not follow a uniform input distribution, and high inclinations are favored. This results in a boxy distribution of stars, with an overdensity towards the center (see Figure 5.7).
The reason for this behaviour lies in the distribution of eccentricities. While the positions of the stars geometrically follow a power law slope, the probability for z given R_{obs} depends on how much the individual star plunges towards the black hole. When one knows the distribution of eccentricities and the distribution of semi-major axes, this "plunging in" is given by the observed velocity vector $\vec{v}$, a piece of knowledge that is neglected in this prior.

The uniform acceleration prior

The uniform acceleration prior has first been used by Lu et al., 2009 and is constructed by drawing the acceleration $a_S(R)$ uniformly in the possible range, i.e. $a_S(R) \in \left[0, \frac{GM_\bullet}{R^2}\right]$. The maximum value for $a_S(R)$ is reached for $z = 0$. The $z-$coordinate is then obtained from

$$z = \sqrt{\left(\frac{GM_\bullet R_{obs}}{a_S(R)}\right)^{2/3} - R^2}\ . \tag{5.4}$$

The cluster of the uniform acceleration prior does not reproduce the linear distribution of eccentricities and produces a tail of high semi-major axes orbits. Similar to the stellar

cusp prior the argument of periapsis ω is not uniformly sampled, but shows an angular dependence. Furthermore, the orbital nodes are biased towards high values, but without the clear concentration towards $\cos(\phi) = \pm 1$ of the stellar cusp prior. Inspecting the distribution of z values, one can make out a zone of avoidance towards z values close to zero. Nevertheless, at least perceptually, the uniform acceleration prior seems to fare slightly better as the distribution of z values is more symmetrical than that for the stellar cusp prior.
The reason for the mismatch from an isotropic cluster lies again in the eccentricity distribution $\frac{dN}{d\epsilon} \propto \epsilon$. Since most orbits lie on eccentric orbits there is a high chance of observing a star far away from the black hole, where the acceleration is low. Therefore, the distribution of acceleration is not uniform but varies radially and depends on the velocity $\vec{v}$ of the star.
For both, the stellar cusp and the uniform acceleration prior, the reason that the prior clusters deviate from that of an isotropic cluster is that the priors only depend on the projected radius $R_{\text{projected}}$ and do not take the velocity of the star into account. To overcome this and to include the velocity, we introduce a new prior which we call the isotropic cluster prior.

The isotropic cluster prior

In subsection 5.4.2, we described the numerical recipe to sample orbital elements for an isotropic cluster from the respective probability distribution functions (PDFs). Since the PDFs are independent, the combined PDF describing an isotropic cluster is simply the product of the individual distributions:

$$\begin{aligned}\mathrm{PDF}_{\mathrm{iso-clus.}} =& \mathrm{PDF(a)} \cdot \mathrm{PDF(e)} \cdot \mathrm{PDF(i)} \cdot \\ & \mathrm{PDF}(\Omega) \cdot \mathrm{PDF}(\omega) \cdot \mathrm{PDF(M)} \\ =& \frac{p-1}{a_{min}} \left(\frac{a}{a_{min}}\right)^{-p} \cdot 2\sin(i) \cdot \\ & \mathcal{U}_{[0,2\pi[}(\Omega) \cdot \mathcal{U}_{[0,2\pi[}(\omega) \cdot \mathcal{U}_{[0,2\pi[}(M),\end{aligned} \tag{5.5}$$

where $\mathcal{U}$ stands for the uniform distribution on the respective interval. We need to express the known distributions of orbital elements as distributions of phase space coordinates. Effectively, we are thus interested in the correct coordinate transformation of the orbital element distributions to phase space coordinate distributions. Any probability distribution can be transformed to a different coordinate system by accounting for the volume filling factor:

$$\mathrm{PDF}_{\mathrm{sys1}} = |\det(\mathrm{Jac})| \cdot \mathrm{PDF}_{\mathrm{sys2}}, \tag{5.6}$$

where det(Jac) stands for the determinant of the Jacobian matrix of the coordinate transformation. In the case of the orbital element coordinate transformation, the Jacobian

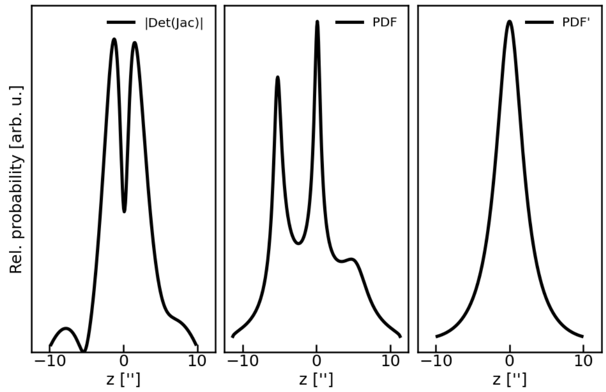

Figure 5.5: Left to right: Determinant of Jacobian (|det(Jac)|), orbital element probability distribution function ($PDF_{\rm iso-clus.}$) and coordinate transformed probability distribution function ($PDF'_{\rm iso-clus.}$) of the star E29 as function of z distance. The transformed $PDF'_{\rm iso-clus.}$ is the product of determinant and the isotropic cluster PDF. Note that the y-axis for each plot is different.

matrix consists of the 36 partial derivatives of the coordinate transforms. Once the analytical form of the determinant has been determined, we obtain the analytical expression for the z distribution of stars in an isotropic cluster:

$$\begin{aligned}\mathrm{PDF}'_{\rm iso-clus.}(\mathrm{z}|\mathrm{pc}_{\rm obs}) =& |\det(\mathrm{Jac}(\mathrm{a}(\mathrm{z}|\mathrm{pc}_{\rm obs}), \dots)| \cdot \\ & \mathrm{PDF}_{\rm iso-clus.}(\mathrm{a}(\mathrm{z}|\mathrm{pc}_{\rm obs}), \dots),\end{aligned} \tag{5.7}$$

where $\mathrm{pc}_{\rm obs}$ stands for the observed phase space coordinates x_{obs}, y_{obs}, vx_{obs}, vy_{obs}, and vz_{obs}. We implement the determinant in C, which allows very fast evaluation of this prior. Figure 5.5 shows an example of the probability distribution of the z values for the star E29 (Paumard et al., 2006) with a projected distance of $\sim 4.3\,''$ and velocity modulus of $\sim$ 280 km/s. It is clear that without the determinant the transformed PDF would have been wrongly estimated. With the determinant the PDF is symmetric around $z = 0$.

5.4.4 Comparison of the different priors

In this section we compare the two different priors that have been used in the past with the isotropic cluster prior. Figure 5.6 compares the z-probability distribution functions for the three priors and the example star E29. For the stellar cusp prior and the isotropic cluster prior the analytic expression are given in Equation 5.3 and Equation 5.7. For the uniform acceleration prior we estimate the PDF by making a histogram of the z-values derived from the prior (see Equation 5.4).

Because the z-PDFs are different, they will lead to different z distributions. To illustrate the effect on our null hypothesis of an isotropic cluster we conduct the following numerical experiment:

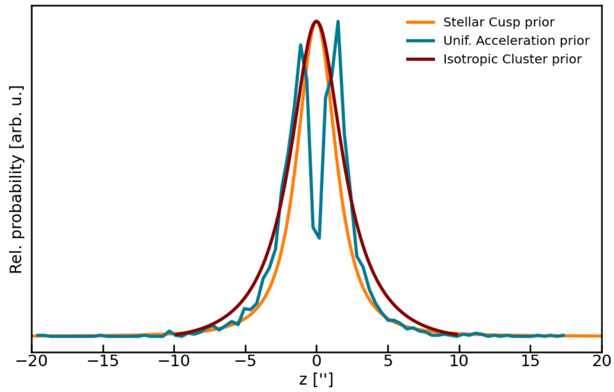

Figure 5.6: Comparison of the probability distribution function of the z values for the star E29: The grey line shows the PDF of the stellar cusp prior (Equation 5.3), the blue line shows the histogram of z-values sampled according to the uniform acceleration prior (Equation 5.4) and the dark red line shows the isotropic cluster prior (Equation 5.7). For better comparison we have normalized the mode of the respective distributions to one.

1. Draw 10000 stars from an isotropic distribution according to the recipe detailed in subsection 5.4.2.

2. Discard the z-coordinate of each star.

3. Re-draw a z-coordinate for each star from its respective prior distribution function.

We call the resulting cluster the "prior cluster", in which each star has new z position. We plot the resulting z vs. x position in the top row of Figure 5.7 for each of the three priors as well as the input isotropic cluster. Plotting the z vs y coordinate yields a qualitatively identical plot. It is evident that the isotropic cluster prior best reproduces the input cluster.

To better compare the respective prior clusters with the input orbital elements we recompute the orbital elements of each star using the newly determined z-position. Figure 5.7 compares the histogram of the input orbital elements with those computed from the re-sampled stars.

The isotropic cluster prior best reproduces the input orbital element distribution, and specifically it does not yield biased distributions of i and Ω which are the parameters we are interested in. This is in contrast to the stellar cusp prior and the uniform acceleration prior. This behavior of the priors was discovered in previous studies (Bartko et al., 2010; Yelda et al., 2014), and both studies tried to de-bias their study by subtracting the mean bias from the density histogram. Our unbiased prior makes this de-biasing step unnecessary. We conclude that the isotropic cluster prior correctly maps the input isotropic cluster on a self-similar realization of itself. We therefore achieve a meaningful null-hypothesis: How different is the observed angular momentum distribution to that of an isotropic cluster.

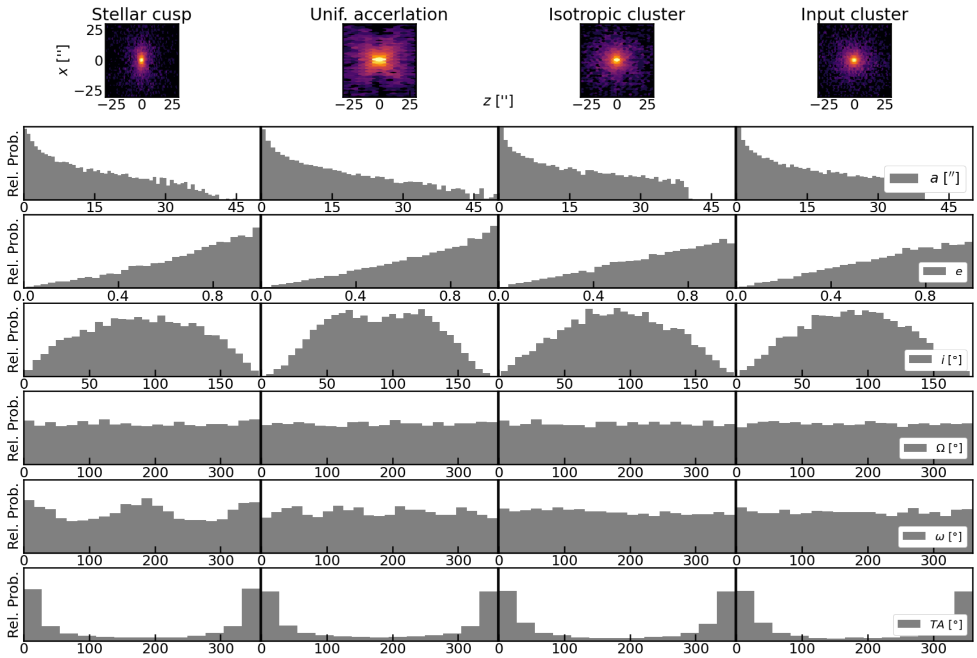

Figure 5.7: Distribution of orbital elements of different *prior-clusters*, draw from the stellar cusp prior, the uniform acceleration prior, the isotropic cluster prior, and the input isotropic cluster. The top panel shows the z vs. x distribution of the different prior clusters. See **??** for details.

We note that the isotropic cluster is not the "best" prior to determine the angular momentum distribution of the young stars in the GC. Given that the presence of at least one star disk is undisputed, a "stellar disk prior" would be more suited to determine the presence of the disk. Such a prior would however change the null-hypothesis to "How different is the observed star distribution to the assumed stellar disk?" and is therefore not suited to find new kinematic features. Once the determinant of the volume filling factor is determined the construction of such a "disk prior" is trivial, and follows the method in section 5.4.3, with the suitable changes to Equation 5.5.

5.4.5 Discrepancy between the Bartko et al. 2009 and Yelda et al. 2014 works

Both Bartko et al., 2009 (abb. Bartko09) and Yelda et al., 2014 (abb. Yelda14) agree on the presence and orientation of the clockwise disk, but the significance of the warp is disputed. This is surprising: while Yelda14 presented an improvement in all relevant numbers (number of stars, number of constrained stars, number of determined orbits) compared to the Bartko09 sample, the improvement is gradual. For example, the total number of young stars in the sample increased by 18 (from 98 to 116), but the sample includes all 98 young stars from Bartko09.

In the following we try explain the apparent discrepancy between the works. For this, we use the data set published in Yelda14, and use exclusively the uniform acceleration prior. We will show that the discrepancy between the work is not due to error, and is dominated by the different definitions of the significance.

Figure 5.8 demonstrates that we can reasonably reproduce the Yelda14 results. The histogram has been normalized to match those of the bounds of the histogram of Yelda14 (Figure 10 in their work) and we use the same colormap and projection. There is broad agreement between the figure presented in Yelda14 and our reproduction[1].

Bartko14 compute the pixel-significance in the same manner as we do:

$$\sigma_{\text{pixel}} = \frac{s_{\text{pixel,obs.}} - < s_{\text{pixel,sim.}} >}{RMS(s_{\text{pixel,sim.}})} \tag{5.8}$$

where $s_{\text{pixel,obs}}$ stands for the pixel value in the observed histogram and $s_{\text{pixel,sim.}}$ stands for the simulated pixels of the mock observations. This is based on the standard approach described in Li and Ma, 1983.

In contrast, Yelda14 use a peak-significance instead of a pixel-significance:

$$\sigma_{\text{peak}} = \frac{s_{\text{peak,obs.}} - < s_{\text{peak,sim.}} >}{RMS(s_{\text{peak,sim.}})} \tag{5.9}$$

[1] However, minor discrepancies exist. For instance, the faint feature next clockwise disk is more "fuzzy" in our reproduction. We speculate that this is most likely due different treatment of unbound stars in the Monte-Carlo simulations, which we do not re-sample. Further, the strength of the smoothing seems decreased compared to Yelda14.

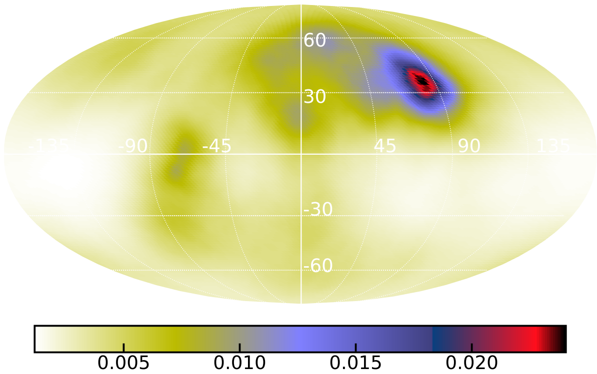

Figure 5.8: Comparison of the histogram of orbital nodes calculated in this work and presented in Figure 10 of Yelda et al., 2014. We have normalized the histogram to the same minimum and maximum values, see text for details.

where $s_{\mathrm{peak,obs.}}$ stands for the observed peak value of a feature, and $s_{\mathrm{peak,sim.}}$ stands for the respective peak values in the simulations. In order to account for the biases introduced by the observations and the uniform acceleration prior, they calculate the peaks in bins of 20° in latitude. Figure 5.9 shows the difference in reported significance between the two methods for the radial slice ranging from 3.2″ to 6.5″. σ_{peak} is much reduced compared to σ_{pixel} and we recover the two seemingly competing conclusions found in Bartko09 and Yelda14: Using the pixel significance we find a significant feature at $\sim 6\sigma_{\mathrm{pixel}}$ (see Figure 11 of Bartko09). In contrast, using the the peak significance σ_{peak} no clearly significant feature is detected.

In the following we will now explore the differences between the two definitions of the significance. Using a set of 2000 mock observations, we calculate the feature with the highest significance for each of the mocks. The histogram of these significances is shown in Figure 5.10. The peak significance is much more conservative, with the mode of the significance corresponding to $\sim 2\sigma_{\mathrm{peak}}$, while significances of $\sim 6\sigma_{\mathrm{pixel}}$ are routinely observed for the pixel significance. Despite this, the histograms are very similar, and seem to be merely shifted realizations of each other.
This becomes even clearer when plotting the respective peak significance against the pixel significance of each mock observation (Figure 5.11). There exists a linear relation between the two definitions (indicated by the trend-line). The horizontal dashed line indicates the maximum significance σ_{pixel} found in the upper panel of Figure 5.9 ($\sim 5.3\sigma$), and the vertical line shows the projection onto $\sigma_{\mathrm{peak}} = 3$ which is consistent with the lower panel of Figure 5.9.
The differences between the to methods are interesting, and is clear from Figure 5.11 that the significance σ_{pixel} is inconsistent with confidence ranges associated with typical

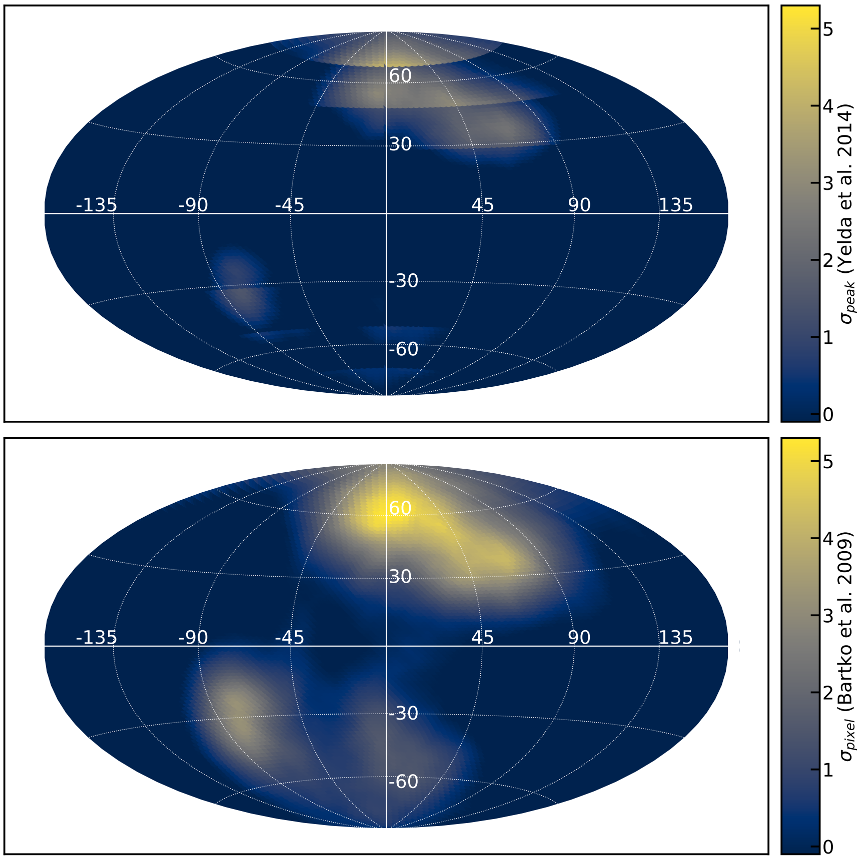

Figure 5.9: Difference of the between significance using the pixel and peak siginifance used in Bartko et al., 2009 and Yelda et al., 2014 for the radial slice ranging from 3.2″ to 6.5″. The data used is taken from Yelda et al., 2014, and we use the uniform acceleration prior.

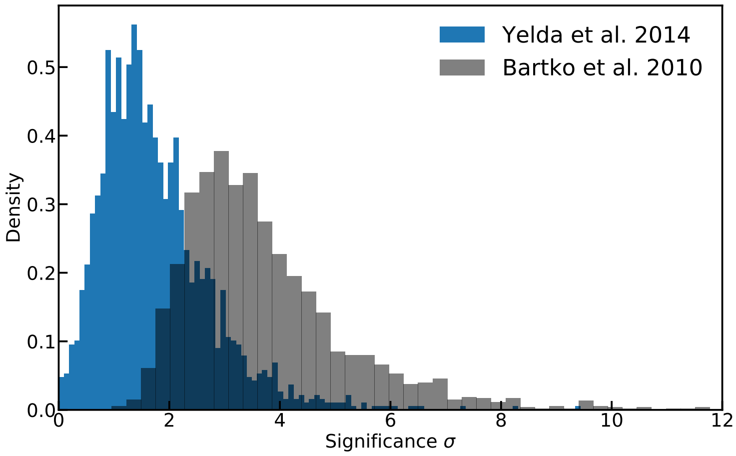

Figure 5.10: Histograms of the highest value of the significance calculated for each mock observation. The black histogram shows the pixel significances σ_{pixel} (Bartko et al., 2009, black) and blue histogram shows the peak significance σ_{peak} (Yelda et al., 2014), respectively.

Gaussian σ. This is not a new problem, and the difficulty of finding confidence ranges of Monte Carlo simulations is commonly discussed in other astronomical observations (see for instance section 4.4 in H.E.S.S. Collaboration et al., 2018 and Stewart, 2009). However, as will be shown in the next section, the significance of the features discussed in this paper are so large that the difference effectively does not matter in our case.

5.5 Results: Application to data

5.5.1 Angular momentum distribution of the young stars in the Galactic Center

In the following section we discuss the angular momentum distribution of young stars in the GC. Figure 5.12 shows the overdensity of angular momentum for six projected radius slices. The density maps are computed using a k-nearest neighbour smoothing (subsection 5.4.1). For stars with determined orbits we sample 100 realizations of the angular momentum vector from the respective uncertainty estimates. For stars without determined orbits, we sample 100 z values from the isotropic cluster prior, and 100 realizations of the measured phasespace vector from the respective uncertainties. We bin our young star samples in six bins with increasing projected distance from the black hole.

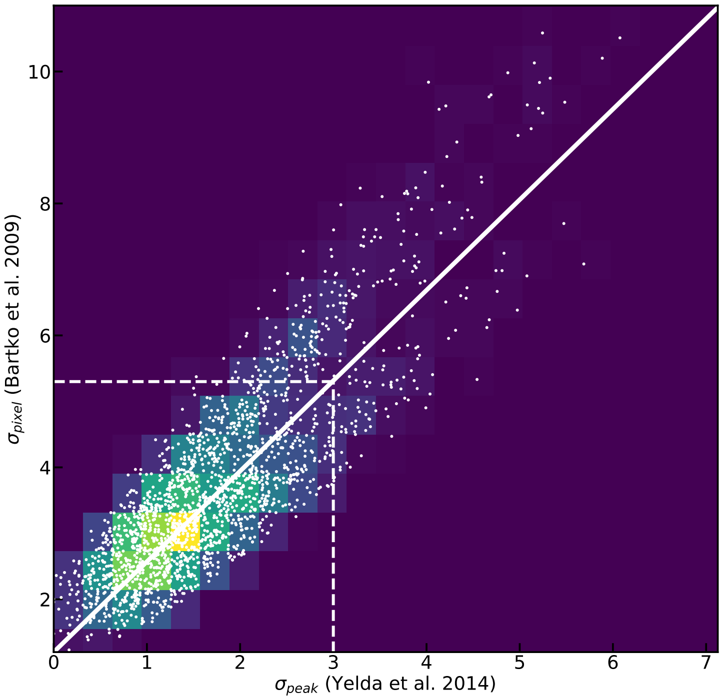

Figure 5.11: 2D histogram of the peak and the pixel sigifcance calculated for 2000 mock observations. The white dots indicate the individual signifcance values, the thick white line indicates the trend. The horizontal dashed line indicates the peak value of σ_{pixel} found in Figure 5.9, and the vertical dashed line presents the projection again consistent with the respective σ_{peak} in Figure 5.9.

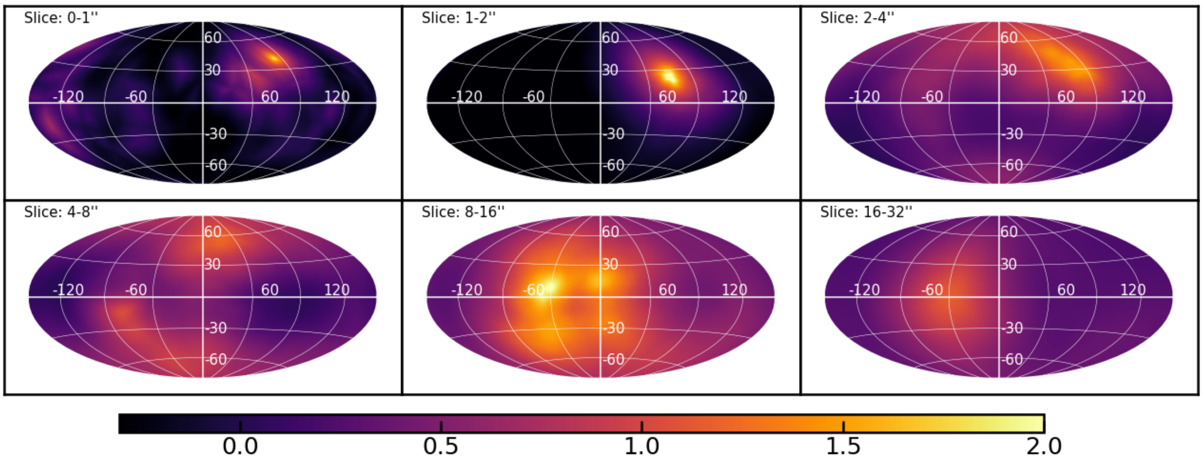

Figure 5.12: Log(significance) of the overdensity of the angular momentum distribution as function of projected radius slice, computed using the isotropic cluster prior. See text for details.

The inner region

Our updated star sample confirms the presence of a warped clockwise disk for stars in a region ranging from $\sim 1''$ to $\sim 4''$ (middle and right plot of top panel in Figure 5.12). In this inner most region, most stars are aligned coherently. We call this the inner part of the warped clockwise disk. For the radial bin ranging from $2''$ to $4''$, the inner part of the clockwise disk is less dominant and starts to change smoothly to the outer part of the warped clockwise disk, present in the intermediate region, discussed in the next section.

The intermediate region

For the radial bin ranging from $4''$ to $8''$ (bottom left panel in Figure 5.12 and Figure 5.13), no single disk structure dominates the density map. Bartko et al., 2009 and Bartko et al., 2010 found an overdensity for their sample of 30 stars in the $3.5''$ as to $7''$. They interpret this as a warped extension of the clockwise disk – which we call outer part of the warped clockwise disk. The significance of the outer part of the warped clockwise disk was estimated at $\sim 6\sigma$ using the stellar cusp prior (Bartko et al., 2009). However, this outer part was disputed by Yelda et al., 2014, who did not find this feature to be significant using the uniform acceleration prior. Figure 5.13 shows the significance of our angular momentum distribution for the projected distance slice $4''$ to $8''$ determined using the isotropic cluster prior. We confirm the outer-part of the warped clockwise disk at a significance of $\sim 16\sigma$. Further, we find the onset of the counter-clockwise disk at a significance of $\sim 10\sigma$ reported by Genzel et al., 2003; Paumard et al., 2006; Bartko et al., 2009 in the this intermediate region.

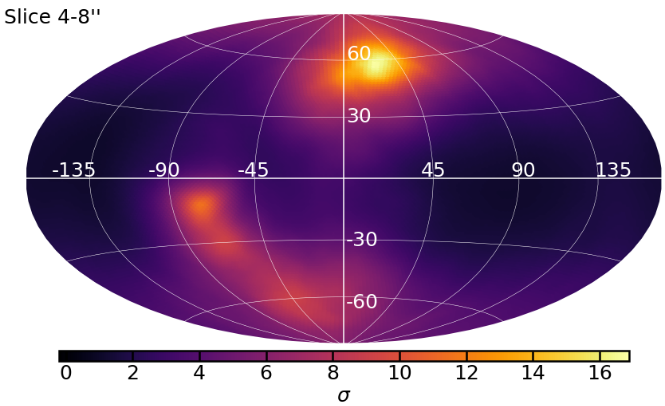

Figure 5.13: Significance of the over-density of angular momentum for stars at a projected distance from 4″ to 8″. The figure is identical to the bottom-left most panel of Figure 5.12, however the color scaling is adapted and in linear scale.

The outer region

For projected distances larger than 8″ we find three prominent features (bottom middle panel in Figure 5.12 and Figure 5.14). First, we confirm the an overdensity of angular momenta at $(\phi, \theta) =\sim (0°, 30°)$ significant at $\sim 35\sigma$. This feature was first reported in the outer most radial bin studied by Bartko et al., 2009 and attributed to the clockwise warped disk. We call this feature the first outer filament. Second, we find the outer continuation of the counter-clockwise disk with similar significance ($\sim 35\sigma$). Most prominently, we find a previously un-reported feature at $(\phi, \theta) =\sim (50°, 20°)$ at very high significance of $> 100\sigma$. We call this feature the second outer filament.

5.6 Results: Estimating the disk membership fraction

In the previous section we have found various significant features when comparing the observed young star distribution with an isotropic cluster. Specifically we have found:

1. The well known inner clockwise disk system ranging from radii $\sim 1''$ to $\sim 4''$. This feature is located at $(\phi = 73°, \theta = 34.5°)$.

2. An extension of the clockwise disk consistent with the disk-warp reported in Bartko et al., 2009 ranging from radii $\sim 4''$ to $\sim 8''$. This feature is located at $(\phi = 23.3°, \theta = 55.6°)$.

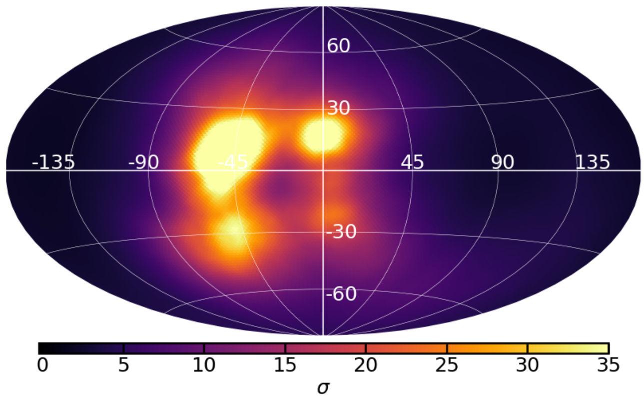

Figure 5.14: Same as Figure 5.13 projected distance from 8″ to 16″, again with adapted color scaling and in linear scale.

Name	$\theta_{overdensity}$	$\phi_{overdensity}$
Inner warped clockwise dis	73.1°	34.5°
Outer warped clockwise disk	23.3°	55.6°
Counter-clockwise disk	-47°	-30.0°
First outer filament	0.0°	16.0°
Second outer filament	-44.2°	11.5°

Table 5.1: Angular momenta direction for different kinematic features in the Galactic Center.

3. We find the counter-clockwise disk located at ($\phi = 127.0°, \theta = -30.0°$) ranging from $\sim 4''$ to $\sim 16''$.

4. A first outer overdensity located at ($\phi = 0.0°, \theta = 16.0°$). This was identified with the outer extension of the warped clockwise disk in Bartko et al., 2009. We call this feature the first outer filament.

5. A previously undetected second outer overdensity located at ($\phi = -44.2°, \theta = 11.5°$) which we call the second outer filament.

The location of these overdensity features is tabulated in Table 5.1. In order to assess the disk membership of each star to one of the specific features, we numerically integrate the star's PDF to calculate the Bayesian evidence. We do so using the statistical software package dynesty (Speagle, 2020; Skilling, 2004; Skilling, 2006a; Skilling, 2006b). Explicitly, we sample the likelihood function in phase space coordinates, which allows sampling only

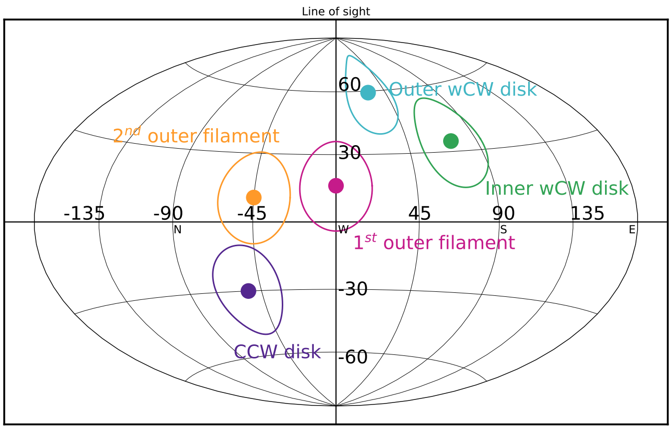

Figure 5.15: Illustration of the location and width of the disk priors assumed, tabulated in Table 5.1.

the allowed part of phase space. We assume a flat prior on the z coordinate of each star, constrained only by the maximum z-distance allowed for a bound orbit. Further, we assume a flat prior on the remaining phase space coordinates with width equal to four times the standard deviation of each coordinate expectation value. Explicitly, we integrate the following likelihood function:

$$\begin{aligned} \log L_{\text{model}} &= \log L_{\text{disk}} + \log L_{\text{star}} \\ &= -0.5(d(i_{\text{disk}}, \Omega_{\text{disk}}, i(x, \dots), \Omega(x, \dots))^2/\sigma^2_{\text{disk}} \\ &\quad + \sum_n (x_{n,obs} - x_i)^2/\sigma^2_{x_n,obs}), \end{aligned} \tag{5.10}$$

where $d(i_{disk}, \Omega_{disk}, i(x, \dots), \Omega(x, \dots))$ stands for the spherical cap distance[2] from the disk angular location $(i_{\text{disk}}, \Omega_{\text{disk}})$, computed for each sample of the phase space coordinates (x, y, z, vx, vy, vz). σ_{disk} is the opening angle of the disk, which we set to 20° for all features. We illustrate the disk priors in Figure 5.15.

While we sample z from a flat prior, including the first summand in Equation 5.10 implicitly assumes a Gaussian prior on the disk location. We can define the likelihood of a star without the disk prior:

$$\begin{aligned} \log L &= \log L_{\text{star}} \\ &= \sum_i (x_{i,obs} - x_i)^2/\sigma^2_{x_i}. \end{aligned} \tag{5.11}$$

Because we integrate the same phase-space (pc) prior volume for each star, the log evidence evaluates to the same value $\int \log L_{\text{star}}\, d\vec{pc} = -5.8$ for each star. For stars with orbital

[2] i.e. the Haversine distance

solutions it suffices to sample i and Ω. Equation 5.10 thus can be rewritten as:

$$\begin{aligned}\log L_{\text{model}} =& \log L_{disk} + \log L_{star} \\ =& -0.5 \times (d(i_{disk}, \Omega_{disk}, i, \Omega))^2/\sigma^2_{disk} + \\ & (i_{obs} - i)^2/\sigma^2_{i_{obs}} + (\Omega_{obs} - \Omega)^2/\sigma^2_{\Omega_{obs}}),\end{aligned} \tag{5.12}$$

The corresponding integral to Equation 5.11 for the stars with determined orbits evaluates to a log evidence of ~ -2.3.
By comparing the log evidence of L_{model} with the log evidence L_{star}, we can now define a disk membership probability for stars with and without orbital solutions. In order to establish disk membership, we require the difference of the log evidence to be smaller than 2. Essentially our procedure corresponds to a log-likelihood cut. However, it can also be viewed from a Bayesian model selection point of view where one compares evidence ratios: If the relative log evidence of L_{star} and L_{model} is smaller than 2, the star is consistent with belonging to the respective disk feature.

Table 4 and Table 6 report stars consistent with belonging to the clockwise disk and the inner warp, Table 5 reports the stars consistent with belonging to the counter-clockwise disk, Table 7 and Table 8 reports the stars consistent with being on the first and second outer filament. In section 5.7 and following sections we discuss the properties of each feature in detail.

5.6.1 Is it necessary to de-bias the disk fraction?

Yelda et al., 2014 have tried to estimated the true disk fraction by comparing the observed distribution against their simulations of an (approximate) isotropic cluster mixed with a stellar disk. This approach is correct under the assumption that the young stars not aligned with the disk are in an isotropic distribution. If the distribution of the not-aligned stars is not isotropic, for instance if several streams of stars exist, this approach underestimates the number of disk members. In subsection 5.5.1 we have shown that the young star population is significantly different from an isotropic star cluster, with different separation-dependent over-densities. We thus do not try do estimate the true disk fraction under the assumption of such a single disk + isotropic cluster model. Consequently, we can not tell the difference of a by-chance aligned star from that of a true disk member. Our disk fraction estimate is 100%, which should be understood as an upper limit. This does not mean that each star has to be a disk member, but that if it could be a disk member, it is counted as one. Further, we impose that each star is at most member of one disk. If a star could be associated with more than one disk, we count it to the feature with the lowest Δ evidence. Ultimately, our disk membership depends on the prior width of the features and the evidence cut. The width of the disk is part of the prior and thus also affects the derived posterior distributions. For all features we have chosen a width of 20°, and an evidence cut of 2. Optimally the width of the disk and the fraction of disk members would be inferred from the data too, which however requires a hierarchical approach which is beyond the scope of this work.

Disk Name	Number of Stars	Brighter/Fainter than $K_{mag} = 14$	IQR semi-major axes	IQR eccentricity
Inner clockwise disk	33	$24/9 = 2.7$	$1.6''$, $2.1''$, $2.7''$	0.4, 0.5, 0.6
Outer clockwise disk	13	$12/2 = 6$	$5.8''$, $7.0''$, $8.5''$	0.2, 0.4, 0.5
Counter clockwise disk	33	$21/12 = 1.8$	$5.4''$, $7.4''$, $12.1''$	0.4, 0.5, 0.6
First outer filament	37	$23/8 = 2.8$	$2.2''$, $5.6''$, $9.3''$	0.4, 0.6, 0.9
Second outer filament	36	$20/16 = 1.3$	$3.7''$, $8.8''$, $12.4''$	0.6, 0.7, 0.9

Table 5.2: Significant kinematic features of the young star population in the Galactic Center. Number of stars, luminosity, semi-major axis and eccentricity distribution.

5.7 Results: Properties of the young stellar components

Marginalizing the prior and likelihood function in Equation 5.10, we obtain posterior phasespace distributions for each star. For the stars that satisfy our disk membership criterion, we compute the orbital elements and obtain the posterior density estimate of orbital elements. Because all stars are independent from one another, we can combine the posterior estimates from each sample and obtain the joint orbital element distribution. Further, even for stars without orbital solution, we can plot a *likely* orbit given our observations and our prior assumption on the different angular momenta features. In subsection 5.5.1 these angular momenta features have been shown to be significant compared to an isotropic cluster (Table 5.1).
In the following we will present these likely orbits. We will discuss their posterior semi-major axes and eccentricity distributions as well as their luminosity distributions. In this discussion only the prior on the preferred direction of angular momenta and our observational data enters. We do not require stars to have certain projected distances or eccentricities. However, we require that all stars belong to at most one feature. The properties of the disk features are tabulated in Table 5.2.

5.7.1 The warped clockwise disk and it's stars

Our updated star sample confirms the presence of a warped clockwise disk. We do not model the clockwise disk as a “warp”, i.e. smooth change of angular momentum. Instead, we define two angular momentum directions motivated from the observed overdensity of angular momentum compared to an isotropic cluster (see Figure 5.12 and Table 5.1). This allows to check if stars consistent with belonging to the clockwise disk warp are indeed similar to the clockwise disk, without imposing the "warpedness" already in the prior.

The inner part of warped clockwise disk and it's stars We find 33 stars which are consistent with being on the inner part of the warped clockwise disk. Only four stars are at a projected distance of greater than $4''$, with the largest projected distance being $\sim 10''$.

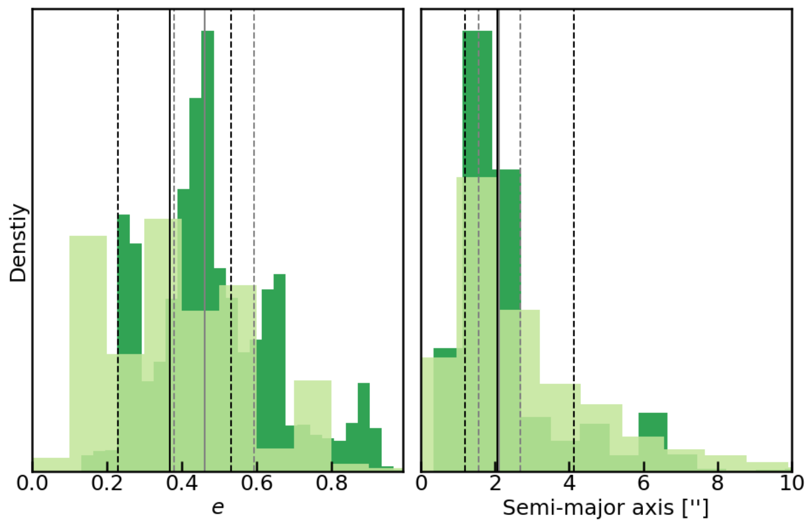

Figure 5.16: Distribution of the eccentricity and the semi-major axis of the stars consistent with belonging to the inner part of the warped clockwise disk. The dark green histograms show the properties of the 5D-constrained stars, the light green histogram show the distribution of stars with determined orbital solutions. The grey and black vertical lines indicate the median, and the dashed lines indicate the IQR of the stars with and without orbit.

The median projected distance is 2.0″, the interquartile range (IQR) of the clockwise disk feature stars is 1.0″ and 3.2″. The majority of the clockwise disk feature stars are bright: 24 of the 33 stars are brighter than $K_{mag} = 14$. Nevertheless, there is no distinctive brightness cut that leads to disk membership: nine stars are fainter than $K_{mag} = 14$, six of which have determined orbital solutions (R1, S5, S11, S31, S66, S87). The median K_{mag} of the clockwise disk feature is 12.7.

Combining the posteriors of each marginalization we obtain the joint distribution of orbital elements. For stars with determined orbital solutions, we sample orbital elements from the respective orbit posterior distributions. Figure 5.16 plots the distribution of the eccentricities, the semi-major axes as well as the distribution of magnitudes. The stars without determined orbits typically have non-zero eccentricities, with a median eccentricity ~ 0.5, highly eccentric orbits are however not preferred by our data. The median semi-major axis is 2.1″. The distribution of the stars with determined orbital solutions broadly agrees with those without a fully determined orbit. The stars with determined orbital solutions have however slightly lower eccentricities, and very high eccentricities are completely suppressed.

In summary, the inner part of the warped clockwise disk is made up of predominately, but not exclusively, of O/WR type stars, on mildly eccentric orbits in the proximity of the black hole.

The outer part of the warped clockwise disk and its stars 13 stars are consistent with belonging to the outer part of the warped clockwise disk. All but two stars are brighter than $K_{mag} = 14$. One faint star is S60, which belongs to the S-star cluster which we consequently remove from the sample. The median magnitude is 12.7. All but one star have projected distances ranging between $4''$ and $\sim 8.6''$, the median projected distance is $\sim 6.6\,''$.

The eccentricity distribution is comparable to the eccentricity distribution of the inner part of the warped clockwise disk, with median eccentricity of ~ 0.4, high eccentricities are not favoured by our data; the median semi major axis is $7.0''$. The star R70 has a determined orbital solution with a semi-major axis of $\sim 3.5''$ and an eccentricity of 0.3, consistent with the 5D-constrained stars.

In summary, this feature consists of eleven O/WR stars and one B stars, on slightly eccentric orbits. The stars are bright, very similar to the inner part of warped clockwise disk stars, but are found at larger radii. The stars in the outer part are thus only different by their angular momentum direction as function of radius. This is consistent with a “warp-picture”, which is a sole result of the data and not the prior. The prior does not impose a radial dependence, or a magnitude selection.

Morphological comparison of the inner and outer part of the warped clockwise disk Figure 5.17 demonstrates the morphological difference between the inner and the outer part of the warped clockwise disk. All but three stars belonging to the inner part of the disk are found centralized within $5''$. In contrast, the stars belonging to the outer part are almost exclusively found in the outside of this region. Since we did not apply any radial binning when calculating the respective log evidences, Figure 5.17 impressively demonstrates that none of the *other* young stars found at larger distances are consistent with belonging to warped-clockwise disk.

5.7.2 The counter-clockwise disk and its stars

33 stars are consistent with belonging to the counter clockwise disk. Only two stars, S4 and S12, have a full orbital solutions, both of which are S-stars which we again discard. 12 stars are brighter than $K_{mag} = 14$, 21 are fainter, and it is therefore more skewed towards fainter, B-type stars, compared to the warped clockwise disk. The median magnitude is 13.5. This feature contains stars mostly at large projected distance, with a median projected distance of $8.0''$. The stars are on modestly eccentric orbits, with a median eccentricity of 0.5. Unlike in the warped clockwise disk, highly eccentric orbits are not entirely suppressed. However, the fraction of the counter-clockwise disk stars on highly eccentric orbits (eccentricity > 0.9) is small. The semi-major axes distribution is similar to the observed projected distances, with a median semi-major axes of $7.4''$.

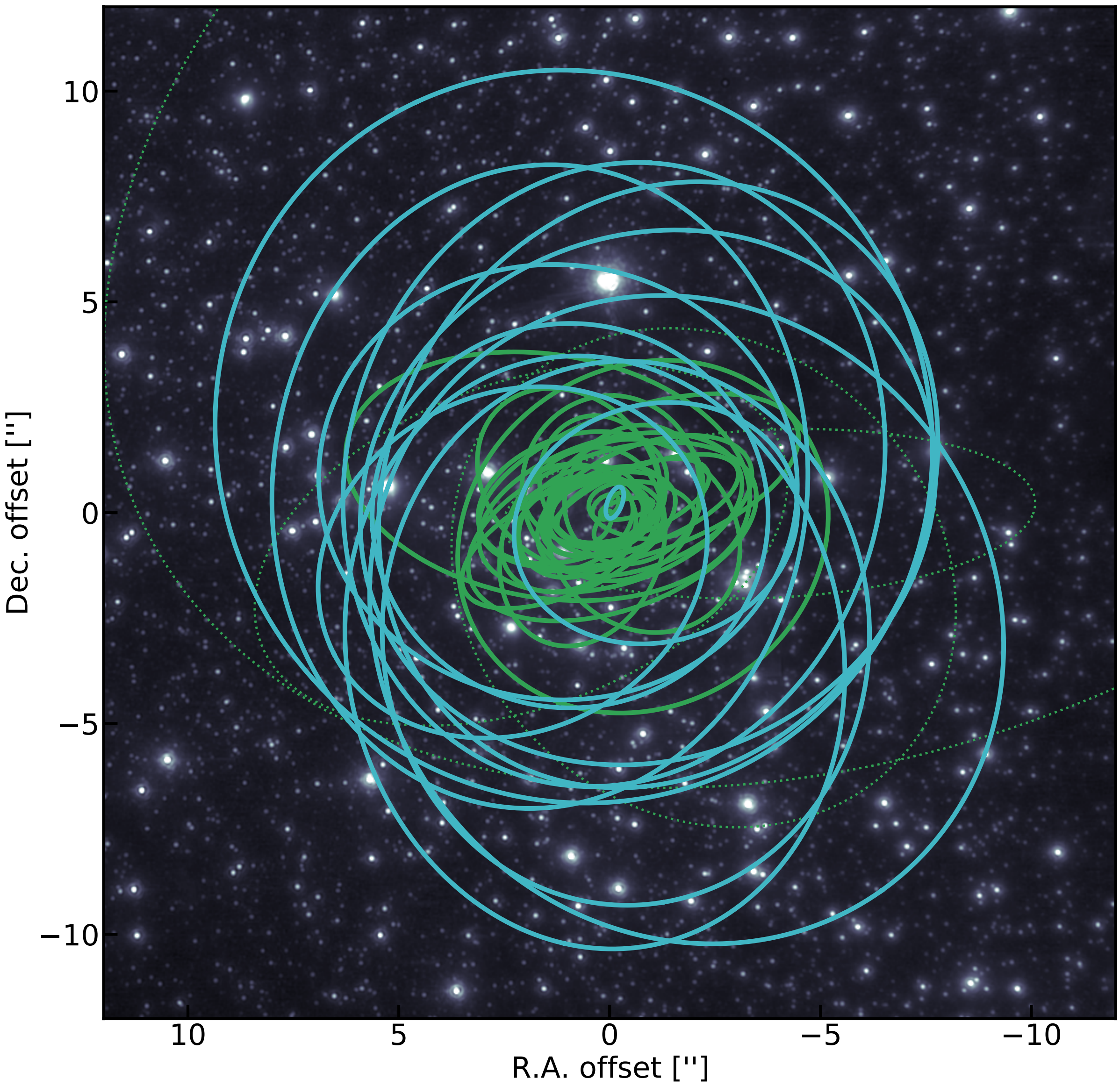

Figure 5.17: Comparison of most likely orbits consistent with belonging to the inner part of the warped clockwise disk (green) and the outer part of the warped clockwise disk (blue). The orbits of the stars shown have been selected based on the disk membership probability, i.e. we do not show orbits with Δ log evidence > 2 (see section 5.6). In both cases we evaluate the disk membership probability for all young stars, i.e. no radial binning has been applied. For stars without determined orbital solution, we show the median posterior orbit. For illustration purposes the three outermost stars of the inner warped-clockwise disk have dashed lines.

5.7.3 The first filament and it's stars

37 stars are consistent with belonging to the first filament. Similar to the warped clockwise disk, the majority of stars are brighter than $K_{mag} = 14$: eight stars are fainter, 23 brighter. The median magnitude is 13.2. The stars are at a median projected distance of 7.0″. The median eccentricity is 0.7, higher than for the warped clockwise disk and the median of semi-major axes is 5.6″. Both the semi-major axes distribution as well as the eccentricity distribution seem to be bi-modal, with a first eccentricity peak at ~ 0.7, and tail of very high eccentricity orbits. Similarly, the semi-major axis distribution is bi-modal, with a closer-in and an outer region. Intriguingly, all stars with very high eccentricity $\epsilon > 0.7$ have small semi-major axes ($> 4\,''$) and projected distances. These stars are not "outlying" in the sense that they have worse Δ log evidences, but seem to be proper first filament members.

5.7.4 The second filament and it's stars

The second filament consists of 36 stars. Two stars have a full orbital solution which however belong to the S-star cluster. Two thirds of the stars belonging to this feature are brighter than $K_{mag} = 14$ (16 B-type stars, 20 O/WR-type stars). Like for the counter-clockwise disk, the stars are at large projected distances: the median distance is 8.8″.
Most of the second filament stars are preferentially on highly eccentric orbits, which differentiates the second filament from the other features. The median eccentricity is 0.7. The distribution of semi-major axes is comparable to the observed projected distances with median 7.8.

5.7.5 Summary of the young stellar components

This analysis has revealed that the young stars can be categorized into four different significant features. 75% of young stars (152 of 201) are consistent with belonging to one of these features. Our analysis has shown that these features cannot only be separated by their angular momentum but also by their distance from Sgr A*. The warped clockwise disk forms a coherent structure ranging from $\sim 1''$ to $\sim 8''$. The first filament has a large range, and can be found ranging from $\sim 3''$ to $\sim 10''$. The counter-clockwise disk feature, and second filament extend the furthest from Sgr A*. We compare the different eccentricity distributions, semi-major axis distributions and the K_{mag} distributions in Figure 5.19.

We plot the most likely orbits of of each star belonging to the respective features in Figure 5.20. This demonstrates the morphological differences of the different features, the radial dependence as well the higher of eccentricity at larger radii.
The morphological differences between these features are best illustrated using the measured projected positions and projected velocity directions shown in Figure 5.21. The color indicates the respective disk membership. It is clear the stars belonging to the inner part of the warped-clockwise disk are centrally concentrated, and that this feature is viewed more edge-on. Stars belonging to the outer part of the warped-clockwise disk are only found

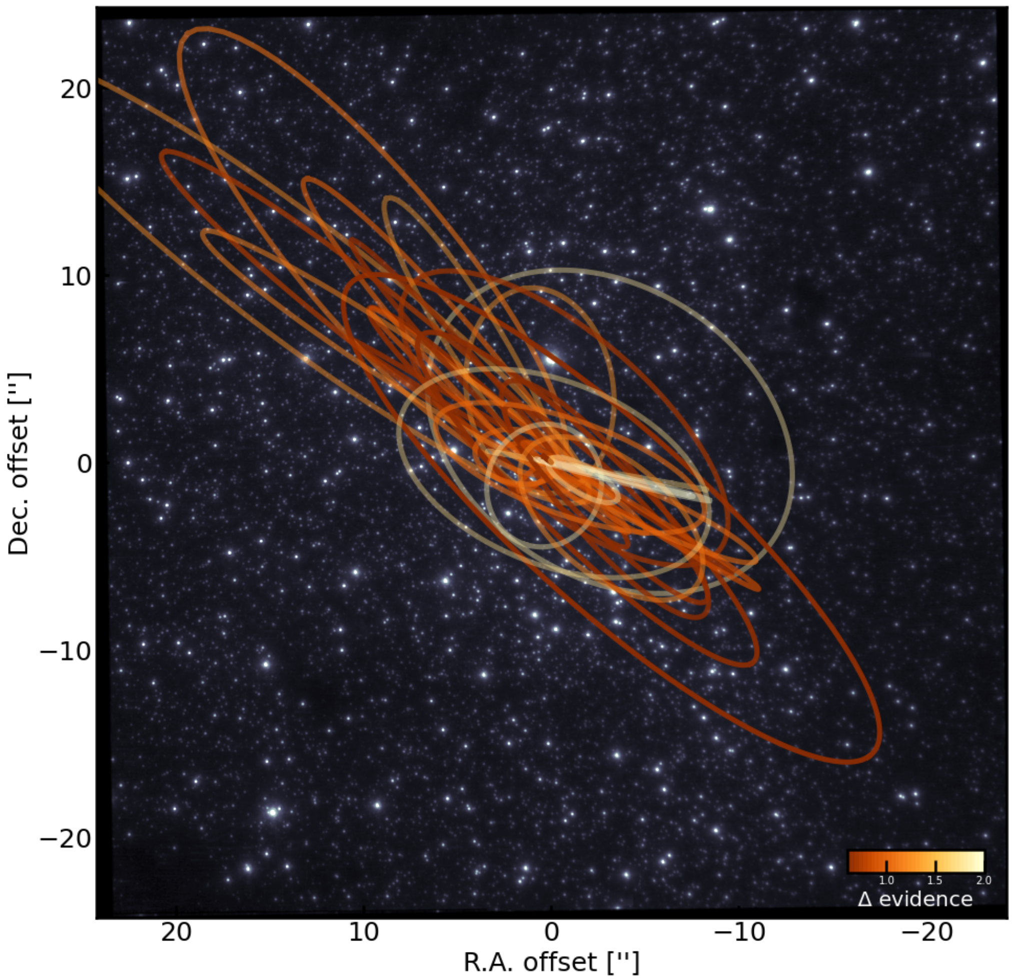

Figure 5.18: Morphological properties of the second outer filament, similar to Figure 5.17. Compared to the warped clockwise disk, these stars are found at much larger projected distances, and have substantially higher eccentricities. The color scale and opaqueness encodes the disk membership probability: darker orbits have higher probability of belonging to this feature than lighter colored orbits.

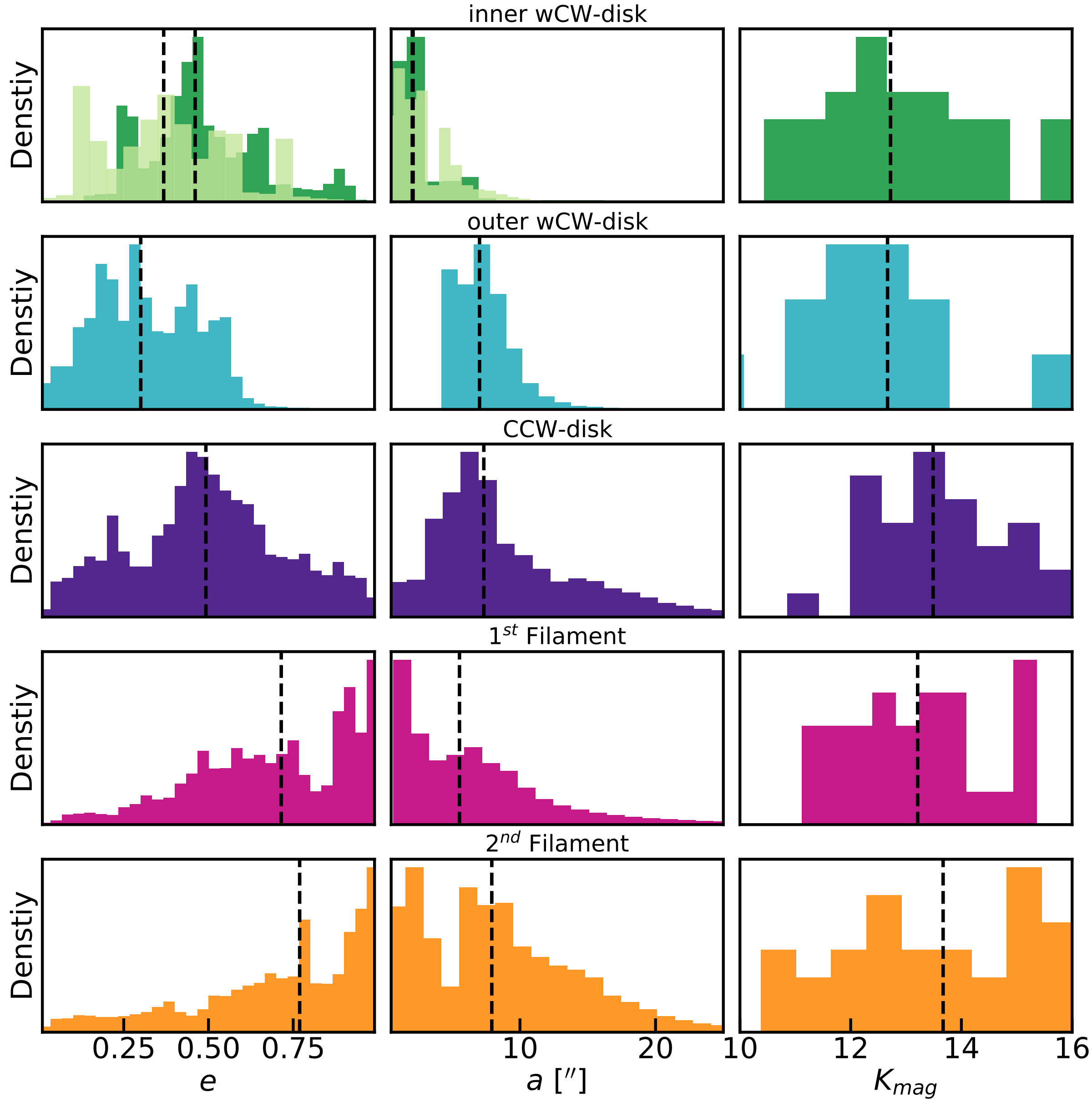

Figure 5.19: Comparison of the eccentricity distributions, the semi-major axis distributions and K_{mag} distributions of the different kinematic features. The top row includes both the distributions of the 5-D constrained stars and the stars with determined orbital solutions.

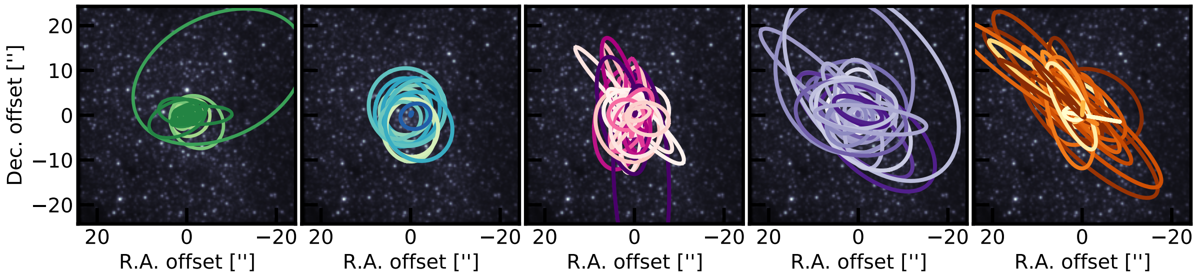

Figure 5.20: Comparison of the different disk-like structures: Left to right - the inner and outer part of the warped clockwise disk, first filament, the counter-clockwise disk and the second filament. Like in the Figure 5.18, the color and opacity encodes the probability of disk membership: bright, more opaque colors have a higher probability of disk membership; lighter more see-through colors have a lower probability.

at intermediate separations. The three outer features are located at large separations. At these large separations a clear dichotomy between stars south and north of Sgr A* exists: stars south of Sgr A* have positive radial velocities, stars north show negative radial velocities. This is consistent with three rather edge-on viewed disk-like features.
We stress that the radial dependence is not imposed by the prior distribution, but is a consequence of the data.
In the following, we discuss if these features should be regarded as independent structures, i.e. if they formed separately, or if a common formation scenario is plausible.

5.8 Discussion

We have preformed the most detailed and largest spectroscopic survey of the central $(+20, -10)$, $(-20, +10)$ arcseconds of the GC. We've reanalyzed, combined and updated the spectra derived for all GC stars observed with ESO's SINFONI instrument taken in AO mode. This has lead to spectra for over 2800 stars. We classified the stars into old, if CO-band heads are discernible, young, if the Brγ line (and other young star lines) are discernible, or candidate, if no line is discernible. This led to the identification of a total of 201 young stars. For 35 young stars full orbital solutions can be derived. Three stars have too high radial velocities to be on bound orbits[3]. For the remaining 158 stars, only radial velocities could be determined. We extend previous Monte-Carlo studies presented in Lu et al., 2009; Bartko et al., 2009; Bartko et al., 2010; Yelda et al., 2014 by introducing a new prior. The proposed prior maps an isotropic cluster onto itself without bias in angular momentum. It is not "better" for answering the question of the true angular momentum distribution of the young stars in the GC. However, it allows for a clean definition of a null-hypothesis: How different is the observed young star distribution from an isotropic cluster. In particular, we ask how different the observed angular momentum distribution

[3]This is likely a consequence of a poorly determined radial velocity or a confusion event.

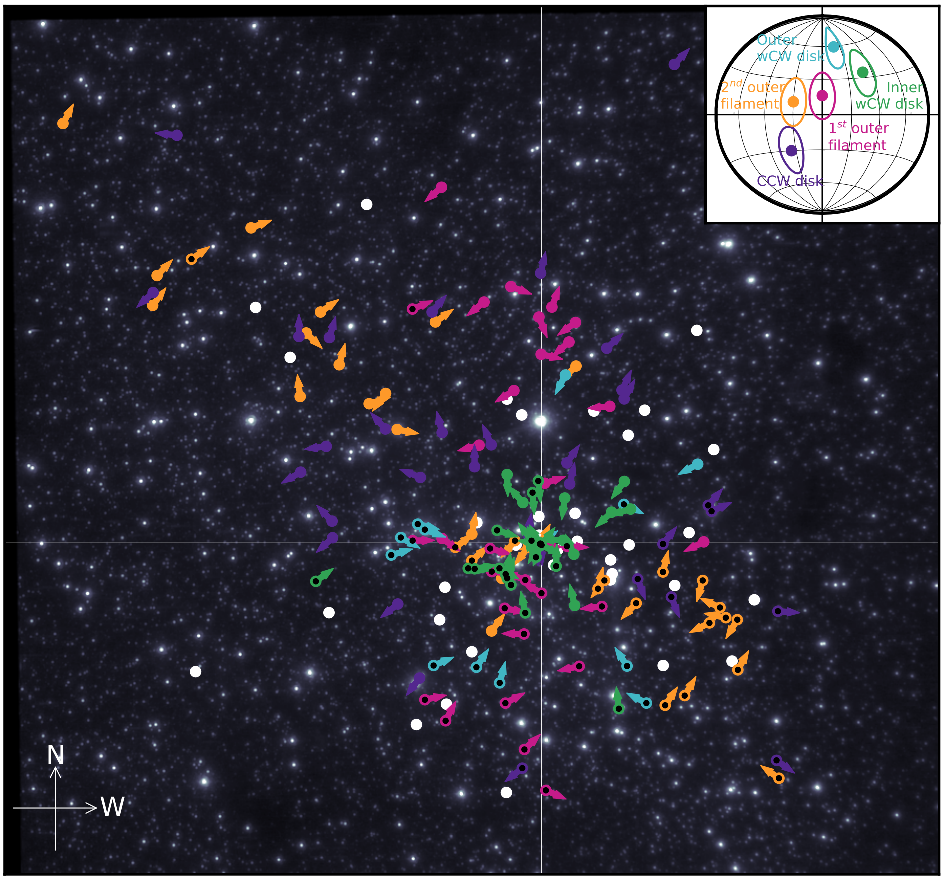

Figure 5.21: Comparison of the projected position and velocity direction of the different disk-like structures: The projected position of all young stars is indicated by a dot, the projected velocity direction is indicated by the arrow; dots with black marking have positive radial velocities. The color of the dots indicate disk membership. The latitude and longitude of the angular momentum direction of the disks are given in the inset. White dots indicate stars not belonging to any of the features.

is from that of the old star cluster present in the GC, which is an isotropic cluster in good approximation (e.g. Pfuhl et al., 2014). Compared to such an idealized isotropic cluster, we found several highly significant over-densities in angular momentum space. This can be intuitively guessed from the distribution of young stars in Figure 5.4 and the SINFONI coverage in Figure 5.2: The distribution of young stars appears relatively homogeneous in the closer proximity of Sgr A*. In contrast, there is a clear absence of young stars North-East of it, despite the comparable spectroscopic coverage in this area. Furthermore we find a clear dependence on radial distance from Sgr A*. We will discuss the details of the angular momentum distribution in the next section.

5.8.1 Distribution of angular momentum of young stars in the Galactic Center

We have found at least four different kinematic features which are significant when compared to an isotropic cluster. Further, we have found that the vast majority (75%) of stars can be attributed to one of these five disk-like features. The angular momentum distribution in the GC is therefore very rich, and significantly different from the old star population. We have demonstrated that the young stars reside in a radial dependent warped-disk and several star-disk like outer filaments. Such a rich structure has been proposed by several simulations of in-situ star formation in an in-falling gas cloud scenario. Bonnell and Rice, 2008 demonstrated that stars can form in massive gas clouds around a massive black hole like Sgr A* and speculated that multiple young star rings may be present in the GC. Löckmann and Baumgardt, 2009 have demonstrated that in the presence of two separate disk systems (like the clockwise and the counter-clockwise system), the disks tidally interact with one another causing a warping of the disks. Kocsis and Tremaine, 2011 show that disk warps naturally arise from the interaction of the disk with the surrounding old star cluster.

Our observations are fully consistent with the results of these simulations: Our analysis has shown a very rich structure in the angular momentum distribution of young stars. This structure is not result of a random orientation of stars, but we have shown that it is significantly different from the distribution of an isotropic cluster.

5.8.2 A warped disk and several filaments of young stars

We have argued that the warped clockwise disk forms a coherent structure ranging from $1''$ to $8''$. The stars share very similar in eccentricity distributions, have similar angular momentum directions and are predominantly made up of O and WR type stars. They are mainly different by the angular momentum as function of separation from the black hole, consistent with the warp-picture. The other features are harder to explain as an extension or warp of the clockwise disk.

The first filament shares some similarities with the warped clockwise disk. For instance, a large number of first filament stars have low eccentricities, and are at larger separation from

the black hole than inner and outer warped clockwise disk stars. This is consistent with being the outer most extension of the warped clockwise disk. Thus it remains possible that the first filament represents the "fuzzy" and outermost extension of an eventually dissolving and warped clockwise disk (Yelda et al., 2014).
However, a considerable fraction of first filament stars have substantially higher eccentricities than the inner and outer part of the warped clockwise disk. These most eccentric stars of the first filament are located closer in, and are thus within the range of the warped clockwise disk. Furthermore, there are less O and WR type stars in the first filament and the WR+O to B star ratio is more comparable to that of the counter-clockwise disk and the second filament.
The counter-clockwise disk possesses a similar eccentricity distribution as the two inner features but shows a drastically different angular momentum direction. Further, there are less O+WR type stars. The second filament has a different angular momentum direction than the warped clockwise disk. It is the most eccentric feature, and has the lowest ratio of O+WR/B stars (1.3).

As discussed before, several simulations of gas accretion disk produced such rich features (Nayakshin, 2006; Nayakshin et al., 2007; Bonnell and Rice, 2008; Löckmann and Baumgardt, 2009). It is plausible that the observed young star population has been formed in several, consecutive star formation events in the more recent history of our Galaxy. Of particular interest is the scenario which was studied in Hobbs and Nayakshin, 2009, in which two Giant Molecular Clouds collide. After the initial collision the two clouds are sent on a plunging orbit and accrete onto Sgr A*. A central accretion disk forms and, depending on the initial conditions, several gas streamers may form. In both the central disk, as well as the gas-streamers stars subsequently form.
Several of the predictions made in this scenario are consistent with our observations. In their simulations with large impact parameter, the inner-most accretion disk stays in a rather compact region around the black hole, consistent with the inner region of the warped clockwise disk in the GC. The remnants of the colliding gas clouds form filaments at larger separations, which do not share the same angular momentum direction as the central disk. This could correspond to the stellar populations found in the counter-clockwise disk as well as the first and second filament. Furthermore, the disks found in the simulations show large scale warps, perfectly consistent with the observed change in angular momentum direction of the warped clockwise disk. In their simulations, the central disk circularizes after an initial period of highly eccentric orbits, while the stars further out remain on more eccentric orbits. We find a similar behavior, but note that our values are overall more eccentric than found in this set of simulations.
Lastly, in the simulations, the star formation is different in the inner and outer regions. In the simulations, mostly heavy stars form in the central disk, the IMF is substantially less top-heavy in the outer filaments. This is consistent with our observations too: The ratio of observed O+WR to B stars is much higher in the warped clockwise disk than in the further out structure. The completeness correction is however difficult and disputed (compare Bartko et al., 2010; Do et al., 2013). Hobbs and Nayakshin, 2009 further caution that their star-formation prescription maybe oversimplified.

5.9 Conclusion

We have spectroscopically investigated the central (-20, 10) arcseconds in right ascension to (-10, 20) arcseconds in declination of the GC. We've identified 201 young stars. Using the formal description of the z-distribution of an isotropic cluster, we confirm that the observed young stars reside in several ordered structures, i.e. very different from an isotropic cluster. Of the 201 young stars, we found that 75% are consistent with belonging to one of four dynamical features. Unlike Yelda et al., 2014, we do not try to estimate the fraction stars aligned with the features by-chance. This would require prior information on how by-chance-aligned stars are distributed. In consequence our estimate of 75% is an upper limit.

We confirm the presence of the warped clockwise disk (Bartko et al., 2009; Bartko et al., 2010): a smooth change in angular momentum of the clockwise disk with function of radius. Using a prior angular momentum direction instead of the uniform acceleration or stellar cusp z-prior we find slightly higher eccentricities ($\epsilon \sim 0.4 - 0.6$) than in past work Lu et al., 2009; Bartko et al., 2009; Bartko et al., 2010; Yelda et al., 2014. We confirm the presence of an outer kinematic feature, which Bartko et al., 2009 attributed to the warped clockwise disk. The feature shares similarities with the warped clockwise disk, but also with the features at larger separations. We call this feature the first filament, but note that it remains possible that it is part of the warped clockwise disk. Further, we confirm the presence of the counter-clockwise disk system at large separations reported in Genzel et al., 2003; Paumard et al., 2006; Bartko et al., 2009. This feature was deemed insignificant by other work Lu et al., 2006; Lu et al., 2009; Yelda et al., 2014. We find that this feature consists mostly of stars at large projected separations, explaining the difficulty of establishing significance in past studies which had smaller spatial coverage. In addition to the features which have been discussed in literature before, we identify a new feature at large separations which we call the second filament. Like the counter-clockwise disk, the second filament is at large projected distances from the black hole. The angular direction of the three outer features are quite comparable. The second filament is, however, substantially more eccentric and we thus argue that the two systems are distinct.

This rich structure in kinematic features has been suggested in different simulations of star formation in an accretion disk around Sgr A*. In particular, the set of simulations by Hobbs and Nayakshin, 2009 in which two giant molecular clouds collide and subsequently accrete show intriguingly comparable features to the ones observed: A small, medium eccentric disk in close proximity of Sgr A*; several remnant star streamers at larger separation which have substantially different angular momenta directions; and higher eccentricities at larger separations. Further, the simulations show differences in the distribution of O and WR type star, with the most heavy stars found in the inner disk – consistent with the apparent distribution of O and WR type stars in the Galactic Center. We thus argue that the a simultaneous formation of all young stars in the Galactic Center remains a feasible scenario, consistent with the latest analysis of the age distribution of the S-star cluster (Habibi et al., 2017). However, the dramatically different kinematic distribution of the B-stars in the central arcsecond remains serious challenge (Boehle et al., 2016; Gillessen et al., 2017) for such a common formation scenario, and more detailed analysis of the age distribution of the young stars are required to confirm or rule out a single star formation event some ~ 6 Myr ago.

Chapter 6

Conclusions and this work in context

6.1 Advances in the physics of the accretion flow of Sgr A*

The first paper presented in this thesis reports the first detection of the variable flux of Sgr A* at 100 µm and 160 µm. These measurements confirm the turn-over of the SED in the far-infrared, and allow to constrain the temperature, electron density and ambient magnetic field strength of the dominant electron population visible in the sub-mm. The inferred temperature of the dominant sub-mm electron population is $\sim 10^{11}$ K, about an order of magnitude higher than inferred from older single telescope sub-mm observations. The significance of that conclusion lies in the optical depth of the emission at 230 GHz, the workhorse frequency for VLBI. With an electron temprature of $\sim 10^{11}$ K, the optical depth at 230 GHz is much smaller than 1. In consequence, the turn over is not caused by the transition from optically thin to thick, and thus the black hole is not hidden behind a photosphere to VLBI experiments like the EHT. These result of the analysis was subsequently, and independently, confirmed by an ALMA band 10 detection at 350 µm (Bower et al., 2019).

The second paper presented in this thesis reports an updated flux distribution of Sgr A* exploiting the sensitivity of GRAVITY. The work is not only aided by the outstanding sensitivity, but most importantly the unmatched resolution of GRAVITY. With a resolution of $\sim$4 mas, GRAVITY can discern Sgr A* from the neighbouring stars and the influence of stray-light is minimized. Therefore, the very complicated background modeling necessary in e.g. Dodds-Eden et al., 2009; Witzel et al., 2012; Witzel et al., 2018 is obsolete.
The results presented in the paper are two fold: the first result is observational, while the second one is interpretative. The observational result is driven by GRAVITY's ability to detect Sgr A* at all times. This allows to measure its median flux of around 1 mJy, and further allows to determine the flux quantiles. As such, it is the first purely empirical measurement of the Sgr A* K-band flux distribution. It does not rely on the assumption of an underlying flux distribution model, like a log-normal probability distribution. Therefore, the observations will serve as gold-standard to compare models of the accretion flow

against. Of particular importance are the faint fluxes measured by GRAVITY, which were not observable using single dish telescopes. The second, interpretative result of Gravity Collaboration et al., 2020f is the modeling of the probability distribution best fit to the observed flux distribution. Previous single-dish analysis of the light curve were severely limited because the turn-over of the flux distribution was not observed. In consequence, the median flux of Sgr A* had to be inferred from a flux distribution model. In previous studies, the flux distribution had been modeled (competingly) by either a single lognormal distribution, a combined lognormal + powerlaw distribution or a single powerlaw distribution (Dodds-Eden et al., 2009; Witzel et al., 2012; Witzel et al., 2018). While both the single lognormal distribution as well as a power-law distribution have no deeper physical motivation[1], the competing log-normal + powerlaw distribution assumes a two-process system responsible for the observed flux. The first process, dubbed 'quiescence state' is responsible for the faint emission of Sgr A*, and the second process is a 'flare state' responsible for the power-law tail of the flux distribution. GRAVITY's ability to observe Sgr A* at all times, and to remove the background flux degeneracy shows that a log-normal probability distribution only poorly describes the observed flux distribution. The observed flux distribution is log-right skewed. I've compared the flux distribution to a variety of different probability distributions, none of which are however motivated physically. In consequence, Gravity Collaboration et al., 2020f favour the two-state log-normal plus tail model of the flux distribution and argue for a distinct physical process which generates Sgr A* near-infrared and X-ray flares.

The third paper presented in this thesis discusses the emission scenario responsible for this secondary flare process. The paper builds on a set of multi-wavelength observations covering the SED 4.5 µm in the mid-infrared to the near-infrared 1.65 µm and up to photon energies from 2 keV 70 keV in the hard X-ray. Observations from four instruments were included in the analysis: Spitzer, GRAVITY (K- and H-band), Chandra and NUstar. Building on the results of the first paper, and two decades of Sgr A* flare observations, the variable flux in the light curve is understood as a flare from a distinct physical process. The paper consists of two parts: first the observational analysis of the flare light curve, which is converted to a time-dependent SED of the flare. In the second, interpretive part of the paper, Abuter et al., 2021 discuss the flare in the context of a single "hot-spot" in the accretion flow. Building on previous works, Abuter et al., 2021 assume that the hot-spot is dominated by a single magnetic field and the electron density is homogeneous. Based on this assumption the parameter space of the hot-spot model is explored, taking into account synchrotron emission, inverse Compton emission and synchrotron self-Compton emission. This is done using a fast, flexible code which can compute the spectra of the emission region based on the integration of the arbitrarily shaped electron distributions which allows to include particle escape-based synchrotron cooling. Two viable solutions to explain the observed SED are found. The first solution has a steep powerlaw electron spectrum and

[1] Lognormal distribution are commonly observed in accreting objects such as X-ray binaries (Uttley et al., 2005), and power-law distributions have been proposed for self-organized critical systems (Aschwanden et al., 2016). However, no study so far has sought to infer such an interpretation for Sgr A*, at least in the near-infrared (but see Li et al., 2015, for such an interpretation of the X-ray flux distribution of Sgr A*).

induces an optically thick synchrotron spectrum in the sub-mm. These electrons serve as seeds to self-Synchrotron Compton emission, which is visible in both the NIR and X-ray. In order for enough Compton scattering to take place, these solutions require very high electron densities, which is difficult to explain with typically inferred ambient densities. The second solution is a synchrotron-only solution, in the sense that all emission stems from the same synchrotron spectrum, and the corresponding Compton emission occurs at higher and un-observed frequencies. This solution does not require specific electron densities, and is thus favoured. However, in contrast to previously observed flares, electron loss through particle escape does not suffice to explain the X-ray spectrum. Instead, the electron distribution needs to be truncated at a Lorentz factor $\approx 10^4$. Since this truncation of the electron distribution is required for all time steps, Abuter et al., 2021 argue that intrinsic truncation due to limited particle acceleration is required and particle loss due to rapid electron cooling is not favoured.

6.2 Advances in the physics of the young star cluster

The distribution of the young star cluster, and especially the question whether there is more than one young star disk has been subject of a heated debate. While there is broad consensus on the basic properties of the clockwise disk, namely the orientation and the eccentricity distribution of the orbits, the question of how coherent the motion of the young star population is, is not settled. The two opposing views are as follows:

- Genzel et al., 2003; Paumard et al., 2006; Bartko et al., 2009; Bartko et al., 2010 find a rich structure in the kinematic distribution of young stars. In addition to the undisputed clockwise disk, they find a population of counter-clockwise disk stars at larger separations. The counter-clockwise disk is similar in stellar population and density, however is more eccentric. Bartko et al., 2009 further complicated this picture by claiming a ‘disk-warp’, which represent a change in angular momentum direction of the clockwise disk stars as function of separation to the black hole.

- Lu et al., 2006; Lu et al., 2009; Yelda et al., 2014 draw a very different, much simpler, picture of the Galactic Center: There a exists a single, sub-dominant population of young stars in clockwise rotation. The remainder of young stars is however in a much more relaxed distribution, with mostly random or isotropic distribution. The fraction of disk young stars is only around $\sim$20%.

Given these opposing views one should investigate the reason for this divergence of opinion. The techniques used in both studies are quite comparable, as is the overall quality of data. Even more so, the data used is quite similar or in many cases even identical. For instance Bartko et al., 2009 used 90 young stars, most of which had been previously reported by Paumard et al., 2006 ($\sim$ 80 stars), which again relied on the earlier results of Genzel et al., 2003. Similarly, while Lu et al., 2009 improved the overall quality of the astrometric data of the stars presented in Paumard et al., 2006, they did not add any new stars. Yelda et al., 2014 presented the largest set of young stars prior to this work with a total of 116 young stars. This is only a 30% increase in the number of stars, but compared to Bartko et al., 2009 the number of stars belonging to a coherent structure **dropped** from ~ 70 stars to ~ 20.

The problem thus must lie in the way how one assigns the membership to a coherent structure. Ultimately, only a few fully determined orbit solutions exist. Because the acceleration drops with separation from the black hole, only very few acceleration constraints for stars at separations larger than the clockwise disk stars exist. And the vast majority of these better constrained stars fall in the separation bin of the clockwise disk.
For the stars further out one has to rely on prior assumptions to derive their properties. I thus argue the crux of the problem lies in these assumptions: depending on the chosen assumptions, the conclusion is substantially different. For instance, while Lu et al., 2006; Lu et al., 2009 and Yelda et al., 2014 have chosen an un-informed approach on the distribution of stars (a uniform distribution of acceleration), Bartko et al., 2009; Bartko et al., 2010 have included more prior knowledge, namely the young star surface density determined by Paumard et al., 2006 and earlier work. Yelda et al., 2014 take an even more cautious approach, and de-contaminate their sample of clockwise stars from the contribution of by-chance samples. They do so by comparing their star sample with an approximate isotropic cluster, or more precisely, the "uniform acceleration prior cluster" (see section 5.4.3). This is, however, an assumption. Under this assumption, they find that only 50% of the stars are consistent with being clockwise disk stars are true disk members. This is in stark contrast to Bartko et al., 2009: Here all stars which could be disk members, are assumed to be disk members.
Thus the main difference in theses works seems to lie in the choice of prior assumption of the distribution of the young stars.

My work on the young stars in the Galactic Center presents the first major (published) increase of known young stars of $\sim 70\%$ compared to Yelda et al., 2014. Not only the number of known young stars increased, but maybe even more importantly, the spectroscopic coverage substantially increased towards the North-East of Sgr A*. This revealed the absence of young stars in this direction, impressively showing the un-isotropic distribution of the young stars in the Galactic Center.
Further, I improved the Monte-Carlo method introduced by Lu et al., 2009. Explicitly, the analytic solution of an isotropic-cluster prior is derived. Using this prior, at first an agnostic approach on the distribution of young stars in the Galactic Center is taken. In the last chapter, the observed distribution is compared to that of an isotropic cluster. This revealed that the updated sample of young star is significantly different from an isotropic cluster. Explicitly, four main kinematic components in the Galactic Center were found.
After this agnostic step, a more informed prior was chosen to determine the properties of the kinematic features. A prior on the direction of the angular momentum of the stellar disks was used to derive the properties of the stars. This approach removes any bias which is introduced by the assumption of an isotropic cluster (or a uniform distribution of accelerations). Under this strong assumption, the properties of the star in the disks can be derived: the posterior distribution of semi-major axes and eccentricities. This approach

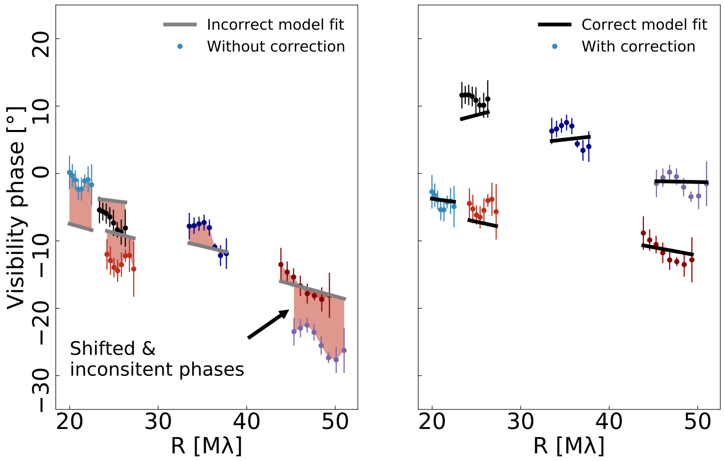

Figure 6.1: Left:Imaging phase of GRAVITY, affected by aberrations in the GRAVITY light path. Right: Corrected phase

does not allow to estimate the *true disk fraction*, i.e. the fraction of star aligned by chance with the disk direction.
This two-stepped approach is better. In the first step no strong evidence for an important isotropic distribution is found. Thus it seems unjustified to assume an important isotropic distribution in the secondary modelling. There is further no theoretical motivation for an isotropic distribution. Neither, local or external formation assumes fast relaxation of the young stars. The dynamical relaxation time scale is much longer than the age of the young stars. A viable candidate for fast relaxation of the young stars would be a intermediate mass black hole. However, so far there is little evidence for the presence of one the Galactic Center.

6.3 Contribution to work not presented in this Thesis

During my PhD I contributed to several projects which are not detailed in this thesis. Most importantly, I contributed to the development of the dual-beam observation mode of GRAVITY. This novel observation mode is required to measure the distance of between to sources which are too far away from each other to be simultaneously observed by GRAVITY. This is the case for S2 and Sgr A* after the peri-center passage of the star in 2019 and the time after.

In order to measure the spatial separations of two sources outside each others interferometric field of view (IFOV), their relative phase difference has to be measured. More specifically, the relative difference of the visibility phase has to be determined, for which the visibility phase has to be referenced against the internal differential optical path differences (dOPD) monitored by the GRAVITY metrology system. This measurement is

severely affected by the optical aberrations in the light path of the metrology system. These aberration introduce a systematic dOPD to the phase measurement, which causes a drift of the astrometric measurement. We introduced a calibration scheme which allowed to improve the astrometric accuracy by almost a factor of four. The details of the procedure are reported in the PhD thesis of F. Widmann (Widmann, 2021). Figure 6.1 shows the visibility phase before and after the correction. Without the correction, the visibility phase is inconsistent with that of a point source and it is shifted with respect to the corrected phase. The shift in phase causes an incorrect separation measurement. This improvement in the GRAVITY metrology system calibration allowed, for the first time in optical interferometry, measurements of position-centroid of Sgr A* with $\sim 100\mu$as precision using only the visibility phase and not the closure phase.
In addition to this more fundamental research in the GRAVITY metrology system, I contributed to the re-analysis of the SINFONI radial velocity of S2 published in GRAVITY Collaboration et al., 2019b and subsequent publications and led the data reduction and extraction of astrometric positions of S29 and S55 peri-center passage in 2021 (GRAVITY Collaboration et al. 2021, in prep.).

6.4 Summary

In summary, this thesis has presented two of the major updates of the Sgr A* SED: The first constraints at Sgr A*'s variable flux in the far infrared as well as the first measurement of the K-band median flux. Furthermore, I've analysed a multi-wavelength data-set of a mid-infrared to X-ray flare, which allowed to infer the properties of the electron distribution responsible for the flare. I proposed that part of the infrared to X-Ray flux ratio can be explained by non-infinity particle acceleration. The last part of the thesis has studied the population of young stars in the Galactic Center. I've presented the largest sample of young stars to date, and used a new statistical method to show that the kinematic properties of the young stars is very rich. This favours a local formation scenario, possibly after the collision of two giant molecular clouds.

Bibliography

Abramowicz, Marek A., Chen, Xingming, Kato, Shoji, Lasota, Jean-Pierre, and Regev, Oded (Jan. 1995). "Thermal Equilibria of Accretion Disks". In: *The Astrophysical Journal Letters* 438, p. L37. DOI: 10.1086/187709. arXiv: astro-ph/9409018 [astro-ph].

Abuter, R. et al. (July 2021). "Constraining particle acceleration in Sgr A* with simultaneous GRAVITY, Spitzer, NuSTAR and Chandra observations". In: *arXiv e-prints*, arXiv:2107.01096, arXiv:2107.01096. arXiv: 2107.01096 [astro-ph.HE].

Alexander, Tal (Dec. 1999). "The Distribution of Stars near the Supermassive Black Hole in the Galactic Center". In: *The Astrophysical Journal* 527.2, pp. 835–850. DOI: 10.1086/308129. arXiv: astro-ph/9907241 [astro-ph].

— (Nov. 2005). "Stellar processes near the massive black hole in the Galactic center [review article]". In: *Physics Reports* 419.2-3, pp. 65–142. DOI: 10.1016/j.physrep.2005.08.002. arXiv: astro-ph/0508106 [astro-ph].

Allen, David A., Hyland, A. R., and Hillier, D. J. (June 1990). "The source of luminosity at the Galactic Centre." In: *Monthly Notice of the Royal Astronomical Society* 244, p. 706.

Aschwanden, Markus J. et al. (2016). "25 Years of Self-Organized Criticality: Solar and Astrophysics". In: *Space Science Reviews* 198.1-4, pp. 47–166. ISSN: 15729672. DOI: 10.1007/s11214-014-0054-6. eprint: 1403.6528.

Baganoff, F. K. et al. (Sept. 2001a). "Rapid X-ray flaring from the direction of the supermassive black hole at the Galactic Centre". In: *Nature* 413.6851, pp. 45–48. DOI: 10.1038/35092510. arXiv: astro-ph/0109367 [astro-ph].

— (Sept. 2001b). "Rapid X-ray flaring from the direction of the supermassive black hole at the Galactic Centre". In: *Nature* 413.6851, pp. 45–48. DOI: 10.1038/35092510. arXiv: astro-ph/0109367 [astro-ph].

Baganoff, F. K. et al. (Dec. 2001c). "The Spatial Profile of the X-ray Emission from Sagittarius A*". In: *American Astronomical Society Meeting Abstracts*. Vol. 33. Bulletin of the American Astronomical Society, 85.03, p. 1429.

Baganoff, F. K. et al. (July 2003a). "Chandra X-Ray Spectroscopic Imaging of Sagittarius A* and the Central Parsec of the Galaxy". In: *The Astrophysical Journal* 591.2, pp. 891–915. DOI: 10.1086/375145. arXiv: astro-ph/0102151 [astro-ph].

— (July 2003b). "Chandra X-Ray Spectroscopic Imaging of Sagittarius A* and the Central Parsec of the Galaxy". In: *The Astrophysical Journal* 591, pp. 891–915. DOI: 10.1086/375145. eprint: astro-ph/0102151.

Baganoff, F. et al. (Dec. 1999). “Chandra Imaging of Sgr A* and the Galactic Center”. In: *American Astronomical Society Meeting Abstracts*. Vol. 195. American Astronomical Society Meeting Abstracts, 62.01, p. 62.01.

Bahcall, J. N. and Wolf, R. A. (Oct. 1976). “Star distribution around a massive black hole in a globular cluster.” In: *The Astrophysical Journal* 209, pp. 214–232. DOI: 10.1086/154711.

Balick, B. and Brown, R. L. (Dec. 1974). “Intense sub-arcsecond structure in the galactic center.” In: *The Astrophysical Journal* 194, pp. 265–270. DOI: 10.1086/153242.

Ball, D., Özel, F., Psaltis, D., and Chan, C.-k. (July 2016). “Particle Acceleration and the Origin of X-Ray Flares in GRMHD Simulations of SGR A”. In: *The Astrophysical Journal* 826, 77, p. 77. DOI: 10.3847/0004-637X/826/1/77.

Barrière, N. M. et al. (May 2014). “NuSTAR Detection of High-energy X-Ray Emission and Rapid Variability from Sagittarius A* Flares”. In: *The Astrophysical Journal* 786, 46, p. 46. DOI: 10.1088/0004-637X/786/1/46.

Bartko, H. et al. (June 2009). “Evidence for Warped Disks of Young Stars in the Galactic Center”. In: *The Astrophysical Journal* 697.2, pp. 1741–1763. DOI: 10.1088/0004-637X/697/2/1741. arXiv: 0811.3903 [astro-ph].

Bartko, H. et al. (Jan. 2010). “An Extremely Top-Heavy Initial Mass Function in the Galactic Center Stellar Disks”. In: *The Astrophysical Journal* 708.1, pp. 834–840. DOI: 10.1088/0004-637X/708/1/834. arXiv: 0908.2177 [astro-ph.GA].

Becklin, E. E., Matthews, K., Neugebauer, G., and Willner, S. P. (Jan. 1978). “Infrared observations of the galactic center. I. Nature of the compact sources.” In: *The Astrophysical Journal* 219, pp. 121–128. DOI: 10.1086/155761.

Becklin, E. E. and Neugebauer, G. (Jan. 1968). “Infrared Observations of the Galactic Center”. In: *The Astrophysical Journal* 151, p. 145. DOI: 10.1086/149425.

— (Sept. 1975). “High-resolution maps of the galactic center at 2.2 and 10 microns.” In: *The Astrophysical Journal Letters* 200, pp. L71–L74. DOI: 10.1086/181899.

Beloborodov, Andrei M. et al. (Sept. 2006). “Clockwise Stellar Disk and the Dark Mass in the Galactic Center”. In: *The Astrophysical Journal* 648.1, pp. 405–410. DOI: 10.1086/504279. arXiv: astro-ph/0601273 [astro-ph].

Blum, R. D., Depoy, D. L., and Sellgren, K. (Mar. 1995). “A Comparison of Near-Infrared Spectra of the Galactic Center Compact He i Emission-Line Sources and Early-Type Mass-losing Stars”. In: *The Astrophysical Journal* 441, p. 603. DOI: 10.1086/175386.

Blum, R. D., Sellgren, K., and Depoy, D. L. (Oct. 1996). “JHKL Photometry and the K-Band Luminosity Function at the Galactic Center”. In: *The Astrophysical Journal* 470, p. 864. DOI: 10.1086/177917. arXiv: astro-ph/9604109 [astro-ph].

Boehle, A. et al. (Oct. 2016). “An Improved Distance and Mass Estimate for Sgr A* from a Multistar Orbit Analysis”. In: *The Astrophysical Journal* 830, 17, p. 17. DOI: 10.3847/0004-637X/830/1/17.

Bonnell, I. A. and Rice, W. K. M. (Aug. 2008). “Star Formation Around Supermassive Black Holes”. In: *Science* 321.5892, p. 1060. DOI: 10.1126/science.1160653. arXiv: 0810.2723 [astro-ph].

Bonnet, Henri et al. (Oct. 2004). “First light of SINFONI AO-module at VLT”. In: *Advancements in Adaptive Optics*. Ed. by Domenico Bonaccini Calia, Brent L. Ellerbroek, and Roberto Ragazzoni. Vol. 5490. Society of Photo-Optical Instrumentation Engineers (SPIE) Conference Series, pp. 130–138. DOI: 10.1117/12.551187.

Bouffard, Élie et al. (Oct. 2019). “No Sign of G2’s Encounter Affecting Sgr A*’s X-Ray Flaring Rate from Chandra Observations”. In: *The Astrophysical Journal* 884.2, 148, p. 148. DOI: 10.3847/1538-4357/ab4266. arXiv: 1909.02175 [astro-ph.GA].

Bower, G. C. et al. (Mar. 2015). “Radio and Millimeter Monitoring of Sgr A*: Spectrum, Variability, and Constraints on the G2 Encounter”. In: *The Astrophysical Journal* 802, 69, p. 69. DOI: 10.1088/0004-637X/802/1/69.

Bower, Geoffrey C., Wright, Melvyn C. H., Falcke, Heino, and Backer, Donald C. (May 2003). “Interferometric Detection of Linear Polarization from Sagittarius A* at 230 GHz”. In: *The Astrophysical Journal* 588.1, pp. 331–337. DOI: 10.1086/373989. arXiv: astro-ph/0302227 [astro-ph].

Bower, Geoffrey C. et al. (Dec. 2018). “ALMA Polarimetry of Sgr A*: Probing the Accretion Flow from the Event Horizon to the Bondi Radius”. In: *The Astrophysical Journal* 868.2, 101, p. 101. DOI: 10.3847/1538-4357/aae983. arXiv: 1810.07317 [astro-ph.HE].

Bower, Geoffrey C. et al. (2019). “ALMA Observations of the Terahertz Spectrum of Sagittarius A*”. In: *The Astrophysical Journal* 881.1, p. L2. ISSN: 2041-8213. DOI: 10.3847/2041-8213/ab3397. eprint: 1907.08319. URL: https://doi.org/10.3847/2041-8213/ab3397.

Boyce, H. et al. (Feb. 2019). “Simultaneous X-Ray and Infrared Observations of Sagittarius A*’s Variability”. In: *The Astrophysical Journal* 871.2, 161, p. 161. DOI: 10.3847/1538-4357/aaf71f. arXiv: 1812.05764 [astro-ph.HE].

Brinkerink, C. D. et al. (Apr. 2015). “ALMA and VLA measurements of frequency-dependent time lags in Sagittarius A*: evidence for a relativistic outflow”. In: *Astronomy & Astrophysics* 576, A41, A41. DOI: 10.1051/0004-6361/201424783.

Broderick, A. E. and Narayan, R. (Feb. 2006). “On the Nature of the Compact Dark Mass at the Galactic Center”. In: *The Astrophysical Journal Letters* 638, pp. L21–L24. DOI: 10.1086/500930. eprint: astro-ph/0512211.

Brown, R. L., Lo, K. Y., and Johnston, K. J. (Dec. 1978). “The radio spectrum of the compact source at the galactic center.” In: *Astronomical Journal* 83, pp. 1594–1597. DOI: 10.1086/112368.

Chael, A. A., Narayan, R., and Sadowski, A. (Sept. 2017). “Evolving non-thermal electrons in simulations of black hole accretion”. In: *Monthly Notice of the Royal Astronomical Society* 470, pp. 2367–2386. DOI: 10.1093/mnras/stx1345.

Chan, C.-k. et al. (Oct. 2015). “Fast Variability and Millimeter/IR Flares in GRMHD Models of Sgr A* from Strong-field Gravitational Lensing”. In: *The Astrophysical Journal* 812, 103, p. 103. DOI: 10.1088/0004-637X/812/2/103.

Chatterjee, Koushik et al. (Nov. 2020). “General relativistic MHD simulations of non-thermal flaring in Sagittarius A*”. In: *arXiv e-prints*, arXiv:2011.08904, arXiv:2011.08904. arXiv: 2011.08904 [astro-ph.HE].

Ciurlo, Anna et al. (Jan. 2020). “A population of dust-enshrouded objects orbiting the Galactic black hole”. In: *Nature* 577.7790, pp. 337–340. DOI: 10.1038/s41586-019-1883-y. arXiv: 2001.08325 [astro-ph.GA].

Crawford, M. K. et al. (June 1985). “Mass distribution in the galactic centre”. In: *Nature* 315.6019, pp. 467–470. DOI: 10.1038/315467a0.

Davelaar, J., Mościbrodzka, M., Bronzwaer, T., and Falcke, H. (Apr. 2018). “General relativistic magnetohydrodynamical κ-jet models for Sagittarius A*”. In: *Astronomy & Astrophysics* 612, A34, A34. DOI: 10.1051/0004-6361/201732025. arXiv: 1712.02266 [astro-ph.HE].

Dexter, J. (Oct. 2016). “A public code for general relativistic, polarised radiative transfer around spinning black holes”. In: *Monthly Notice of the Royal Astronomical Society* 462, pp. 115–136. DOI: 10.1093/mnras/stw1526.

Dexter, J., Agol, E., and Fragile, P. C. (Oct. 2009). “Millimeter Flares and VLBI Visibilities from Relativistic Simulations of Magnetized Accretion Onto the Galactic Center Black Hole”. In: *The Astrophysical Journal Letters* 703, pp. L142–L146. DOI: 10.1088/0004-637X/703/2/L142.

Dexter, J., Agol, E., Fragile, P. C., and McKinney, J. C. (July 2010). “The Submillimeter Bump in Sgr A* from Relativistic MHD Simulations”. In: *The Astrophysical Journal* 717, pp. 1092–1104. DOI: 10.1088/0004-637X/717/2/1092.

Dexter, J. and Fragile, P. C. (July 2013). “Tilted black hole accretion disc models of Sagittarius A*: time-variable millimetre to near-infrared emission”. In: *Monthly Notice of the Royal Astronomical Society* 432, pp. 2252–2272. DOI: 10.1093/mnras/stt583.

Dexter, J. et al. (Aug. 2014). “An 8 h characteristic time-scale in submillimetre light curves of Sagittarius A*”. In: *Monthly Notice of the Royal Astronomical Society* 442, pp. 2797–2808. DOI: 10.1093/mnras/stu1039.

Dexter, J et al. (Apr. 2020). “A parameter survey of Sgr A* radiative models from GRMHD simulations with self-consistent electron heating”. In: *Monthly Notices of the Royal Astronomical Society*. staa922. ISSN: 0035-8711. DOI: 10.1093/mnras/staa922. URL: https://doi.org/10.1093/mnras/staa922.

Dexter, J. et al. (May 2020). “A parameter survey of Sgr A* radiative models from GRMHD simulations with self-consistent electron heating”. In: *Monthly Notice of the Royal Astronomical Society* 494.3, pp. 4168–4186. DOI: 10.1093/mnras/staa922. arXiv: 2004.00019 [astro-ph.HE].

Dexter, J. et al. (Oct. 2020). “Sgr A* near-infrared flares from reconnection events in a magnetically arrested disc”. In: *Monthly Notice of the Royal Astronomical Society* 497.4, pp. 4999–5007. DOI: 10.1093/mnras/staa2288. arXiv: 2006.03657 [astro-ph.HE].

Dexter, Jason and Fragile, P Chris (2012). “Tilted black hole accretion disc models of Sagittarius A*: time-variable millimetre to near-infrared emission”. In: *Mon. Not. R. Astron. Soc* 000, pp. 1–17. arXiv: arXiv:1204.4454v1. URL: https://arxiv.org/pdf/1204.4454.pdf.

Dibi, S. et al. (June 2014). “Exploring plasma evolution during Sagittarius A* flares”. In: *Monthly Notice of the Royal Astronomical Society* 441.2, pp. 1005–1016. DOI: 10.1093/mnras/stu599. arXiv: 1504.03495 [astro-ph.HE].

Diolaiti, E. et al. (July 2000). "StarFinder: an IDL GUI-based code to analyze crowded fields with isoplanatic correcting PSF fitting". In: *Adaptive Optical Systems Technology*. Ed. by P. L. Wizinowich. Vol. 4007. Proc. SPIE, pp. 879–888. DOI: 10.1117/12.390377. eprint: astro-ph/0004101.

Do, T. et al. (Feb. 2009). "A Near-Infrared Variability Study of the Galactic Black Hole: A Red Noise Source with NO Detected Periodicity". In: *The Astrophysical Journal* 691, pp. 1021–1034. DOI: 10.1088/0004-637X/691/2/1021.

Do, T. et al. (Feb. 2013). "Stellar Populations in the Central 0.5 pc of the Galaxy. I. A New Method for Constructing Luminosity Functions and Surface-density Profiles". In: *The Astrophysical Journal* 764.2, 154, p. 154. DOI: 10.1088/0004-637X/764/2/154. arXiv: 1301.0539 [astro-ph.SR].

Do, Tuan et al. (2019). "Unprecedented Near-infrared Brightness and Variability of Sgr A*". In: *The Astrophysical Journal* 882.2, p. L27. ISSN: 2041-8213. DOI: 10.3847/2041-8213/ab38c3. URL: https://doi.org/10.3847/2041-8213/ab38c3.

Dodds-Eden, K. et al. (June 2009). "Evidence for X-Ray Synchrotron Emission from Simultaneous Mid-Infrared to X-Ray Observations of a Strong Sgr A* Flare". In: *The Astrophysical Journal* 698, pp. 676–692. DOI: 10.1088/0004-637X/698/1/676.

Dodds-Eden, K. et al. (Feb. 2011). "The Two States of Sgr A* in the Near-infrared: Bright Episodic Flares on Top of Low-level Continuous Variability". In: *The Astrophysical Journal* 728, 37, p. 37. DOI: 10.1088/0004-637X/728/1/37.

Dodds-Eden, Katie et al. (2010). "Time-dependent models of flares from sagittarius a". In: *The Astrophysical Journal* 725.1, pp. 450–465. ISSN: 15384357. DOI: 10.1088/0004-637X/725/1/450. URL: https://iopscience.iop.org/article/10.1088/0004-637X/725/1/450/pdf.

Doeleman, S. S. et al. (Sept. 2008). "Event-horizon-scale structure in the supermassive black hole candidate at the Galactic Centre". In: *Nature* 455, pp. 78–80. DOI: 10.1038/nature07245.

Dolence, J. C., Gammie, C. F., Shiokawa, H., and Noble, S. C. (Feb. 2012). "Near-infrared and X-Ray Quasi-periodic Oscillations in Numerical Models of Sgr A*". In: *The Astrophysical Journal Letters* 746, L10, p. L10. DOI: 10.1088/2041-8205/746/1/L10.

Eatough, R. P. et al. (Sept. 2013). "A strong magnetic field around the supermassive black hole at the centre of the Galaxy". In: *Nature* 501, pp. 391–394. DOI: 10.1038/nature12499.

Eckart, A. and Genzel, R. (Oct. 1996). "Observations of stellar proper motions near the Galactic Centre". In: *Nature* 383.6599, pp. 415–417. DOI: 10.1038/383415a0.

— (Jan. 1997). "Stellar proper motions in the central 0.1 PC of the Galaxy". In: *Monthly Notice of the Royal Astronomical Society* 284.3, pp. 576–598. DOI: 10.1093/mnras/284.3.576.

Eckart, A., Genzel, R., Hofmann, R., Sams, B. J., and Tacconi-Garman, L. E. (May 1995). "High Angular Resolution Spectroscopic and Polarimetric Imaging of the Galactic Center in the Near-Infrared". In: *The Astrophysical Journal Letters* 445, p. L23. DOI: 10.1086/187880.

Eckart, A. et al. (Nov. 2004). "First simultaneous NIR/X-ray detection of a flare from Sgr A*". In: *Astronomy & Astrophysics* 427, pp. 1–11. DOI: 10.1051/0004-6361:20040495. arXiv: astro-ph/0403577 [astro-ph].

Eckart, A. et al. (2006). "Polarimetry of near-infrared flares from Sagittarius A". In: *Astronomy and Astrophysics* 455.1, pp. 1–10. ISSN: 00046361. DOI: 10.1051/0004-6361:20064948. eprint: 0610103 (astro-ph). URL: http://dx.doi.org/10.1051/0004-6361:20064948.

Eckart, A. et al. (Dec. 2008). "Simultaneous NIR/sub-mm observation of flare emission from Sagittarius A*". In: *Astronomy & Astrophysics* 492.2, pp. 337–344. DOI: 10.1051/0004-6361:200810924. arXiv: 0811.2753 [astro-ph].

Eckart, A. et al. (June 2009). "Modeling mm- to X-ray flare emission from Sagittarius A*". In: *Astronomy & Astrophysics* 500.3, pp. 935–946. DOI: 10.1051/0004-6361/200811354. arXiv: 0904.2460 [astro-ph.CO].

Eckart, A. et al. (Jan. 2012). "Millimeter to X-ray flares from Sagittarius A*". In: *Astronomy & Astrophysics* 537, A52, A52. DOI: 10.1051/0004-6361/201117779.

Eisenhauer, F. et al. (July 2005). "SINFONI in the Galactic Center: Young Stars and Infrared Flares in the Central Light-Month". In: *The Astrophysical Journal* 628.1, pp. 246–259. DOI: 10.1086/430667. arXiv: astro-ph/0502129 [astro-ph].

Etxaluze, M., Smith, H. A., Tolls, V., Stark, A. A., and González-Alfonso, E. (Oct. 2011). "The Galactic Center in the Far-infrared". In: *Astronomical Journal* 142, 134, p. 134. DOI: 10.1088/0004-6256/142/4/134.

Falcke, H., Mannheim, K., and Biermann, P. L. (Oct. 1993). "The Galactic Center radio jet." In: *Astronomy & Astrophysics* 278, pp. L1–L4. arXiv: astro-ph/9308031 [astro-ph].

Falcke, H. and Markoff, S. (Oct. 2000). "The jet model for Sgr A*: Radio and X-ray spectrum". In: *Astronomy & Astrophysics* 362, pp. 113–118. eprint: astro-ph/0102186.

Falcke, H. et al. (1998). "SGR A* and Company – Multiwavelength Observations of SGR A* and VLA Search for "Sgr A*'s" in LINERs". In: *IAU Colloq. 164: Radio Emission from Galactic and Extragalactic Compact Sources.* Ed. by J. A. Zensus, G. B. Taylor, and J. M. Wrobel. Vol. 144. Astronomical Society of the Pacific Conference Series, p. 323. eprint: astro-ph/9706245.

Fazio, G. G. et al. (Sept. 2004). "The Infrared Array Camera (IRAC) for the Spitzer Space Telescope". In: *The Astrophysical Journal Supplement Series* 154.1, pp. 10–17. DOI: 10.1086/422843. arXiv: astro-ph/0405616 [astro-ph].

Fazio, Giovanni et al. (May 2018). *The Vital Infrared to X-ray Link in the Sgr A* Accretion Flow.* Spitzer Proposal.

Feldmeier-Krause, A. et al. (Dec. 2015). "KMOS view of the Galactic centre. I. Young stars are centrally concentrated". In: *Astronomy & Astrophysics* 584, A2, A2. DOI: 10.1051/0004-6361/201526336. arXiv: 1509.04707 [astro-ph.GA].

Fellenberg, Sebastiano D. von et al. (2018). "A Detection of Sgr A* in the Far Infrared". In: *The Astrophysical Journal* 862.2, p. 129. DOI: 10.3847/1538-4357/aacd4b. URL: https://doi.org/10.3847/1538-4357/aacd4b.

Forrest, W. J., Shure, M. A., Pipher, J. L., and Woodward, C. E. (Apr. 1987). "Brackett alpha images of the Galactic center". In: *The Galactic Center*. Ed. by Donald C. Backer. Vol. 155. American Institute of Physics Conference Series, pp. 153–156. DOI: 10.1063/1.36414.

Fritz, T. K. et al. (Aug. 2011). "Line Derived Infrared Extinction toward the Galactic Center". In: *The Astrophysical Journal* 737.2, 73, p. 73. DOI: 10.1088/0004-637X/737/2/73.

Fruchter, A. S. and Hook, R. N. (Feb. 2002). "Drizzle: A Method for the Linear Reconstruction of Undersampled Images". In: *The Publications of the Astronomical Society of the Pacific* 114, pp. 144–152. DOI: 10.1086/338393. eprint: astro-ph/9808087.

Fruscione, Antonella et al. (June 2006). "CIAO: Chandra's data analysis system". In: *Society of Photo-Optical Instrumentation Engineers (SPIE) Conference Series*. Ed. by David R. Silva and Rodger E. Doxsey. Vol. 6270. Society of Photo-Optical Instrumentation Engineers (SPIE) Conference Series, 62701V, p. 62701V. DOI: 10.1117/12.671760.

GRAVITY Collaboration et al. (2018a). "Detection of orbital motions near the last stable circular orbit of the massive black hole SgrA*". In: *Astronomy & Astrophysics* 618, p. L10. ISSN: 0004-6361. DOI: 10.1051/0004-6361/201834294. URL: https://doi.org/10.1051/0004-6361/201834294.

GRAVITY Collaboration et al. (2018b). "Detection of the gravitational redshift in the orbit of the star S2 near the Galactic centre massive black hole". In: *Astronomy & Astrophysics* 615, p. L15. ISSN: 0004-6361. DOI: 10.1051/0004-6361/201833718. URL: https://doi.org/10.1051/0004-6361/201833.

GRAVITY Collaboration et al. (2019a). "A geometric distance measurement to the Galactic center black hole with 0.3% uncertainty". In: *Astronomy & Astrophysics* 625, p. L10. ISSN: 0004-6361. DOI: 10.1051/0004-6361/201935656. URL: https://www.aanda.org/10.1051/0004-6361/201935656.

— (2019b). "A geometric distance measurement to the Galactic center black hole with 0.3 uncertainty". In: *Astronomy & Astrophysics* 625, p. L10. ISSN: 0004-6361. DOI: 10.1051/0004-6361/201935656. URL: https://www.aanda.org/10.1051/0004-6361/201935656.

Garmire, Gordon P., Bautz, Mark W., Ford, Peter G., Nousek, John A., and Ricker George R., Jr. (Mar. 2003). "Advanced CCD imaging spectrometer (ACIS) instrument on the Chandra X-ray Observatory". In: *X-Ray and Gamma-Ray Telescopes and Instruments for Astronomy*. Ed. by Joachim E. Truemper and Harvey D. Tananbaum. Vol. 4851. Society of Photo-Optical Instrumentation Engineers (SPIE) Conference Series, pp. 28–44. DOI: 10.1117/12.461599.

Gehrels, N. (Apr. 1986). "Confidence Limits for Small Numbers of Events in Astrophysical Data". In: *The Astrophysical Journal* 303, p. 336. DOI: 10.1086/164079.

Genzel, R., Eckart, A., Ott, T., and Eisenhauer, F. (Oct. 1997). "On the nature of the dark mass in the centre of the Milky Way". In: *Monthly Notice of the Royal Astronomical Society* 291.1, pp. 219–234. DOI: 10.1093/mnras/291.1.219.

Genzel, R., Eisenhauer, F., and Gillessen, S. (Oct. 2010). “The Galactic Center massive black hole and nuclear star cluster”. In: *Reviews of Modern Physics* 82, pp. 3121–3195. DOI: 10.1103/RevModPhys.82.3121.

Genzel, R., Hollenbach, D., and Townes, C. H. (May 1994). “The nucleus of our Galaxy”. In: *Reports on Progress in Physics* 57.5, pp. 417–479. DOI: 10.1088/0034-4885/57/5/001.

Genzel, R., Pichon, C., Eckart, A., Gerhard, O. E., and Ott, T. (Sept. 2000). “Stellar dynamics in the Galactic Centre: proper motions and anisotropy”. In: *Monthly Notice of the Royal Astronomical Society* 317.2, pp. 348–374. DOI: 10.1046/j.1365-8711.2000.03582.x. arXiv: astro-ph/0001428 [astro-ph].

Genzel, R., Thatte, N., Krabbe, A., Kroker, H., and Tacconi-Garman, L. E. (Nov. 1996). “The Dark Mass Concentration in the Central Parsec of the Milky Way”. In: *The Astrophysical Journal* 472, p. 153. DOI: 10.1086/178051.

Genzel, R. and Townes, C. H. (Jan. 1987). “Physical conditions, dynamics, and mass distribution in the center of the galaxy.” In: *Annual Review of Astronomy and Astrophysics* 25, pp. 377–423. DOI: 10.1146/annurev.aa.25.090187.002113.

Genzel, R. et al. (Oct. 2003a). “Near-infrared flares from accreting gas around the supermassive black hole at the Galactic Centre”. In: *Nature* 425, pp. 934–937. DOI: 10.1038/nature02065. eprint: astro-ph/0310821.

Genzel, R. et al. (Sept. 2003b). “The Stellar Cusp around the Supermassive Black Hole in the Galactic Center”. In: *The Astrophysical Journal* 594.2, pp. 812–832. DOI: 10.1086/377127. arXiv: astro-ph/0305423 [astro-ph].

Genzel, R et al. (2003). “The stellar cusp around the supermassive black hole in the Galactic Center”. In: *The Astrophysical Journal*, pp. 812–832. URL: https://iopscience.iop.org/article/10.1086/377127/pdf.

Genzel, Reinhard (Feb. 2021). “A Forty Year Journey”. In: *arXiv e-prints*, arXiv:2102.13000, arXiv:2102.13000. arXiv: 2102.13000 [astro-ph.GA].

Gerhard, Ortwin (Jan. 2001). “The Galactic Center HE I Stars: Remains of a Dissolved Young Cluster?” In: *The Astrophysical Journal Letters* 546.1, pp. L39–L42. DOI: 10.1086/318054. arXiv: astro-ph/0005096 [astro-ph].

Ghez, A. M., Klein, B. L., Morris, M., and Becklin, E. E. (Dec. 1998). “High Proper-Motion Stars in the Vicinity of Sagittarius A*: Evidence for a Supermassive Black Hole at the Center of Our Galaxy”. In: *The Astrophysical Journal* 509.2, pp. 678–686. DOI: 10.1086/306528. arXiv: astro-ph/9807210 [astro-ph].

Ghez, A. M., Morris, M., Becklin, E. E., Tanner, A., and Kremenek, T. (Sept. 2000). “The accelerations of stars orbiting the Milky Way’s central black hole”. In: *Nature* 407.6802, pp. 349–351. DOI: 10.1038/35030032. arXiv: astro-ph/0009339 [astro-ph].

Ghez, A. M. et al. (Sept. 2003). “Full Three Dimensional Orbits For Multiple Stars on Close Approaches to the Central Supermassive Black Hole”. In: *Astronomische Nachrichten Supplement* 324, pp. 527–533. DOI: 10.1002/asna.200385103. eprint: astro-ph/0303151.

Ghez, A. M. et al. (Feb. 2004). “Variable Infrared Emission from the Supermassive Black Hole at the Center of the Milky Way”. In: *The Astrophysical Journal Letters* 601.2, pp. L159–L162. DOI: 10.1086/382024. arXiv: astro-ph/0309076 [astro-ph].

Ghisellini, Gabriele (2013). *Radiative Processes in High Energy Astrophysics*. Vol. 873. DOI: 10.1007/978-3-319-00612-3.

Gillessen, S et al. (2006). "Variations in the spectral slope of Sagittarius A* during a near-infrared flare". In: *The Astrophysical Journal* 640, pp. 163–166.

Gillessen, S. et al. (Feb. 2009). "Monitoring Stellar Orbits Around the Massive Black Hole in the Galactic Center". In: *The Astrophysical Journal* 692.2, pp. 1075–1109. DOI: 10.1088/0004-637X/692/2/1075. arXiv: 0810.4674 [astro-ph].

Gillessen, S. et al. (2012). "A gas cloud on its way towards the supermassive black hole at the Galactic Centre". In: *Nature* 481.7379, pp. 51–54. ISSN: 00280836. DOI: 10.1038/nature10652.

Gillessen, S. et al. (Mar. 2017). "An Update on Monitoring Stellar Orbits in the Galactic Center". In: *The Astrophysical Journal* 837, 30, p. 30. DOI: 10.3847/1538-4357/aa5c41.

Graciá-Carpio, J., Wetzstein, M., and Roussel, H. (Dec. 2015). "The JScanam Map-Maker Method Applied to Herschel/ Photometer Observations". In: eprint: 1512.03252 (astro-ph.IM).

Gravity Collaboration et al. (Apr. 2020a). "Detection of the Schwarzschild precession in the orbit of the star S2 near the Galactic centre massive black hole". In: *Astronomy & Astrophysics* 636, L5, p. L5. DOI: 10.1051/0004-6361/202037813. arXiv: 2004.07187 [astro-ph.GA].

Gravity Collaboration et al. (Nov. 2020b). "Dynamically important magnetic fields near the event horizon of Sgr A*". In: *Astronomy & Astrophysics* 643, A56, A56. DOI: 10.1051/0004-6361/202038283. arXiv: 2009.01859 [astro-ph.HE].

— (Nov. 2020c). "Dynamically important magnetic fields near the event horizon of Sgr A*". In: *Astronomy & Astrophysics* 643, A56, A56. DOI: 10.1051/0004-6361/202038283. arXiv: 2009.01859 [astro-ph.HE].

Gravity Collaboration et al. (Mar. 2020d). "Modeling the orbital motion of Sgr A*'s near-infrared flares". In: *Astronomy & Astrophysics* 635, A143, A143. DOI: 10.1051/0004-6361/201937233. arXiv: 2002.08374 [astro-ph.HE].

— (Mar. 2020e). "Modeling the orbital motion of Sgr A*'s near-infrared flares". In: *Astronomy & Astrophysics* 635, A143, A143. DOI: 10.1051/0004-6361/201937233. arXiv: 2002.08374 [astro-ph.HE].

Gravity Collaboration et al. (2020f). "The flux distribution of Sgr A". In: *Astronomy and Astrophysics* 638. ISSN: 14320746. DOI: 10.1051/0004-6361/202037717. URL: https://doi.org/10.1051/0004-6361/202037717.

Gravity Collaboration et al. (Mar. 2021a). "Improved GRAVITY astrometric accuracy from modeling optical aberrations". In: *Astronomy & Astrophysics* 647, A59, A59. DOI: 10.1051/0004-6361/202040208. arXiv: 2101.12098 [astro-ph.GA].

— (Mar. 2021b). "Improved GRAVITY astrometric accuracy from modeling optical aberrations". In: *Astronomy & Astrophysics* 647, A59, A59. DOI: 10.1051/0004-6361/202040208. arXiv: 2101.12098 [astro-ph.GA].

H.E.S.S. Collaboration et al. (Apr. 2018). "The H.E.S.S. Galactic plane survey". In: *Astronomy & Astrophysics* 612, A1, A1. DOI: 10.1051/0004-6361/201732098. arXiv: 1804.02432 [astro-ph.HE].

Habibi, M. et al. (2017). "Twelve Years of Spectroscopic Monitoring in the Galactic Center: The Closest Look at S-stars near the Black Hole". In: *The Astrophysical Journal* 847.2, p. 120. ISSN: 1538-4357. DOI: 10.3847/1538-4357/aa876f. eprint: 1708.06353. URL: https://doi.org/10.3847/1538-4357/aa876f.

Hansen, Brad M. S. and Milosavljević, Miloš (Aug. 2003). "The Need for a Second Black Hole at the Galactic Center". In: *The Astrophysical Journal Letters* 593.2, pp. L77–L80. DOI: 10.1086/378182. arXiv: astro-ph/0306074 [astro-ph].

Harrison, Fiona A. et al. (June 2013). "The Nuclear Spectroscopic Telescope Array (NuSTAR) High-energy X-Ray Mission". In: *The Astrophysical Journal* 770.2, 103, p. 103. DOI: 10.1088/0004-637X/770/2/103. arXiv: 1301.7307 [astro-ph.IM].

Hillier, D. John and Miller, D. L. (Mar. 1998). "The Treatment of Non-LTE Line Blanketing in Spherically Expanding Outflows". In: *The Astrophysical Journal* 496.1, pp. 407–427. DOI: 10.1086/305350.

Hobbs, Alexander and Nayakshin, Sergei (Mar. 2009). "Simulations of the formation of stellar discs in the Galactic Centre via cloud-cloud collisions". In: *Monthly Notice of the Royal Astronomical Society* 394.1, pp. 191–206. DOI: 10.1111/j.1365-2966.2008.14359.x. arXiv: 0809.3752 [astro-ph].

Hora, J. L. et al. (2014). "Spitzer/irac observations of the variability of sgr A and the object G2 at 4.5 μm". In: *Astrophysical Journal* 793.2, p. 120. ISSN: 15384357. DOI: 10.1088/0004-637X/793/2/120. eprint: 1408.1951. URL: http://sha.ipac.caltech.edu/.

Hornstein, S. D. et al. (Oct. 2007). "A Constant Spectral Index for Sagittarius A* during Infrared/X-Ray Intensity Variations". In: *The Astrophysical Journal* 667, pp. 900–910. DOI: 10.1086/520762.

Howes, G. G. (Nov. 2010). "A prescription for the turbulent heating of astrophysical plasmas". In: *Monthly Notice of the Royal Astronomical Society* 409, pp. L104–L108. DOI: 10.1111/j.1745-3933.2010.00958.x.

Ichimaru, S. (June 1977). "Bimodal behavior of accretion disks - Theory and application to Cygnus X-1 transitions". In: *The Astrophysical Journal* 214, pp. 840–855. DOI: 10.1086/155314.

Ingalls, James G. et al. (Sept. 2012). "Intra-pixel gain variations and high-precision photometry with the Infrared Array Camera (IRAC)". In: *Space Telescopes and Instrumentation 2012: Optical, Infrared, and Millimeter Wave*. Ed. by Mark C. Clampin, Giovanni G. Fazio, Howard A. MacEwen, and Jr. Oschmann Jacobus M. Vol. 8442. Society of Photo-Optical Instrumentation Engineers (SPIE) Conference Series, 84421Y, 84421Y. DOI: 10.1117/12.926947.

Issaoun, S. et al. (Jan. 2019). "The Size, Shape, and Scattering of Sagittarius A* at 86 GHz: First VLBI with ALMA". In: *The Astrophysical Journal* 871.1, 30, p. 30. DOI: 10.3847/1538-4357/aaf732. arXiv: 1901.06226 [astro-ph.HE].

Jansen, F. et al. (Jan. 2001). "XMM-Newton observatory. I. The spacecraft and operations". In: *Astronomy & Astrophysics* 365, pp. L1–L6. DOI: 10.1051/0004-6361:20000036.

Jansky, Karl G. (Dec. 1933a). "Electrical phenomena that apparently are of interstellar origin". In: *Popular Astronomy* 41, pp. 548–555.

— (July 1933b). "Radio Waves from Outside the Solar System". In: *Nature* 132.3323, p. 66. DOI: 10.1038/132066a0.

Jiménez-Rosales, A. and Dexter, J. (May 2018). "The impact of Faraday effects on polarized black hole images of Sagittarius A*." In: *Monthly Notice of the Royal Astronomical Society*. DOI: 10.1093/mnras/sty1210.

Jin, Chichuan, Ponti, Gabriele, Haberl, Frank, and Smith, Randall (July 2017). "Probing the interstellar dust towards the Galactic Centre: dust-scattering halo around AX J1745.6-2901". In: *Monthly Notice of the Royal Astronomical Society* 468.3, pp. 2532–2551. DOI: 10.1093/mnras/stx653. arXiv: 1703.05179 [astro-ph.HE].

Jin, Chichuan, Ponti, Gabriele, Haberl, Frank, Smith, Randall, and Valencic, Lynne (July 2018). "Effects of interstellar dust scattering on the X-ray eclipses of the LMXB AX J1745.6-2901 in the Galactic Centre". In: *Monthly Notice of the Royal Astronomical Society* 477.3, pp. 3480–3506. DOI: 10.1093/mnras/sty869. arXiv: 1802.00637 [astro-ph.HE].

Johnson, M. D. et al. (Dec. 2015). "Resolved magnetic-field structure and variability near the event horizon of Sagittarius A*". In: *Science* 350, pp. 1242–1245. DOI: 10.1126/science.aac7087.

Johnson, Michael D. et al. (Oct. 2018). "The Scattering and Intrinsic Structure of Sagittarius A* at Radio Wavelengths". In: *The Astrophysical Journal* 865.2, 104, p. 104. DOI: 10.3847/1538-4357/aadcff. arXiv: 1808.08966 [astro-ph.GA].

Jones, T. W. and Hardee, P. E. (Feb. 1979). "Maxwellian synchrotron sources". In: *The Astrophysical Journal* 228, pp. 268–278. DOI: 10.1086/156843.

Kardashev, N. S. (Dec. 1962). "Nonstationarity of Spectra of Young Sources of Nonthermal Radio Emission". In: *Sov. Astronom.* 6, p. 317.

Kellermann, K. I., Shaffer, D. B., Clark, B. G., and Geldzahler, B. J. (June 1977). "The small radio source at the galactic center." In: *The Astrophysical Journal Letters* 214, pp. L61–L62. DOI: 10.1086/182443.

Kocsis, Bence and Tremaine, Scott (Mar. 2011). "Resonant relaxation and the warp of the stellar disc in the Galactic Centre". In: *Monthly Notice of the Royal Astronomical Society* 412.1, pp. 187–207. DOI: 10.1111/j.1365-2966.2010.17897.x. arXiv: 1006.0001 [astro-ph.GA].

Krabbe, A., Genzel, R., Drapatz, S., and Rotaciuc, V. (Nov. 1991). "A Cluster of He i Emission-Line Stars in the Galactic Center". In: *The Astrophysical Journal Letters* 382, p. L19. DOI: 10.1086/186204.

Krabbe, A. et al. (July 1995). "The Nuclear Cluster of the Milky Way: Star Formation and Velocity Dispersion in the Central 0.5 Parsec". In: *The Astrophysical Journal Letters* 447, p. L95. DOI: 10.1086/309579.

Künsch, H. R. (1989). "The Jackknife and the Bootstrap for general stationary observations". In: *The Annals of Statistics* 17.3, pp. 1217–1241. DOI: 10.1080/01621459.1994.10476870. URL: https://projecteuclid.org/euclid.aos/1176347265.

Lacy, J. H., Baas, F., Townes, C. H., and Geballe, T. R. (Jan. 1979). "Observations of the motion and distribution of the ionized gas in the central parsec of the Galaxy." In: *The Astrophysical Journal Letters* 227, pp. L17–L20. DOI: 10.1086/182858.

Lacy, J. H., Townes, C. H., Geballe, T. R., and Hollenbach, D. J. (Oct. 1980). "Observations of the motion and distribution of the ionized gas in the central parsec of the Galaxy. II." In: *The Astrophysical Journal* 241, pp. 132–146. DOI: 10.1086/158324.

Lacy, J. H., Townes, C. H., and Hollenbach, D. J. (Nov. 1982). "The nature of the central parsec of the Galaxy". In: *The Astrophysical Journal* 262, pp. 120–134. DOI: 10.1086/160402.

Lenzen, R. et al. (Mar. 2003). "NAOS-CONICA first on sky results in a variety of observing modes". In: *Instrument Design and Performance for Optical/Infrared Ground-based Telescopes*. Ed. by M. Iye and A. F. M. Moorwood. Vol. 4841. Proc. SPIE, pp. 944–952. DOI: 10.1117/12.460044.

Levin, Yuri and Beloborodov, Andrei M. (June 2003). "Stellar Disk in the Galactic Center: A Remnant of a Dense Accretion Disk?" In: *The Astrophysical Journal Letters* 590.1, pp. L33–L36. DOI: 10.1086/376675. arXiv: astro-ph/0303436 [astro-ph].

Li, T. P. and Ma, Y. Q. (Sept. 1983). "Analysis methods for results in gamma-ray astronomy." In: *The Astrophysical Journal* 272, pp. 317–324. DOI: 10.1086/161295.

Li, Ya-Ping, Yuan, Feng, and Wang, Q. Daniel (July 2017). "A magnetohydrodynamic model for multiwavelength flares from Sagittarius A* (I): model and the near-infrared and X-ray flares". In: *Monthly Notice of the Royal Astronomical Society* 468.3, pp. 2552–2568. DOI: 10.1093/mnras/stx655. arXiv: 1611.02904 [astro-ph.HE].

Li, Ya Ping et al. (2015). "Statistics of X-Ray Flares of Sagittarius a: Evidence for Solar-Like Self-Organized Criticality Phenomena". In: *The Astrophysical Journal* 810.1, p. 19. ISSN: 15384357. DOI: 10.1088/0004-637X/810/1/19. eprint: 1506.02946. URL: http://dx.doi.org/10.1088/0004-637X/810/1/19.

Libonate, S., Pipher, J. L., Forrest, W. J., and Ashby, M. L. N. (Jan. 1995). "Near-Infrared Spectra of Compact Stellar Wind Sources at the Galactic Center". In: *The Astrophysical Journal* 439, p. 202. DOI: 10.1086/175165.

Liu, H. B. et al. (Sept. 2016). "The 492 GHz emission of Sgr A* constrained by ALMA". In: *Astronomy & Astrophysics* 593, A44, A44. DOI: 10.1051/0004-6361/201628176.

Löckmann, U. and Baumgardt, H. (Apr. 2009). "On the number of young stellar discs in the Galactic Centre". In: *Monthly Notice of the Royal Astronomical Society* 394.4, pp. 1841–1846. DOI: 10.1111/j.1365-2966.2009.14466.x. arXiv: 0901.1660 [astro-ph.GA].

Loeb, Abraham and Waxman, Eli (Mar. 2007). "Properties of the radio-emitting gas around Sgr A*". In: *Journal of Cosmology and Astroparticle Physics* 2007.3, 011, p. 011. DOI: 10.1088/1475-7516/2007/03/011. arXiv: astro-ph/0702043 [astro-ph].

Lu, J. R. et al. (Dec. 2006). "Galactic Center Youth: Orbits and Origins of the Young Stars in the Central Parsec". In: *Journal of Physics Conference Series*. Vol. 54. Journal of Physics Conference Series, pp. 279–287. DOI: 10.1088/1742-6596/54/1/044.

Lu, J. R. et al. (Jan. 2009). “A Disk of Young Stars at the Galactic Center as Determined by Individual Stellar Orbits”. In: *The Astrophysical Journal* 690.2, pp. 1463–1487. DOI: 10.1088/0004-637X/690/2/1463. arXiv: 0808.3818 [astro-ph].

Lu, J. R. et al. (Feb. 2013). “Stellar Populations in the Central 0.5 pc of the Galaxy. II. The Initial Mass Function”. In: *The Astrophysical Journal* 764.2, 155, p. 155. DOI: 10.1088/0004-637X/764/2/155. arXiv: 1301.0540 [astro-ph.SR].

Lupton, R. et al. (Feb. 2004). “Preparing Red-Green-Blue Images from CCD Data”. In: *The Publications of the Astronomical Society of the Pacific* 116, pp. 133–137. DOI: 10.1086/382245. eprint: astro-ph/0312483.

Lynden-Bell, D. (Aug. 1969). “Galactic Nuclei as Collapsed Old Quasars”. In: *Nature* 223.5207, pp. 690–694. DOI: 10.1038/223690a0.

Lynden-Bell, D. and Rees, M. J. (Jan. 1971). “On quasars, dust and the galactic centre”. In: *Monthly Notice of the Royal Astronomical Society* 152, p. 461. DOI: 10.1093/mnras/152.4.461.

Macquart, Jean-Pierre and Bower, Geoffrey C. (Apr. 2006). “Understanding the Radio Variability of Sagittarius A*”. In: *The Astrophysical Journal* 641.1, pp. 302–318. DOI: 10.1086/500317. arXiv: astro-ph/0512288 [astro-ph].

Malyshev, D., Chernyakova, M., Neronov, A., and Walter, R. (Oct. 2015). “Leptonic origin of the 100 MeV γ-ray emission from the Galactic centre”. In: *Astronomy & Astrophysics* 582, A11, A11. DOI: 10.1051/0004-6361/201526120. arXiv: 1503.05120 [astro-ph.HE].

Mao, S. A., Dexter, J., and Quataert, E. (Apr. 2017). “The impact of non-thermal electrons on event horizon scale images and spectra of Sgr A*”. In: *Monthly Notice of the Royal Astronomical Society* 466, pp. 4307–4319. DOI: 10.1093/mnras/stw3324.

Mao, S. Alwin, Dexter, Jason, and Quataert, Eliot (2016). “The impact of non-thermal electrons on event horizon scale images and spectra of Sgr A*”. In: *Monthly Notices of the Royal Astronomical Society* 466.December, pp. 4307–4319. ISSN: 0035-8711. DOI: 10.1093/mnras/stw3324. eprint: 1611.04601 (astro-ph.HE). URL: https://academic.oup.com/mnras/article/466/4/4307/2733855.

Markoff, S., Falcke, H., Yuan, F., and Biermann, P. L. (Nov. 2001). “The Nature of the 10 kilosecond X-ray flare in Sgr A*”. In: *Astronomy & Astrophysics* 379, pp. L13–L16. DOI: 10.1051/0004-6361:20011346. arXiv: astro-ph/0109081 [astro-ph].

Marrone, D. P. et al. (July 2008). “An X-Ray, Infrared, and Submillimeter Flare of Sagittarius A*”. In: *The Astrophysical Journal* 682, 373-383, pp. 373–383. DOI: 10.1086/588806.

Martins, F. et al. (June 2007). “Stellar and wind properties of massive stars in the central parsec of the Galaxy”. In: *Astronomy & Astrophysics* 468.1, pp. 233–254. DOI: 10.1051/0004-6361:20066688. arXiv: astro-ph/0703211 [astro-ph].

Melia, F. and Falcke, H. (2001). “The Supermassive Black Hole at the Galactic Center”. In: *Annual Review of Astronomy and Astrophysics* 39, pp. 309–352. DOI: 10.1146/annurev.astro.39.1.309. eprint: astro-ph/0106162.

Melia, Fulvio (Mar. 1992). “An Accreting Black Hole Model for Sagittarius A *”. In: *The Astrophysical Journal Letters* 387, p. L25. DOI: 10.1086/186297.

Melia, Fulvio (May 1994). “An Accreting Black Hole Model for Sagittarius A *. II. A Detailed Study”. In: *The Astrophysical Journal* 426, p. 577. DOI: 10.1086/174094.

Melia, Fulvio, Jokipii, J. R., and Narayanan, Ajay (Aug. 1992). “A Determination of the Mass of Sagittarius A * from Its Radio Spectral and Source Size Measurements”. In: *The Astrophysical Journal Letters* 395, p. L87. DOI: 10.1086/186494.

Meyer, L. et al. (2009). “A power-law break in the near-infrared power spectrum of the galactic center black hole”. In: *The Astrophysical Journal* 694.1 PART 2, pp. 87–91. ISSN: 15384357. DOI: 10.1088/0004-637X/694/1/L87. URL: http://iopscience.iop.org/article/10.1088/0004-637X/694/1/L87/pdf.

Morris, Mark (May 1993). “Massive Star Formation near the Galactic Center and the Fate of the Stellar Remnants”. In: *The Astrophysical Journal* 408, p. 496. DOI: 10.1086/172607.

Morris, Mark, Ghez, A. M., and Becklin, E. E. (Jan. 1999). “The galactic center black hole: clues for the evolution of black holes in galactic nuclei”. In: *Advances in Space Research* 23.5-6, pp. 959–968. DOI: 10.1016/S0273-1177(99)00219-7.

Morris, Mark and Serabyn, Eugene (Jan. 1996). “The Galactic Center Environment”. In: *Annual Review of Astronomy and Astrophysics* 34, pp. 645–702. DOI: 10.1146/annurev.astro.34.1.645.

Mościbrodzka, M. and Falcke, H. (Nov. 2013). “Coupled jet-disk model for Sagittarius A*: explaining the flat-spectrum radio core with GRMHD simulations of jets”. In: *Astronomy & Astrophysics* 559, L3, p. L3. DOI: 10.1051/0004-6361/201322692.

Mościbrodzka, M., Gammie, C. F., Dolence, J. C., Shiokawa, H., and Leung, P. K. (Nov. 2009). “Radiative Models of SGR A* from GRMHD Simulations”. In: *The Astrophysical Journal* 706, pp. 497–507. DOI: 10.1088/0004-637X/706/1/497.

Mossoux, E. et al. (May 2016). “Multiwavelength study of the flaring activity of Sagittarius A in 2014 February-April”. In: *Astronomy & Astrophysics* 589, A116, A116. DOI: 10.1051/0004-6361/201527554. arXiv: 1603.01048 [astro-ph.HE].

Narayan, R. and Yi, I. (June 1994). “Advection-dominated accretion: A self-similar solution”. In: *The Astrophysical Journal Letters* 428, pp. L13–L16. DOI: 10.1086/187381. eprint: astro-ph/9403052.

Narayan, Ramesh, Yi, Insu, and Mahadevan, Rohan (Apr. 1995). “Explaining the spectrum of Sagittarius A* with a model of an accreting black hole”. In: *Nature* 374.6523, pp. 623–625. DOI: 10.1038/374623a0.

Nayakshin, Sergei (Oct. 2006). “Massive stars in subparsec rings around galactic centres”. In: *Monthly Notice of the Royal Astronomical Society* 372.1, pp. 143–150. DOI: 10.1111/j.1365-2966.2006.10772.x. arXiv: astro-ph/0512255 [astro-ph].

Nayakshin, Sergei, Cuadra, Jorge, and Springel, Volker (July 2007). “Simulations of star formation in a gaseous disc around Sgr A* - a failed active galactic nucleus”. In: *Monthly Notice of the Royal Astronomical Society* 379.1, pp. 21–33. DOI: 10.1111/j.1365-2966.2007.11938.x. arXiv: astro-ph/0701141 [astro-ph].

Neilsen, J. et al. (Sept. 2013). “A Chandra/HETGS Census of X-Ray Variability from Sgr A* during 2012”. In: *The Astrophysical Journal* 774, 42, p. 42. DOI: 10.1088/0004-637X/774/1/42.

Neilsen, J. et al. (Feb. 2015). "The X-Ray Flux Distribution of Sagittarius A* as Seen by Chandra". In: *The Astrophysical Journal* 799, 199, p. 199. DOI: 10.1088/0004-637X/799/2/199.

Neugebauer, G., Becklin, E. E., Matthews, K., and Wynn-Williams, C. G. (Feb. 1978). "Infrared observations of the galactic center. III. 2.2 micron spectroscopy." In: *The Astrophysical Journal* 220, pp. 149–155. DOI: 10.1086/155889.

Nowak, M. A. et al. (Nov. 2012). "Chandra/HETGS Observations of the Brightest Flare Seen from Sgr A*". In: *The Astrophysical Journal* 759, 95, p. 95. DOI: 10.1088/0004-637X/759/2/95.

Ott, S. (Dec. 2010). "The Herschel Data Processing System HIPE and Pipelines Up and Running Since the Start of the Mission". In: *Astronomical Data Analysis Software and Systems XIX*. Ed. by Y. Mizumoto, K.-I. Morita, and M. Ohishi. Vol. 434. Astronomical Society of the Pacific Conference Series, p. 139.

Özel, F., Psaltis, D., and Narayan, R. (Sept. 2000). "Hybrid Thermal-Nonthermal Synchrotron Emission from Hot Accretion Flows". In: *The Astrophysical Journal* 541, pp. 234–249. DOI: 10.1086/309396. eprint: astro-ph/0004195.

Ozernoy, L. M. (Jan. 1993). "Evaluating the mass of a putative black hole at the Galactic center". In: *Back to the Galaxy*. Ed. by Stephen S. Holt and Francis Verter. Vol. 278. American Institute of Physics Conference Series, pp. 69–72. DOI: 10.1063/1.43951.

Ozernoy, Leonid M. (Jan. 1989). "Constraints on and Alternatives to a Massive Black Hole at the Galactic Center (review)". In: *The Center of the Galaxy*. Ed. by Mark Morris. Vol. 136, p. 555.

Pacholczyk, A. G. (1970). *Radio astrophysics. Nonthermal processes in galactic and extragalactic sources.*

Pandya, A., Zhang, Z., Chandra, M., and Gammie, C. F. (May 2016). "Polarized Synchrotron Emissivities and Absorptivities for Relativistic Thermal, Power-law, and Kappa Distribution Functions". In: *The Astrophysical Journal* 822, 34, p. 34. DOI: 10.3847/0004-637X/822/1/34.

Paumard, T., Maillard, J. P., Morris, M., and Rigaut, F. (Feb. 2001). "New results on the helium stars in the galactic center using BEAR spectro-imagery". In: *Astronomy & Astrophysics* 366, pp. 466–480. DOI: 10.1051/0004-6361:20000227. arXiv: astro-ph/0011215 [astro-ph].

Paumard, T. et al. (June 2006). "The Two Young Star Disks in the Central Parsec of the Galaxy: Properties, Dynamics, and Formation". In: *The Astrophysical Journal* 643.2, pp. 1011–1035. DOI: 10.1086/503273. arXiv: astro-ph/0601268 [astro-ph].

Perrin, G. and Woillez, J. (2019). "Single-mode interferometric field of view in partial turbulence correction Application to the observation of the environment of Sgr A with GRAVITY". In: *Astronomy and Astrophysics* 625, p. 48. ISSN: 14320746. DOI: 10.1051/0004-6361/201834013. eprint: 1903.10937. URL: https://doi.org/10.1051/0004-6361/201834013.

Pfuhl, O. et al. (Nov. 2011). "The Star Formation History of the Milky Way's Nuclear Star Cluster". In: *The Astrophysical Journal* 741.2, 108, p. 108. DOI: 10.1088/0004-637X/741/2/108. arXiv: 1110.1633 [astro-ph.GA].

Pfuhl, O. et al. (Feb. 2014). “Massive Binaries in the Vicinity of Sgr A*”. In: *The Astrophysical Journal* 782.2, 101, p. 101. DOI: 10.1088/0004-637X/782/2/101. arXiv: 1307.7996 [astro-ph.GA].

Pilbratt, G. L. et al. (July 2010). “Herschel Space Observatory. An ESA facility for far-infrared and submillimetre astronomy”. In: *Astronomy & Astrophysics* 518, L1, p. L1. DOI: 10.1051/0004-6361/201014759.

Poglitsch, A. et al. (July 2008). “The Photodetector Array Camera and Spectrometer (PACS) for the Herschel Space Observatory”. In: *Space Telescopes and Instrumentation 2008: Optical, Infrared, and Millimeter*. Vol. 7010. Proc. SPIE, 701005, p. 701005. DOI: 10.1117/12.790016.

Ponti, G. et al. (Dec. 2015). “Fifteen years of XMM-Newton and Chandra monitoring of Sgr A: evidence for a recent increase in the bright flaring rate”. In: *Monthly Notice of the Royal Astronomical Society* 454.2, pp. 1525–1544. DOI: 10.1093/mnras/stv1537.

Ponti, G. et al. (June 2017). “A powerful flare from Sgr A* confirms the synchrotron nature of the X-ray emission”. In: *Monthly Notice of the Royal Astronomical Society* 468, pp. 2447–2468. DOI: 10.1093/mnras/stx596.

Porquet, D. et al. (Aug. 2003). “XMM-Newton observation of the brightest X-ray flare detected so far from Sgr A*”. In: *Astronomy & Astrophysics* 407, pp. L17–L20. DOI: 10.1051/0004-6361:20030983. arXiv: astro-ph/0307110 [astro-ph].

Porquet, D. et al. (Sept. 2008). “X-ray hiccups from Sagittarius A* observed by XMM-Newton. The second brightest flare and three moderate flares caught in half a day”. In: *Astronomy & Astrophysics* 488.2, pp. 549–557. DOI: 10.1051/0004-6361:200809986. arXiv: 0806.4088 [astro-ph].

Portegies Zwart, Simon F., McMillan, Stephen L. W., and Gerhard, Ortwin (Aug. 2003). “The Origin of IRS 16: Dynamically Driven In-Spiral of a Dense Star Cluster to the Galactic Center?” In: *The Astrophysical Journal* 593.1, pp. 352–357. DOI: 10.1086/376439. arXiv: astro-ph/0303599 [astro-ph].

Quataert, Eliot (Aug. 2002). “A Thermal Bremsstrahlung Model for the Quiescent X-Ray Emission from Sagittarius A*”. In: *The Astrophysical Journal* 575.2, pp. 855–859. DOI: 10.1086/341425. arXiv: astro-ph/0201395 [astro-ph].

Rees, M. J. (Jan. 1982). “The Compact source at the Galactic Center”. In: *The Galactic Center*. Ed. by G. R. Riegler and R. D. Blandford. Vol. 83. American Institute of Physics Conference Series, pp. 166–176. DOI: 10.1063/1.33482.

Ressler, S. M., Tchekhovskoy, A., Quataert, E., and Gammie, C. F. (May 2017). “The disc-jet symbiosis emerges: modelling the emission of Sagittarius A* with electron thermodynamics”. In: *Monthly Notice of the Royal Astronomical Society* 467.3, pp. 3604–3619. DOI: 10.1093/mnras/stx364.

Rieke, G. H. and Low, F. J. (Sept. 1973). “Infrared maps of the galactic nucleus.” In: *The Astrophysical Journal* 184, pp. 415–425. DOI: 10.1086/152340.

Ripperda, Bart, Bacchini, Fabio, and Philippov, Alexander A. (Sept. 2020). “Magnetic Reconnection and Hot Spot Formation in Black Hole Accretion Disks”. In: *The Astrophysical Journal* 900.2, 100, p. 100. DOI: 10.3847/1538-4357/ababab. arXiv: 2003.04330 [astro-ph.HE].

Rousset, G. et al. (Feb. 2003). "NAOS, the first AO system of the VLT: on-sky performance". In: *Adaptive Optical System Technologies II*. Ed. by P. L. Wizinowich and D. Bonaccini. Vol. 4839. Proc. SPIE, pp. 140–149. DOI: 10.1117/12.459332.

Sánchez-Portal, M. et al. (July 2014). "The pointing system of the Herschel space observatory. Description, Calibration, Performance and improvements". In: *Experimental Astronomy* 37, pp. 453–479. DOI: 10.1007/s10686-014-9396-z.

Scargle, Jeffrey D. (June 2020). "Studies in Astronomical Time-series Analysis. VII. An Enquiry Concerning Nonlinearity, the rms-Mean Flux Relation, and Lognormal Flux Distributions". In: *The Astrophysical Journal* 895.2, 90, p. 90. DOI: 10.3847/1538-4357/ab8d38.

Scepi, Nicolas, Dexter, Jason, and Begelman, Mitchell C. (July 2021). "Sgr A* X-ray flares from non-thermal particle acceleration in a magnetically arrested disc". In: *arXiv e-prints*, arXiv:2107.08056, arXiv:2107.08056. arXiv: 2107.08056 [astro-ph.HE].

Schödel, R., Merritt, D., and Eckart, A. (July 2009). "The nuclear star cluster of the Milky Way: proper motions and mass". In: *Astronomy & Astrophysics* 502.1, pp. 91–111. DOI: 10.1051/0004-6361/200810922. arXiv: 0902.3892 [astro-ph.GA].

Schödel, R., Najarro, F., Muzic, K., and Eckart, A. (2010). "Peering through the veil: near-infrared photometry and extinction for the Galactic nuclear star cluster". In: *Astronomy and Astrophysics* 511, A18. ISSN: 0004-6361. DOI: 10.1051/0004-6361/200913183. URL: http://archive.eso.org/asm/ambient-server?.

Schödel, R. et al. (Oct. 2002a). "A star in a 15.2-year orbit around the supermassive black hole at the centre of the Milky Way". In: *Nature* 419.6908, pp. 694–696. DOI: 10.1038/nature01121. arXiv: astro-ph/0210426 [astro-ph].

— (Oct. 2002b). "A star in a 15.2-year orbit around the supermassive black hole at the centre of the Milky Way". In: *Nature* 419, pp. 694–696. DOI: 10.1038/nature01121. eprint: astro-ph/0210426.

Schödel, R. et al. (Oct. 2003). "Stellar Dynamics in the Central Arcsecond of Our Galaxy". In: *The Astrophysical Journal* 596.2, pp. 1015–1034. DOI: 10.1086/378122. arXiv: astro-ph/0306214 [astro-ph].

Schödel, R. et al. (Aug. 2011). "The mean infrared emission of Sagittarius A*". In: *Astronomy & Astrophysics* 532, A83, A83. DOI: 10.1051/0004-6361/201116994.

Scott, David W. (2015). *Multivariate density estimation: Theory, practice, and visualization: Second edition*. 2nd. John Wiley & Sons, Inc., pp. 1–360. ISBN: 9781118575574. DOI: 10.1002/9781118575574. URL: https://onlinelibrary.wiley.com/doi/book/10.1002/9781118575574.

Serabyn, E., Carlstrom, J. E., and Scoville, N. Z. (Dec. 1992). "The Continuum Flux from Sagittarius A * at 222 GHz". In: *The Astrophysical Journal Letters* 401, p. L87. DOI: 10.1086/186677.

Serabyn, E. et al. (Nov. 1997). "High-Frequency Measurements of the Spectrum of Sagittarius A*". In: *The Astrophysical Journal Letters* 490, pp. L77–L81. DOI: 10.1086/311010.

Shcherbakov, R. V., Penna, R. F., and McKinney, J. C. (Aug. 2012). "Sagittarius A* Accretion Flow and Black Hole Parameters from General Relativistic Dynamical and

Polarized Radiative Modeling". In: *The Astrophysical Journal* 755, 133, p. 133. DOI: 10.1088/0004-637X/755/2/133.

Simons, D. A. and Becklin, E. E. (May 1996). "High Resolution 3.8 micron Imaging of the Galactic Center". In: *Astronomical Journal* 111, p. 1908. DOI: 10.1086/117929.

Sironi, Lorenzo and Beloborodov, Andrei M. (Aug. 2020). "Kinetic Simulations of Radiative Magnetic Reconnection in the Coronae of Accreting Black Holes". In: *The Astrophysical Journal* 899.1, 52, p. 52. DOI: 10.3847/1538-4357/aba622. arXiv: 1908.08138 [astro-ph.HE].

Skilling, John (Nov. 2004). "Nested Sampling". In: *Bayesian Inference and Maximum Entropy Methods in Science and Engineering: 24th International Workshop on Bayesian Inference and Maximum Entropy Methods in Science and Engineering*. Ed. by Rainer Fischer, Roland Preuss, and Udo Von Toussaint. Vol. 735. American Institute of Physics Conference Series, pp. 395–405. DOI: 10.1063/1.1835238.

Skilling, John (2006a). "Nested sampling for general Bayesian computation". In: *Bayesian Analysis* 1.4, pp. 833 –859. DOI: 10.1214/06-BA127. URL: https://doi.org/10.1214/06-BA127.

— (2006b). "Nested sampling for general Bayesian computation". In: *Bayesian Analysis* 1.4, pp. 833 –859. DOI: 10.1214/06-BA127. URL: https://doi.org/10.1214/06-BA127.

Smothers, Ronald (1998). *Commemorating a Discovery in Radio Astronomy.* URL: https://www.nytimes.com/1998/06/09/nyregion/commemorating-a-discovery-in-radio-astronomy.html (visited on 06/14/2021).

Speagle, Joshua S. (Apr. 2020). "DYNESTY: a dynamic nested sampling package for estimating Bayesian posteriors and evidences". In: *Monthly Notice of the Royal Astronomical Society* 493.3, pp. 3132–3158. DOI: 10.1093/mnras/staa278. arXiv: 1904.02180 [astro-ph.IM].

Stewart, I. M. (Mar. 2009). "Maximum-likelihood detection of sources among Poissonian noise". In: *Astronomy & Astrophysics* 495.3, pp. 989–1003. DOI: 10.1051/0004-6361:200811311. arXiv: 0901.3276 [astro-ph.IM].

Stone, J. M. et al. (July 2016). "Far Infrared Variability of Sagittarius A*: 25.5 hr of Monitoring with Herschel". In: *The Astrophysical Journal* 825, 32, p. 32. DOI: 10.3847/0004-637X/825/1/32.

Strüder, L. et al. (Jan. 2001). "The European Photon Imaging Camera on XMM-Newton: The pn-CCD camera". In: *Astronomy & Astrophysics* 365, pp. L18–L26. DOI: 10.1051/0004-6361:20000066.

Subroweit, M. et al. (May 2017). "Submillimeter and radio variability of Sagittarius A*. A statistical analysis". In: *Astronomy & Astrophysics* 601, A80, A80. DOI: 10.1051/0004-6361/201628530.

Tamblyn, Peter et al. (Jan. 1996). "The Peculiar Population of Hot Stars at the Galactic Center". In: *The Astrophysical Journal* 456, p. 206. DOI: 10.1086/176641.

Trap, G. et al. (Apr. 2011). "Concurrent X-ray, near-infrared, sub-millimeter, and GeV gamma-ray observations of Sagittarius A*". In: *Astronomy & Astrophysics* 528, A140, A140. DOI: 10.1051/0004-6361/201015157. arXiv: 1102.0192 [astro-ph.HE].

Trippe, S. et al. (Dec. 2008). "Kinematics of the old stellar population at the Galactic centre". In: *Astronomy & Astrophysics* 492.2, pp. 419–439. DOI: 10.1051/0004-6361:200810191. arXiv: 0810.1040 [astro-ph].

Uttley, P., McHardy, I. M., and Vaughan, S. (2005). "Non-linear X-ray variability in X-ray binaries and active galaxies". In: *Monthly Notices of the Royal Astronomical Society* 359.1, pp. 345–362. ISSN: 00358711. DOI: 10.1111/j.1365-2966.2005.08886.x. eprint: 0502112 (astro-ph).

Vaughan, S., Edelson, R., Warwick, R. S., and Uttley, P. (2003). "On characterizing the variability properties of X-ray light curves from active galaxies". In: *Monthly Notices of the Royal Astronomical Society* 345.4, pp. 1271–1284. ISSN: 00358711. DOI: 10.1046/j.1365-2966.2003.07042.x. URL: https://academic.oup.com/mnras/article-abstract/345/4/1271/1071679.

Verner, D. A., Ferland, G. J., Korista, K. T., and Yakovlev, D. G. (July 1996). "Atomic Data for Astrophysics. II. New Analytic FITS for Photoionization Cross Sections of Atoms and Ions". In: *The Astrophysical Journal* 465, p. 487. DOI: 10.1086/177435. arXiv: astro-ph/9601009 [astro-ph].

Waisberg, Idel (2019). *Optical Interferometry of Compact Objects: Testing General Relativity and the Extremes of Accretion.* Tech. rep.

Weisskopf, Martin C., Tananbaum, Harvey D., Van Speybroeck, Leon P., and O'Dell, Stephen L. (July 2000). "Chandra X-ray Observatory (CXO): overview". In: *X-Ray Optics, Instruments, and Missions III.* Ed. by Joachim E. Truemper and Bernd Aschenbach. Vol. 4012. Society of Photo-Optical Instrumentation Engineers (SPIE) Conference Series, pp. 2–16. DOI: 10.1117/12.391545. arXiv: astro-ph/0004127 [astro-ph].

Werner, Gregory R. and Uzdensky, Dmitri A. (June 2021). "Reconnection and particle acceleration in 3D current sheet evolution in moderately-magnetized astrophysical pair plasma". In: *arXiv e-prints*, arXiv:2106.02790, arXiv:2106.02790. arXiv: 2106.02790 [astro-ph.HE].

Werner, M. W. et al. (Sept. 2004). "The Spitzer Space Telescope Mission". In: *The Astrophysical Journal Supplement Series* 154.1, pp. 1–9. DOI: 10.1086/422992. arXiv: astro-ph/0406223 [astro-ph].

Widmann, F (Nov. 2021). "Instrumental progress to test General Relativity in the Galactic Center".

Wilms, J., Allen, A., and McCray, R. (Oct. 2000a). "On the Absorption of X-Rays in the Interstellar Medium". In: *The Astrophysical Journal* 542.2, pp. 914–924. DOI: 10.1086/317016. arXiv: astro-ph/0008425 [astro-ph].

— (Oct. 2000b). "On the Absorption of X-Rays in the Interstellar Medium". In: *The Astrophysical Journal* 542.2, pp. 914–924. DOI: 10.1086/317016. arXiv: astro-ph/0008425 [astro-ph].

Witzel, G. et al. (Dec. 2012). "Source-intrinsic Near-infrared Properties of Sgr A*: Total Intensity Measurements". In: *The Astrophysical Journal Supplement Series* 203, 18, p. 18. DOI: 10.1088/0067-0049/203/2/18.

Witzel, G. et al. (Aug. 2018). "Variability Timescale and Spectral Index of Sgr A* in the Near Infrared: Approximate Bayesian Computation Analysis of the Variability of the

Closest Supermassive Black Hole”. In: *The Astrophysical Journal* 863.1, p. 15. ISSN: 1538-4357. DOI: 10.3847/1538-4357/aace62. eprint: 1806.00479.

Wollman, E. R., Geballe, T. R., Lacy, J. H., Townes, C. H., and Rank, D. M. (Apr. 1976). “Spectral and spatial resolution of the 12.8 micron Ne II emission from the galactic center.” In: *The Astrophysical Journal Letters* 205, pp. L5–L9. DOI: 10.1086/182078.

— (Dec. 1977). “Ne II 12.8 micron emission from the galactic center. II.” In: *The Astrophysical Journal Letters* 218, pp. L103–L107. DOI: 10.1086/182585.

Wong, Kai, Zhdankin, Vladimir, Uzdensky, Dmitri A., Werner, Gregory R., and Begelman, Mitchell C. (Apr. 2020). “First-principles Demonstration of Diffusive-advective Particle Acceleration in Kinetic Simulations of Relativistic Plasma Turbulence”. In: *The Astrophysical Journal Letters* 893.1, L7, p. L7. DOI: 10.3847/2041-8213/ab8122. arXiv: 1901.03439 [astro-ph.HE].

Xu, Ya-Di, Narayan, Ramesh, Quataert, Eliot, Yuan, Feng, and Baganoff, Frederick K. (Mar. 2006). “Thermal X-Ray Iron Line Emission from the Galactic Center Black Hole Sagittarius A*”. In: *The Astrophysical Journal* 640.1, pp. 319–326. DOI: 10.1086/499932. arXiv: astro-ph/0511590 [astro-ph].

Yelda, S. et al. (Mar. 2014). “Properties of the Remnant Clockwise Disk of Young Stars in the Galactic Center”. In: *The Astrophysical Journal* 783.2, 131, p. 131. DOI: 10.1088/0004-637X/783/2/131. arXiv: 1401.7354 [astro-ph.GA].

Yoon, D. et al. (Dec. 2020). “Spectral and imaging properties of Sgr A* from high-resolution 3D GRMHD simulations with radiative cooling”. In: *Monthly Notice of the Royal Astronomical Society* 499.3, pp. 3178–3192. DOI: 10.1093/mnras/staa3031. arXiv: 2009.14227 [astro-ph.HE].

Yuan, F., Lin, J., Wu, K., and Ho, L. C. (June 2009). “A magnetohydrodynamical model for the formation of episodic jets”. In: *Monthly Notice of the Royal Astronomical Society* 395, pp. 2183–2188. DOI: 10.1111/j.1365-2966.2009.14673.x.

Yuan, F., Markoff, S., and Falcke, H. (Sept. 2003a). “A Jet-ADAF Model for Sgr A*”. In: *Astronomische Nachrichten Supplement* 324, pp. 453–458. DOI: 10.1002/asna.200385044.

Yuan, F. and Narayan, R. (Aug. 2014). “Hot Accretion Flows Around Black Holes”. In: *Annual Review of Astronomy and Astrophysics* 52, pp. 529–588. DOI: 10.1146/annurev-astro-082812-141003.

Yuan, F., Quataert, E., and Narayan, R. (Nov. 2003b). “Nonthermal Electrons in Radiatively Inefficient Accretion Flow Models of Sagittarius A*”. In: *The Astrophysical Journal* 598, pp. 301–312. DOI: 10.1086/378716. eprint: astro-ph/0304125.

— (May 2004). “On the Nature of the Variable Infrared Emission from Sagittarius A*”. In: *The Astrophysical Journal* 606, pp. 894–899. DOI: 10.1086/383117. eprint: astro-ph/0401429.

Yusef-Zadeh, F., Roberts, D., Wardle, M., Heinke, C. O., and Bower, G. C. (Oct. 2006). “Flaring Activity of Sagittarius A* at 43 and 22 GHz: Evidence for Expanding Hot Plasma”. In: *The Astrophysical Journal* 650, pp. 189–194. DOI: 10.1086/506375. eprint: astro-ph/0603685.

Yusef-Zadeh, F. et al. (July 2008). “Simultaneous Chandra, CSO, and VLA Observations of Sgr A*: The Nature of Flaring Activity”. In: *The Astrophysical Journal* 682.1, pp. 361–372. DOI: 10.1086/588803. arXiv: 0712.2882 [astro-ph].

Yusef-Zadeh, F. et al. (Nov. 2009a). “Simultaneous Multi-Wavelength Observations of Sgr A* During 2007 April 1-11”. In: *The Astrophysical Journal* 706, pp. 348–375. DOI: 10.1088/0004-637X/706/1/348.

— (Nov. 2009b). “Simultaneous Multi-Wavelength Observations of Sgr A* During 2007 April 1-11”. In: *The Astrophysical Journal* 706.1, pp. 348–375. DOI: 10.1088/0004-637X/706/1/348. arXiv: 0907.3786 [astro-ph.GA].

Zhao, J.-H. et al. (Mar. 2003). “Variability of Sagittarius A*: Flares at 1 Millimeter”. In: *The Astrophysical Journal Letters* 586, pp. L29–L32. DOI: 10.1086/374581. eprint: astro-ph/0302062.

Zylka, R. and Mezger, P. G. (Jan. 1988). “Observations of SGR A west and SGR A at lambda 1.3 mm.” In: *Astronomy & Astrophysics* 190, pp. L25–L28.

Zylka, R., Mezger, P. G., and Lesch, H. (July 1992). “Anatomy of the Sagittarius A complex. II. Lambda 1300 mu.m and lambda 870 mu.m continuum observations of SGR A * and its submm/IR spectrum.” In: *Astronomy & Astrophysics* 261, pp. 119–129.

Appendix

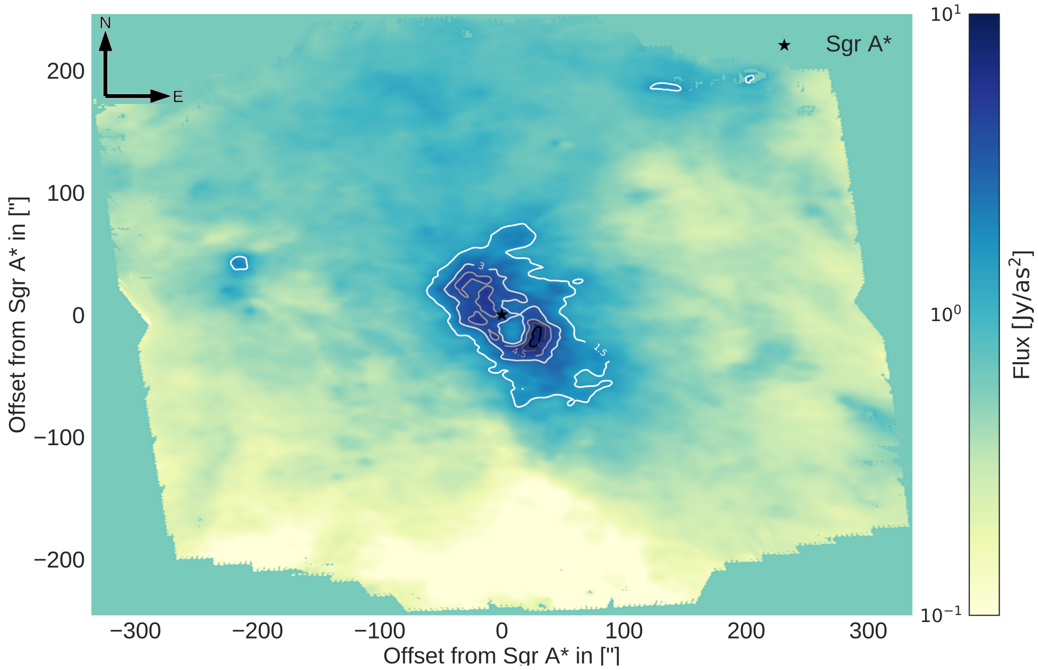

Figure 2: Blue band median image of March 15 and 21. The integration time is ∼ 16 hours. The color scale is logarithmic. JScanam creates images with relative intensities. To overcome this, we have normalized the images in Figure 2, 3 and 4, so that the pixel with the lowest flux value has a flux of 0 Jy.

A1 Appendix: A Detection of Sagittarius A* in the Far-Infrared

A1.1 Median maps

We plot the median images of the three bands in Figures 2, 3 and 4. Since the images are pointing corrected, the images presented here are the highest resolution images of the Galactic Center to date. Since JScanam does not produce images of absolute intensity we have normalized the maps such that the darkest pixel contains zero flux.

A1.2 Pointing offset correction

Herschel experiences pointing offset errors. Simply aligning the images by shifting them on top of one another is not sufficient, as the pointing error smears out the images. This hinders the 1/f noise removal of JScanam from performing optimally. Therefore the pointing correction needs to be handled iteratively.

We correct the pointing offset as follows:

1. Reduce the raw level 2 data by running JScanam. For all observations, this creates sets of images impaired by the pointing errors.

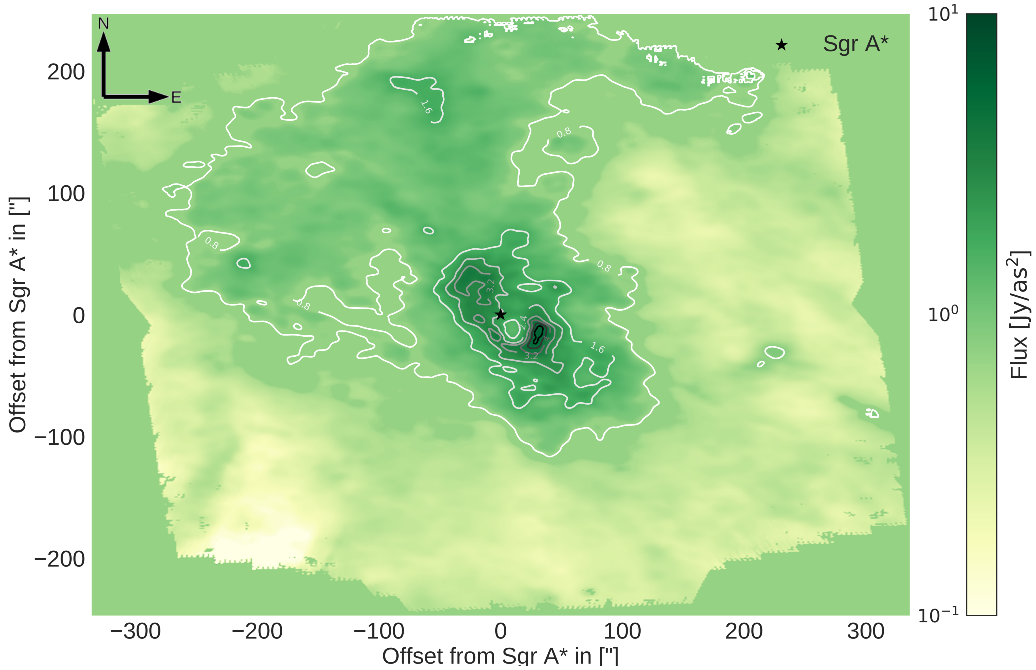

Figure 3: As in Figure 2 for the green band median image. The observation dates are March 17 and 19, totaling to an integration time of $\sim$ 16 hours.

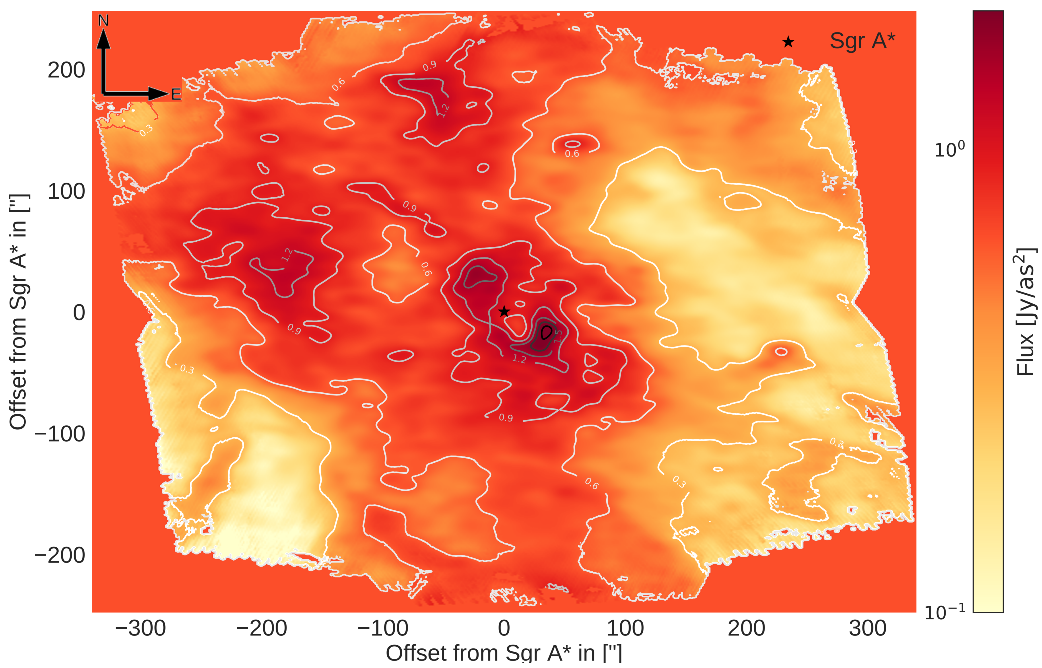

Figure 4: As in Figure 2 for the red band median image and all nights. The integration time is around 40 hours.

2. Compute the pointing offsets of these images using the HIPE method PhotHelper.getOptimalShift. This routine computes the offsets of the first image of an observation to the subsequent ones. The pointing offsets are then saved for further processing.

3. Correct the just calculated pointing offsets in the raw level 2 data, using the HIPE method PhotHelper.shiftFramesCoordinates[2]. This functions shifts the raw level 2 data, so that the offsets are neutralized. The shifted level 2 data of an observation is now, in first order, aligned to its first image.

4. Rerun JScanam, using the shifted level 2 data. Since the images are now better aligned the averaged image of the observation is less smeared out. Because of that, 1/f noise removal of JScanam performs more efficiently. This allows for a sharper images, and therefore, when we recalculate the pointing offsets (repeat step 2) they decrease.

5. Add the newly calculated pointing offsets (from step 3) together with the pointing offsets from the first iteration (step 2). The combined point offsets are now again applied to the raw level 2 data, shifting it. This creates a new set of shifted level 2 data.

6. JScanam always uses two observations with scan directions for the reduction. These observations are tilted against each other and the scanning pattern is different. JScanam reduces both observations at the same time. Since both directions are impaired by the pointing offset error, the pointing offsets in one observation impair the calculation of the pointing offsets in the other observation. To minimize this effect, we restart the pointing offset correction from step 1. The difference to before is that we now always pair the raw level 2 data of one observation with the shifted level 2 data of another observation. The uncorrected observation is reduced together with the shifted one and its pointing offsets are determined and corrected as before (steps 1 to 5).

7. We iterate this last step four times, always determining the pointing offsets of one observation. After the last iteration, the pointing offsets in all observations are smaller than $0.05''$.

A1.3 Noise characteristics

We have verified that the fluxes in the reference pixels are approximately Gaussian distributed, see Figure 5. This justifies the way we have calculated our error bars and the false alarm rate. Figure 6 shows the histograms for all nights. For March 19 the uncertainty in the manual fine tuning (c.f. 2.2.2 and Appendix A1.4) causes a positive skew of the histogram.

[2]Both routines are available for use in HIPE version 15.0 2412

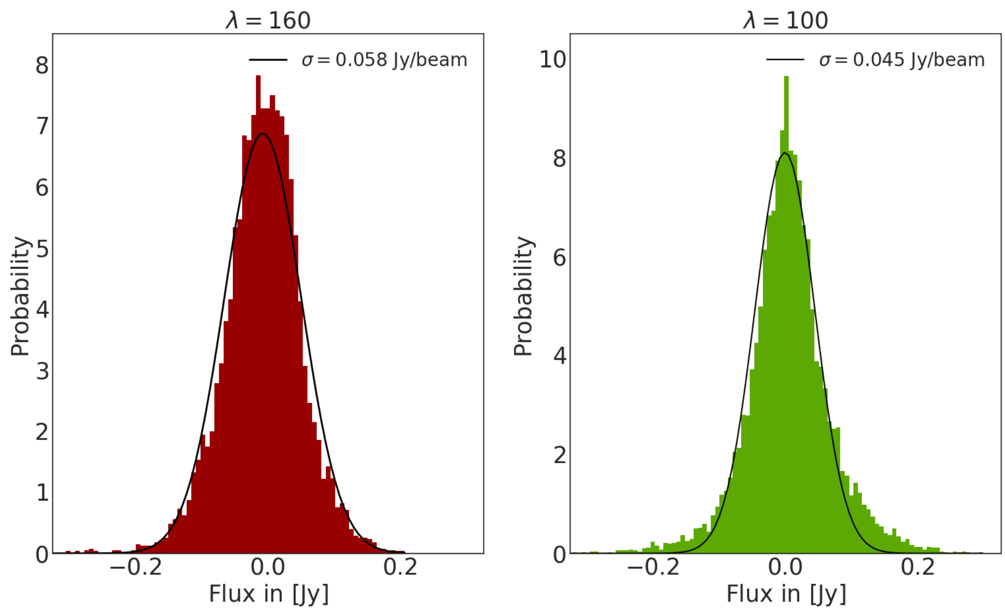

Figure 5: Histogram of all measured amplitudes of the reference pixels during the March 17 observation; the left histogram is for the red band and the right for the green band. The standard deviation is $\sigma = 0.06$Jy/beam for the red band and $\sigma = 0.05$Jy/beam for the green band.

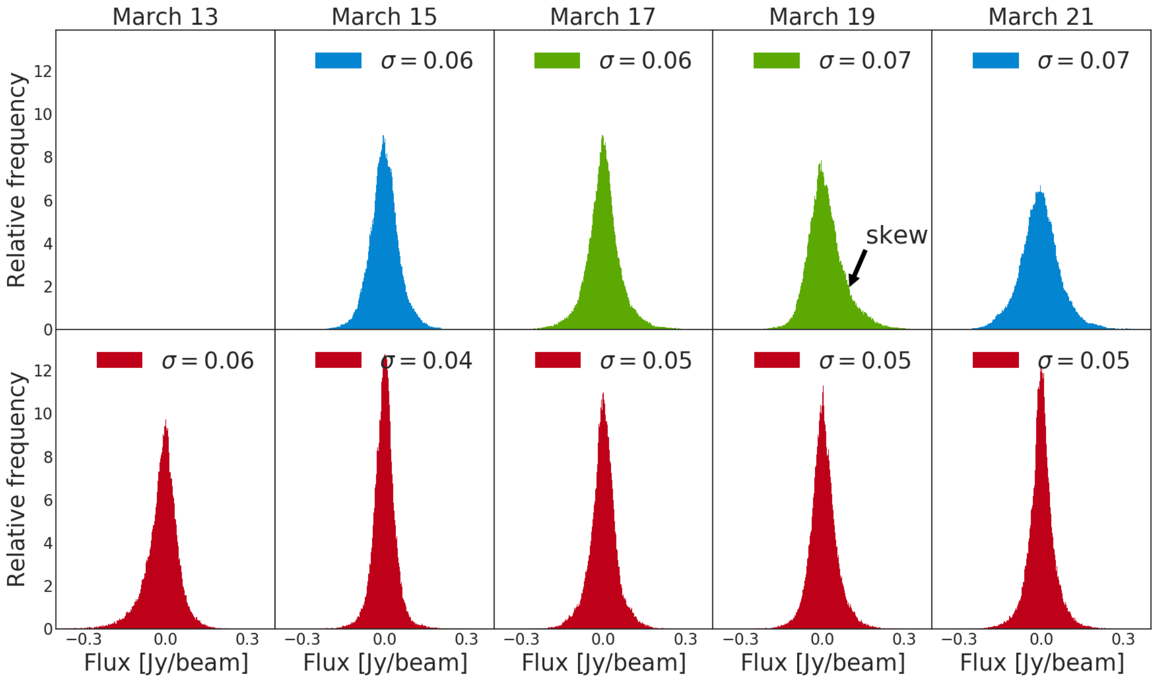

Figure 6: As in Figure 5, but for all nights. For March 19 the skew induced by the dedicated drift correction is visible, which has not been corrected in this histogram.

A1.4 Manual fine tuning

Manual fine tuning for March 17

For the March 17 observation, one notices that the flux at the position of Sgr A* varies more than at the reference points. Inspection shows a discernible point source. Consequently, we only use the first five and the last ten maps to compute the median map and the linear fit. This is a robust method as the linear slope is predominantly constrained by the boundary points and there are still enough (15) maps to compute a well-defined median. The validity of this can be checked by inspecting the reference light curves: the signal drifts are efficiently removed for all reference light curves. We point out that the variability is significant even without this additional step.

Manual fine tuning for March 19

For the March 19 observation, a flux increase occurs during the middle and end times of the observation. This makes a robust correction of the linear drift more difficult. The increase in flux in the middle of the observation is only very weak. It is not clear if including it is reasonable or not. Thus we have no obvious criterion which maps to include for the linear drift correction.

To account for this systematic uncertainty, we test different combinations of maps, which we deem reasonable. Depending on the linear drift correction we obtain different values of

the flux excursions. We estimate the systematic uncertainty as the minimal and maximal value produced with these corrections. For the red band light curve this adds a systematic uncertainty of ± 0.02 Jy for the peak flux. For the green band the systematic uncertainty is $+0.05 \ -0.01$ Jy. The light curves shown in Figure 2.4 are for the choice which we consider the most reasonable: The first 14 maps as well as maps 20 to 30 determine the linear drift correction. In addition, we neglect the first map of this observation, as a glitch in the reduction rendered it unusable.
As the flux excursion happens during the end of the observation, the linear drift is intrinsically less constrained (because we extrapolate drift for the last maps of this observation based on the previous maps). This manifests itself as an on average increase of the reference light curves at the end of the night. To correct this we subtract the mean of the reference light curves in each map. This is only necessary for this night, as the drift for the other observations is well constrained.

Manual fine tuning for other observations

The light curves of the March 13 and 15 observation show weak excursions (Figure 7). However, even after the manual fine tuning of the linear drift correction, none of the excursions are significant. The March 21 observation shows no excursion.

A1.5 Other observations

All available light curves are shown in Figure 7.

March 13: The blue light curve of the first observation, March 13, experiences a 'U-like' drop. We were not able to identify the source of this signal drift nor were we able to correct it. We therefore neglected the blue March 13 observation for all analysis. The parallel red band observation is seemingly unimpaired, however caution is clearly advised.

March 15: There is no significant flux excursion in the blue light curve. The flux excursion seen in the red light curve is not significant and we cannot find a discernible point source at the position of Sgr A*; even after the manual fine tuning. Thus, we cannot claim a detection here and consequently do not use this observation to derive estimates for the SED.

March 21: No flux excursions are identifiable in neither of the light curves of this observation. The parallel NIR light curves show weak NIR flares with an intensity comparable to those of the March 17 NIR flares.

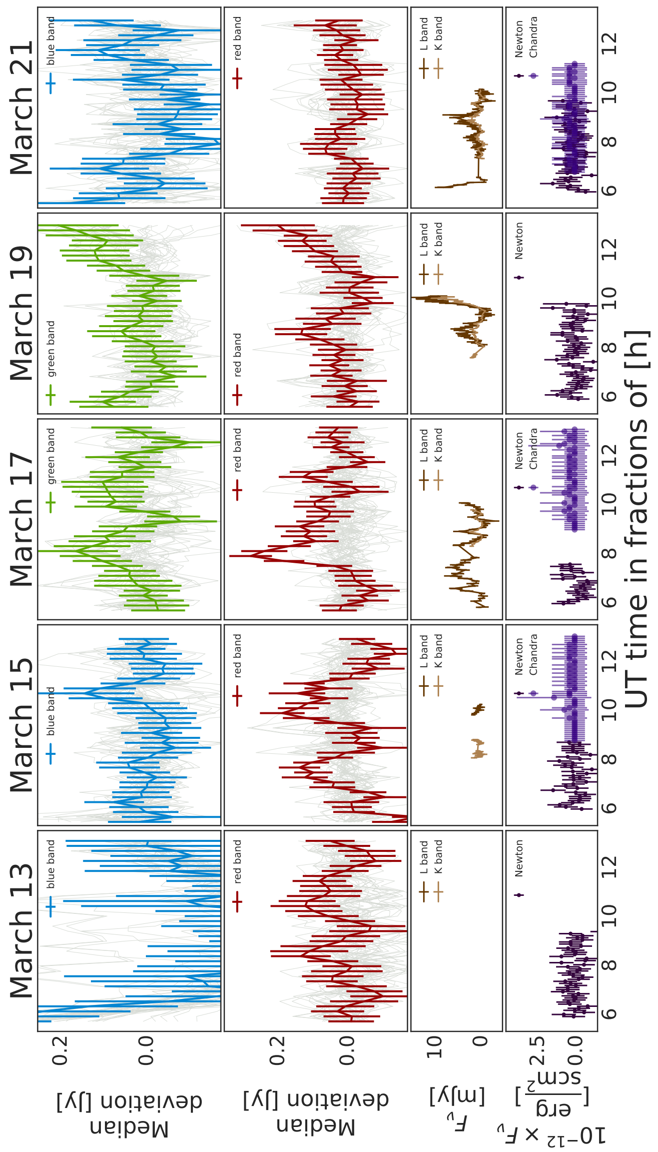

Figure 7: All available light curves. The top two panels show the FIR light curves obtained with Herschel/PACS. The top row are the light curves of the blue and green band (color coded). The panel below is the light curve of the red band. The grey light curves are the light curves of the reference positions (see Section 2.2.3). The lower two panels show the NIR (L' and K band) and X-ray parallel observations from NACO, XMM-Newton and Chandra, where available.

A1.6 Integrated residual maps

The integrated residual maps show extended flux patches. These are moderately correlated with the regions of high intensity. However, this correlation is not perfect. We are thus not able to correct for these artefacts. We argue that these patches not real, but they occur as we reach the sensitivity limit of our data. All regions which show extended flux patches experience a high variance σ^2. We illustrate this in Figure 8, where we plot the integrated residual map of March 17 and the variance map of this observation. For the computation of the variance map we have excluded the 3 maps with the peak flux of Sgr A*. In the left of Figure 8 we have circled regions of extended flux patches. In the variance map, these patches clearly stand out. The region of Sgr A* on the other hand is not effected by such an extended patch. In addition, the point source visible in the residual maps, as well as in the integrated residual map, is substantially different from these extended flux patches. This is illustrated in Figure 9. In this figure we plot the red band integrated residual map (left) and a so called η map (right). The value of the pixels in the η map is defined as follows:

$$\eta_{x,y} = [\tilde{\chi}^2_{x,y}/A_{x,y}]^{-1} \ , \tag{1}$$

where $\tilde{\chi}^2_{x,y}$ is the χ^2 of a PSF fitted to the pixel (x, y) and $A_{x,y}$ is the amplitude of the PSF fitted to this value. Therefore, each pixel in the η map represents how well a point source with significant flux fits the data. A good fit is characterized by a high value of η. This is a similar concept to the one used in the StarFinder algorithm (Diolaiti et al., 2000). Inspecting the η map reveals that, for the March 17 observation, the only region where we can fit a PSF with a low $\tilde{\chi}^2$ and significant flux is the position of Sgr A*.
We repeat this for March 19 and both observations together in Figure 10. For March 19 the situation is more ambiguous than for March 17. This reflects the lower significance of the signal.

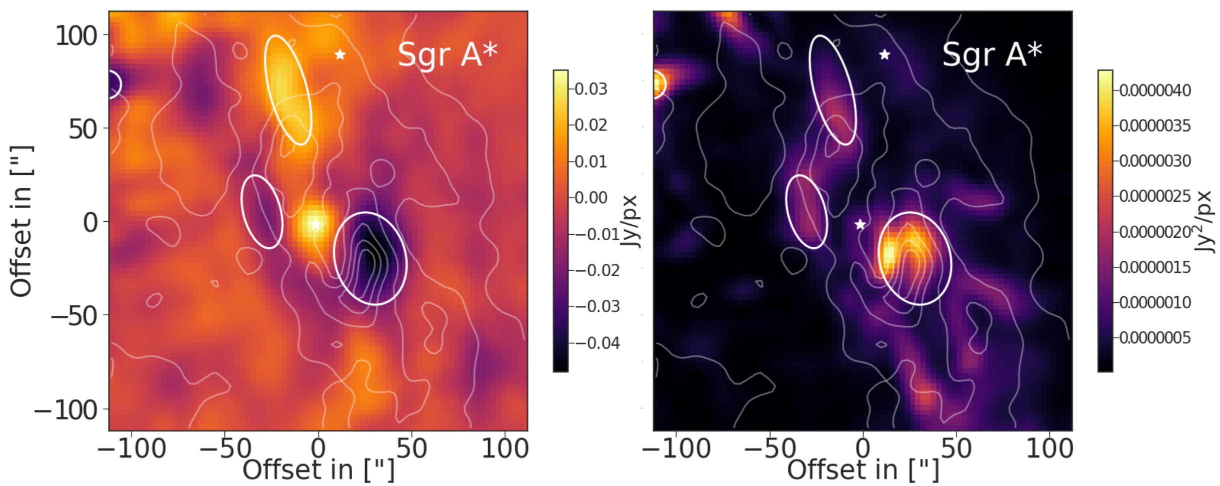

Figure 8: Right: red band integrated residual map of March 17. Left: variance map of the residual maps make up the integrated residual map. The extended flux patches in the integrated residual maps have been circled in both plots.

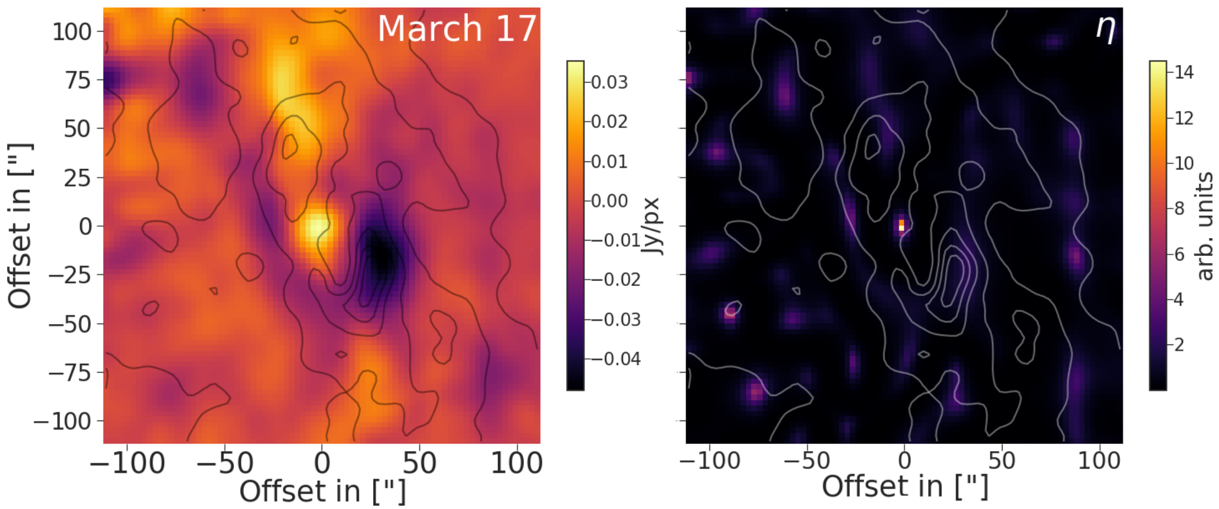

Figure 9: Significance of point sources in the red band integrated residual map: The upper left image shows the integrated residual map of March 17. The map below depicts the inverse of the $\tilde{\chi}^2$ value of a PSF fitted to each pixel of the integrated residual map. The large map to the right shows the same, with the difference that the inverse of the $\tilde{\chi}^2$ value is weighted with the amplitude A of the respective PSF.

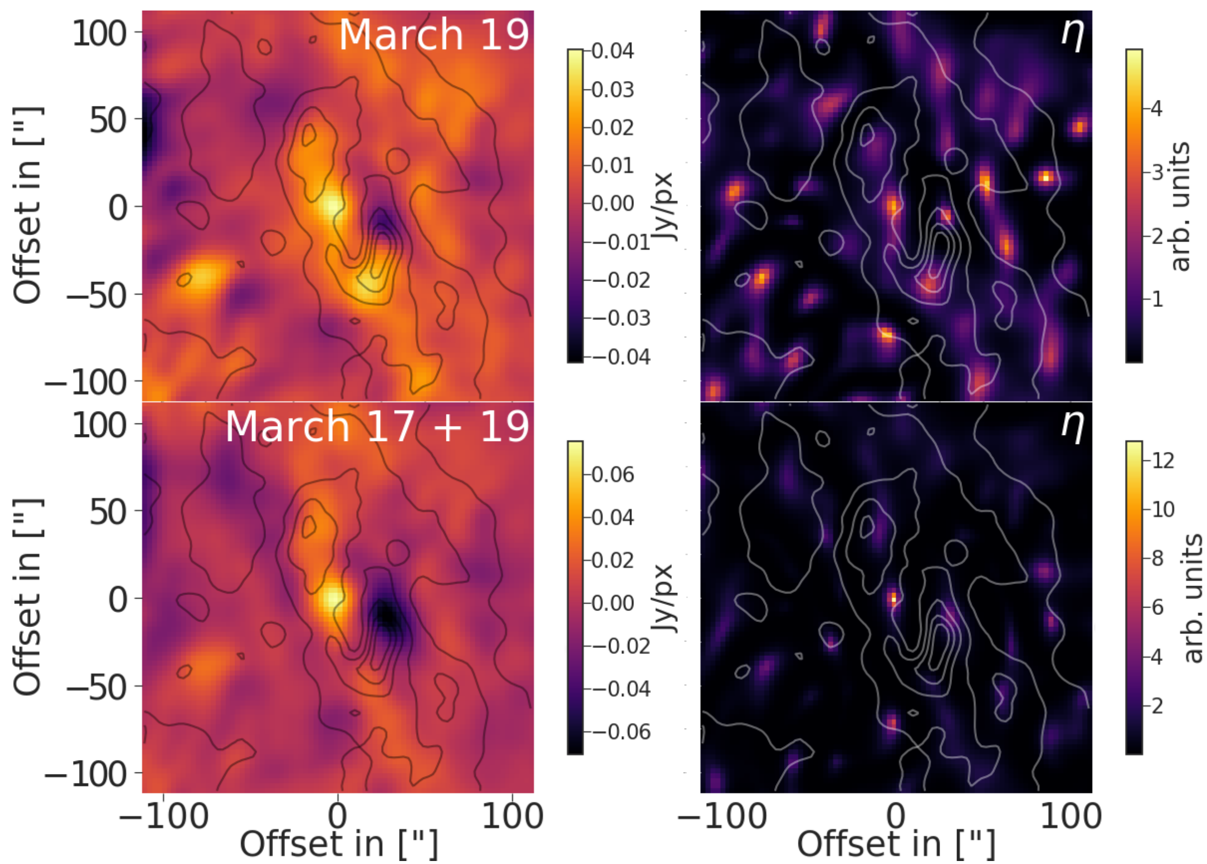

Figure 10: Significance of a point source in the red band integrated residual maps: Similar to Figure 9, but for the March 19 observation as well as the integrated residual map for both observations, March 17 and 19.

A2 Appendix: The Flux Distribution of Sagittarius A*

A2.1 Detection limit

Binary fits

Data selection plays a crucial role when working with flux ratios obtained by fitting a binary model. We rigorously reject data which has been observed under bad conditions or with instrument malfunctions. In addition, bad fits should be removed from the sample. We must make sure that the MCMC fit has converged. Furthermore, in the case of non- or spurious detections one must ensure that the fit result does not reflect the initial conditions. Most importantly, one must pay special attention that fits are not rejected because of low flux as this skews the resulting flux distribution. To ensure that the fitted flux ratios are sound we define four different data selection schemes which we benchmark against each other:

1. Manual data rejection: all fit results are visually inspected and the data is qualified according to the quality of the fit and the data.

2. Astrometric outlier rejection: We calculate the best fit orbit, using all data. We than reject 20 % of the data that is most outlying, based on the inverse variance weighted distance from orbit position and the fit position.

3. Significance of binary rejection: We compare a binary fit to a single point source fit. If the significance binary model is less than 3σ better than the point source, the data is rejected.

4. No rejection: We use all data points regardless of their apparent quality.

All of these selection criteria can partially be flux-dependent, even when no data are rejected[3]. To reduce this bias, we redraw the rejected data from the measured accepted data. Such a simple bootstrapping does not take into account the correlation in the light curve, and the data should be re-drawn from self-similar parts of the data (block bootstrapping (Künsch, 1989)). However, in our case, the light curve is not long enough to have sampled many high flux states, so a self-similar redrawing from high and low flux states did not alter the results. We thus opt for the simpler bootstrapping approach.
We find that the manual data rejection (1.) the astrometric outlier rejection (2.) and no rejection yield (3.) consistent results. Only the significance of binary rejection (4.) deviates from the other rejection schemes. In the first three cases, the flux distribution of the rejected data closely follows that of the accepted data. In contrast, the significance

[3] While the SNR of Sgr A* is flux dependent, the quality of the data is not. For instance, if bad data systematically cause the fits to have artificially high fluxes, those flux bins will be overrepresented in the resulting flux distribution.

of binary rejection scheme shows a strong correlation with the flux and we exclude this scheme. We conclude that the data rejection is mostly unbiased for the manual rejection, the outlier rejection and no rejection. We thus use the simplest scheme, with no rejection, to derive our results.
To asses the detection limit we use different tools. First the convergence of the MCMC chains for the binary fits was checked and proper convergences was ensured. We visually checked that binary features are detectable in the visibility amplitude, the squared visibilities and the closure phases.
To obtain qualitative criteria if Sgr A* is detected, we explicitly checked all files with a measured flux density below 0.3 mJy. We compared the fitted position with the theoretical position based on the orbit. We find that the fitted positions derived at low fluxes do not perform differently from the observations with higher fluxes.
A third qualifier is significance of a binary against a single source model. For the first polarization, we find twelve exposures with a significance below 3σ and five exposures with a significance below 1σ. For the second polarization, 17 exposures fall below a significance of 3σ, and six files below 1σ. Notably, only one file from 2018 shows a significance below 3σ.
We further investigate the files with low fluxes in order to ensure that the binary signal that is observed stems from Sgr A* and not from another source within the IFOV. We do this by simplifying the fitting procedure and only allow for the binary flux, a visibility scaling and the background flux. We keep the binary separation fixed and run fits over a finely sampled grid with 10000 points ± 10 mas around the best fit position. Because this is computationally expensive we only check one file per year. Since it is expected that a transient background source is visible at least for a few months, this is enough to ensure that the measured signal is not caused by a transient background source.
We find that in both the 2017 and 2018 tested cases, there is significant flux at the separation of Sgr A* and S2. While there are several degenerate solutions with similar intensity, the fit at the SgrA*–S2 separation has the lowest χ^2. Furthermore, because S2 and Sgr A*'s positions are very well determined from the orbit fitting (and the other, brighter measurements in the respective nights), we ascribe the degenerate positions at other separations to side lobes of the beam and argue that the S2–SgrA* binary dominates the fit result.

A2.2 Flux error model

In order to model the flux distribution with an analytic PDF model the observational uncertainties need to be taken into account. Noise has a smoothing effect on the flux distribution. Each measurement is uncertain with a given probability distribution, and when creating a histogram of the data, the measurements may fall into a wrong bin with a probability governed by the error PDF. In this paper we assume the noise to be normally distributed, with a flux-dependent standard deviation. Unlike in similar photometric studies, our noise analysis is limited by the number of observables: The only two observables which are readily available are S2 and Sgr A*. S2 can only be used to estimate the uncertainty at very high fluxes and it is, thus, of limited use. Furthermore we found the formal fit

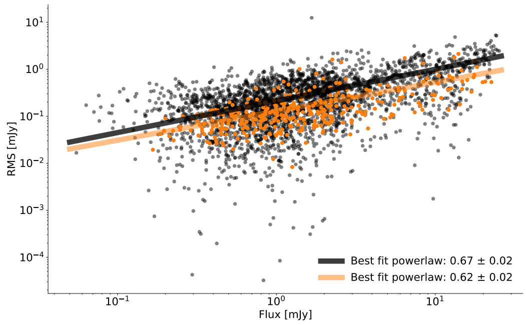

Figure 11: Noise as a function of flux: The RMS is determined from the differences of the two measured polarizations (black points) and the residuals of fourth order polynomial subtracted light curve of Sgr A*. Both relations can be described by single power law functions, for which we plot the best fitting realization.

uncertainties to be poor estimators of the uncertainty. Consequently, we use two empirical approaches to determine the uncertainty. In a first approach, we use the difference between the two polarizations to estimate uncertainty. In the second approach, we assume that the intrinsic light curve is a smooth function, which we can fit with a low order polynomial. We estimate the uncertainties by measuring the standard deviation of the residuals, after subtracting the best fit polynomial. For the second approach we found that polynomials of fourth and fifth order are sufficiently flexible to describe the light curve.

Both approaches are limited. In the first case, only two measurements determine the uncertainty, and the intrinsic polarization of Sgr A* inflate the measured uncertainty. In the second case, the assumption of smoothness is imposed, and the order of the polynomial can not be rigorously quantified. However, both measurements quantitatively agree with one another in that the RMS scatter is described by a single power law of $\sigma = 0.3 \times F^{0.6}$, see Figure 11. The exponent of 0.6 is consistent with the power law description used in photometric studies of the light curve and is consistent with a photon noise origin (e.g., Dodds-Eden et al., 2011; Fritz et al., 2011).

A3 Appendix: Constraining Particle Acceleration in Sgr A* with Simultaneous GRAVITY, Spitzer, NuSTAR, and Chandra observations

A3.1 Synchrotron self-Compton of the SYN–SYN scenario

The SSC component of the SYN–SYN scenario peaks at frequencies higher than the X-ray band. Unfortunately, for the parameter ranges we assume (Table 4.4), this peak is not bright enough to be detectable in the GeV bands by for example *Fermi* (e.g.: Malyshev

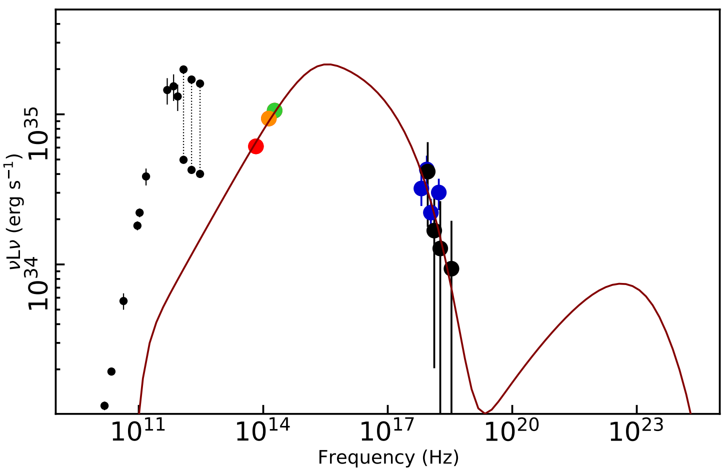

Figure 12: Mean SED of Sgr A* during the flare, including the SSC component of the PLCoolγ_{max} model. This component peaks at $\nu \sim 10^{23}$ Hz.

et al., 2015). However, it poses a possibility to constrain the radius and the particle density of the otherwise optically thin spectrum. At small enough radii and high enough densities, the falling flank of the SSC spectrum starts to contribute to the $2 - -70$ keV band of *NuSTAR*. For instance, at $B = 30$ G, the emission region is constrained to $\sim$0.3 $\mathrm{R_S}$. This demonstrates the importance of further parallel NIR–X-ray observations with as wide as possible spectral range.

A3.2 Accounting for the acquisition camera transmission curve and the different spectral slopes of S2 and Sgr A*

The GRAVITY flux measurements derived in both bands are measurements of the flux ratios of the S2 and Sgr A*. The spectral dependence of the reddened flux of Sgr A* and S2 can be approximated as a power law with different indices:

$$\begin{aligned} F_{S2}(\lambda) &= F_{S2_0} \cdot \frac{\lambda}{\lambda_0}^{\alpha_{S2}} \\ F_{Sg}(\lambda) &= F_{Sg_0} \cdot \frac{\lambda}{\lambda_0}^{\alpha_{Sg}}, \end{aligned} \tag{2}$$

where F_{x_0} denotes the flux of the respective source at wavelength λ_0. For S2, the spectral slope α_{S2} can be determined from the NACO photometry in the H and K bands (Gillessen et al., 2017, e.g.:).

To account for the effect of different spectral slopes on the flux ratio in the H band, we have to take the filter curves of the acquisition camera, the VLTI, and GRAVITY into account. This can be achieved by expressing the flux of both sources on the acquisition camera detector as functions of the respective effective wavelengths as follows:

$$\begin{aligned} F_{S2}(\lambda) &= F_{K,S2} \cdot \frac{\lambda_{eff,S2}}{\lambda}^{\alpha_{S2}} \\ F_{SgrA}(\lambda) &= F_{K,SgrA} \cdot \frac{\lambda_{eff,S2}}{\lambda}^{\alpha_{SgrA}} . \end{aligned} \tag{3}$$

Here the effective wavelength, assuming a power-law flux dependence, is given by

$$\lambda_{eff}(\alpha) = \frac{\int F_{\lambda}(\alpha) \cdot \lambda \; d\lambda}{\int F_{\lambda}(\alpha) d\lambda}, \tag{4}$$

where $F_{\lambda} = F_{source}(\alpha) \cdot T(\lambda)$ is the power-law source flux multiplied by the instrument transmission $T(\lambda)$. The observed flux ratio in the H band can then be expressed as

$$r_H = \frac{\int F_{K,S2} \cdot \left(\frac{\lambda_{eff,S2}}{\lambda_K}\right)^{\alpha_{S2}} d\lambda}{\int F_{K,SgrA} \cdot \left(\frac{\lambda_{eff,SgrA}}{\lambda_K}\right)^{\alpha_{SgrA}} d\lambda}, \tag{5}$$

where $F_{K/H,S2}$ is the observed flux in the K band, and $\lambda_{eff,S2/SgrA}$ are the acquisition camera effective wavelength of S2 and Sgr A*. We obtain $\lambda_{eff,S2}$ in the H band using the acquisition camera transmission curve and the reddened power-law flux relation determined from NACO photometry.

Using the functional relation for the effective Sgr A* wavelength in the H band, we can rewrite this as

$$\left(\frac{\lambda_{eff,SgrA}(\alpha_{SgrA})}{\lambda_K}\right) = \left(\frac{\lambda_{eff,S2}(\alpha)}{\lambda_K}\right)^{\alpha_{S2}} \cdot \frac{r_K}{r_H}, \tag{6}$$

where r_K and r_H are the observed flux ratios in the H and K bands. We can numerically solve this equation for the effective wavelength $\lambda_{eff,SgrA}$. Once $\lambda_{eff,SgrA}$ and α_{SgrA} are determined, we can plug these into equation 3 to obtain the reddened H-band flux density F_{λ}. We converted F_{λ} to flux density F_{ν} and de-redden through the standard approach $F_{dered.} = F_{red.} \cdot 10^{0.4 \cdot m_H}$, with m_H as discussed in section 4.2.6.

A3.3 Effect of the column density on the IR and X-ray spectral slope, and inferred parameters

As discussed in Section 4.2.2, we chose three different column density values $n_{\mathrm{H}} = 1.0 \times 10^{23}\mathrm{cm}^{-2}$, $n_{\mathrm{H}} = 1.6 \times 10^{23}\mathrm{cm}^{-2}$, $n_{\mathrm{H}} = 2.0 \times 10^{23}\mathrm{cm}^{-2}$. We fitted the *Chandra* mean spectrum of the flare assuming each of the above-mentioned values of the column density and computed the respective corrections in order to de-absorb the spectrum. Similarly, we varied the infrared extinction and scaled the flux density according to the uncertainties reported in Table 4.2. Figure 13, shows the de-absorbed data and the resulting fits to the data sets. For the SYN–SYN model, we assumed the same parameters as for the

Parameter	SYN–SYN model $\log_{10}(n_e)$ γ_{max}	SSC–SSC model $\log_{10}(n_e)$, B, γ_{max}
$M_{IR} = 0.95, 2.42, 4.13;\ n_H = 1.0 \times 10^{23}$ cm^{-2}	6.243 ± 0.015, 39620 ± 3808	9.75 ± 0.03, (17.1 ± 0.25) G, 276 ± 29
$M_{IR} = 0.97, 2.42, 4.21;\ n_H = 1.6 \times 10^{23}$ cm^{-2}	6.240 ± 0.011, 47179 ± 3824	9.74 ± 0.02, (19.2 ± 0.3) G, 244 ± 13
$M_{IR} = 1.0, 2.42, 4.29;\ n_H = 2.0 \times 10^{23}$ cm^{-2}	6.249 ± 0.014, 51113 ± 5436	9.74 ± 0.01, (19.5 ± 0.1) G, 245 ± 14

Table 1: Effect of different choices of the neutral absorption column density. The fit parameters for the SYN–SYN model and the SSC–SSC model derived from a least-squares fitting. The models are described in Appendix A3.3. The reported uncertainties were derived from the covariance matrix.

PLCoolγ_{max} model (see Table 4.4). For the SSC–SSC model, we assumed fixed radius $1R_S$, a fixed slope of the electron distribution $p = 3.1$, and a fixed minimum acceleration $\gamma_{min} = 10$. We fit the particle density, magnetic field, and maximum acceleration. Table 1 reports the best-fit results. While the inferred parameters of the best-fit solution change slightly, the main conclusions of the paper are not affected by the choice of the specific extinction value: the SYN–SYN model requires a $\gamma_{max} \sim 10^4$ to explain the observed flux ratios in the NIR and X-ray. In contrast, in one-zone models, the SSC–SSC scenario requires particle densities 10^3 higher than typically inferred for the ambient accretion flow.

A3.4 Analytical formulation of the non-thermal electron distributions

We considered nonthermal electron distributions for the modeling of the flare SED in this paper. These are either in the form of a plain power law or a broken power law. In this section, we describe the analytical form of these distributions.

- The formulation of the power-law electron distribution is given in Equation 7. In that equation, n_e is the electron density, p is the power-law index, and γ_{min} and γ_{max} are the low- and high-energy limits of the electron population,

$$\frac{dn_{\rm pl}}{d\gamma} = n_e \times \begin{cases} N_{\rm pl}\gamma^{-p}, & \text{if } \gamma_{min} \le \gamma \le \gamma_{max} \\ 0, & \text{otherwise,} \end{cases} \tag{7}$$

  where $N_{\rm pl}$ is the normalization of the distribution,

$$N_{\rm pl} = \frac{p-1}{{\gamma_{min}}^{1-p} - {\gamma_{max}}^{1-p}}. \tag{8}$$

- We provide a generic formulation of a broken power-law electron distribution in Equation 9. Since we consider synchrotron cooling as the origin of the break at γ_b, we enforced $p_2 = p_1 + 1$. For readability, we used the notation p in the main text for all power-law indices. In the case of cooled synchrotron spectra it corresponds to p_1,

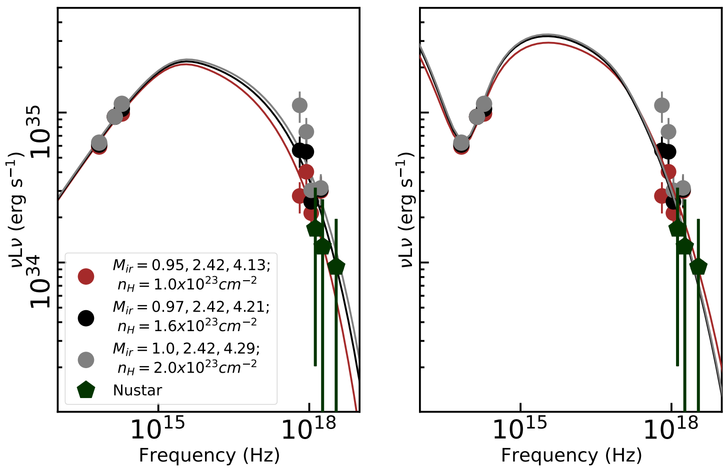

Figure 13: Effect of different neutral material column density: NIR data same as Figure 4.4. Both panels: the red, black and gray lines show the data corrected with different plausible neutral material column densities, which are reported in the legend of the left panel. The *NuSTAR* data have not been re-reduced (green pentagons) because the high-energy data is only marginally affected. The lowest energy bin from the *NuSTAR* spectrum has been removed because it might be affected by the extinction. The models in the left panel are PLCoolγ_{max} type models, the SCC-SSC type models are plotted on the right, and the color indicates the respective data set fitted.

$$\frac{dn_{\rm bpl}}{d\gamma} = n_e \times \begin{cases} N_{\rm bpl}\gamma^{-p_1}, & \text{if } \gamma_{min} \le \gamma \le \gamma_b \\ N_{\rm bpl}\gamma^{-p_2}\gamma_b^{p_2-p_1}, & \text{if } \gamma_b < \gamma \le \gamma_{max} \\ 0, & \text{otherwise,} \end{cases} \tag{9}$$

where $N_{\rm bpl}$ is the normalization of the distribution,

$$N_{\rm bpl} = \left[\left(\frac{\gamma_{min}^{1-p_1} - \gamma_b^{1-p_1}}{p_1 - 1} \right) + (\gamma_b)^{p_2-p_1} \left(\frac{\gamma_b^{1-p_2} - \gamma_{max}^{1-p_2}}{p_2 - 1} \right) \right]^{-1} . \tag{10}$$

Considering synchrotron cooling in the presence of particle escape as the origin for the broken power-law distribution, a sharp cooling break in the electron distribution is not physical. However, the exact determination of the spectral shape is beyond the scope of this work. Furthermore, our observational data does not provide useful constraints on the cooling break itself, and thus the determination of the proper shape of the break is not required. For simplicity, we use the form given in Equation 9.

In above formulas, the electron distributions are truncated at both γ_{min} and γ_{max}. As a more physical alternative, we use an exponential cutoff instead of a sharp truncation at γ_{max},

$$\frac{dn_{\rm expc}}{d\gamma} = \begin{cases} (dn/d\gamma)\exp(-\gamma/\gamma_{max}), & \text{if } \gamma_{min} \le \gamma \le 10 \times \gamma_{max} \\ 0, & \text{otherwise,} \end{cases} \tag{11}$$

that is, we simply smooth the high-energy cutoff of the original electron distributions with an exponential function. The high energy limit is extended from γ_{max} to $10 \times \gamma_{max}$.

A4 Appendix: The Young Stars in the Galactic Center

A4.1 Tables: Young stars with orbits

MPE	Pau.	UCLA	a [as]	σa [as]	e	σe	i [°]	σi [°]	Ω [°]	$\sigma\Omega$ [°]	ω [°]	$\sigma\omega$ [°]	P [yr]	σP [yr]	t_0 [yr]	σt_0 [yr]
S18			0.28	0.01	0.24	0.01	107.18	0.6	51.23	0.37	3.5	5.45	54.12	3.41	1989.75	0.74
S13	E3	S0-20	0.26	>0.01	0.43	>0.01	22.96	0.12	74.05	0.55	245.86	0.77	49.51	0.15	2004.89	0.01
S9	E9	S0-5	0.27	>0.01	0.64	>0.01	82.63	0.11	156.18	0.05	153.22	0.45	50.93	0.52	1977.35	0.4
S4	E6	S0-3	0.35	>0.01	0.4	>0.01	80.3	0.05	258.8	0.04	293.66	0.9	75.26	0.71	1959.39	0.73
S175			0.37	0.01	0.98	0.01	87.83	0.19	325.99	0.27	68.14	0.14	81.76	2.21	2009.51	>0.01
S14	E2		0.3	>0.01	0.99	>0.01	105.27	0.89	222.92	0.67	330.5	0.54	60.76	0.53	2000.32	0.03
S60			0.41	0.01	0.7	0.01	124.87	0.55	168.31	1.65	25.8	1.04	95.07	5.16	2024.8	0.27
S12	E5	S0-19	0.3	>0.01	0.89	>0.01	33.59	0.32	231.09	0.96	316.94	0.83	59.06	0.13	1995.58	0.03

S31	E7	S0-8	0.44	>0.01	0.56	>0.01	109.57	0.04	137.39	0.05	311.38	0.31	104.92	0.34	2018.16	0.01
S8	E10	S0-4	0.4	>0.01	0.81	>0.01	74.19	0.24	315.15	0.14	347.42	0.29	92.08	0.35	1983.95	0.19
S29			0.39	>0.01	0.97	>0.01	144.11	1.37	6.26	1.99	205.08	1.85	89.85	0.7	2021.43	0.02
S1	E4	S0-1	0.61	0.01	0.57	0.01	119.19	0.09	342.32	0.13	122.98	0.52	174.78	3.63	2001.79	0.07
S19			0.59	0.02	0.78	0.02	71.76	0.08	344.94	0.15	158.67	0.4	165.66	10.38	2005.64	0.03
S33			0.75	0.01	0.54	0.01	64.35	0.86	99.28	2.04	299.96	1.88	236.01	6.22	1904.31	8.04
S42			0.38	0.01	0.75	0.01	39.85	0.18	319.29	1.88	42.63	1.14	84.42	2.25	2022.59	0.08
S67	E15	S1-3	1.16	0.01	0.27	0.01	135.66	0.48	95.9	3.04	208.75	0.81	453.13	6.77	1685.57	10.92
S71			0.98	0.01	0.9	0.01	74.18	0.13	34.84	0.29	338.96	1.19	354.7	3.65	1686.51	3.86
S66	E17	S1-2	1.37	0.02	0.14	0.02	131.64	0.5	92.87	2.12	121.65	8.01	583.93	14.64	1774.34	21.17
S96	E20	S1-11	1.56	0.03	0.13	0.03	126.14	0.46	115.64	0.36	234.1	1.9	710.53	20.48	1623.76	8.99
S91			1.91	0.07	0.34	0.07	115.63	0.24	110.07	0.18	344.37	0.65	957.92	52.64	1075.96	52.77
S83	E16	S0-15	1.18	>0.01	0.17	>0.01	129.95	0.05	97.04	0.2	188.27	0.02	464.74	0.88	2022.31	0.49
R14	E22	S1-14	2.78	0.08	0.44	0.08	118.86	0.25	113.28	0.76	158.8	1.17	1659.39	73.8	3510.03	74.77
S97	E23	S1-16	2.41	0.38	0.37	0.38	113.6	1.03	112.67	0.99	24.61	9.26	1360.81	325.27	2125.26	19.9
R44		S2-21	4.97	0.48	0.39	0.48	127.85	1.11	85.3	1.72	218.21	3.1	3964.44	576.82	1934.91	13.95
S87	E21	S1-12	4.14	0.03	0.36	0.03	115.27	0.2	106.64	0.84	305.55	5.76	3059.27	29.16	-877.69	40.06
S2	E1		0.12	>0.01	0.88	>0.01	134.68	0.03	228.17	0.03	66.26	0.03	16.05	>0.01	2018.38	>0.01
R34			1.85	0.02	0.61	0.02	136.94	0.36	333	1.37	58.88	0.88	902.73	13.67	1506.63	9.97
S22			1.06	0.02	0.39	0.02	107.7	0.12	291.01	0.14	84.69	1.98	398.26	10.27	1991.82	0.85
S6	E11	S0-7	0.65	0.01	0.85	0.01	87.5	0.07	84.46	0.13	117.36	0.51	190.3	3.14	2111.16	1.85
R85	E56	I.34W	6.59	1.7	0.34	1.7	128.27	2.87	110.77	1.03	181.05	2.38	6055.99	2343.35	2019.38	31.46
R70	E54	S4-36	3.48	0.01	0.35	0.01	147.27	0.18	115.55	0.98	43.19	1.8	2326.65	12.68	3667.56	16.75
R1	E29	S2-7	2.63	0.06	0.53	0.06	125.09	0.32	117.28	1.52	243.87	1.17	1523.25	50.46	4005.64	45.51
S5	E8	S0-26	0.53	0.01	0.72	0.01	115.96	0.37	128.58	0.81	271.99	0.4	140.03	3.4	1954.49	1.41
S72	E18	S1-8	2.2	0.05	0.33	0.05	119.18	0.36	316.04	0.64	205.09	1.97	1184.02	41.41	1055.3	41.4
R39	E40	S3-5	3.22	1.46	0.01	1.46	122.23	8.07	107.05	0.05	359.99	4.71	2067.22	1403.78	2054.44	27.1
R30	E32	S2-15	6.36	0.14	0.61	0.14	113.02	0.38	94.51	1.49	12.33	1.74	5739.49	184.24	2242.8	7.55

Table 2: Stars with determined orbital solutions. Pau. abbreviates Paumard et al., 2006

A4.2 Tables: Young stars without orbits

#	Tri. ID	Pau. ID	UCLA ID	Alt. names	K_{mag}	R [″]	Sou. vLSR	*R.A.* [″]	$\sigma R.A.$ [mas]	*Dec.* [″]	$\sigma Dec.$ [mas]	$v_{R.A.}$ [km/s]	$\sigma v_{R.A.}$ [km/s]	$v_{Dec.}$ [km/s]	$\sigma v_{Dec.}$ [km/s]	v_z [km/s]	σv_z [km/s]
0	41		S7-216	I.6W	10.9	7.9	t.w.	-7.73607	0.13	1.39504	0.18	87.5	1.7	202.2	2.8	71.0	36.9
1	163	E35	S2-16	I.29 NE1	12.3	2.3	Pau.	-1.00111	0.09	2.06472	0.07	-349.2	0.6	-48.9	0.4	-98.1	68.5
2	283	E36	S2-19		12.7	2.3	Pau.	0.44190	0.08	2.29963	0.09	-319.9	0.4	26.0	0.5	41.2	18.8
3	571		S3-17		13.5	3.2	MPE	-1.41736	0.64	2.84290	0.33	256.3	9.3	60.6	4.9	-67.4	50.7
4	387	E38	S2-74	R46	13.2	2.8	Pau.	0.18116	0.09	2.76872	0.09	-341.6	0.5	36.6	0.4	35.2	22.8
5	349	E61		I.34NW	13.2	4.7	Pau.	-3.75269	0.14	2.83748	0.15	-213.2	2.3	-159.9	1.8	-151.4	29.8
6	149		S6-89		12.0	6.2	Pau.	5.44076	0.13	3.02582	0.13	98.1	1.9	-246.2	1.9	-128.5	67.2
7	238				12.5	11.4	t.w.	10.88630	0.17	3.25710	0.12	-64.8	2.3	-110.7	1.7	-130.7	28.1

8	640	E44	S3-25	R81	13.8	3.3	MPE	1.46037	0.13	2.94958	0.12	-278.8	0.6	9.8	0.7	-85.7	27.3
9	276	E59	I.7SE	I.7SE R60	13.1	4.6	Pau.	2.95516	0.14	3.46359	0.12	225.8	0.9	-0.6	0.7	-151.9	96.6
10	256		S7-236		12.7	7.9	t.w.	-7.08677	0.12	3.59196	0.12	-92.7	1.9	-174.1	1.5	-90.6	73.9
11	496	E52	S3-331		13.6	3.8	t.w.	-1.24685	0.13	3.63401	0.12	227.5	1.5	158.0	1.7	-154.3	42.7
12	566				13.7	8.9	t.w.	-7.82635	0.27	4.20889	0.28	14.8	6.3	167.7	6.1	-135.0	53.8
13	289	E85	S10-7		12.6	10.7	t.w.	9.71444	0.08	4.42600	0.13	-21.6	1.2	-158.5	2.0	-147.6	40.3
14	412		S5-235		13.2	5.3	t.w.	2.78624	0.12	4.55223	0.15	-41.0	1.6	-154.8	2.0	-66.5	51.3
15	124	E62	S4-364	R67	12.1	5.0	t.w.	2.19868	0.11	4.48614	0.10	243.7	0.7	-103.4	0.6	-150.9	36.5
16	327	E70	S6-93	I.7E1 (ESE)	12.7	6.7	Pau.	4.44120	0.15	4.96573	0.13	183.8	6.0	-46.6	5.2	-82.2	86.4
17	228	E66	S6-90	I.7SW	12.4	6.3	Pau.	-3.95089	0.14	4.92088	0.17	6.5	2.1	-138.3	2.5	-348.9	53.5
18	194				12.1	8.7	t.w.	6.94696	0.21	5.20279	0.14	124.7	2.3	-112.6	2.1	-216.6	44.3
19	72		I.10W	I.10W	11.0	8.3	t.w.	6.50133	0.55	5.14416	0.49	-39.5	17.7	191.3	20.6	-164.4	53.6
20	141				11.9	5.9	Pau.	0.89591	0.13	5.80990	0.12	-97.8	1.9	125.5	1.8	-498.2	20.9
21	426	E68	S6-95	I.7W	13.3	6.5	Pau.	-2.42612	0.14	5.99296	0.13	187.5	4.6	5.6	3.6	-300.4	113.4
22	982				14.5	7.6	t.w. MPE	-4.71018	0.12	5.98147	0.16	66.0	1.7	168.9	2.4	-74.1	74.2
23	1075				14.8	7.0	t.w.	-3.12104	0.20	6.22993	0.22	-12.9	3.8	-146.7	4.2	-230.6	44.0
24	6039	E71	S6-100		13.8	6.7	Pau.	1.57264	0.33	6.50982	0.55	-193.6	6.7	105.6	11.0	-282.5	153.7
25	438		S7-19		13.3	7.5	t.w. MPE	-3.79957	0.14	6.49040	0.13	198.3	2.1	110.3	1.7	-51.8	52.8
26	145	E90			11.6	12.8	Pau.	10.89210	0.12	6.66659	0.22	7.2	1.7	-1.2	2.9	-192.0	39.0
27	667				13.7	9.8	t.w.	7.03130	0.18	6.81468	0.23	-112.3	4.4	-82.9	5.2	-199.7	78.3
28	563				13.7	7.1	t.w.	1.23737	0.21	6.95135	0.19	-86.4	2.7	-141.5	3.4	-131.2	43.7
29	462		S7-20		13.4	7.9	t.w. MPE	-3.70753	0.11	6.93792	0.12	193.1	1.5	90.3	1.5	-18.9	54.0
30	117	E73	S7-10		11.6	7.7	t.w.	-1.09174	0.09	7.63062	0.08	-176.7	1.3	-93.2	1.3	-143.5	30.8
31	450		S8-15		13.2	8.2	Yel.	-1.59329	0.12	8.03911	0.09	-114.9	3.9	-122.8	3.7	-9.2	49.7
32	6293				13.3	12.2	t.w.	9.17849	0.83	8.07686	0.80	84.6	52.9	19.4	18.7	-148.9	48.9
33	1050				14.4	14.1	t.w.	11.34287	0.19	8.44936	0.25	42.8	2.3	-57.1	3.2	-50.9	92.2
34	69	E75	S8-4		11.1	8.5	t.w.	-0.01747	0.10	8.54243	0.07	-30.8	5.5	132.1	6.5	-209.0	54.4
35	425		S9-13		13.2	9.3	t.w.	-3.02305	0.15	8.80299	0.12	103.7	1.9	113.8	1.8	-97.9	78.3
36	628	E77	S9-23		13.6	9.2	t.w.	-1.27069	0.15	9.14331	0.17	-94.3	2.1	-108.4	2.1	-218.9	103.3
37	892				14.1	13.3	t.w.	9.47072	0.29	9.27860	0.32	103.6	4.1	30.0	4.5	-133.1	41.8
38	6053				13.8	14.4	t.w.	10.94691	0.10	9.41759	0.22	92.2	17.8	0.2	0.3	-206.0	60.6
39	1077				14.7	11.9	t.w.	-7.00140	0.22	9.66195	0.15	11.9	4.4	-198.5	3.6	242.8	69.8
40	191	E83	S10-5	I.15SW	12.0	10.2	Pau.	-1.57109	0.14	10.03093	0.12	-53.1	2.4	-74.4	1.5	-171.9	63.4
41	110	E84	S10-4		11.3	10.2	t.w.	0.08287	0.11	10.24086	0.09	-79.7	1.7	31.9	1.3	-278.3	38.9
42	6049				13.8	12.1	t.w.	5.80365	0.73	10.59286	0.56	55.3	13.5	137.6	11.0	59.9	28.0
43	599				13.0	16.8	t.w.	12.89808	0.68	10.69651	0.20	-9.9	13.1	27.2	4.2	-356.0	103.4
44	6038	E86	S10-48		15.1	10.7	Pau. Yel.	-0.54099	0.25	10.72329	0.10	55.0	5.7	18.9	2.3	-208.1	49.6
45	6042				14.7	20.9	MPE	17.54567	0.43	11.36067	0.25	-75.6	8.9	-82.3	5.2	-20.3	51.6
46	153	E88	S11-5	I.15NE	11.7	11.8	Pau.	1.36917	0.12	11.67842	0.13	-26.7	1.8	73.3	2.0	-63.1	40.0
47	6055	E89			14.4	12.3	t.w. MPE	-0.00571	0.16	12.27541	0.52	94.7	3.7	21.2	8.9	-87.2	71.1
48	392				12.8	20.4	t.w.	15.79520	0.32	12.87517	0.37	68.7	6.0	100.7	6.9	10.4	44.3
49	797				13.9	19.4	t.w. MPE	13.09939	0.27	14.29659	0.31	14.5	4.0	37.6	3.8	-61.4	58.0
50	2158				15.4	17.3	t.w.	7.89660	0.40	15.37209	0.49	-97.3	8.5	-66.3	9.7	-208.8	90.3

51	1029				14.4	16.7	t.w.	4.44112	0.25	16.12724	0.25	-49.0	5.1	-56.4	5.2	-136.4	45.3
52	10007			out.-1	12.0	28.8	Yel.	21.61571	131.45	19.01698	116.22	69.4	5.4	37.5	4.7	-55.0	47.0
53	6059			out.-2	14.9	22.4	Yel.	-6.04643	3.93	21.59581	3.77	87.9	10.4	85.7	11.3	0.6	55.1
54	6045	E48		I.13E4	11.8	3.5	Pau.	-3.21112	0.09	-1.40829	0.29	-231.3	1.7	23.7	5.0	63.6	75.5
55	2794				15.4	14.4	t.w.	10.69713	0.26	9.58150	0.36	-36.0	3.7	36.4	4.8	-206.3	37.0
56	4002				15.8	24.8	t.w.	16.44464	0.70	18.58738	1.10	11.1	10.0	-97.2	14.8	-99.3	148.4
57	1519				15.1	10.1	t.w.	7.77190	0.28	6.41182	0.21	40.0	5.2	126.9	3.8	-200.2	61.7
58	999				14.7	8.4	t.w. MPE	4.34736	0.81	-7.23252	0.25	-33.4	26.3	-150.4	7.7	209.4	105.2
59	1928				15.4	11.2	t.w. MPE	-0.14564	0.16	-11.24421	0.43	-43.2	2.3	100.7	6.1	121.2	53.9
60	3221				15.9	11.2	t.w.	4.73808	0.27	10.11947	0.15	94.3	3.9	133.3	2.2	-34.2	61.0
61	505	E87	S11-21		13.5	11.2	t.w.	2.56980	0.14	10.94189	0.15	-81.9	2.0	-103.5	2.2	-199.4	48.7
62	1984				15.4	9.3	t.w.	-5.60366	0.22	-7.38477	0.20	114.0	3.1	77.6	2.5	181.6	66.9
63	5027				16.7	21.2	t.w.	17.34700	0.51	12.11384	0.60	67.6	6.7	66.3	8.7	-58.3	45.0
64	3636				15.8	20.7	t.w.	17.56689	0.87	10.85727	0.86	52.9	30.0	30.6	36.8	-58.0	41.3
65	1697				15.4	8.7	t.w.	-4.79071	0.39	-7.23401	0.41	83.9	9.4	-166.9	9.3	146.7	103.1
66	2054				15.4	5.6	t.w.	-5.63960	0.42	-0.07162	0.41	124.8	10.0	97.6	9.2	40.0	92.5
67	172		S7-228		12.0	7.9	t.w. MPE	-7.74674	0.12	1.68575	0.19	102.6	1.6	87.6	2.5	159.1	53.6
68	924				14.3	15.2	t.w.	-10.83416	0.35	-10.59268	0.22	21.6	10.2	-25.1	6.0	150.8	31.5
69	4273				16.6	11.6	t.w.	4.88054	0.48	10.53533	0.43	85.2	12.0	72.6	10.2	-207.1	147.0
70	32	E46		I.13E1	10.7	3.4	t.w.	-2.95920	0.28	-1.64916	0.14	-139.4	3.5	-107.1	1.7	34.9	29.6
71	164	E28	S2-4	I.16 SSE2	12.3	2.1	Yel.	1.47277	0.06	-1.47447	0.06	313.8	0.4	103.0	0.4	208.2	27.8
72	10005		S2-50		15.3	2.3	Yel.	1.70018	0.16	-1.50870	0.13	78.1	2.2	66.0	1.4	-52.1	112.3
73	1307		S3-3		15.1	3.1	Yel.	3.08004	0.22	-0.65759	0.33	134.5	3.7	152.6	5.3	45.4	29.4
74	385		S1-1	R6	13.5	1.0	Gil.	1.04560	6.27	0.03311	5.97	227.1	0.2	44.6	0.4	536.0	0.0
75	6082			S93	15.4	1.1	Gil.	1.07884	0.12	0.16520	0.16	-114.7	1.5	-94.6	2.2	159.1	28.7
76	1342	E13	S0-31		15.4	0.7	Gil.	0.56887	10.21	0.44755	11.12	247.2	0.6	34.4	0.5	-262.7	100.1
77	1333	E12	S0-11		15.6	0.5	Gil.	0.49518	11.49	-0.06380	13.57	-140.5	0.4	-110.2	0.4	-41.6	67.0
78	832		S0-9		14.7	0.6	Gil.	0.22690	14.66	-0.60635	12.81	345.3	0.3	-210.7	0.3	156.7	54.1
79	6077				17.9	0.4	Gil.	0.19781	32.36	0.29388	32.32	299.1	9.8	-321.6	19.0	270.5	68.7
80	6084		S1-33		15.1	1.2	Yel.	-1.23863	0.10	-0.03386	0.09	-11.2	0.6	192.7	0.5	3.2	16.6
81	10006		S2-58		14.0	2.5	Yel.	2.15342	1.66	-1.17055	2.62	-28.1	0.8	255.1	1.2	61.9	31.3
82	6296		S3-314		15.5	3.8	Yel.	3.83020	1.79	-0.12036	2.31	118.9	1.2	160.2	1.3	13.3	18.2
83	178		S3-2		12.2	3.1	Yel.	3.06459	0.10	0.54448	0.10	160.6	0.7	30.4	0.8	-447.2	22.9
84	388		S5-237		13.2	5.6	Yel.	5.50480	0.19	0.98012	0.33	-59.4	3.3	244.6	4.7	34.5	16.1
85	469	E57	S4-169		13.5	4.4	Pau. t.w.	4.42516	0.12	0.25988	0.11	-106.7	1.8	150.6	1.8	-84.2	50.6
86	519	E72	S6-82		13.6	6.7	Pau.	6.71581	0.21	-0.48061	0.34	60.2	3.5	209.3	5.9	91.0	102.7
87	4862				16.7	14.5	t.w. MPE	9.96849	0.28	10.50405	0.45	43.8	9.4	64.3	10.6	-52.2	152.4
88	1282		S2-76		15.2	2.8	Yel.	-0.23156	0.24	2.80308	0.23	14.2	3.4	41.7	2.6	-18.9	69.6
89	229				12.7	11.4	t.w.	1.58128	0.10	-11.28210	0.16	-41.2	1.6	-18.0	2.4	162.4	67.4
90	497				13.7	10.2	t.w.	0.99022	0.11	-10.13985	0.14	-91.1	1.8	-115.5	2.0	55.1	70.9
91	634				13.9	14.5	t.w.	-10.63798	0.32	-9.84287	0.21	-62.2	12.7	89.3	5.6	100.0	38.8
92	78				11.4	9.4	t.w.	0.75508	0.11	-9.33208	0.11	58.6	1.4	61.3	1.4	195.7	50.1
93	96	E80	S9-9	I.9SE	11.8	9.9	Pau.	5.65695	0.15	-8.18150	0.19	-52.1	2.0	-67.0	2.6	119.5	106.1
94	6040	E76	S9-20	I.9SW	13.2	9.1	Pau.	4.30397	0.32	-8.03425	0.38	84.7	6.8	42.5	9.9	191.1	66.5
95	157		S8-7		12.1	8.3	t.w.	-3.69044	0.18	-7.42071	0.17	186.3	3.6	-21.2	2.7	60.0	30.2

96	243		S7-16		12.7	7.4	t.w.	1.62069	0.11	-7.24675	0.12	75.5	1.8	143.6	2.3	135.4	74.7
97	6295				12.1	8.8	t.w.	5.25694	0.34	-7.07123	0.30	8.0	6.7	36.7	6.3	207.0	107.2
98	63	E79	S9-114	AF	11.0	9.5	t.w.	-6.50895	0.17	-6.90214	0.27	101.0	2.8	60.8	4.6	155.7	50.2
99	71	E69	S6-63		11.4	6.6	t.w.	1.84516	0.13	-6.31453	0.11	227.7	2.1	60.0	3.4	140.8	39.7
100	210				12.3	8.0	t.w.	5.40038	0.20	-5.95261	0.19	-137.6	3.1	-104.7	2.6	-16.6	52.0
101	619				13.6	16.7	t.w.	15.63094	0.28	-5.86463	0.23	254.2	8.3	151.8	5.6	-83.3	88.9
102	73				11.2	10.6	t.w.	-8.92005	0.15	-5.74358	0.14	107.2	2.0	59.6	2.1	111.9	18.8
103	169	E65	I.9W	I.9W	12.1	6.3	Pau.	2.87892	0.12	-5.60405	0.15	204.2	1.9	136.5	2.1	136.9	67.1
104	423		S5-187	S5-187	13.2	5.8	t.w.	-1.70504	0.14	-5.53100	0.16	-33.5	1.9	-155.9	2.4	10.4	52.8
105	371				13.0	6.8	t.w.	-3.93026	0.73	-5.54228	0.44	234.8	9.6	-155.5	7.4	38.7	47.6
106	183				12.2	7.4	t.w. MPE	4.85346	0.17	-5.54619	0.14	86.6	1.9	208.5	1.9	19.4	55.8
107	364				13.1	7.8	t.w.	-5.51646	0.20	-5.56841	0.20	-18.4	4.1	196.4	4.3	57.5	46.4
108	6041	E82	S10-136		13.2	10.1	Pau.	-8.61883	0.24	-5.31270	0.40	-80.1	4.6	139.5	9.3	-72.1	72.7
109	310		S5-191		12.9	5.8	t.w.	3.18965	0.19	-4.86952	0.16	-55.2	2.4	-141.3	1.9	107.0	38.5
110	218	E55	S4-71	R75	12.6	4.1	t.w.	0.77398	0.06	-4.06227	0.07	3.4	0.4	-174.5	0.4	63.6	50.8
111	914		S4-196		14.4	4.5	t.w.	2.22522	0.30	-3.93992	0.29	199.3	4.3	150.6	4.4	-27.8	115.0
112	136	E74	S8-181	AF NW	11.9	8.4	Pau.	-7.61325	0.12	-3.58604	0.15	-67.6	5.7	-141.5	3.1	54.6	73.5
113	112		S5-183	S5-183	11.6	5.8	t.w.	4.61476	0.13	-3.43525	0.15	-179.5	1.6	-78.0	2.0	-187.0	39.1
114	247				12.4	9.5	t.w. MPE	-8.87355	0.11	-3.44397	0.14	-121.9	1.5	-74.3	2.6	67.6	52.6
115	313		S9-143		12.8	9.0	t.w.	-8.36240	0.12	-3.35608	0.13	24.5	1.7	-121.3	2.0	190.8	96.9
116	-1		S10-50		14.7	10.1	Yel.	9.54824	408.36	-3.18128	307.07	-19.0	7.8	-149.5	6.4	88.5	87.4
117	18	E41	I.33E	I.33E, R54	11.0	3.2	Pau.	0.66176	0.06	-3.12562	0.07	261.5	0.4	-55.0	0.4	169.7	20.5
118	383				13.2	11.2	MPE	-10.71378	0.11	-3.09565	0.15	-9.4	1.8	133.7	2.3	169.9	47.6
119	237	E47	S3-30	R42	12.6	3.4	t.w.	1.67000	0.07	-2.96310	0.05	-31.3	0.5	151.8	0.3	31.9	54.9
120	221	E53	S3-374	R64	12.7	3.9	Pau.	-2.74767	0.11	-2.82012	0.10	-19.4	0.6	-171.5	0.6	17.8	22.2
121	265		S8-196		12.6	8.6	t.w.	-8.08601	0.13	-2.90700	0.10	30.6	3.3	-64.7	3.7	208.9	49.6
122	6051	E43	S3-19		12.0	3.2	Pau.	-1.58166	0.15	-2.78548	0.09	287.5	4.6	-66.9	3.0	-122.5	47.2
123	6627		S7-30	S7-30	14.0	7.0	t.w.	6.47995	2.09	-2.67962	2.46	-101.1	7.3	-127.6	5.4	-27.4	48.9
124	578		S5-34		13.7	5.1	t.w.	-4.31319	0.35	-2.71983	0.82	-135.7	7.4	-125.1	16.2	18.6	78.7
125	320	E81	S9-283	AFN WNW	12.8	9.9	Pau.	-9.60670	0.20	-2.55478	0.15	64.6	2.6	-50.4	2.4	37.6	72.1
126	6044				15.0	6.4	t.w.	-5.83611	0.24	-2.53867	0.22	-131.2	7.2	51.3	7.0	239.3	21.0
127	64	E33	S2-13	I.33N	11.7	2.2	t.w.	-0.04844	0.06	-2.19802	0.09	135.8	0.4	-236.0	0.6	39.0	45.1
128	231	E45	S3-26		12.7	3.3	Yel.	-2.60948	0.08	-2.08260	0.08	224.4	0.5	52.4	0.5	60.1	30.3
129	10006		S4-262		16.8	4.7	Yel.	4.29051	26.47	-1.91401	22.00	-48.3	1.2	-196.0	2.1	39.9	57.9
130	30	E34	S2-17		11.2	2.3	t.w. MPE	1.28217	0.06	-1.87551	0.06	354.3	0.3	-14.7	0.4	64.5	43.5
131	353		S6-96	S6-96	13.0	6.4	t.w. MPE	-6.04464	0.25	-1.95065	0.39	-24.9	3.5	283.3	4.9	-20.1	51.9
132	956		S10-32	S10-32	14.5	10.3	t.w.	10.19469	0.15	-1.71080	0.14	110.9	1.7	150.5	2.3	214.8	73.6
133	94	E26	S1-24	I.16SSW	11.8	1.8	t.w.	0.72112	0.08	-1.60515	0.07	97.9	0.4	-258.3	0.4	153.5	40.3
134	34	E51	I.13E2	I.13E2	10.8	3.6	Fritz	-3.17210	0.14	-1.73202	0.25	-247.8	2.2	20.6	4.2	63.0	30.9
135	6046	E58	S7-180	I.3E	13.5	7.5	t.w.	-7.34555	0.22	-1.65065	0.27	-121.5	2.9	-32.9	3.5	103.5	38.3
136	362	E60	S4-258		12.4	4.7	Pau.	-4.37896	0.14	-1.63966	0.13	-168.8	2.0	61.4	2.0	320.4	77.7
137	132	E30	S2-6	I.16SSE1 R29	12.3	2.1	Pau. Yel.	1.60887	0.05	-1.34653	0.06	306.2	0.4	72.5	0.4	179.9	25.5
138	386		S5-236	S5-236	13.3	5.7	t.w.	-5.55408	0.15	-1.29457	0.10	195.9	2.4	47.7	1.8	142.8	52.0
139	174	E50	S3-10	I.16SE3	12.3	3.5	Pau.	3.34664	0.16	-1.13914	0.08	-22.1	1.0	198.4	0.5	306.0	60.3

				R79													
140	928	E42	S3-96		14.3	3.2	Yel.	-3.13110	0.38	-0.66042	0.40	-33.9	5.7	207.4	6.1	41.8	45.1
141	266	E25	S1-22	W14	12.9	1.7	t.w.	-1.62041	0.07	-0.49944	0.04	310.8	0.4	-133.4	0.3	-293.6	95.9
142	562	E14	S0-14	R13 W9	14.0	0.8	Gil.	-0.75405	10.06	-0.28714	8.63	94.2	0.2	-58.9	0.2	-57.0	22.4
143	324		S2-22	R34	13.0	2.3	t.w.	2.31737	0.07	-0.24924	0.07	-66.3	0.9	232.8	1.0	91.4	43.6
144	1210				14.5	4.0	t.w. MPE	-3.97965	0.21	-0.07189	0.30	29.8	3.3	-8.0	4.1	-71.6	68.6
145	186	E64	S5-231		12.0	5.8	t.w. MPE	5.81326	0.35	0.08010	0.30	3.0	4.8	197.6	4.3	28.3	81.0
146	644		S7-161	S7-161	13.7	7.4	t.w.	-7.36747	0.12	0.05917	0.16	-72.3	2.2	-147.2	2.8	-31.6	76.2
147	396	E24	S1-21	W7	13.5	1.6	Yel.	-1.64325	0.05	0.10190	0.06	161.1	0.6	-219.9	0.9	-25.9	69.5
148	6080				15.7	1.1	MPE	-1.03195	0.69	0.21609	0.53	5.0	5.9	-183.9	4.9	-343.3	108.4
149	287	E78	S9-1	PMM20 01B1b	12.8	9.5	Pau.	9.45792	0.10	0.27966	0.12	-98.2	1.5	-108.5	1.6	-214.6	113.8
150	58	E67	S6-81	I.1E	11.1	6.4	t.w.	6.36728	0.21	0.25059	0.18	-104.9	7.2	187.7	4.4	9.9	29.4
151	1182				15.0	6.7	t.w. MPE	-6.69250	0.18	0.50257	0.18	-114.3	2.3	-203.9	2.3	152.5	97.7
152	37	E27	S2-9	I.16CC	11.2	2.1	Pau.	2.00265	0.13	0.55329	0.07	-75.6	1.4	244.4	1.1	246.2	29.8
153	52	E63	I.1W	I.1W	9.3	5.3	Pau.	5.26254	0.65	0.60162	0.72	-112.6	10.5	315.0	10.5	45.1	47.7
154	2	E39	I.16NE	I.16NE	9.2	3.1	Pau.	2.88734	0.24	0.99219	0.21	108.3	3.3	-356.7	2.8	-9.4	21.9
155	297				12.8	9.5	t.w.	9.44270	0.18	1.03930	0.26	52.2	3.2	-50.5	5.9	-251.9	37.4
156	16	E19	S1-9	R3 I.16NW	11.0	1.2	Gil.	0.08387	9.86	1.21967	10.09	236.2	0.3	26.8	0.3	-14.9	15.4
157	22	E31	S2-10	I.29N	11.0	2.1	Pau.	-1.58471	0.13	1.41130	0.13	186.0	0.7	-233.2	0.9	-189.5	94.8
158	691		S3-190	S3-190	14.1	3.5	Yel.	-3.16372	0.09	1.43188	0.13	-118.4	0.6	-127.1	0.7	-249.8	89.4

Table 3: Young stars without determined orbital solutions. Radial velocities determined in this work are annotated with this work – t.w., Trippe et al., 2008 is abbreviated Tri., Paumard et al., 2006 as Pau., Gillessen et al., 2017 as Gil., Yelda et al., 2014 as Yel. IRS stars are abbreviated as I.

A4.3 Tables: Properties of stars consistent with belonging to angular momentum overdensities

Delta Evidence	MPE	Mag	Orbit	Paumard	R	UCLA	index
1.23236	S31	15.85	yes	E7	0.140883	S0-8	8.0
0.284251	S67	12.35	yes	E15	0.785569	S1-3	15.0
0.257495	S66	14.80	yes	E17	0.91267	S1-2	17.0
0.111609	S96	10.75	yes	E20	1.01648	S1-11	18.0
0.151909	S91	12.72	yes		1.24012		19.0
0.156153	S83	13.73	yes	E16	0.970887	S0-15	20.0
0.122042	R14	13.2434	yes	E22	1.49567	S1-14	21.0
0.229224	S97	10.83	yes	E23	1.20495	S1-16	22.0
0.431062	R44	13.56	yes		2.39507	S2-21	23.0
0.150007	S87	14.23	yes	E21	1.88273	S1-12	24.0
0.0788419	R85	11.95	yes	E56	3.14758	IRS34W	29.0

0.130773	R1	14.05	yes	E29	0.802778	S2-7	31.0
0.569367	S5	15.37	yes	E8	0.0669288	S0-26	32.0
0.127589	R39	12.21	yes	E40	1.77438	S3-5	34.0
0.359158	R30	11.58	yes	E32	2.42514	S2-15	35.0
1.21663		12.26	no	E35	2.29462	S2-16	NaN
1.30642		12.70	no	E36	2.34171	S2-19	NaN
1.21927		13.18	no	E38	2.77465	S2-74	NaN
1.29563		13.22	no	E61	4.70471		NaN
1.14487		13.81	no	E44	3.29133	S3-25	NaN
1.42171		14.78	no		6.96803		NaN
1.02538		12.31	no	E28	2.08402	S2-4	NaN
1.77592	S11	14.7349	no		0.647205	S0-9	NaN
1.34486		13.25	no	E76	9.11443	S9-20	NaN
1.08638		12.0764	no		8.28775	S8-7	NaN
1.99746		12.1135	no		8.81132		NaN
1.15591		10.96	no	E41	3.19491		NaN
1.32925		12.0253	no	E43	3.20321	S3-19	NaN
1.98846		12.73	no	E45	3.33866	S3-26	NaN
1.17552		11.24	no	E34	2.27189	S2-17	NaN
0.816577		14.47	no		10.3372	S10-32	NaN
1.02802		12.27	no	E30	2.09801	S2-6	NaN
0.752306		12.34	no	E50	3.53519	S3-10	NaN
1.13523		12.86	no	E25	1.69564	S1-22	NaN
1.72061		15.70	no		1.05415		NaN
1.25565		11.16	no	E27	2.07763	S2-9	NaN
1.07359		14.06	no		3.47266	S3-190	NaN

Table 4: Stars consistent with belonging to the clockwise disk.

index	MPE	UCLA	Paumard	Mag	R	Delta Evidence	Orbit
7	S12	S0-19	E5	15.48	0.0306114	0.869801	yes
0		S7-216		10.8521	7.86087	1.48128	no
3		S3-17		13.49	3.17676	1.42991	no
6		S6-89		11.95	6.22556	1.91016	no
9			E59	13.14	4.55295	1.25763	no
11		S3-331	E52	13.60	3.84197	1.38002	no
13		S10-7	E85	12.59	10.6752	0.850875	no
15		S4-364	E62	12.14	4.99596	1.4844	no
16		S6-93	E70	12.74	6.66203	1.9463	no
18				12.14	8.67924	0.476479	no
25		S7-19		13.2978	7.5208	1.23329	no
26			E90	11.57	12.7703	1.14776	no

29		S7-20		13.3627	7.86642	1.18854	no
32				13.3406	12.2262	0.992025	no
35		S9-13		13.18	9.3076	1.67622	no
47			E89	14.44	12.2754	1.38127	no
52		outer-1		11.96	28.7782	1.28205	no
53		outer-2		14.867	22.4266	1.28966	no
56				15.8499	24.8177	1.35955	no
60				15.94	11.1737	1.57827	no
64				15.7765	20.6513	1.89283	no
67		S7-228		12.0222	7.92802	1.50092	no
75	S93			15.38	1.09141	1.80819	no
76	S26	S0-31	E13	15.4293	0.721656	1.65122	no
77	S7	S0-11	E12	15.5999	0.497586	1.6382	no
87				16.7216	14.4812	1.86302	no
90				13.7248	10.1881	1.44307	no
91				13.8585	14.4931	1.75828	no
100				12.2566	8.03726	1.12067	no
102				11.2038	10.6092	1.84185	no
118				13.1939	11.152	0.922799	no
123		S7-30		14.05	7.01209	1.2573	no
126				14.9965	6.36436	0.720289	no
136		S4-258	E60	12.45	4.67586	0.651513	no
149		S9-1	E78	12.76	9.46204	1.60932	no
155				12.7962	9.49969	1.37407	no

Table 5: Stars consistent with belonging to the counter clockwise disk.

index	MPE	UCLA	Paumard	Mag	R	Delta Evidence	Orbit
6	S60			16.76	0.113085	0.629584	yes
30	R70	S4-36	E54	12.82	2.08898	0.656347	yes
10		S7-236		12.666	7.94508	1.3941	no
30		S7-10	E73	11.62	7.70832	1.05606	no
36		S9-23	E77	13.57	9.23117	1.30484	no
40		S10-5	E83	11.97	10.1532	1.78867	no
65				15.3536	8.67658	1.53632	no
84		S5-237		13.25	5.59141	1.15228	no
85		S4-169	E57	13.53	4.43282	1.95868	no
86		S6-82	E72	13.56	6.73303	1.50384	no
96		S7-16		12.6886	7.42579	1.71009	no
99		S6-63	E69	11.36	6.57862	0.921401	no
103			E65	12.13	6.3003	1.06481	no
105				12.9989	6.79444	1.0242	no

106			12.2293	7.36999	1.69583	no
143	S2-22		13.03	2.33073	1.99339	no
145	S5-231	E64	12.01	5.81382	1.60709	no
150	S6-81	E67	11.08	6.3722	1.47119	no
153		E63	9.328	5.297	0.938662	no

Table 6: Stars consistent with belonging to the inner warp feature.

MPE	UCLA	Paumard	Mag	R	Δ Evidence	Orbit
S9	S0-5	E9	15.15	0.091365	1.38003	yes
S60			16.76	0.113116	0.589293	yes
	S5-235		13.21	5.33721	1.95023	no
			14.78	6.96797	0.958125	no
			13.71	7.06065	1.15084	no
	S8-4	E75	11.12	8.54245	0.321072	no
	S9-23	E77	13.57	9.2312	0.983455	no
	S10-5	E83	11.97	10.1532	0.673866	no
	S10-4	E84	11.29	10.2412	0.360631	no
			13.8392	12.0786	1.61299	no
	S10-48	E86	15.11	10.7369	1.76352	no
	S11-5	E88	11.70	11.7584	1.19523	no
			13.87	19.3905	1.95884	no
			14.4037	16.7276	0.872181	no
			15.3588	11.2452	1.91458	no
	S11-21	E87	13.51	11.2396	0.531913	no
			15.3722	9.27017	1.86716	no
			15.3536	8.67654	1.52626	no
			14.3489	15.152	1.82959	no
	S1-33		15.06	1.2391	1.43069	no
	S2-58		14.04	2.45128	0.99258	no
	S4-169	E57	13.53	4.4328	1.72397	no
			16.7216	14.4813	1.87428	no
	S2-76		15.15	2.81263	1.45724	no
			12.6724	11.3924	1.95734	no
			11.4295	9.36258	0.50663	no
	S9-20	E76	13.25	9.11447	1.2888	no
	S7-16		12.6886	7.42576	0.981402	no
			12.1135	8.81131	1.71294	no
	S5-187		13.21	5.78784	1.15952	no
			12.2293	7.36998	1.94377	no
	S4-71	E55	12.61	4.13535	1.1851	no
	S3-30	E47	12.65	3.4013	1.13645	no

S3-374	E53	12.73	3.93736	1.02151	no
S2-13	E33	11.71	2.19857	1.75181	no
S1-24	E26	11.82	1.7597	1.69777	no
S2-22		13.03	2.33074	1.45088	no
S5-231	E64	12.01	5.81383	1.35316	no
S7-161		13.6985	7.36771	1.74088	no
		15.70	1.05406	1.95867	no
S3-190		14.06	3.47265	1.7133	no

Table 7: Stars consistent with beging on outer warp of the clockwise disk.

MPE	UCLA	Paumard	Mag	R	Δ Evidence	Orbit
S4	S0-3	E6	14.58	0.091998	1.90794	yes
S14		E2	15.63	0.00271191	0.0173749	yes
S2		E1	14.16	0.0107373	1.44597	yes
			12.4966	11.3631	1.85805	no
	IRS10W		10.9925	8.29025	1.99354	no
		E90	11.57	12.7704	0.561536	no
			13.6698	9.79173	0.463197	no
			13.71	7.06064	1.24503	no
	S7-10	E73	11.62	7.70833	1.77437	no
	S8-15		13.20	8.19548	1.24777	no
			13.3406	12.2262	0.875552	no
			14.1015	13.2585	1.55044	no
			13.7893	14.4404	1.44733	no
			13.8392	12.0786	1.7897	no
			14.7092	20.9025	1.34779	no
			12.7599	20.3779	1.0109	no
			13.87	19.3904	0.882945	no
			14.4037	16.7275	1.21626	no
	outer-1		11.96	28.7817	1.22527	no
			15.4278	14.3609	0.223891	no
			15.0569	10.0754	0.611814	no
			15.94	11.1737	1.2928	no
	S11-21	E87	13.51	11.2396	1.53688	no
			15.3722	9.27012	0.551794	no
			16.6731	21.158	0.798925	no
			15.7765	20.651	1.18804	no
			15.41	5.64006	1.65611	no
			14.3489	15.152	0.281202	no
			16.5563	11.611	1.77148	no
		E46	10.703	3.38768	0.919629	no

	S2-4	E28	12.31	2.08402	1.69374	no
	S2-50		15.34	2.27306	0.983683	no
	S3-3		15.1047	3.14943	1.12699	no
S93			15.38	1.09142	1.20983	no
S7	S0-11	E12	15.5999	0.496342	1.10106	no
	S3-314		15.50	3.83191	1.05654	no
	S3-2		12.25	3.11262	1.6286	no
			16.7216	14.4813	0.294344	no
	S2-76		15.15	2.81263	1.73484	no
	S9-114	E79	11.00	9.48721	0.556273	no
			11.2038	10.6092	0.709141	no
	S5-187		13.21	5.78785	1.98491	no
	S4-196		14.4433	4.52485	1.68582	no
	S8-181	E74	11.88	8.41553	1.14199	no
			12.3832	9.51841	1.17089	no
	S9-143		12.8182	9.01071	1.68612	no
	S8-196		12.557	8.59268	1.07554	no
	S5-34		13.7426	5.09913	0.966934	no
	S3-26	E45	12.73	3.33865	1.81866	no
	S7-180	E58	13.5213	7.52872	1.9775	no
	S2-6	E30	12.27	2.098	1.8105	no
	S5-236		13.2592	5.70296	1.91062	no
	S7-161		13.6985	7.3677	1.75061	no

Table 8: Stars consistent with beging on the newly detected disk.

Danksagung

The list of people I want to say thank you to is long. First and foremost my family, my parents for their continued love and support, for always keeping my back free and for enabling the incredibly privileged life that I live. The family in Günzgen, for building the save social background that I needed during my childhood, my cousins Niels, David, Joshua, Samuel, Joanna, Eva, Phillip, Christina for being my “substitute sibilings”; as well as all my aunts and uncles. Specifically, I would like to thank my ‘Patenonkel’ and ‘Patentante’ Franz & Claudia for all the entertainment, fun and wisdom shared (as well as the all bank notes that enabled the former).

Next, I would like to thank my supervisors here in Garching Prof. Reinhard Genzel, Dr. Stefan Gillessen and Dr. Frank Eisenhauer for guiding my through my PhD. Here, I would like to thank specifically Stefan for believing in me and guiding me through my maybe-a-bit-rough start; Frank for entrusting me to work at the heart of what is probably one of the most exciting current instruments in astronomy and probably science in general; and Prof. Genzel for the very personal guidance, encouragement and support during my PhD and enabling my next projects. Second most important was my "indirect supervisor" Michi Bauböck, who always has and had an open ear, time and patience for even the most-stupidest of crazy ideas. I would also like to thank Jason Dexter for being an incredibly knowledgeably guy who always has had an open ear and more than one suggestion for me, Julia Stadler for being the most amazing statistic support that one can have, and Jinyi Shangguang and Taro Shimizu for all the general GRAVITY related support.

I would like to thank my friends, going from oldest to closest in time: I would like to thank Sven Rutschmann (Sven) & Niklas Granacher (Dj Nikkk), Moritz Helfrich (Momo), Juan Velten (Juan), Jan Heinig (Jan), Fabian Böhler (Böhler), Roman Risch (Roman), Mario Gersbach (Mario), Anna Schnell (Anna), Angela Wegmann (Angie), Svenja Dickmann (Sveni), Elena Wiehn (Elena), Daniela Fuchs (Dani). The Konstanz-Connection: Philip Lindner (Lindner), Fabian Hersperger (ferby a.k.a. Bergsperger), Benjamin Graf (benni), Fabian Hägele (Hägi a.k.a. kleiner Hagel a.k.a. tower-of-power a.k.a. organizer456), Lukas Bächlin (beachlin), Milan Wesseler (der Wesseler), Tamino Taylor (Tamino), Janek Zähringer (Janek Z), Philipp Balz (Balzi). The Munich crew: Riccardo Arcodia (Ricky a.k.a. the son of god), Fruzsina Kovacs (Fruzsi a.k.a. Fruzco a.k.a. the daughter of god), Nicola Locatelli (Tosca a.k.a. the ugly man), Adam Malyali (Adam Smith), Jacob Ider-Chitham (DJ ...), and Felix Widmann (Flexi) – also for all the science stuff.

Finally, I would like to thank Oksana for being with me.

Lebenslauf

Sebastiano Daniel Maximilian von Fellenberg
Nationalities: German, Swiss

24.07.1991	Zürich, Switzerland
1998 – 2002	Primary School, Hohentengen am Hochrhein, Germany
2002 – 2004	Middle School School, Hohentengen am Hochrhein, Germany
2004 – 2006	High School School, Waldshut, Germany
2006 – 2009	High School School, Shanghai, China
2009 – 2011	High School School, Waldshut, Germany
2011	Abitur, Waldshut, Germany
2011 – 2014	Bachelor in Physics, Universität Konstanz
2015 – 2017	Master in Nuclear, Particle, and Astrophysics, Technische Universität München
2017 –	P.h.D. in Astronomy, Max Planck for Extraterrestrial Physics
	& Ludwigs-Maximilians Universität München